FACULTY OF SCIENCES

DEPARTMENT OF GEOGRAPHY

Characterization of ionospheric irregularities and their influence on high-accuracy positioning with GPS over mid-latitudes

PhD THESIS

submitted in partial fulfillment of the requirements
for the degree of Doctor in Sciences

Gilles WAUTELET

Academic year 2012–2013

This manuscript is submitted in partial fulfillment
of the requirements for the degree of Doctor in Sciences
on March 27, 2013.

Supervisor:	Dr. R. Warnant	-	ULg (Liège)
President:	Dr. R. Billen	-	ULg (Liège)
Examinators:	Dr. M. Aquino	-	IESSG (Nottingham, UK)
	Dr. J-C Gérard	-	ULg (Liège)
	Dr. M. Hernandez-Pajares	-	UPC (Barcelona, Spain)
	Dr. V. Pierrard	-	IASB (Brussels)

Gilles WAUTELET
Characterization of ionospheric irregularities and their influence on high-accuracy positioning with GPS over mid-latitudes

Geomatics Unit, Department of Geography
Faculty of Sciences, University of Liège
Allée du Six Août, 17 B-4000 Liège
Belgium
Tel. +32-4-366 57 44
E-mail. gilles.wautelet@ulg.ac.be

Abstract

Over the last decade came major breakthroughs in satellite navigation and positioning, due to the development of precise positioning techniques based on Global Positioning System (GPS) signals. Modern processing methods, such as the Real-Time Kinematics (RTK), allow the GPS user to determine its position in real-time with an accuracy of a few centimeters. The success of these algorithms relies on the cancellation and/or the mitigation of the various errors affecting signal propagation. Among these errors is the delay due to the ionospheric refraction. More particularly, the presence of irregularities in the ionospheric plasma is responsible for positioning errors reaching several (deci)meters. As a result, there is a growing demand from GPS user communities (such as land surveyors or civil engineers) to be informed, if possible in advance, of the occurrence of irregularities that might impact on their positioning solution.

Based on a ten years GPS dataset collected over Belgium, this thesis aims at assessing, understanding and modeling the occurrence of ionospheric irregularities as well as estimating their effects in terms of positioning accuracy. Firstly, we carry out a climatological study of irregularities to identify and characterize the most recurrent features. We can distinguish two main irregularity types: those due to space weather events (such as Coronal Mass Ejections – CMEs – or solar flares) and the others, constituting the bulk of irregularities observed at a single station and referred to as "quiet-time" irregularities, as they occur during quiet geomagnetic conditions. These latter are then divided into two groups: the first is made up of Medium-Scale Traveling Ionospheric Disturbances (MSTIDs) which occur during autumn/winter daytime. In the second group are the summer nighttime irregularities, which are rapid fluctuations of the Total Electron Content (TEC) probably associated with spread-F phenomenon.

Next, we develop a model of quiet-time irregularity occurrence, based on a statistical analysis of the aforementioned dataset. Computations rely on several mathematical modeling tools, such as the Principal Component Analysis (PCA), the Generalized Least-Squares (GLS) algorithm and the AutoRegressive and Moving Average (ARMA) method. The resulting climatological model is made up of two components reproducing daily profile as well as secular variations of the ionospheric variability for a typical GPS station in Belgium.

The last part of this work deals with the impact of irregularities on relative positioning. This technique allows the measurement of the vector (called baseline) joining the receiver (user station) to a reference station whose position is accurately known. More precisely, we assess the effect of baseline length and orientation during the occurrence of MSTIDs and geomagnetic storms through the processing of the Belgian Dense Network, made up of 66 dual-frequency GPS stations. Finally, the relationship between positioning error and the presence of ionospheric irregularities detected at a single station is investigated, filling the gap between the scientific and the GPS-user communities.

Résumé

Ces dernières années, des avancées capitales ont été réalisées dans le domaine de la navigation par satellites, en particulier grâce au développement de méthodes de positionnement de haute précision basées sur les signaux issus du *Global Positioning System* (GPS). Ces méthodes modernes, telles que le *Real-Time Kinematics* (RTK), permettent à l'utilisateur de déterminer sa position instantanément, et ce avec une précision centimétrique. Le succès de ces algorithmes est basé sur l'annulation et/ou l'atténuation des différentes erreurs qui affectent la propagation des signaux GPS, parmi lesquelles figure le délai induit par la réfraction ionosphérique. Plus particulièrement, la présence d'irrégularités dans le plasma ionosphérique est responsable d'erreurs de position pouvant atteindre plusieurs (déci)mètres. Il existe donc une réelle demande émanant des utilisateurs de GPS – comme les géomètres ou les ingénieurs civils – désireux d'être informés de l'occurrence de ces irrégularités affectant la précision de leur mesure de position.

Appuyant ses résultats sur une banque de données GPS couvrant dix années de mesure, cette thèse a pour mission d'évaluer, comprendre et modéliser l'occurrence des irrégularités ionosphériques ainsi que d'estimer leurs effets en termes de précision du positionnement. Tout d'abord, la réalisation d'une étude climatologique de ces irrégularités a permis l'identification et la caractérisation des motifs les plus récurrents de la série temporelle. Nous avons ainsi pu distinguer deux principaux types d'irrégularités. Les premières sont générées par les évènements de la météo spatiale (*space weather*), tels les éjections de masse coronale ou les éruptions solaires. Le second type, qui représente la majorité des irrégularités détectées, a reçu le qualificatif de "quiet-time", étant donné le contexte géomagnétique calme dans lequel elles sont observées. Cette dernière catégorie a ensuite été divisée en deux groupes, dont le premier comprend les perturbations itinérantes de moyenne échelle (*Medium-Scale Traveling Ionospheric Disturbances*, ou MSTIDs), apparaissant généralement durant les mois d'automne et d'hiver en journée. Dans le second groupe, on retrouve les irrégularités nocturnes estivales, qui correspondent à des variations rapides du contenu électronique total (*Total Electron Content*, ou TEC), ces dernières étant probablement associées à une phénomène de *spread-F*.

Dans un deuxième temps, nous avons mis sur pied un modèle d'occurrence des irrégularités "quiet-time", basé sur une analyse statistique de la banque de données susmentionnée. Cette modélisation s'appuie sur une multitude d'outils mathématiques, tels que l'analyse en composantes principales (ACP), les moindres carrés généralisés ou encore la méthode auto-régressive à moyenne mobile (*AutoRegressive and Moving Average*, ou ARMA). Le modèle climatologique résultant se divise en deux composantes reproduisant aussi bien le profil journalier que les variations séculaires de la variabilité ionosphérique observée à partir d'une station GPS en Belgique.

La dernière partie de notre travail concerne l'effet de ces irrégularités sur le positionnement relatif. Cette technique consiste en la mesure du vecteur (appelé ligne de base) joignant le récepteur de l'utilisateur à un autre récepteur (appelé station de

référence) dont la position est connue avec une grande précision. Nous avons évalué plus spécifiquement l'influence de la longueur ainsi que de l'orientation de la ligne de base sur l'amplitude de l'erreur de position durant l'occurrence d'une MSTID ou encore d'une tempête géomagnétique de grande envergure. Ces calculs ont été effectués sur l'ensemble des 160 lignes de base qu'offre le réseau dense belge de stations permanentes GPS, constitué de 66 stations GPS bi-fréquence. Enfin, nous avons étudié la relation entre l'erreur de position et la présence d'irrégularités ionosphériques détectées à une station, ce qui nous a dès lors permis de faire le lien entre, d'une part, la communauté scientifique et de l'autre celle des utilisateurs de GPS.

S'il est généralement admis qu'une thèse de doctorat est le fruit d'un travail personnel, il serait injuste de ne pas remercier à leur juste valeur celles et ceux qui m'ont accompagné et encouragé tout au long de cette aventure périlleuse.
Tout d'abord, je souhaiterais remercier mon promoteur, Mr Warnant, pour m'avoir permis de faire mes preuves dans la recherche ainsi que pour la confiance qu'il m'a accordée durant ces six années. Plus particulièrement, je tiens à le remercier pour ses conseils toujours pertinents et la très grande liberté d'action qu'il m'a octroyée.
Le rôle important joué par les membres de mon comité de thèse mérite aussi d'être souligné : Mme Pierrard, Mr Gérard, merci pour les conseils avisés dont vous m'avez fait part à chaque entrevue.
La qualité de l'environnement professionnel est également un facteur de réussite prépondérant dans le cadre d'une thèse. A ce titre, je souhaiterais remercier mes anciens collègues du bâtiment B de l'IRM pour leur professionnalisme et leurs compétences. Plus particulièrement, j'aimerais remercier Luis, Nico et Alessandro pour m'avoir initié à l'univers du Libre ainsi que pour leur infinie patience lors de mon apprentissage du Bash, du C ou encore du LaTeX. Un merci particulier à Koen pour m'avoir inculqué les rudiments du R, logiciel sans lequel la majorité des résultats de cette thèse n'auraient jamais vu le jour. J'en profite aussi pour remercier celles et ceux qui m'ont aidé à surmonter les difficultés que j'ai rencontrées durant mon parcours sinueux. Merci à Yves Cornet, Stan Stankov, Jean-Claude Gérard et Cédric Heuchenne pour leur savoir-faire spécifique et leur grande disponibilité. Merci également à Matthieu et Benoît pour les nombreuses discussions fertiles et leur relecture attentive.
Les longues journées d'été l'auraient été bien plus encore sans les inoubliables parties de Wo(a)rmux, Doom et autres Quake, les dîners maatjes ou encore le visionnage intensif de certains passages de films cultissimes[1]. Merci à Alessandro, Sami, Almudena, Sabri et Bart pour ces heures de détente professionnelle ! Merci également à Sandrine, pour avoir été une collègue attentionnée et attentive, ainsi que pour les bons conseils qu'elle m'a prodigués.
Enfin, que serais-je sans ma famille, mes amis et mon entourage ? Et plus particulièrement sans mes parents qui m'ont, depuis ma plus tendre enfance, toujours encouragé dans la voie scientifique que je m'étais choisie. Merci également à mon frère Denis pour ses talents graphiques et littéraires. Ma dernière pensée va à ma douce et tendre Masha, dont la gentillesse et l'enthousiasme sans limites m'ont appris à surmonter chaque difficulté avec le sourire...

[1] Ow ! My balls !

La vraie Science est une ignorance qui se sait.

Montaigne

Contents

Chapter 1

Introduction

Surveying is one of the oldest professions. It dates back to the Ancient Egyptian civilization according to historical texts mentioning the first Earth's measurements. Measurements of land plots after the floods of the river Nile as well as alignments succeeding to the building of the famous pyramids were the first works achieved by the ancestors of the land surveyors. A few hundred years later, the Greek Eratosthenes was the first to calculate the Earth's circumference by measuring the distance separating the today's Aswan and Alexandria cities. This first experiment led to an extremely accurate measurement at that time, despite of the low precision of the technique used: the distance was deduced from the number of steps between the two cities. The 17th century saw lots of scientific progress and, in particular, the invention of the theodolite enabled accurate measurement of angles. Later, the development of sophisticated optics and electronics allowed the modern surveyor to perform local measurements with a millimeter accuracy. A major breakthrough was the development of Global Navigation Satellite Systems (GNSS) whose pioneer is the famous Global Positioning System (GPS). This latter has been designed by the American Department of Defense (DoD) and declared operational for civil use in 1995. At the present time, other navigation systems exist, like the Russian GLONASS or the future European Galileo, whose Full Operational Capability is foreseen by this decade's end. With a nominal constellation of 20–30 satellites orbiting on a Medium-Earth Orbit (altitude is about 20000 km), GNSS allow the user to measure his position everywhere on the globe, at any time and with the same level of accuracy.

The use of GPS in surveying covers a wide range of applications and methods, depending on the precision required. In this thesis, we will focus on the relative positioning technique, such as the Real-Time Kinematics (RTK). This technique, broadly used within networks of reference stations, allows to measure the user position in real-time with an accuracy of a few centimeters. The principle of relative positioning relies on the measurement of the vector (called baseline) joining the receiver (user station) to a reference station whose position is accurately known. The use of differenced measurements between the two stations allows to mitigate or even cancel out all common errors. Among them is the delay induced by the ionospheric refraction, which can be considered similar between the two stations as the two satellite-to-receiver paths are approximately parallel. This assumption is realistic and gives satisfactory results if the ionospheric plasma is spatially correlated and if

the stations are close to each other, generally less than 20 km. However, the presence of high-frequency variability in the ionospheric plasma can dramatically decrease the spatial autocorrelation so that the residual ionospheric error could not be neglected anymore and could contaminate the positioning solution. As an example, such irregularities may bias the ambiguity resolution process, leading to positioning errors of several decimeters, even for baselines as short as 10 km. For this reason, ionospheric variability can be considered as the most important limitation to the accuracy and the reliability of the relative positioning technique.

Based on 10 years of GPS measurements in Belgium, this thesis will attempt to answer the following questions.

- How irregular is the ionospheric variability? Does it exhibit some recurrent patterns? How large and how numerous are ionospheric irregularities over mid-latitude regions?
- What are the main physical mechanisms involved in their generation? Are we able to model and forecast them? If not, is there another way of forecasting irregularity occurrence at a single GPS station?
- As irregularities impact on relative positioning, is it possible to forecast the induced positioning error for an RTK user? In addition, how reliable would be the forecast?

Such questions have been studied and discussed throughout the whole manuscript whose organization is the following.
Chapters 2 and 3 contextualize the present research by summarizing the main achievements found in the literature and by providing fundamentals required to understand the developments done in the frame of the next chapters.
In chapter 4, a climatological study of ionospheric irregularities is presented, based on 10 years of GPS data in Belgium. The occurrence rate as well as the amplitude are investigated to identify the most recurrent patterns observed from a Belgian station. At the end of the chapter, several physical mechanisms are proposed to explain the irregularity occurrence.
A climatological model of such irregularities is then presented in chapter 5. This purely statistical model aims at forecasting the regular ionospheric variability observed at a GPS station.
Finally, chapter 6 proposes to assess the influence of irregularities on relative positioning by the analysis of the 161 baselines belonging to the Belgian Dense Network (BDN). In particular, the effect of baseline length and orientation on the positioning error are examined.

Chapter 2

The Earth's ionosphere

Contents

The story of ionospheric research begins with the first transatlantic radio transmission operated by Guglielmo Marconi in 1901. The distance between the transmitter (located at Poldhu in Cornwall) and the receiver (at St John's, Newfoundland, Canada) was about 3500 km. Assuming a straight line propagation, this wireless experiment would not be achieved because of the sphericity of the Earth. Explanation of the physical phenomenon involved in the transatlantic transmission emerged from Arthur Kennelly and Oliver Heaviside, who were the first to predict the existence of a reflective atmospheric layer. This region, called E-layer, consists in an ionized gas layer located at an altitude of about 100–150 km and has been firstly observed by Edward Appleton in 1924. E-layer ionization rate and altitude are varying with local time and latitude, which implies that radio wave propagation is changing over time, as observed by Marconi in another experiment. Considering this particular behavior with respect to incident radio waves, the following definition of the ionosphere has been proposed by Davies [24]: "The ionosphere is defined as that part of the upper atmosphere where sufficient ionization can exist to affect the propagation of radio waves". With the first artificial satellites came the discovery and the study of the ionospheric structure and its strong relationships with geomagnetic and solar environments. Later, the development of navigation systems like the American Global Positioning System (GPS) opened new perspectives in ionospheric

study as they offer a global coverage at any time. More particularly, the ionosphere remains the main error source in satellite positioning so that the understanding of its spatial and temporal behaviors will play a key role in precise positioning techniques. This chapter gives an overview of the regular and irregular ionosphere, mainly focused on mid-latitude regions. First we briefly describe the solar atmosphere, which is the origin of the existence of the terrestrial ionosphere. The next section is devoted to its layer structure, leading to the definition of the Total Electron Content (TEC) which is a fundamental parameter in satellite navigation. In the last part we review the various TEC irregularities, which constitute the main limitation of real-time positioning accuracy.

2.1 Solar atmosphere and space weather

Without the Sun, terrestrial ionosphere would not exist. Indeed, production of free electrons in the ionosphere mainly results from interactions between neutral molecules and Extreme Ultraviolet (EUV) or X-rays coming from the external regions of the Sun. Ionization rate is strongly related to the incoming radiation, which results in regular cycles in the electron concentration N_e. Superimposed to the ionospheric regular behavior are the so-called irregularities, whose a given part find their origin in large-scale solar phenomena such as coronal eruptions propagating into the interplanetary medium.

2.1.1 The Sun

2.1.1.1 Internal and atmospheric structures

Sun structure is made up of two major parts: the internal structure and the solar atmosphere. The first part is divided into three main layers: the core, the radiative and the convective zones (figure 2.1).
In the *core* take place all thermonuclear reactions producing gamma rays and rising the temperature up to $15 \cdot 10^6$ K. This layer extends to approximately the third of the solar radius, where begins the transition zone called *radiative zone*. At the top of the internal structure is the *convective zone* which extends from about 70% of the solar radius to the Sun's surface.
Similarly, solar atmosphere is divided into three layers which are the photosphere, the chromosphere and the corona. *Photosphere* is the lowest layer which constitutes the Sun's surface visible to the naked eye. The bulk of visible light comes from this layer which is also the coldest of the Sun (about 6000 K). Ionized matter is organized in large convection cells called granules between which intense magnetic fields are confined. Photosphere is also peppered with dark regions called *sunspots* in which intense and unipolar magnetic fields take place. These are the coolest features of the Sun, with temperatures dropping to 4000 K.

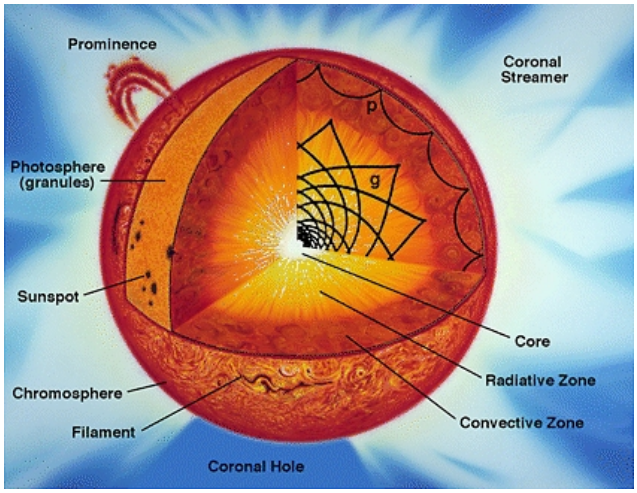

Figure 2.1 – Structure of the Sun. (From Encyclopaedia Britannica Inc., 1989)

Just above the photosphere is the *chromosphere* where temperature increases with altitude. Contrary to the photosphere whose the emitting spectrum consists in a continuum, the chromosphere is only visible in monochromatic radiations corresponding to specific emission lines: for example the red line of hydrogen (Hα), ultraviolet line of calcium (CAIIH), Lyman-α ultraviolet line... Let us also note that the chromospheric emission takes the form of a continuum in the radio frequency band (mm to cm wavelengths). The common features of the chromosphere are the *prominences*, the dark *filaments* and the *plages*. These latter are bright regions surrounding sunspots while filaments correspond to dense and cooler regions which follow the magnetic loops emerging from the photosphere. When such structures are visible out of the limb, they are called prominences.

The outermost layer of the solar atmosphere, which is also the less dense, is called the *corona*. Similarly to the chromosphere, temperature is increasing with altitude and can reach several millions of degrees. This extreme temperature allows electrons and protons to escape from the Sun's gravity field to constitute a continuous stream flowing into the interplanetary medium: the *solar wind*. Coronal spectrum consists mainly in emitting lines in the EUV and X domains[1] which are related to the minor constituents of the corona.

Main coronal features can be observed in solar images taken in various EUV/X wavelengths, as shown in figure 2.2. Among them, one can identify:

[1]EUV wavelength varies between 100 and 500Å while X-rays domain is divided into two groups: soft X-rays (1-100Å) and hard X-rays (0.01-1Å).

- *Coronal loops.* As coronal density is very low, magnetic fields are growing in the corona where their complex topology is revealed by ion motion (tracers).

- *Coronal holes.* These are large zones less dense and colder than the mean corona. They do not emit in the X-ray domain, which explains the "hole" appearing on X-ray images. Coronal holes correspond to large unipolar regions of the photosphere, allowing a fast solar wind to flow along the open magnetic field lines.

2.1.1.2 Solar cycle and rotation

The Sun follows an activity cycle, called *solar cycle*, driven by the solar dynamo and whose period and amplitude are varying from a cycle to another. On average, a solar cycle lasts 11 years and its maximum level is reached after a rapid increase of 4 years. Monitoring of the solar cycle is mainly achieved by the analysis of several quantities called indices. Among them is the *International Sunspot Number*, also called *Wolf sunspot number* (R), which measures the number of sunspots and groups of sunspots observed on the photosphere[2].

Another solar activity proxy is $F_{10.7}$, the radio flux at wavelength 10.7 cm (2.8 GHz), observed daily at the radio station of Penticton, Ottawa (Canada) since 1950. This index is quite well correlated with the sunspot number although the observed layer on the Sun is not identical (photosphere for sunspots and top of the chromosphere for $F_{10.7}$). Scientific literature proposes lots of other solar activity indices that will not be developed here, such as the Total Solar Irradiance (TSI) [29, 65] or MgII core-to-wing index [28, 96].

The Sun also accomplishes a rotation on itself whose period is approximately 25 days at the solar equator and up to 35 days at the poles, called *differential rotation*. From the Earth's point of view, the mean solar rotation, called *synodic rotation period*, lasts 27.3 days.

Solar corona extends up to the limit of the interstellar space. Inside this influence zone called *heliosphere* flows the solar wind, accompanied by the Interplanetary Magnetic Field (IMF) which corresponds to the extension of the solar magnetic field into the interplanetary medium. As the Sun is rotating on its axis, solar wind and IMF do not travel the interplanetary medium radially but follow a spiral shape[3] which crosses the Earth's orbit with an angle of 45°.

[2]This daily index, defined by Rudolf Wolf in 1848, is computed as $R = k(10g + f)$, where k is a numeric constant depending on the instrumentation and the location of the observation, g the number of sunspot groups and f the number of individual sunspots. Its world archive is located in Brussels, at the Royal Observatory of Belgium.

[3]The spiral shape of IMF, called *Parker's spiral*, has been suggested by Eugene Parker in the 1950s.

2.1.2 Solar activity

2.1.2.1 Corotating interaction regions

During solar minimum, solar magnetic field is globally bipolar with high-latitude coronal holes blowing a fast solar wind while the equatorial region belches out a slow solar wind, originating from bright coronal loops. Topology of these regions changes with solar cycle, so that coronal holes migrate towards low latitudes during high solar activity periods[4]. These two different kinds of stream are also prone to solar rotation, leading to an alternation between slow and fast winds. When a fast wind region catches up with a slow one, a front shock appears and the resulting region is called a Corotating Interaction Region (CIR). CIRs are recurrent patterns in the heliosphere since they are associated with solar rotation. Their occurrence can be foreseen by monitoring IMF and solar wind parameters.

2.1.2.2 EUV and X rays variability

The solar emission in EUV and X domains is subject to an extremely large variability over the solar cycle. As those radiations are responsible for the ionization of the Earth's ionosphere (see next section), identifying the phenomena responsible for their enhancements and depletions can therefore help to understand ionospheric variations.
The intensity of EUV and X radiations is strongly correlated with the solar cycle: during solar maximum, Sun's photosphere is peppered with sunspots from which large coronal loops are emerging. Bright emission in the EUV/X lines is therefore enhanced during high solar activity periods, which is illustrated in figure 2.2[5]. In addition to this modulated background, transient events called *solar flares* release tremendous amount of energy in the form of EUV and X rays. Those radiation bursts, due to magnetic reconnection between coronal loops, are responsible for sharp ionization increases in the illuminated ionosphere. As an example, figure 2.2 illustrates the solar flare of October 28 2003 in visible, EUV (white flash) and X domains.

2.1.2.3 Coronal mass ejections

Generally associated with solar flares are the Coronal Mass Ejections (CMEs). They consist in a release of solar energetic particles propagating from the corona towards the heliosphere. This structure, which can measure several times the solar radius, may interact with the terrestrial magnetosphere and cause magnetic storms (see

[4]Difference between the two wind flows lies in the speed (between 250 and 400 km/s for the slow wind and between 400 and 800 for the fast one) but also in the density: slow wind is denser than the fast wind.

[5]The distance between the Sun and the Earth being about $150 \cdot 10^6$ km, solar radiation takes about 8 minutes to reach Earth's atmosphere.

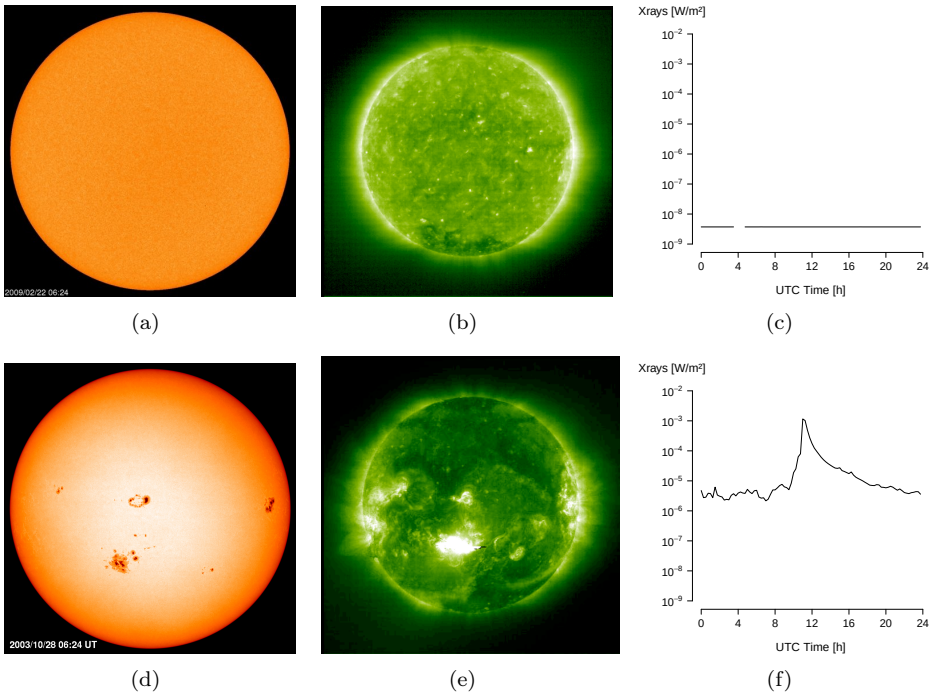

(a) (b) (c)

(d) (e) (f)

Figure 2.2 – Solar activity during solar minimum (a)-(c) and solar maximum (d)-(f). (a) and (d) show photosphere and sunspots coming from SOHO/MDI (credit: ESA/NASA), while (b) and (e) show corona in 195Å wavelength from SOHO/EIT (credit: ESA/NASA). Finally, (c) and (f) display X-ray flux (1–8Å) extracted from GOES satellites (credit: NOAA/SWPC).

following section). CMEs propagate in the interplanetary medium at speeds ranging from 100 to 2600 km/s, with a mean value of 490 km/s [112], taking therefore 1 to 5 days to cross the Earth's orbit. Let us note that, like CIRs, CMEs are also prone to solar rotation so that their propagation in the interplanetary space also follows a spiral shape. As for solar flares, CME occurrence varies with the solar cycle and are more numerous during solar maximum.

2.1.3 Space weather and geomagnetism

Consequences of interactions between solar phenomena such as CIRs and CMEs and the Earth's magnetic field are complex and numerous. They are grouped into the umbrella term *space weather*, which refers to "the variable conditions on the Sun and in the space environment that can influence the performance and reliability of space-borne and ground-based technological systems, as well as endanger life or health" (The American Meteorological Society, 2008).

It is therefore important to observe space weather parameters to be able to forecast the threats due to such events. Usual parameters such as the module and the direction of IMF, density and speed of the solar wind are routinely measured *in situ* by different satellites like the ACE spacecraft (NASA).
Earth's magnetic field can be assimilated to a dipole whose field lines run from the south to the north pole. Magnetic poles do not coincide with geographic ones as the magnetic dipole is tilted with respect to the Earth's rotation axis. The Earth's being located inside the heliosphere, geomagnetic field is thus exposed to solar wind so that its shape is stretched on the opposite side of the Sun, forming the *magnetotail* (figure 2.3).

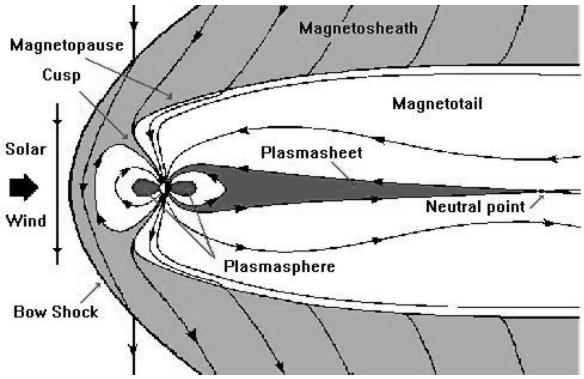

Figure 2.3 – The Earth's magnetosphere. (From [70])

One can define the terrestrial *magnetosphere* as the upper zone of the atmosphere within which the movement of charged particles is driven by the geomagnetic field only; the external medium being under the influence of the solar wind and the IMF. As geomagnetic field lines are oriented northwards, any negative value of the IMF vertical component (Bz) weakens the Earth's magnetic shield and exposes the magnetosphere (and the lower layers) to a stream of solar charged particles. While they interact with atoms and molecules in polar regions, one can observe light emission in specific lines (depending of the atom/molecule species involved): the auroras. The magnetospheric response to such abrupt changes in solar wind parameters is called *geomagnetic storm*[6] and consists in three successive phases:

1. The *initial phase* begins with a shock corresponding to the compression of the magnetosphere, consecutive to the impact of an interplanetary shock. After the shock, the ram pressure increases during tens of minutes.

[6] A more detailed definition and a complete review of geomagnetic storms can be found in [37].

2. The *main phase* corresponds to the creation of an enhanced ring current mainly made up of ions and located between 2 and 7 R_E (Earth's radius). This current is, at the equator, opposite in direction to the Earth's dipole field. It is mainly characterized by a depletion of the Disturbance Storm Time (DST) index (see below). The duration of the main phase is generally between 2 and 8 hours, depending on the severity of the disturbance.

3. The *recovery phase* describes the return to normal conditions, characterized by a progressive recovery in DST index. This phase can last from several hours up to 7 days.

Geomagnetic disturbances are identified using geomagnetic indices whose the most known are the planetary K index Kp and the DST index. These measurements are derived from magnetic measurements collected at several magnetic observatories. Basically, geomagnetic field **B** is a vector field whose geographic coordinates at a given location are X (northwards), Y (eastwards) and Z (local vertical). The horizontal component of **B** is denoted **H** and is, like the three aforementioned quantities, measured in nanoTesla (nT). One also defines the magnetic declination D as the angle between **B** and the local meridian and the magnetic field inclination I, or *dip* angle, which is the angle between **B** and the horizontal plane.
The geomagnetic index Kp is a weighted average of 13 local K indices obtained from magnetic observatories located at a latitude between 44° and 60° (north or south). For a given station, K-index consists in a quasi-logarithmic index characterizing the maximum deviation of the horizontal component **H** relative to an assumed quiet day. K index is difficult to interpret since several phenomena can influence the geomagnetic field in such latitudes: field-aligned currents due to neutral winds, magnetopause currents and auroral electrojets [37]. Kp is a 3-hour index whose values range from 0 (quiet) to 9 (severe storm).
DST index directly assesses the geomagnetic storm intensity as it is a measure of the magnetospheric energy input. It quantifies the decrease in **H** intensity due to the enhancement of the ring current. DST is a hourly index obtained by merging the observations related to four observatories located at a magnetic latitude between $+40°$ and $-40°$ [7].

2.2 Morphology and principal characteristics

2.2.1 Layers and ionization

Earth's atmosphere can be divided in several layers whose nomenclature and characteristics are based upon the variation of a given parameter. If we consider the variation of the temperature with altitude, one gets the well-known classification in four

[7] Details concerning the method used to determine DST are available in [110].

layers, from bottom to top: troposphere–stratosphere–mesosphere–thermosphere (figure 2.4). Taking into account the ionization rate, the atmosphere of the Earth can be divided into two main layers: the neutral atmosphere and the ionized atmosphere, called ionosphere. As ion and electron densities are about 1000 times smaller than that of neutral particles, the ionosphere is a weakly ionized plasma. Variation of electron concentration at a given point results from the combination of electron production, loss and transport processes, as expressed by the continuity equation:

$$\frac{dN_e}{dt} = q - L - \mathrm{div}(N_e \mathbf{v}) \tag{2.1}$$

where N_e is the electron concentration, q the electron production rate, L the electron loss rate and $\mathbf{v}$ the plasma mean velocity. Electron production q is due to the ionization of the different neutral components by incoming solar radiation. Loss phenomenon are mainly caused by recombination of electrons with positive ions while transport processes consist in plasma diffusion, plasma motion induced by neutral winds or by electromagnetic drift due to the presence of an electric field [24] (see below).

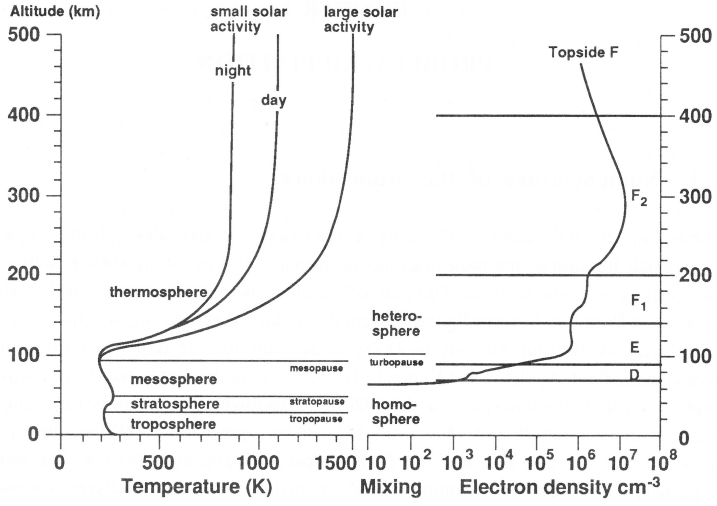

Figure 2.4 – Earth's atmosphere nomenclature with respect to temperature (*left*) and electron density (*right*) distribution. (From [95])

Ionosphere extends from about 60 to 1000 km and its vertical structure is divided into three main layers: the D-, E- and F-regions (figure 2.4). Specific photochemical reactions describing production and loss rates take place in each of these layers, which results in a local peak of the electron density. Figure 2.5 illustrates ion and neutral density profiles which are detailed in the following text.

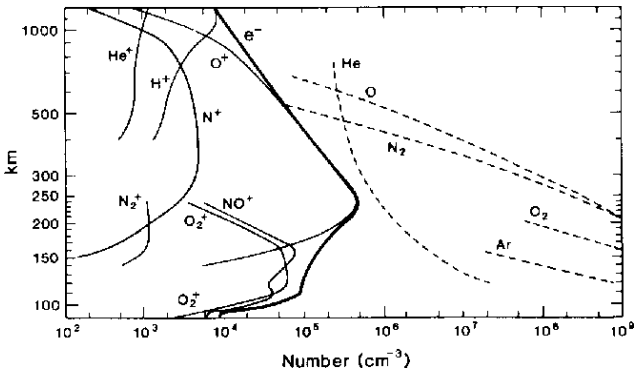

Figure 2.5 – Daytime density profiles of neutrals and ions during quiet solar conditions. (From [22])

2.2.1.1 D-layer

This is the lowest region of the ionosphere (60–90 km) which appears during daytime only. Absence of nighttime D-layer is due to the rapid recombination of electrons with molecular ions like N_2^+ and O_2^+, the main neutral constituents at these altitudes being N_2 and O_2. These neutral molecules are directly ionized by cosmic rays (intergalactic origin) or solar X-rays (between 1 and 10Å). Above 70 km, the minority constituent NO is ionized by Lyman-α radiation (1216Å) to form NO^+ ions, which leads to the D-peak.
Electron concentration in D-layer ranges from 10^7 to 10^{10} e^-/m^3.

2.2.1.2 E-layer

This layer, at an altitude between 90 and 130 km, was the first to be discovered because of its reflective properties with respect to low-frequency radio waves used in telecommunications. Similarly to D-layer, majority neutrals are N_2 and O_2 but majority ions are O_2^+ and NO^+. These molecular ions are obtained by direct ionization of O_2 and N_2, the latter being transformed into NO^+ or O_2^+ by conversion or charge transfer.
Electron concentration in the E-layer varies between 10^{10} and 10^{11} e^-/m^3 but drops to about 10^9 during nighttime due to recombination processes.

2.2.1.3 F-layer

This is the upper and the only permanent layer of the Earth's ionosphere, with an altitude ranging from 130 to 1000 km. Major neutrals are N_2 and atomic oxygen O, the latter being the main constituent above 200 km. Therefore, ion production in the F-region is due to the ionization of atomic oxygen O by Far Ultraviolet

(FUV) or EUV radiations. F-region sometimes exhibits a double peak in the electron concentration N_e, corresponding to two sub-layers F_1 and F_2 showing specific photochemical reactions.

- In the F_1-layer, charge transfer to the most abundant neutrals O_2 and N_2, followed by ion–electron recombination, is responsible for the loss of O^+ ions.
- In the F_2-region, the majority neutral is O and ion production is very efficient. Still proportional to $[O_2]$ and $[N_2]$, loss of O^+ is therefore smaller than in the F_1-layer. As a consequence, electron density in F_2-layer depends on the neutral atomic/molecular ratio, which is mainly determined by air motion and diffusion (transport processes).
  Electron density of the F_2-peak (250-300 km) is the largest value along the whole ionospheric profile and strongly depends on solar activity, as EUV and X ionizing radiations show a solar cycle dependence. Its value fluctuates between 10^{11} (solar minimum, noon) and $5 \cdot 10^{12}$ e^-/m^3 (solar maximum, noon). In the region located above this peak, called *topside*, N_e is decreasing exponentially with height.

2.2.2 Transport

In D, E and F_1-layers, ion and electron concentrations are mostly driven by production and loss rates. Since neutral density is relatively large, recombinations are rapid and charged particle motion corresponds to that of the neutral background: electrons and ions are not able to move under the action of electric and geomagnetic fields. The transport term (expressed in equation 2.1) can thus be neglected with respect to photoionization and recombination processes [24] and these layers are said to be in photochemical equilibrium [66]. This is not the case of the F_2-layer, where the weak density allows charged particles to be subject to geomagnetic and electric fields. More particularly, their motion is constrained to magnetic topology: except for the $(\mathbf{E} \times \mathbf{B})$ drift for which ions and electrons can move across magnetic field lines (see below), charged particles motion is mainly along the lines of force. As a result, transport process can not be neglected neither in the F_2-layer nor in the topside region where this term becomes the predominant one.
When a particle of charge q is exposed to the presence of a magnetic field $\mathbf{B}$ and an electric field $\mathbf{E}$, it is subject to the Lorentz force

$$\mathbf{F} = q(\mathbf{E} + \mathbf{v} \times \mathbf{B}) \tag{2.2}$$

where $\mathbf{v}$ is the particle velocity vector. In the absence of an electric field, the particle motion in a constant and uniform magnetic field is helicoidal, resulting from the addition of a translation along $\mathbf{B}$ (due to the speed component parallel to $\mathbf{B}$) and a rotation around $\mathbf{B}$ (due to the magnetic force related to the perpendicular component of $\mathbf{v}$). The radius of the circle described in the plane perpendicular to $\mathbf{B}$

is called the *Larmor radius* r_L and can be easily computed, considering a uniform circular motion:

$$F = ma = m\frac{v^2}{r_L} = |q|vB \qquad \Rightarrow r_L = \frac{mv}{|q|B} \tag{2.3}$$

with v corresponding to the particle velocity perpendicular to the magnetic field and m being the particle mass. The corresponding angular speed, also called angular cyclotron frequency, is $w = \frac{|q|}{m}B$.
The Larmor frequency, also called *gyrofrequency*, is defined as follows:

$$f_L = \frac{w}{2\pi} = \frac{|q|}{2\pi m}B \tag{2.4}$$

Positive and negative particles rotate in opposite senses; the sense of rotation of a negatively charged ion being given by the fingers of the right hand when the right thumb points in the direction of the magnetic field [24]. From equations (2.3) and (2.4) one can observe that the radius and frequency depends on the particle mass.
In the presence of both electric and magnetic fields, the guiding center of the helix drifts with a velocity $\mathbf{V}$ given by

$$\mathbf{V} = \frac{(\mathbf{E} \times \mathbf{B})}{B^2} \tag{2.5}$$

This drift is perpendicular to both electric and magnetic fields and is independent of the particle charge (magnitude and sign) and of the particle mass. Therefore, electrons and positive ions move in the same direction with the same speed.
Considering the aforementioned motion principles, one can identify three different mechanisms responsible for plasma motion in the ionosphere: the ambipolar diffusion, the motion due to thermospheric neutral winds and the electromagnetic drift ($\mathbf{E} \times \mathbf{B}$). As already mentioned, the first two processes allow plasma to flow along the magnetic field lines while the third one is responsible for the motion across the lines.

2.2.2.1 Ambipolar diffusion

In the same manner as for neutral particles, electrons and ions are subject to diffusion, resulting from the equilibrium between pressure gradients and gravitational forces. However, they have to diffuse together and at the same speed in order to maintain the electro-neutrality of the ionospheric plasma; this mechanism is called *ambipolar diffusion*. If particle density is weak enough, which is the case in the F_2- and in the topside regions, charged particles have to follow the magnetic field lines (field-aligned diffusion), so that ambipolar diffusion has to be mapped along these lines of force. Considering the dipolar shape of the geomagnetic field, diffusion is therefore inhibited at the equator ($I = 0°$) while it exhibits maximum values at the geomagnetic poles ($I = 90°$).

2.2.2.2 Thermospheric winds

Thermospheric winds originate from the pressure gradients existing between warm air of the dayside (solar radiations heat the neutral atmosphere) and cold air of the night side: these are the atmospheric tides. Thus, a complex system of horizontal winds is flowing and the motion is transferred to charged particles by collisions. In the F_2-layer, such winds make electrons and ions moving along the geomagnetic field lines, resulting in upliftings or downwellings of the plasma. If we consider the northern mid-latitude region (*i.e.* in Belgium), wind system mainly consists in an equatorward motion during nighttime while the winds are oriented polewards during daytime. This implies an uplifting of the plasma during nighttime and a downwelling during daytime.

2.2.2.3 Electromagnetic drift

We have seen that thermospheric winds are essentially of tidal origin, due to the thermal gradients between day and night hemispheres. In the E-region, where neutral density is larger than in the F-region, charged particle motion corresponds to that of the neutral background. As a consequence, this flow of charged particles gives birth to electric currents known as Solar quiet (Sq) currents[8] [64, 108]. The combination of Sq electric currents (due to **E**) and of the geomagnetic field **B** results in a drift of the charged particles, in a direction perpendicular to both fields. It comes that any westward or eastward current will induce a drift in the vertical direction, allowing plasma to move across the magnetic field lines and reach F-region heights. The drift velocity is given by

$$v = \frac{E}{B} \cos I \tag{2.6}$$

what implies that this value is zero for polar regions ($I = 90°$) and maximum for the dip equator ($I = 0°$). It is worth noting that this is exactly the opposite than for the ambipolar diffusion, which is maximum at the poles and inhibited at the equator.

2.2.3 Ionospheric monitoring and general features

2.2.3.1 Monitoring the ionosphere

Except for *in situ* measurements made by rockets and satellites, sounding of the ionospheric plasma is generally achieved by the use of electromagnetic waves, mainly in the radio band. Before discussing about interactions between plasma and radio

[8] Intensity of Sq current system depends on solar heating, and therefore on solar activity. In addition to the solar-driven currents, atmospheric tides due to lunar gravitational attraction are also the origin of ionospheric currents, called L currents. Effects of this E-region dynamo can be observed in time series of geomagnetic observations, such as the horizontal components **X** and **Y** used to compute local K-index [90].

waves, let us recall some basic plasma properties. The plasma frequency f_{N_i}, which quantifies charged particle oscillations, is defined as

$$f_{N_i} = \sqrt{\frac{N_i e^2}{4\pi^2 \varepsilon_0 M}} \tag{2.7}$$

with N_i the single-charged particle (electron or ion) i density in the plasma, e the electron charge, ε_0 the permittivity of free space and M the particle mass [24]. Considering a perpendicular propagation of an electromagnetic wave in a plasma, perpendicular reflection occurs when the wave frequency f equals (or is lower than) the plasma frequency f_N, the plasma being considered as homogeneous with electron density[9] N. If $f > f_N$, the incoming wave passes through the plasma.

Adapted to the ionospheric context, this property allows to probe the ionospheric vertical structure from the ground by sending vertical electromagnetic waves at different frequencies: this is the principle of the ionospheric sounding. An emitting antenna sends radio pulses with frequency ranging from 1 to 30 MHz in the vertical direction while another antenna receives the reflected signals. From this basis, one can compute the travel time of the different pulses, which allows to associate a reflecting height with each frequency. These observations are then presented in a graphical way called ionogram, which depicts the vertical structure of the ionosphere, more especially from the E-region to the F_2-peak, as shown in figure 2.6[10].

A critical frequency is associated with each layer, as they all exhibit a local maximum in N_e. As a matter of example, let us cite the critical frequencies of E and F_2 regions f_0E, f_0F_2 and their associated heights h'_E and h'_{F2}[11]. Let us note that f_0F_2 is the largest frequency able to be reflected by the ionosphere.

A more sophisticated technique of ionospheric observation is based on the principle of the incoherent scattering. Powerful transmitters emit frequencies much higher than f_0F_2 on a small part of the ionosphere, not especially located at the vertical of the sounding device. Most of incident waves pass through the ionosphere but a small part is scattered back and collected by a receiving antenna. This observation technique allows to access a wide range of ionospheric parameters, such as electronic and ion temperature, density, plasma speed but also neutral wind speed and temperature, electric field... However, the extremely high cost of the technique limits the number of observation facilities: it exists less than ten incoherent scatter radars in

[9] Moreover, the reflected wave is made up of two characteristic rays called respectively the ordinary and the extraordinary waves. The first one is related to a reflected wave as it would be the case in the absence of the geomagnetic field. All these properties can be demonstrated based on the Appleton-Hartree formula, whose considerations and developments can be found in [24, 108].

[10] Ionospheric sounders are not able to probe the D-region as its study needs the use of very low frequencies which cannot be emitted by conventional measuring devices. Electron density in the D-region has however been investigated and the interested reader can find results in [24].

[11] The interested reader is referred to Piggot and Rawer [76] where ionograms interpretation guidelines can be found.

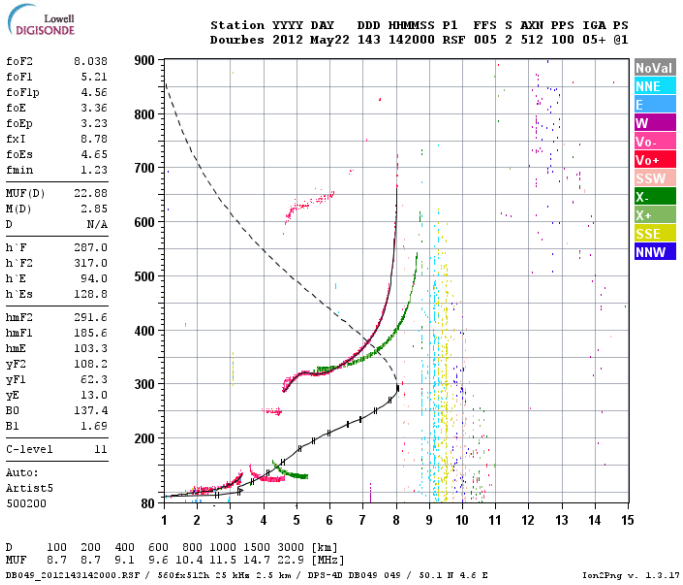

Figure 2.6 – Ionogram of DOUR station (50.1N, 4.6E) on May 22nd, 2012 at 1425 LT. It depicts the variations of the virtual height of reflection (in km) as a function of the radio frequency (in MHz). The height is said virtual as it does not correspond to the true height of reflection, that has to be computed. For a given layer, the critical frequency corresponds to the frequency where the reflection height becomes infinite while the virtual height is defined as the minimum height at which the trace is horizontal [76]. Red and pink data correspond to reflections of the ordinary wave while green ones are related to the extraordinary wave. The frequency difference between ordinary and extraordinary traces is approximately half of the gyrofrequency f_L. Numerical values of the critical frequencies f_0E and f_0F_2 together with their virtual heights h'_E and h'_{F2} also figure in the left column. Note the presence of a sporadic E-layer, or Es-layer, whose formation mechanism is briefly described in section 2.3.

the world. Among them one can cite the first station at Jicamarca (Peru), Millstone Hill (USA, Massachusetts), Arecibo (Puerto Rico) or the European project EISCAT (Norway/Sweden/Finland).

In addition to ground based measurement, the advent of the spatial age offered new opportunities in ionospheric studies. Orbiting at altitudes higher than the top of the ionosphere, artificial satellites such as those belonging to Global Navigation Satellite Systems (GNSS) allow trans-ionospheric observations. By the joint use of ground receivers and satellite transmitters (with $f \gg f_0F_2$), it is therefore possible to measure the TEC, defined as the integral of the electron density N_e along the

satellite-to-receiver path[12] and generally expressed in TEC Units (TECUs), with $1\,\text{TECU} = 10^{16}\ e^-/m^2$. VTEC monitoring by GNSS is a relatively cheap method which allows an excellent spatio-temporal coverage, as several GNSS satellites can be observed simultaneously from any point located near (or on) the Earth's surface. At the present time, GNSS receivers are worldwide distributed and global networks such as the International GNSS Service (IGS) collect and freely distribute the observations. From this basis, several centers are dedicated to the computation of Global Ionospheric Maps (GIMs), which provide instantaneous "snapshots" of the worldwide VTEC distribution with latency less than one hour [51]. Details concerning TEC computation with GNSS will be tackled in the frame of the next chapter[13].

To investigate the ionospheric topside, several polar-orbiting spacecrafts have been sent to probe the ionosphere from above, in the same manner as ground-based ionospheric sounders do. They allow to derive the topside electron density profile and its contribution to VTEC, measured by another technique (mainly GNSS). Another mission of topside sounders is the measurement of ion density (O^+ and H^+), allowing to locate the transition height, which is the altitude marking the transition between topside ionosphere (O^+) and plasmasphere (H^+). Topside and plasmaspheric electron contents can also be derived from the radio-occultation technique, whose principle relies on GNSS observations performed by receivers installed on Low Earth Orbit (LEO) satellites. In addition to electron density, other atmospheric parameters such as density, temperature and pressure can be derived.

To complete the list of the ionospheric observation methods, let us mention the airglow measurements. In the F-layer and in the absence of photoionization (nighttime), excited atomic oxygen, which is the main constituent at this altitude, changes to a more stable state by emitting photons in two main lines: green (557.7 nm) and red (630 nm). Night airglow observations are achieved by installing full sky imagers taking photographs in the aforementioned wavelengths, but especially for the 630 nm band which is the brightest airglow source [108]. Of course, the major drawback of the method is the absolute need of a clear sky.

2.2.3.2 General features of the ionosphere

Ionospheric composition and morphology is varying with the time of the day, season, solar activity and geomagnetic conditions. According to geomagnetic dip angle, one can subdivide the ionosphere into three principal regions, each of them exhibiting specific features and mechanisms (figure 2.7). As mid-latitude regions constitute the area of interest of this thesis, we will mainly focus our description on these regions.

[12] Satellites being rarely at the zenith of the receiver, TEC values correspond to slant observations and, to avoid confusion, only the terms Vertical TEC (VTEC) and Slant TEC (STEC) will be considered from now on.

[13] The interested reader can however refer to [15, 62, 73, 88, 98] for additional information.

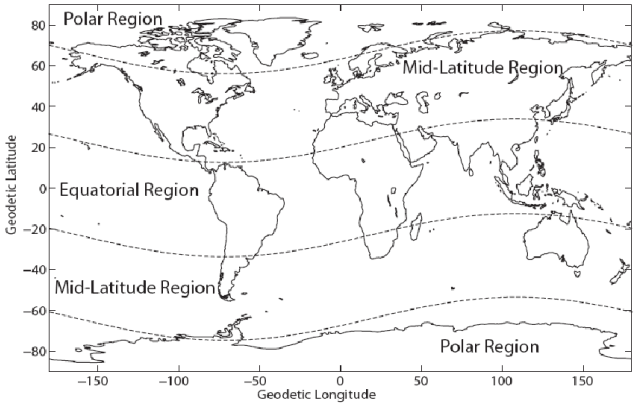

Figure 2.7 – Ionospheric regions depend on geomagnetic dip angle. From high to low latitudes we can observe the polar (or auroral) regions, the mid-latitude regions and the equatorial region. (From [66])

Polar (or auroral) regions. Also called high-latitude regions, the auroral regions are located above the 60° parallels, where the nearly vertical magnetic field lines allow the ionosphere to be in close relationship with the magnetosphere. Magnetospheric conditions are mainly driven by space weather phenomena, in particular by the solar wind carrying the IMF. This implies energetic particles like protons and electrons to precipitate directly in the polar ionosphere, leading to highly variable electron density and TEC. While the ionization in equatorial and mid-latitude regions is mainly due to solar radiations, ionization in polar regions is also partially due to particle precipitation, hence a strong geomagnetic control of these regions. This is particularly true during the polar night (absence of EUV solar flux).

The equatorial region. It corresponds to the latitude band of 20° located on either side of the geomagnetic equator. An important feature of this region is the narrow strip of 3–4° wide where is located, at a height of about 105 km, an important eastward electric field called Equatorial Electrojet (EEJ). The EEJ finds its origin in concentrated Sq currents at dip equator, which result in large conductivity[14] in the east–west direction[15]. Magnetic field lines being horizontal at the geomagnetic equator, the ($\mathbf{E} \times \mathbf{B}$) drift is very efficient and induce a plasma convection (uplift) called *fountain effect*. Plasma is therefore

[14]This typical conductivity of the equatorial region is sometimes called Cowling conductivity [108].

[15]One can also precise that Sq currents intensity depends on local time, season and solar activity. For example, Sq currents are 50% stronger during solar maximum periods than during sunspot minimum [24].

transported towards higher latitudes to form the ionization crests (around 15–20° on either side of dip equator). These electron density maxima occurring in the late afternoon (around 1900 LT), together with the related trough at the equator, are referred to as the *equatorial anomaly*, also called Appleton anomaly. The crests are clearly visible on figure 2.8 where a GIM is depicted during solar maximum.

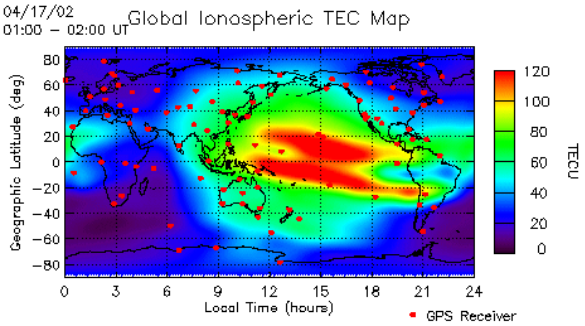

Figure 2.8 – Global ionospheric VTEC map. Distinct features such as the equatorial anomaly (the two crests on both sides of the dip equator) or the mid-latitude trough (VTEC depletion around 60°, between 2100 and 0200 LT) can be observed. (From [69])

Mid-latitude regions. In these regions extending from about 20 to 60°, electron density results from the equilibrium between ionization and losses, but also from transport processes like those due to neutral winds or ambipolar diffusion. Here, the ionosphere is neither under the influence of the fountain effect nor affected by polar particle precipitation. However, if one could expect larger f_0F_2 and VTEC values during summertime (due to a higher ionization level), observations show the opposite, exhibiting N_e and VTEC maximum in winter. This so-called *winter anomaly* is due to changes in the molecular-to-atomic ratio of the neutral atmosphere, which implies a variation in the recombination rate[16]. This ratio exhibits larger values during summer than during winter; electron recombination is therefore more efficient in the summer hemisphere, hence a lower electron density.

From November to January, an enhancement of f_0F_2 is systematically observed

[16]Changes in the molecular/atomic ratio seem to depend on the temperature of the upper atmosphere, and thus on season and solar activity. Indeed, an increased upper atmosphere temperature increases the scale height of atmospheric species $H = \frac{kT}{Mg}$, which results in an upward motion of heavier species. For example, summer conditions imply larger scale heights and therefore an upward movement of O_2 and N_2, which favors electron recombination [78, 108].

in both hemispheres: this is the *December anomaly* [108]. In the northern hemisphere, winter and December anomalies are in phase and are therefore superimposed. The cause for its occurrence is still uncertain, although it seems to be of geomagnetic origin.

Another distinct feature of mid-latitude region is the presence of a VTEC depletion at geomagnetic latitude ranging from 50 to 70° and observed nighttime between 2100 and 0200 LT, called *mid-latitude trough*. Like the equatorial anomaly, mid-latitude trough is clearly visible in figure 2.8. The origin of such depletion, consisting in a decreasing O^+ concentration in the nighttime F-region, seems to be related to the geographic area (lower edge of the auroral oval) and to the ion velocity in the rest frame of the neutral particles [80].

In order to illustrate VTEC behavior at mid-latitude regions, figure 2.9 depicts VTEC monthly medians at Brussels (50.5° N, 4.4° E) during high and low solar activity periods.

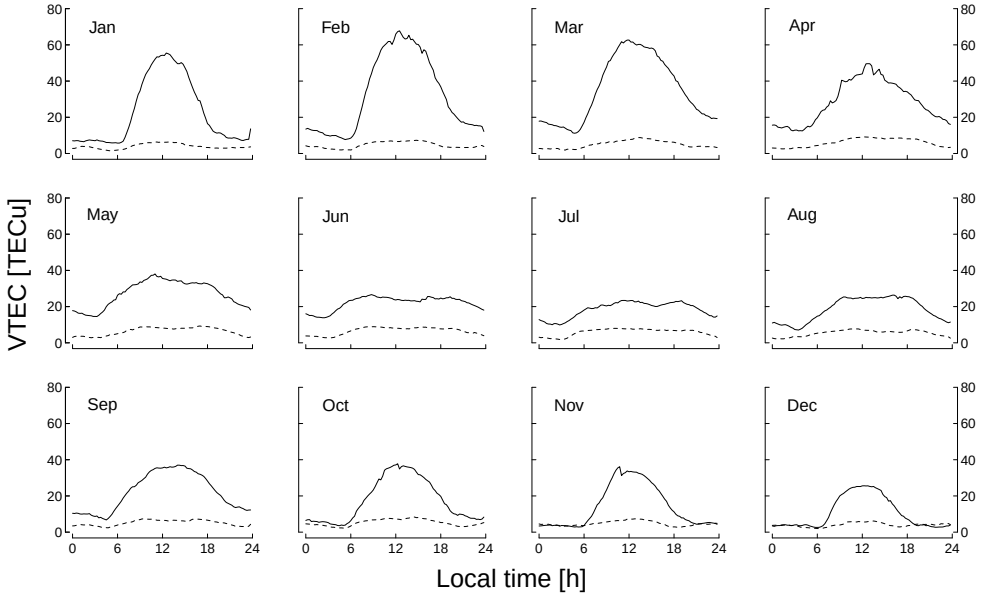

Figure 2.9 – VTEC monthly medians at Brussels (50.5° N, 4.4° E) for 2002 (plain) and 2008 (dotted), derived from GPS measurements. Details on VTEC computation can be found in [98].

The main VTEC features visible in figure 2.9 can be summarized as follows:

- Solar activity dependence: VTEC values are larger during high solar activity periods. This is particularly true for daytime profile, where the daily maximum can be up to 6 times larger during solar maximum. As

an example, VTEC values of 60 or 70 TECU are regularly observed during high solar activity periods whereas maximum values do not exceed 10 TECU during solar minimum.

- Combined winter/December anomalies: daytime VTEC peak is larger during autumn-winter months, which is valid for high solar activity periods only. Indeed, VTEC during solar minimum do not seem to follow the same behavior as during solar maximum: while the ratio winter/summer can reach the value of 2.5 (Feb/Aug) during solar maximum, it takes values very close to 1 during low activity periods. This seems to be related to solar cycle dependence of the temperature in the upper atmosphere, which implies variations of the winter anomaly [108].
- Diurnal variation: maximum values occur during daytime while minimum are observed at night, just before sunrise. VTEC diurnal shape is related to sunshine length, which leads to a sharp peak during winter and a flatter but longer curve in the summertime.

Let us add that some authors mention a secondary VTEC maximum (called *winter night enhancement*) which seems to be difficult to validate at BRUS (figure 2.9). This mid-latitude VTEC enhancement is more pronounced during winter than during summer and covers wide geographical areas, such as USA and Europe [24, 108].

For a more detailed discussion about ionospheric climatology and physics, the interested reader can refer to [4, 24, 78, 108].

2.3 Ionospheric irregularities

In the previous section, physical mechanisms responsible for the regular behavior of the ionosphere have been detailed. To these regular patterns are superimposed several types of disturbances that can be associated with space weather events, or not. Such disturbances, which will be further referred to as "ionospheric irregularities", have been observed worldwide with different techniques such as ionosondes, backscatter radars, airglow or more recently GNSS. This section aims at examining the different phenomena responsible for ionospheric irregularities. More particularly, we will focus our description on mid-latitude regions, which correspond to the geomagnetic context of this thesis. Furthermore, let us mention that irregularities due to very rare events such as eclipses or Galactic Cosmic Rays (GCRs) will not be discussed here.

2.3.1 Space weather related irregularities

Space weather irregularities are mainly due to two phenomena which are geomagnetic disturbances and solar flares.

1. **Geomagnetic disturbances.** In the section 2.1.3, we have seen that geomagnetic disturbances are quantified based on geomagnetic indices such as DST or Kp. Solar-originating phenomena responsible for geomagnetic disturbances are CMEs and CIRs. While the first ones may induce major geomagnetic storms and substorms (extreme DST and K values)[17], the geomagnetic effects of the latter are more moderate, with K values rarely exceeding 5.

   Ionospheric response to geomagnetic disturbances is extremely complex as it depends not only on the incoming disturbance itself (IMF parameters, especially B_z, particle speed...) but also on the ionospheric background, which is varying with local time and location on Earth. The underlying physics being complicated, it is therefore usual practice to describe geomagnetic effects in the ionosphere in terms of effects they induce in VTEC, with respect to background ("normal") conditions. One can distinguish:

   (a) **Positive phase of the ionospheric storm**. VTEC values observed are larger than the background value (VTEC *enhancement*). This is mainly due either to a downwelling of neutral atomic oxygen O, leading to a larger photoionization rate, or to a plasma uplift of the F-layer [36].

   (b) **Negative phase of the ionospheric storm**. VTEC values observed are lower than the background value (VTEC *depletion*). As being the opposite of the positive phase, a negative phase is due to a decrease of the neutral atomic/molecular ratio, hence a larger recombination rate and a decreasing VTEC.

   Ionospheric storms, and especially the super storm of October 29-30 2003 (called "Halloween storm"), have been extensively studied in the literature. Depending on location on Earth and local time, several morphological structures responsible for ionospheric storms (positive or negative) have been identified mainly based on TEC measurements (GPS or radio-occultation techniques), but also with scatter radars and ionosondes.

   - Based on ionograms coming from UK and Belgium, Warnant et al. [100] observed that the negative phase (-50% of background VTEC) was due to a sharp decrease of the F-layer height. Large VTEC irregularities were also related to descending intermediate E-F layer.
   - A tongue of ionization originating from high-latitude regions propagates equatorwards [36, 52, 67]. In addition, such ionization tongue seems to be related to polar patches moving in an anti-sunward direction across the polar cap [27]. Steep VTEC gradients due to these (sub-)polar structures were also investigated by Stankov et al. [89], which analyzed GPS satellite

[17] A rather complete definition of geomagnetic storm and substorm as well as an exhaustive list of related references can be found in [37].

ionospheric traces during the Halloween events. Associated with the polar tongue of ionization and patches are small-scale irregularities (about tens to hundreds of meters). Located on their edges, such irregularities seem to be responsible for variations in both amplitude and phase of GPS signals known as ionospheric scintillations [27, 36, 85].

- A "super fountain effect" due to an increased ($\mathbf{E} \times \mathbf{B}$) plasma uplift at low latitudes [7, 62]. Equatorial anomaly crests extend therefore to mid-latitude regions (up to 25-30° of dip latitude), as observed in VTEC which increased by about 40 to 250% of its background value [62]. These authors also noticed a strong correlation between negative component of B_z and the positive phase of the ionospheric storm.
- Generally associated with geomagnetic storms and substorms are the Large-Scale Traveling Ionospheric Disturbances (LSTIDs). They consist in wave-like fluctuations of the electron density, with periods ranging from 30 min to 3 hours and horizontal velocities between 400 and 1000 m/s. They are understood to be the plasma signature of Atmospheric Gravity Waves (AGWs) triggered by particle precipitation, Lorentz forces or Joule heating in polar regions [1, 30, 34, 50]. Therefore they are rather associated with intense geomagnetic events like CME-induced storms than to moderate conditions due to CIRs. LSTIDs motion is essentially equatorwards due to their polar origin, but their amplitude seems to decrease more rapidly in the daytime hemisphere as LSTIDs are damped by the large VTEC background [91]. VTEC effects of LSTIDs have been investigated by several authors, in particular by Ding et al. [30] who reported a maximum amplitude of 3 TECU during the Halloween storm.

2. **Solar flares**. As they consist in abrupt increases of EUV and X-rays fluxes, their impact on the ionosphere is limited to the daylight hemisphere. Furthermore, the regions located near the sub-solar point are the most vulnerable as incoming rays are perpendicular to the Earth's surface. Solar flares produce an enhanced ionization level over a wide altitude range (from D- to F-region) called Sudden Ionospheric Disturbance (SID). However, every flare has its individual face, as pointed out by Tsurutani et al. (2005) [93], which analyzed several flares based on their emission in FUV, EUV, soft and hard X-rays. It comes that the most powerful flares in the X domain (e.g. the X28 flare of 4 November 2003) are not producing the most dramatic increases in VTEC. Indeed, VTEC major contributing region being the F-region, the most important emission domain lies in the EUV. Effect in VTEC is mainly a steep increase in the sunlit hemisphere, especially near the sub-solar point, with values reaching up to 25 TECU [93]. While EUV flux returns back to its background values in less than an hour, VTEC takes several hours to decay. The relationship between those Sudden Increase in TEC (SITEC) and the solar zenith angle have been investigated for several representative flares in [45, 52].

2.3.2 Other irregularities

One can summarize the causes of ionospheric irregularities which are not due to space weather events in three main categories: sporadic E-layers, spread-F layers and Traveling Ionospheric Disturbances (TIDs).

1. **Sporadic E-layers.** Sporadic E-layers, or Es-layers, are short-lived ionospheric phenomena, highly variable in space and time that can be observed at all latitudes. They have been well studied with backscatter radars and ionosondes, which allowed to derive not only occurrence statistics but also physical properties such as their plasma frequency f_0E_s, virtual height $h'E_s$ or thickness of the layer. Es consist sometimes in opaque layers (total blanketing of the upper layers on ionograms, with a critical frequency denoted f_bE_s), sometimes in semi-transparent layers which can be understood as patchy clouds of ionization. Besides, such patchy sporadic-E seem to be more prevalent than opaque ones [41]. *In situ* measurements show that metallic ions are the majority constituents of sporadic E; their origin is probably found in minority atmospheric neutral constituents or in meteor showers. Height of Es-layers varies generally between 90 and 125 km – but is sometimes as low as 60 km! – while their thickness ranges from 0.6 to about 5 km [107]. Values of f_0E_s or f_bE_s are strongly variable, reaching sometimes 30 MHz, which is much larger than "classical" f_0E [24]. At mid-latitudes, typical values of f_0E_s range between 2 and 10 MHz.

   However, Es-layers are not so sporadic as their name implies: in polar regions, nocturnal E-sporadic can be observed between 2000 and 2300 LT, especially during the whole polar night during which their occurrence rate is close to 90%. Similarly to polar regions, equatorial region shows also few seasonal variation but sporadic-E are daytime phenomena, occurring very frequently and generally between 0900 and 1800 LT. Again, some regular pattern can also be found for mid-latitude regions, especially between May and August, where their maximum occurrence is around 1100 LT and 1900 LT. Let us mention that solar cycle variation of Es occurrence and f_0Es seems to be very difficult to establish: some authors mention a positive correlation with sunspot number while others observed negative ones [106, 107]. Moreover, year-to-year variability of Es occurrence can be considerable and mechanisms responsible for such variation are still not understood [106].

   Causes of sporadic-E occurrence change with the geomagnetic region considered. While Es occurrence in the equatorial region seems to be correlated to the EEJ, polar Es are associated with auroral corpuscular bombardment (energetic electron precipitation from the magnetosphere). In mid-latitude regions, the predominant theory explaining the formation of Es is the wind-shear theory, well described in [41, 106–108]. According to this theory, vertical shears in neutral winds due to diurnal and semidiurnal thermospheric tides

force metallic ions to move vertically and confine them into thin layers. Wind shear theory can also explain the descent rate observed for Es-layers, which is the order of 1-2 km/h. Mid-latitude Es, also referred to as Tidal Ion Layers (TILs), exhibit a life cycle that can be summarized as follows [41, 107]:

- Formation at an altitude of around 120-125 km, with low f_0E_s values (due to the few ion accumulation). Es formation is organized in a semidiurnal pattern: the first near sunrise (∼0600 LT) and the second around 1800 LT.
- Descent at speeds of about 1-2 km/h with the f_0E_s peak value due to ion accumulation during the descent (∼110 km).
- Disappearance at about 100 km with low f_0E_s values due to ion recombination.

One can also point out that there could be overlapping of two Es-layers, the first being located at about 100 km and the second approximately 20 km above.

2. **Spread-F.** The term "spread-F" is used to describe an height spreading of the F-region trace in ionograms resulting from irregular plasma [24]; it is therefore rather used to describe ionograms than to explain the physical mechanisms involved. Observations of spread-F with several types of radars and airglow recordings show that plasma irregularities are mapped along the geomagnetic field lines: one speaks about Field-Aligned Irregularities (FAI). FAIs are organized in patches of several hundreds of kilometers wide but with sizes perpendicular to **B** as small as 1 m. A key property of the phenomenon is the existence of regions characterized by turbulent upwelling and abrupt plasma uplifts [40]. Patches of ionization (also called plasma bubbles) are responsible for high fading rates on radio waves called scintillations, which are mainly studied with specific GNSS receivers. Spread-F are generally observed at high-latitudes and in the equatorial region where they exhibit specific occurrence rate and signature in ionograms.

   (a) In the equatorial region, spread-F are mainly nighttime events as they occur in the evening hours, between 2100 and 0100 LT during equinoxes or local summer. They seem to be associated with rising plumes of ionization due to the evening rise of the fountain effect. Ionogram signature of equatorial spread-F consists in a range spreading: the traces away from the critical frequency show broadening in range or the presence of additional traces, or both [76].

   (b) In polar regions, which also include a part of the mid-latitude regions, spread-F occurrence rate starts at 40° dip latitude and increases with latitude to occur 100% of the time during summer nighttime at geomagnetic poles. Around noon, summer occurrence is about 50-60%. During winter, they are observed 100% of the time. Several studies show that

mid-latitude spread-F occurrence is influenced by solar cycle: it increases with a decreasing solar activity. Let us however point out that mid-latitude spread-F may occur during geomagnetic storms [24]. Contrary to equatorial spread-F, the signature of polar and mid-latitude spread-F in ionograms is mainly a frequency spreading: traces near the critical frequency are broadened in frequency and may show additional traces similar to a normal critical frequency trace [76]. Many mechanisms have been proposed to explain the occurrence patterns and properties of mid-latitude spread-F. Among them, Haldoupis et al. [40] suggested that unstable Es-layers play a role in their generation. Observations of simultaneous Es-layers and spread-F led these authors to propose the following mechanism: an eastward polarization electric field set up inside unstable Es-layer can map along the magnetic field lines up to the F-region, where plasma uplifts are created mainly by ($\mathbf{E} \times \mathbf{B}$) drifts. If their study is only based on a limited amount of days, it seems to be admitted by the scientific community that spread-F are linked to the occurrence of patchy Es-layers at mid-latitudes.

3. **Traveling ionospheric disturbances.** TIDs consist in moving wave-like fluctuations of the electron concentration characterized by a velocity, period, wavelength and a direction of propagation. They are understood as the signature of AGWs into the ionospheric plasma, this latter playing the role of a passive tracer. Indeed, the AGW first disturbs the background neutral gas which is the major constituent of the ionosphere, before the disturbance is transmitted to charged particles by ion-neutral collisions [46, 48]. In the F-layer, neutral density is very weak and charged particles motion is mapped along the magnetic field lines. The passage of an AGW modifies therefore charged particles height with up/down motions, which implies different recombination rates, translated in changes in f_0F_2, hF_2 and N_e.

   Since 1960s, TIDs have been widely investigated with several types of instruments. First detection was achieved with ionosondes and $h'F_2$ recordings, while more sophisticated radars allowed to access to electron and ion temperature, speed and density. More recently, airglow measurements opened new research perspectives by all-sky imaging, revealing fronts of raised and lowered plasma due to the presence of TIDs [72, 74, 82]. These wave-like structures can also be detected in VTEC maps built from GNSS networks [82, 92]. As a fact, the combination of several observation methods constitutes the best approach to guarantee the reliability of the results.

   TIDs can be divided into two main categories: Large-Scale (LSTIDs) and Medium-Scale Traveling Ionospheric Disturbances (MSTIDs). The first ones, which have already been described in section 2.3.1, originate from auroral regions from which they travel equatorwards with speeds between 400 and 1000 m/s [46]. MSTIDs have smaller propagation speeds (50-400 m/s) and

wavelengths (a few hundreds kilometers). Their period ranges between 10 and 60 minutes while their direction of propagation seems to vary with local time. Moreover, MSTIDs are not linked to geomagnetic activity, which is not the case of LSTIDs. While the origin of the latter is well-established, the occurrence of MSTIDs is not totally understood yet and lots of complex mechanisms have been proposed by the scientific community.

Climatological studies of MSTIDs have been carried out to find their origin and the underlying physical mechanisms (see for instance [43, 54, 82, 86, 92, 95] and the excellent review of Hocke and Schlegel [46]). Based on these studies, MSTIDs can be divided into two main classes, depending on their time of occurrence: daytime and nighttime MSTIDs.

- **Daytime MSTIDs**, also called classical MSTIDs, have a maximum occurrence rate around 1200 LT and propagate equatorwards [43] or south-southeastward [54, 92]. They occur mainly during autumn and winter months and exhibit a positive correlation with solar activity. Propagation speed lies between 100 and 400 m/s and their associated wavelength ranges from 100 to 350 km; the related period is larger than 12 min. Daytime MSTID amplitude has been measured by several techniques (such as the differences in f_0F_2, N_e or in VTEC, normalized by the background value) and the value depends on the technique used[18]. For example, GPS-TEC measurements led to amplitudes of 1-2% [92] while measurements derived from the differential Doppler shift technique show values ranging from 1 to 10% [95].

  Causes of classical MSTIDs can be divided into two main types: *in situ* generation in the ionosphere and tropospheric phenomena propagating upwards. AGWs generated *in situ* are mainly due to the passage of the solar terminator[19], causing instabilities between two regions in thermal equilibrium [8]. However, based on a climatological study of MSTIDs with radiotelescopes in the Netherlands, van Velthoven [95] concluded that the terminator is not the main cause of the observed MSTIDs. The other mechanism responsible for MSTIDs is the classical interaction between upward propagating AGWs and the ionospheric plasma. Sources of AGWs are multiple and lie mainly in the troposphere. Tackling the detection of AGWs in the ionosphere implies not only to understand the mechanisms of their generation but also their propagation up to the ionospheric layer. Therefore, the problem has to be decomposed into two components:

  (a) **Sources.** AGW potential sources are associated with powerful meteorological processes, such as jetstreams, severe storms or the pas-

[18] Indeed, observational biases can strongly affect the results [5, 35]; this is the reason why a section has been devoted to that topic (see section 3.3.2).

[19] The solar terminator is the line separating the illuminated and the shaded hemispheres.

sage of fronts. Several authors have supported this hypothesis, like Bertin et al. [10] who observed a positive correlation between MSTID occurrence and wind shears due to the presence of tropospheric jets or frontal systems. Another study shows that jetstreams emit enough power to generate AGWs able to propagate over a long distance away from their source region [63]. It is also thought that orography can play a role in the generation of AGWs as the air flow over mountains might generate perturbations. The tropospheric origin of observed MSTIDs can be proved by observing their signature in the lower ionosphere (D-region) by radio wave absorption measurements [56]. In the potential sources of AGWs let us also mention earthquakes, called "ionoquakes" once detected as TIDs in the ionosphere [3, 79].

(b) **Propagation.** An AGW can be detected in the ionosphere as a TID only if both source and propagation mechanisms are efficient. These considerations have been discussed in Hocke and Schlegel [46] and in Hunsucker [50] where several propagating gravity wave modes (direct, reflected, ducted...) are presented. The mechanisms detailed are out of the scope of this thesis but it seems important to highlight the fact that an AGW can be observed at a certain horizontal distance of its source region. That means that AGWs are propagating upward in a cone whose vertex corresponds to the source region. During its ascent, the wave is prone to atmospheric filtering due to the background neutral wind [9, 10, 54, 56, 95]. Moreover, steep temperature gradients around the mesopause in summer seem to block the AGW upward propagation or even reflect it, which would explain the winter maximum of occurrence [13, 54].

Considering potential sources and transfer mechanisms, van Velthoven [95] proposes to explain the origin of MSTIDs by nonlinear interactions between AGWs generated from below (jets, fronts, orography...) with primary waves of large amplitude like LSTIDs or tides. He argues that lower atmospheric waves cannot directly generate the AGWs detected in the ionosphere but that their interaction with other large-scale gravity waves or tide might constitute a plausible mechanism, consistent with the observations.

- **Nighttime MSTIDs**, also called non-classical MSTIDs, propagate mostly southwestward in the northern hemisphere and northwestward in the southern one with speeds ranging from 50 to 150 m/s [43, 53, 54, 82, 92]. Their wavelength and periods seem to be larger than for classical MSTIDs, with wavelengths of about 500 km and periods of 1-2 hours. In the same way as for daytime ones, their amplitude varies with the technique used: in the airglow intensity, the amplitude reaches 26% but the corresponding value in TEC measured by GPS is only 8% [82]. Some other studies led

to VTEC amplitude values of 1-5% [92], which is larger than amplitudes found in the case of classical MSTIDs. Moreover, the same authors point out that nighttime MSTIDs occurrence is anti-correlated with solar cycle. Peaks of occurrence appear around the summer solstice (first maximum) and the winter solstice (secondary maximum).

These fundamental differences in properties and occurrence rates suggest that physical mechanisms are completely different from those of daytime ones. Indeed, orientation of nighttime MSTIDs is not aligned with the magnetic field lines. As a consequence, it has been suggested that additional electric forces in the F-layer are the origin of the mainly westward motion. If the electric forces are thought to occur in the F-region, a coupling between E and F-layers tends to become the point of convergence between the several mechanisms proposed in the literature. Indeed, Kelley [53] suggests that AGWs originate from auroral zones where their generation, due to Joule heating, occurs all the time, even during quiet geomagnetic periods. During their propagation towards the equatorial region, a filtering mechanism proposed by Perkins [75][20] damps all but the waves whose direction of propagation corresponds to the one predicted by its theory, which is southwestward in the northern hemisphere and northwestward in the southern one. Once at mid-latitudes, it is argued that coupling between E and F-regions amplifies the AGWs which become MSTIDs. Let us note that this amplification mechanism does consider the presence of Es-layers and small-scale irregularities that can be linked to spread-F phenomenon (more details about coupling mechanisms can be found in [18, 19, 113]).

Another mechanism has been proposed by Afraimovich et al. [2]. Using magnetoconjugate observations of ionospheric irregularities by GPS, they suggest that nighttime MSTIDs are of MagnetoHydroDynamic (MHD) nature. He argues that slow magnetosonic waves generated by the solar terminator at the magnetoconjugate point are ducted along the magnetic field lines to be observed as MSTIDs during nighttime. However, no coupling between E- and F-layers is mentioned in his work.

[20]The Perkins instability is a mid-latitude phenomenon predicted by Perkins in 1973 [75]. In his model, he investigates the conditions during which the F-region equilibrium may or not be unstable. During nighttime, gravity compensates for plasma uplift mainly due to a southward wind or an eastward electric field (see section 2.2.2). Perkins found that this equilibrium is unstable if it exists a northward component of the electric field. It results instabilities, consisting in propagating plasma sheets of ionization with wavefronts oriented from NW to SE in the northern hemisphere.

Chapter 3

Global Positioning System (GPS)

Contents

This chapter provides a general background about the GPS system and its use in the frame of ionospheric studies. A particular attention will be turned to observational biases occurring in the case of ionospheric observations with a single station.

3.1 System overview

GPS was designed in the 1970s by the US Department of Defense (DoD) to obtain accurate values of position, velocity and time anywhere on the globe and at any time. The system is often presented as being divided into three segments: the space, control and user segments. The *space segment* is constituted by the satellite constellation made up of about 30 satellites, organized in six orbital planes of approximately 55° inclination (tilt relative to the equator). Orbit type is a nearly circular Medium Earth Orbit (MEO) with a revolution period of about 12 hours and an altitude of 20200 km. This orbital configuration provides a global coverage with four to eight simultaneously observable satellites above 15° elevation at any time of day [47]. GPS satellites have an on-board atomic clock to generate the different signals which will allow the user to accurately measure his position, speed and time. Satellites are generally identified with their Pseudo Random Noise (PRN) code, referring to the unique ranging code they broadcast (see below). The *control segment* steers the whole system by monitoring satellite position and the drift of their atomic clocks with

respect to the GPS time, which is the reference time system for GPS applications. Finally, the *user segment* is the term used to designate all receivers able to track and process GPS signals. At the present time, a wide range of receivers have been developed by the industrial sector to meet the needs of principal groups of users, such as geodetic receivers used in the frame of this thesis.

Original[1] GPS signal is made up of two carriers in the radio L-band denoted L_1 and L_2 and whose frequencies are respectively 1575.42 and 1227.60 MHz. Two ranging codes are modulated on these carriers: a civil Coarse/Acquisition (C/A) code and a military code called P-code[2]. In addition, a navigation message (sometimes referred to as D-code) is also broadcast to allow receivers to compute the position of the satellites or other useful quantities related to the constellation.

Signal modulation scheme of the GPS system is illustrated in figure 3.1 where the different observables provided by the system are displayed. One can see that C/A code is only modulated on L_1 carrier while P(Y)-code, like D-code, is modulated on both L_1 and L_2 carriers.

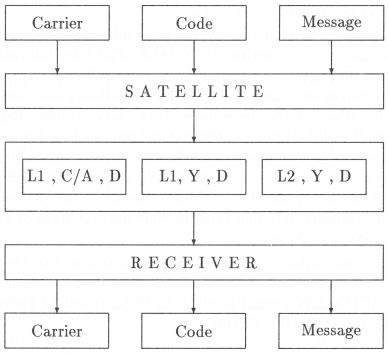

Figure 3.1 – Ranging codes C/A, Y and the navigation message D are modulated on L_1 and L_2 carriers. (From [47])

GPS observables are divided into two main types: code and phase measurements[3]. The first are related to the ranging codes C/A and P(Y) while phase measurements are achieved using carriers only.

[1] Even if the current constellation includes a few satellites broadcasting on a third frequency called L_5, all measurements performed in the frame of this thesis are related to the "classic" dual-frequency system L_1/L_2 described in this section.

[2] It is worth mentioning that a system called Anti-Spoofing replaces the P-code by the Y-code whose only users authorized by the DoD have access to. Even if measurements similar to P-code ones remain possible, the main drawback is that the signal-to-noise ratio of the observable is lower than for "direct" Y-code measurements.

[3] It exists also a third type of observable, called *Doppler measurement*, but its use is rather rare in practice [47].

- In the case of **code** measurement, the receiver estimates the travel time of the PRN originating from a given satellite by correlating it with an internal replica of the PRN. The code measurement on the ith carrier P_i, defined as the distance between the satellite and the receiver, can therefore be computed as follows (considering a propagation in vacuum):

$$P_i = c\,(t_r - t^s) \qquad [m] \tag{3.1}$$

  with t_r the reading of the receiver clock at signal reception time and t^s the reading of the satellite clock at emission time.

- In the case of **phase** measurement, the observable is defined as the phase difference between the incoming signal and a copy generated by the receiver. As only a fractional phase can be measured, an unknown integer number of cycles called *ambiguity* has to be estimated to compute the distance between the receiver and the satellite. The simplified mathematical model of phase measurements can thus be written as

$$\phi_i = \lambda_i\,(\phi(t_r) - \phi(t^s) + N_r^s) \qquad [m] \tag{3.2}$$

  with λ_i the wavelength of the ith carrier, $\phi(t_r)$ the phase in the receiver at t_r, $\phi(t^s)$ the phase in the satellite at t_s and N_r^s the integer phase ambiguity.

  Let us mention that equations (3.1) and (3.2) constitute very simple models of code and phase observables; their complete mathematical model will be detailed in the next section.

Precision of a GPS observable is inversely proportional to its wavelength; in practice, it is generally assumed that the precision is about a hundredth of the wavelength. This information is summarized in table 3.1 where it is clear that phase measurements are much more accurate than code measurements.

	C/A-code	**P(Y)-code**	**L_1/L_2 phase**
Wavelength	300 m	30 m	0.19 - 0.24 m
Precision	3 m	0.3 m	2 - 2.5 mm

Table 3.1 – Approximate wavelengths and precisions of the different GPS observables.

GPS system has been developed for positioning purposes, whose different modes can be divided into three main categories:

1. **Absolute positioning**. The receiver makes stand-alone measurements based on code and/or phase measurements related to a minimum of four satellites. Considering code measurements only, the positioning accuracy is meter-level.

In the case of Precise Point Positioning (PPP), mixed code/phase measurements are used and centimeter-level positions can be obtained.

2. **Differential positioning**. This is a particular case of absolute positioning since the receiver still makes absolute positioning with codes and/or phases, but uses additional corrections (called *differential* corrections) provided by a (network of) reference station(s) to improve its accuracy. This application is more accurate than absolute positioning but requires a permanent link with the reference station. This is the case of the so-called Real-Time Kinematics (RTK) technique mainly used by surveyors, civil engineers or more recently farmers.

3. **Relative positioning**. The receiver computes differences of code and/or phase measurements with those of another receiver for which the position is accurately known. It consists therefore in computing the vector linking these two stations called *baseline*. This is the most precise positioning technique which requires, as for the differential method, a permanent link with the reference station to get a real-time positioning solution. This is also the case for the RTK technique that will be used in chapter 6.

Let us mention that the user position can be computed either in real-time (on the field) or *a posteriori*. In the latter case, a computer is needed to make the necessary computations[4].

3.2 GPS observations: description and handling

This section tackles the mathematical model of GPS observables, which are the code and phase observation equations, and their related error sources. Later, one will see how to mitigate or isolate their influence by using specific observation combinations.

3.2.1 Mathematical model and error sources

As previously mentioned, GPS observables are generally divided into two main categories: code and phase measurements, the latter being more precise but ambiguous. Let us consider a one-way measurement between the satellite s and the receiver r made on the ith carrier. The mathematical model of code (*pseudo-range*) and phase observations can be expressed as follows [47, 84]:

$$\begin{aligned} P_i &= \rho + \Delta\rho + I_i + T + M_i + c\,(\Delta t^s - \Delta t_r) \\ &\quad + c\,(D_i^s + D_{r,i}) + \epsilon_i \end{aligned} \tag{3.3}$$

[4]Global and regional data centers provide hourly and daily GPS files in the Receiver INdependent EXchange (RINEX) format [39], which is the international exchange format of GPS data.

$$\begin{aligned}\phi_i &= \rho + \Delta\rho - I_i + T + m_i + c\,(\Delta t^s - \Delta t_r) \\ &\quad + c\,(d_i^s + d_{r,i}) + \mathrm{PCV}_i^s + \mathrm{PCV}_{r,i} + \lambda_i N_i + \varepsilon_i \end{aligned} \tag{3.4}$$

with

P_i the code measurement on frequency f_i [m] ;

ϕ_i the phase measurement on frequency f_i [m] ;

f_i the GPS frequency, with $f_1 = 1\,575.42$ MHz and $f_2 = 1\,227.60$ MHz ;

ρ the geometric distance between the satellite and the antenna [m] ;

$\Delta\rho$ the error on ρ due to the orbit error [m] ;

I_i the ionospheric delay on frequency f_i [m] ;

T the tropospheric delay [m] ;

M_i the code multipath error on frequency f_i [m] ;

m_i the phase multipath error on frequency f_i [m] ;

c the speed of light in vacuum [m/s] ;

Δt^s and Δt_r the clock errors related to satellite s and receiver r respectively [s] ;

D_i^s and $D_{r,i}$ the code hardware delays on the ith frequency, respectively for the satellite s and the receiver r [s] ;

d_i^s and $d_{r,i}$ the phase hardware delays on the ith frequency, respectively for the satellite s and the receiver r [s] ;

PCV_i^s and $\mathrm{PCV}_{r,i}$ the phase center variations and offsets on the ith frequency, for the satellite s and the receiver r respectively [m] ;

λ_i the wavelength related to f_i [m] ;

N_i the initial ambiguity on frequency f_i (integer number) ;

ϵ_i the code measurement noise on f_i [m] ;

ε_i the carrier phase measurement noise on f_i [m].

Principles related to the different error sources detailed in equations (3.3) and (3.4) are summarized below.

Orbit error. One can define the orbit error as the difference between the computed and the true position of the satellite emitting antenna. If the projection of this error along the satellite-to-receiver path is non-null, the theoretical range ρ is affected by a range error term $\Delta\rho$.
In practice, there are two main ways to compute the satellite position: the broadcast ephemeris and the precise ephemeris. The first are part of the navigation message sent by the satellites (D-code) and allow a real-time computation of the satellite position with an accuracy of about 1 m [51, 55]. Precise ephemeris are not available in real-time: they are based on observations related to several GPS stations belonging to a global tracking network and distributed by the IGS. While final (*i.e.* the most precise) orbits can reach 2.5 cm accuracy[5] [51], intermediate accuracy levels can also be obtained from the IGS, the product latency depending on the precision required. Let us mention that recent developments in orbit modeling led to real-time products, such as the "ultra-rapid" orbits offering an accuracy of about 5 cm.

Ionospheric delay. GPS signals do not travel into free space and their velocity depends on the refractive index of the medium. More precisely, the refractive index of the ionosphere, given by the Appleton-Hartree formula[6], depends on the frequency of the incoming wave: the ionosphere is said to be a dispersive medium[7]. Furthermore, the value of the refractive index is different for wave groups and monochromatic carriers:

$$n_{i,gr} = 1 + 40.3\,\frac{N_e}{f_i^2} + \frac{a}{f_i^3} + \frac{b}{f_i^4} + ... \tag{3.5}$$

$$n_{i,ph} = 1 - 40.3\,\frac{N_e}{f_i^2} + \frac{a}{f_i^3} + \frac{b}{f_i^4} + ... \tag{3.6}$$

with $n_{i,gr}$ the refractive group index and $n_{i,ph}$ the refractive phase index on the ith frequency, N_e the electron density and f_i the carrier frequency. The terms a, b do not depend on f_i but are varying with N_e and the geomagnetic field projection along the satellite-to-receiver path. Let us mention that equations (3.5) and (3.6) are valid considering high-frequencies only ($f_i > 100$ MHz) [42].

[5] Satellite coordinates computation algorithms for both broadcast and precise orbits are described in [17, 47, 77, 83].

[6] The complete formula can be found in [24, 57].

[7] Dispersion can be defined as a dependence of the phase velocity on the wavelength or the frequency.

It comes from (3.5) and (3.6) that GPS codes C/A and P(Y) will travel with a group velocity $v_{i,gr} = c/n_{i,gr}$, depending on the ith carrier considered, while L_i carriers will travel with a phase velocity $v_{i,ph} = c/n_{i,ph}$[8]. One can also conclude that $n_{i,gr} > 1$ while $n_{i,ph} < 1$, which implies that ionospheric refraction induces a group delay for codes ($v_{i,gr} < c$) and a phase advance ($v_{i,ph} > c$) for carriers. The ionospheric effect can be defined as the length difference between the real satellite-to-receiver path (*i.e.* considering ionospheric refraction) and the theoretical value assuming a propagation in free space:

$$I = \int n\,ds - \int ds = \int (n-1)\,ds$$

with n the refractive index, corresponding either to the group index n_{gr} or to the phase index n_{ph} and ds an incremental length of the satellite-to-receiver path. It is worth noting that this latter equation assumes that the signal is propagating along the geometrical path, so that changes in the propagation direction (called bending effect) induced by refraction index variations are neglected here.

Considering equations (3.5) and (3.6), the ionospheric effect on GPS code and phase measurements (on the ith carrier) becomes:

$$I_{i,gr} = \int \left(40.3\,\frac{N_e}{f_i^2} + \frac{a}{f_i^3} + \frac{b}{f_i^4} + ...\right) ds \tag{3.7}$$

$$I_{i,ph} = -\int \left(40.3\,\frac{N_e}{f_i^2} + \frac{a}{f_i^3} + \frac{b}{f_i^4} + ...\right) ds \tag{3.8}$$

One can demonstrate that the influence of terms of order higher than f_i^{-2} is negligible if frequencies are larger than 1 GHz, which is the case of GPS signals [71, 84, 88]. Indeed, these higher-order terms constitute less than 1% of the total ionospheric delay [49], so that equations (3.7) and (3.8) are generally truncated after the first-order term[9]. Defining STEC as the integral of the electron density along the satellite-to-receiver path

$$\text{STEC} = \int N_e\,ds\ ,$$

[8] In a dispersive medium, phase and group velocities are related to each other by the Rayleigh equation $v_{gr} = v_{ph} - \lambda\,\frac{dv_{ph}}{d\lambda}$.

[9] However, let us stress that higher-order terms have to be taken into account for precise applications, such as geodetic measurements.

equations (3.7) and (3.8) can be rewritten as follows:

$$I_{i,gr} = 40.3 \frac{\text{STEC}}{f_i^2} = -I_{i,ph} \tag{3.9}$$

The ionospheric effect is thus proportional to the STEC value and is equal, in absolute value, for code and phase measurements. From equation (3.9) it comes that the value of 1 TECU is responsible for an ionospheric delay (or advance) of 16.2 cm on L_1 and 26.7 cm on L_2. Considering that vertical values of about 20 TECU are regularly observed in Belgium, one can deduce that a common value of the ionospheric delay for a satellite observed at zenith ranges between 3 and 5 meters, depending on the frequency. Considering a slant line of sight, values of about 100 TECU can be frequently observed even in mid-latitude regions, which corresponds to an ionospheric delay ranging between 15 and 25 m.

Tropospheric delay. The troposphere constitutes the lowest part of the Earth's atmosphere and is made up of neutral constituents. It extends from the Earth's surface to the tropopause, located at an altitude between 10 and 15 km. By extension, the effect of the neutral atmosphere on radio wave propagation is called *tropospheric refraction*, even if a small fraction is of stratospheric origin. Similarly to ionospheric delay, one defines the tropospheric delay as the length difference of the satellite-to-receiver path induced by tropospheric refraction:

$$T = \int n\, ds - \int ds = \int (n-1)\, ds$$

with $n > 1$, which means that the tropospheric effect corresponds to a lengthening of the ray path, still neglecting the bending effect. Contrary to ionospheric refraction, tropospheric refraction is not dispersive so that the delay is identical on all frequencies (*i.e.* $T_1 = T_2$).

The tropospheric delay is generally separated into two main components: the first corresponding to the dry atmosphere (hydrostatic component) and the second to the wet atmosphere, due to the presence of water vapor. 90% of the total tropospheric delay comes from the dry atmosphere, which is the less variable component. The amount of tropospheric delay in the zenith direction is about 2.4 m and, like the ionospheric delay, increases with the zenith angle of the satellite line of sight.

Multipath. When a GPS signal arrives in the vicinity of the receiver's antenna, it can suffer from several reflections before being received. Reflected signals are therefore superimposed to the direct one, causing interferences in the receiver known as *multipath* delays. Multipath effect depends on local environment surrounding the antenna, such as the ground, walls, vehicles, trees... but also

on the geometry constituted by reflecting surfaces and satellite lines of sight. Since this geometry is changing over time, multipath also varies with time which results in periodic effects. Moreover, as GPS constellation repeats every sidereal day[10], multipath effect exhibits an identical pattern from day to day, with a time lag of about 4 minutes.

The amplitude of multipath effect is different for code and phase measurements; the effect on codes being two orders of magnitude larger than those related to phase measurements. Theoretical considerations show that multipath delay can reach 15 m for P(Y)-code, 150 m for C/A-code and 5-6 cm for phase measurements (corresponding to one fourth of the carrier wavelength). In practice, upmarket models of GPS receivers and antennas, such as those used in geodesy and atmospheric research, are designed to mitigate the effect of multipath. For example, let us mention the use of "choke ring" antennas or specific combinations in the processing step to isolate and reduce the effect. Moreover, as multipath reflections are often observed near the horizon, it is common use to consider an elevation cut-off angle: GPS satellites having an elevation value lower than the cut-off angle are excluded from the observations. Considering permanent stations like those belonging to IGS or EUREF networks, monitoring tools allow the users to estimate the multipath effect on code measurements. For example, the BRUS station (Brussels, Belgium) exhibits code multipath value of about 0.8 m for L_1 carrier, which is much lower that the maximum theoretical value[11].

Clock errors. Atomic clocks of GPS satellites are not perfectly synchronized with GPS time, which is the time frame used for GPS applications and monitored by the GPS control segment. Satellite clock drift Δt^s can however be modeled by a polynomial as follows [17]:

$$\Delta t^s = a_0 + a_1(t^s - t_{0c}) + a_2(t^s - t_{0c})^2 \tag{3.10}$$

where a_0, a_1, a_2 some numerical coefficients, t^s the current time and t_{0c} the reference time for the clock model.

However, this drift model does not suit to precise applications, such as precise positioning. Similarly to orbit products, IGS provides several clock products whose latency depends on the precision required. For example, while the real-time broadcast model (polynomial model, see above) has an accuracy of 5 ns,

[10] A sidereal day corresponds to the time it takes to the Earth to make a complete rotation around its axis. The length of the sidereal day, shorter than that of the solar day, equals 23 hours, 56 minutes and about 4 seconds.

[11] If the value of 0.8 m seems rather low in comparison with theoretical values, it is worth noting that half of IGS permanent stations exhibit code multipath values lower than 0.4 m for the L_1 carrier. As a matter of example, the station of BRUX, which replaced BRUS station in the early 2012, shows multipath values on L_1 lower than 0.2 m [51].

final clock product of IGS reaches an accuracy of ~ 0.075 ns, with a latency ranging from 12 to 18 days [51]. Real-time data are also available from the IGS: the so-called "ultra-rapid" product offers satellite clocks with an accuracy of about 3 ns.

Similarly to satellite clock error, the lack of synchronization of the receiver clock with GPS time leads to the receiver clock error Δt_r. As the receiver's oscillator, generally a quartz, is less stable than atomic clocks, Δt_r may reach very large values so that the drift cannot be easily modeled. This is the reason why the receiver clock error is generally considered as an unknown parameter in the positioning algorithm. Let us mention that some receivers belonging to IGS of EUREF permanent networks are connected with external atomic clocks.

For the sake of completeness, it should be stressed that clock errors also include relativistic effects, which take into account the relative velocity and gravitational potential differences between satellites and terrestrial receivers.

Hardware delay. Delays are generated during the passage of signals through the electronics of the satellite and receiver. These hardware delays are different for code and phase measurements, different from frequency to frequency but can be considered as rather stable with time. This latter property can be used to calibrate receivers in order to compute the TEC [98], whose accuracy mainly depends on that of code hardware delays. If their absolute value is very difficult to estimate, the inter-frequency delays, generally denoted Inter-Frequency Biases (IFB), can be computed with a good approximation by forming observable differences (see section 3.2.2). Common values for code IFB are about 3 ns (1 m) for satellites and 10 ns (3 m) for receivers [88].

Phase center variations and offset. When dealing with positioning system, the goal is to determine the geometric distance between the satellite and the receiver. More precisely, the two end points must correspond to the electrical phase center (called true phase center) of the antennas. Phase center variations, which are different for each frequency, have to be considered for satellites as well as for receivers.

For each GPS satellite, the three-dimensional offset between the satellite center of mass (position to which broadcast orbits refer to) and the true phase center has been determined and is provided to users through IGS antenna files[12]. The offset is made up of two components: 1) the so-called Phase Center Offset (PCO), which is the mean value of the offset, and 2) the Phase Center Variations (PCV), referring to the nadir-dependent variations of the true phase

[12]The international exchange format used by IGS is the ANTenna EXchange (ANTEX) format [55, 81].

center with respect to the mean center. Order of magnitude of PCO for GPS satellites is about 1 m while PCV values are the order of a few millimeters.

Similarly to satellite calibrations, the IGS also provides PCO and PCV values for a large number of commercial antenna models (with or without radome[13]). Receiver's PCO is related to the distance from the Antenna Reference Point (ARF) to the mean phase center. PCVs are related to elevation and azimuth-dependent variations of the true phase center with respect to the mean center. Order of magnitude for PCO of receiver antennas is about 10-15 cm while PCV values exceed rarely 1 cm.

Measurement noise. Measurement noise corresponds to the random error induced by the receiving equipment, which is mainly made up of receiver and antenna hardwares and connecting wires. The noise value depends not only on the type and frequency of the observable but also on the satellite elevation[14]: the higher the satellite is in the sky, the lower the noise level is. Measurement noise is generally assumed to be equivalent to a hundredth of the considered wavelength; however, some recent studies indicate that lower values should be used [6, 25, 26, 88].

3.2.2 Observation combinations and differencing

Linear combinations of GPS observables can be used to cancel or mitigate unwanted effects common to several observables, such as the atmospheric refraction. However, they can also be used to isolate specific effects or interesting properties, which is the case of ionospheric study with GPS. In the classic dual-frequency system which will be used in this thesis, there are basically five types of observables. Recalling that C/A-code is modulated on L_1 only while P(Y)-code is modulated on both L_1 and L_2 carriers, there are three code observables C_1, P_1, P_2 and two phase observables L_1 and L_2.

Linear combination properties. A linear combination of two phase observables can be written as follows:

$$\varphi_{12} = a\,\varphi_1 + b\,\varphi_2 \tag{3.11}$$

where a and b are two float coefficients and φ_i is the phase measurement on the ith carrier, expressed in cycles.

[13] A radome is a protective housing for antenna, made from a material transparent to radio waves.
[14] More precisely, it depends on the Carrier-to-Noise power density ratio (C/N_0) that can be measured by the receiver and which is expressed in dB-Hz.

It is demonstrated that the frequency of the new combination φ_{12} is

$$f_{12} = a\, f_1 + b\, f_2 \tag{3.12}$$

It comes from (3.12) that the combination wavelength is $\lambda_{12} = c/f_{12}$, and thus

$$\lambda_{12} = \frac{c}{a\, f_1 + b\, f_2} \tag{3.13}$$

Assuming that φ_1 and φ_2 are independent variables with a respective noise level σ_1 and σ_2, variance propagation law allows to compute the noise on the combination:

$$\sigma_{12} = \sqrt{a^2\, \sigma_1^2 + b^2\, \sigma_2^2} \tag{3.14}$$

Ionospheric-free combination. The combination allowing to cancel out the effect of the ionospheric refraction on the first order (*i.e.* the term $40.3\, \frac{\mathrm{STEC}}{f_i^2}$) is the Ionospheric-Free (IF) combination:

$$\text{For codes :} \qquad P_{IF} = \frac{1}{f_1^2 - f_2^2}\, \left(f_1^2\, P_1 \; - \; f_2^2\, P_2 \right) \tag{3.15}$$

$$\text{For phases :} \qquad \phi_{IF} = \frac{1}{f_1^2 - f_2^2}\, \left(f_1^2\, \phi_1 \; - \; f_2^2\, \phi_2 \right) \tag{3.16}$$

This combination is widely used in the case of PPP technique, which allows to obtain a centimeter-level accuracy using code and phase measurements with only one receiver. In accordance with equation (3.14), the noise level on the IF combination is computed as follows:

$$\sigma_{P_{IF}} = \sqrt{\left(\frac{f_1^2}{f_1^2 - f_2^2} \right)^2 \sigma_{P_1}^2 \; + \; \left(\frac{f_2^2}{f_1^2 - f_2^2} \right)^2 \sigma_{P_2}^2} \; \simeq \; 3\, \sigma_{P_i}$$

$$\sigma_{\phi_{IF}} = \sqrt{\left(\frac{f_1^2}{f_1^2 - f_2^2} \right)^2 \sigma_{\phi_1}^2 \; + \; \left(\frac{f_2^2}{f_1^2 - f_2^2} \right)^2 \sigma_{\phi_2}^2} \; \simeq \; 3\, \sigma_{\phi_i}$$

One can see that if the IF combination allows to cancel out the ionospheric term, its noise level is about three times larger than for a single observation. In the case of phase measurements, another disadvantage is that IF ambiguity is a float number, which may cause problems in fixing L_1 and L_2 ambiguities to their right integer value.

Geometric-free combination. The Geometric-Free (GF) combination allows to isolate the ionospheric term:

$$\text{For codes :} \qquad P_{GF} = P_1 - P_2 \tag{3.17}$$

$$\text{For phases :} \qquad \phi_{GF} = \phi_1 - \phi_2 \tag{3.18}$$

The main property of the combination is that all frequency-independent terms are removed, which are the distance term, the orbit error, the tropospheric refraction and receiver and satellite clock errors. Considering (3.4), the GF combination of phase measurements can be rewritten as:

$$\begin{aligned} \phi_{GF} &= \phi_1 - \phi_2 \\ &= \alpha\,\mathrm{STEC} + m_{GF} + c\,(d^s_{GF} + d_{r,GF}) + \mathrm{PCV}^s_{GF} \\ &\quad + \mathrm{PCV}_{r,GF} + N_{GF} + \varepsilon_{GF} \end{aligned} \tag{3.19}$$

with:

α a numerical coefficient, $\alpha = -1.05046\ 10^{-17}\ [\mathrm{m^3/e^-}]$;

m_{GF} the multipath term on GF phase combination $m_{GF} = m_1 - m_2$;

d^s_{GF} and $d_{r,GF}$ the phase hardware delays on GF phase combination, respectively in the satellite s and in the receiver r, where $d^s_{GF} = d^s_1 - d^s_2$ and $d_{r,GF} = d_{r,1} - d_{r,2}$;

PCV^s_{GF} and $\mathrm{PCV}_{r,GF}$ the phase center variations and offsets on GF phase combination, respectively in the satellite s and in the receiver r, where $\mathrm{PCV}^s_{GF} = \mathrm{PCV}^s_1 - \mathrm{PCV}^s_2$ and $\mathrm{PCV}_{r,GF} = \mathrm{PCV}_{r,1} - \mathrm{PCV}_{r,2}$;

N_{GF} the float ambiguity on GF phase combination $N_{GF} = \lambda_1 N_1 - \lambda_2 N_2$;

ε_{GF} the noise on GF phase combination $\varepsilon_{GF} = \varepsilon_1 - \varepsilon_2$.

This equation is the basis of the TEC computation with GPS signals. In particular, it shows that the precision of TEC reconstruction based on GPS data depends on inter-frequency phase hardware delays, multipath, phase center variations but also on the GF ambiguity, which can be solved using code measurements only[15].

The main drawback of GF combination is, like for IF combination, that it does not provide integer ambiguities. However, the noise level in the GF is lower than for the IF: $\sigma_{\phi_{GF}} \simeq 1.6\,\sigma_{\phi_1}$.

[15] This latter point implies that final TEC accuracy depends, in a classic dual-frequency system, on the accuracy of code measurements [88, 98].

For the sake of completeness, let us also mention the existence of other frequency combinations, such as the Wide-Lane (WL), Narrow-Lane (NL) and the Melbourne-Wübenna (also called L_6) combinations [23, 57].

Time differencing. Instead of making linear combinations of different frequencies, one can also perform differences between (consecutive) observation epochs. Making time differences simplifies observation equations as the terms which are constant with time are removed.

Let us illustrate this principle with the GF combination, which will be used in chapter 4: if t_k and t_m are two observation epochs and considering (3.19), one can write the time-differenced GF combination $\Delta\phi_{GF}$ as follows:

$$\begin{aligned} \Delta\phi_{GF} &= \phi_{GF}(t_k) - \phi_{GF}(t_m) \\ &= \alpha\,(\mathrm{STEC}(t_k) - \mathrm{STEC}(t_m)) + m_{GF}(t_k) - m_{GF}(t_m) \\ &\quad + N_{GF}(t_k) - N_{GF}(t_m) + \varepsilon_{GF}(t_k) - \varepsilon_{GF}(t_m) \end{aligned} \tag{3.20}$$

We can see that hardware delays and PCVs disappeared as they exhibit stable values with time. Moreover, if t_k and t_m are close to each other (consecutive epochs for example), multipath influence is mitigated. Indeed, as multipath corresponds to a periodic effect (with periods about tens of minutes), residual multipath effect $m_{GF}(t_k) - m_{GF}(t_m)$ is smaller than for a single epoch observation if the time difference $t_k - t_m$ is significantly smaller than multipath period.
Let us note that assuming an identical noise level σ for each single observation, the time difference would exhibit a noise level equals to $\sigma_\Delta = \sqrt{2}\,\sigma$, so the initial noise is amplified by a factor of about 1.4.

Single and double differencing. Another way of simplifying observation equations is making the use of observation differences between satellites and/or receivers. As observation differences can be either formed between receivers or between satellites, one defines the Single Difference (SD) as the difference formed by data observed simultaneously at two receivers on the same satellite. The advantage of SD lies in the cancellation of all errors common to the two stations: satellite clock error and the common part of atmospheric errors. Moreover, if the stations are not far from each other, the residual atmospheric effects can be neglected, which simplifies the SD expression. As for time differences, if one assumes that the two one-way measurements have an equal precision σ, SD will be characterized by a noise level of $\sqrt{2}\,\sigma$.

Double Difference (DD) is defined as the difference between two SDs made at the same time and related to two observed satellites. Forming DDs allows to cancel errors common to the satellites and the receivers. Thus, in addition to satellite clock error and common atmospheric biases, receiver clock errors are also canceled in DDs. Analogously to SD, the noise term on a DD is larger

than that of an undifferenced measurement. Considering a precision σ for an undifferenced measurement, the corresponding DD noise level is $\sigma_{DD} = 2\,\sigma$.

3.3 The use of GPS in ionospheric studies

3.3.1 Basic principles

GNSS are generally considered as "satellites of opportunity" for ionospheric research. Indeed, each constellation being made up of about 30 satellites, receivers are able to track several satellites simultaneously, and therefore to perform multiple ionospheric observations at a given epoch. Moreover, GNSS receivers are relatively low-cost, compared to other ionospheric probing devices such as ionosondes or radars. As already stated, we will use the GPS system only in the frame of this thesis, but the methodology developed here can be applied to other systems without any loss of generality.
In ionospheric studies with GPS, it is common use to assimilate the ionosphere to a simple geometric shape. Generally, ionospheric plasma is assumed to be confined into a spherical shell, infinitesimally thin, containing all free electrons. If other models exist, such as the thick layer model, they have not been used in the frame of this thesis. However, these alternative models are presented and compared to the thin model in appendix A. Considering a GPS satellite and a ground receiver, one calls Line of Sight (LoS) the satellite-to-receiver path while the intersection between the ionospheric shell (at an altitude h) and the LoS is the Ionospheric Pierce Point (IPP), as illustrated in figure 3.2(a). In practice, satellites having an elevation lower than the cut-off angle are excluded from the dataset to avoid contamination by multipath and noise. Cut-off angle value results mainly from a compromise between the quality of the signal and the number of satellites available. In the frame of this work, cut-off values of 20° and $h = 400$ km have been used; discussion about the choice of these values is given in section 4.1.2. For example, figure 3.2(b) shows the IPPs for a 24 h observation session in Brussels. Based on figure 3.2(b), several comments can be made:

- All IPPs are located in the mid-latitude region, which means that all GPS measurements collected in Belgium are related to a mid-latitude ionosphere and that phenomenon specific to polar or equatorial region will not be observed.

- IPPs are rather homogeneously distributed in latitude and in longitude around the station, except for the lack of coverage located north of the station. As a consequence, IPPs may be related to quite different local times: maximum difference in longitude is about 25°, which means that the largest local time difference between two simultaneously observed IPPs is nearly 2 hours. Such longitudinal gradients in VTEC may influence positioning algorithms, especially for dawn and dusk sectors [33, 68].

- Latitude range reaches up to 15° (∼1600 km), which implies that, similarly to longitudinal VTEC gradients, latitudinal ones are also present in the data.

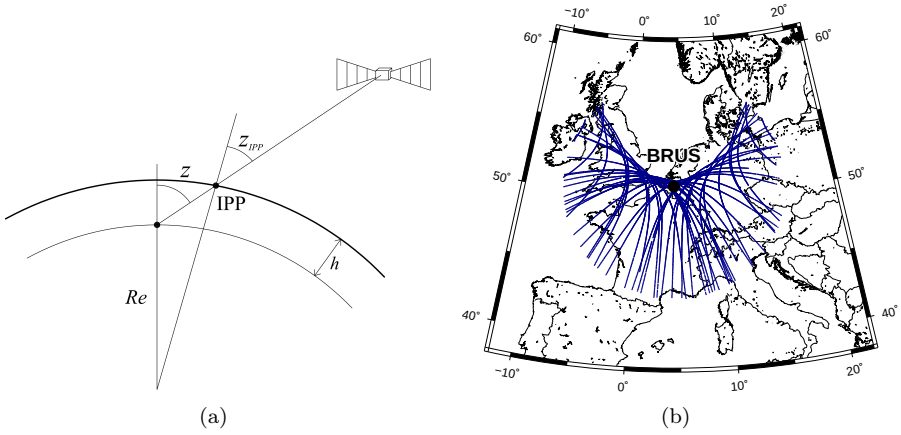

(a) (b)

Figure 3.2 – (a) Thin spherical shell model. The Ionospheric Pierce Point (IPP) corresponds to the intersection of the Line of Sight (LoS) with the spherical shell at an altitude h. (b) Map of the IPPs for the station of Brussels (BRUS), with an elevation cut-off of 20° and $h = 400$ km.

In the frame of ionospheric studies, STEC is computed for all IPPs in view and converted to VTEC using a Mapping Function (MF). The MF (which depends on the shell model, see appendix A) used in this thesis is the thin single layer MF. The conversion between slant and vertical TEC values is achieved by the use of the MF:

$$\mathrm{MF} = \frac{\mathrm{STEC}}{\mathrm{VTEC}} = \frac{1}{\cos(z_{\mathrm{IPP}})} \tag{3.21}$$

where z_{IPP} is the zenith angle of the satellite at the IPP.

3.3.2 Observational bias

Using moving satellites to monitor the TEC and its variations in time and space induces some observational biases. Indeed, there is a relative movement between the moving observer (the satellite), the moving structure (the ionospheric irregularity) and the receiver station which is also moving due to the Earth rotation. As a consequence, one-way measurements are affected by the relative movement between the satellite and the ionospheric disturbance. More precisely, only the projection of the velocity vector of the satellite $\mathbf{v}$ on the direction of propagation of the disturbance $\mathbf{k}$ matters. In other words, one can expect no relative effect if both directions are perpendicular, *i.e.* if $\mathbf{v} \cdot \mathbf{k} = 0$.

Mainly, there are two elements constituting the **v** vector: its direction (as already mentioned, with respect to the ionospheric disturbance) and its absolute value, depending notably on satellite elevation and on the assumed ionospheric height. For example, figure 3.3(a) shows IPP traces for three satellites, exhibiting different geometric conditions: while PRN 06 and PRN 30 start from 20° to reach nearly 90°, PRN 17 culminates at about 35° elevation, which can be considered as a low value. Their corresponding velocity on the ionospheric shell is displayed in figure 3.3(b), where we can see that the largest values correspond to low elevations. Velocities range from less than 50 m/s to about 350 m/s; thus, velocity values may change with a ratio of 1:7 according to the satellite elevation.

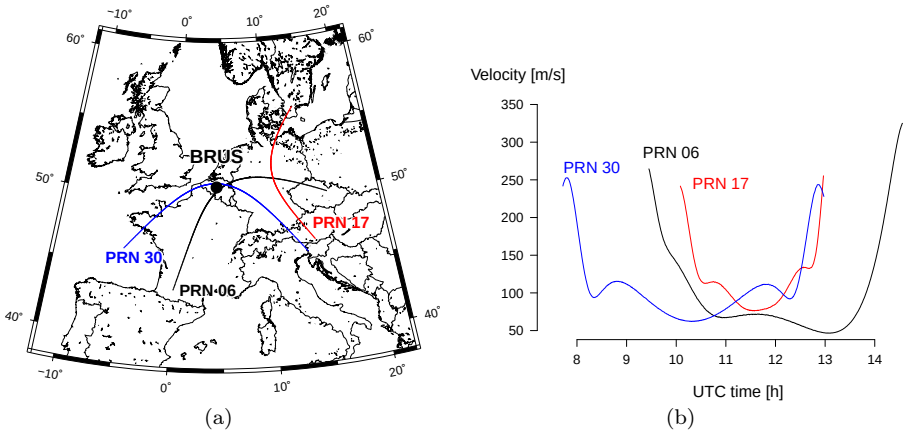

(a) (b)

Figure 3.3 – IPP velocity values for three GPS satellites (PRN 06, 17 and 30). The ionospheric shell height is h=400 km and the elevation cut-off angle equals 20°.

The analysis of the combined effect of IPP velocity and direction can be achieved using simulations. In his master's thesis, Wautelet [102] developed a tool simulating both GPS constellation and MSTIDs within a given geographical area. This software has been used to simulate the IPP trace of a given satellite (PRN 13), observed from Brussels (BRUS) station, on the ionospheric shell at 400 km and using an elevation cut-off angle of 20°. The IPP trace of this satellite is displayed in figure 3.4(a). Then, several MSTIDs have been simulated in order to meet the following configurations between satellite and MSTID motion:

1. satellite motion is parallel to MSTID at low elevation;
2. satellite motion is anti-parallel to MSTID at low elevation;
3. satellite motion is perpendicular to MSTID at low elevation;
4. satellite motion is parallel to MSTID at high elevation;

5. satellite motion is anti-parallel to MSTID at high elevation;
6. satellite motion is perpendicular to MSTID at high elevation.

Based on the IPP trace depicted in figure 3.4(a), low elevation values have been chosen at the end of the satellite visibility period (east of the station), where velocities are about 350 m/s. High elevation IPPs are chosen near the station, where $|\mathbf{v}| \simeq 50$ m/s. Let us add that the simulated MSTID exhibits the same properties for all the aforementioned cases: wavelength of 200 km and velocity of 200 m/s, giving a period of about 16 min. These parameters are coherent with the values related to typical daytime MSTIDs, as detailed in section 2.3.2.
Figures 3.4(b) and (c) depict GPS GF phase measurements for the six cases previously mentioned. They show that the apparent period of the MSTID is reduced if satellite and TID motions are anti-parallel. Indeed, the simulated period of 16 min is reduced to about 9 min for low elevation IPPs while values of about 12 min are observed at high elevation. Conversely, for satellites moving in the same direction than the MSTID, apparent periods are stretched: values of about 25 min might be observed with high elevation data while observations at low elevation do not exhibit any wave cycle. Indeed, as the satellite is moving together with the structure, the MSTID is not detected at all. Finally, as expected, apparent periods corresponding to motions perpendicular to that of the MSTID are mostly equal to the simulated period, e.g. around 16 min. We can conclude that observational bias is enhanced for satellite trajectories that are roughly parallel to the disturbance motion.
The retrieval of TID period and amplitude is also depending on the sampling rate of the observations, which is related to the IPP velocity on the ionospheric shell. Indeed, one needs a minimum number of observations to completely resolve (detect) a full TID wavelength in phase measurements. Given a fixed sampling rate, there are some geometrical conditions that do not fulfill this minimum number, for example when the relative velocity between the TID and the satellite is very large. It results some distortions not only in the apparent period (as stated above) but also in the amplitude, as demonstrated in Wautelet [102]. In this study, it has been concluded that sampling rate effect mainly affects disturbances of small wavelengths and/or large velocities. As an example, the author recommends high-rate observations (e.g. 1 sec data) to allow the detection of very small wavelengths (< 10 km) typical of Small-Scale Traveling Ionospheric Disturbances (SSTIDs).
Another observational bias is due to the integral nature of TEC measurement and to the simplified ionospheric model used, which is the infinitesimally thin layer. Indeed, let us consider an N_e enhancement inside a given slab of plasma observed through a fixed LoS, e.g. a link towards a geostationary satellite (figure 3.5). The observed STEC variations can be caused by effective variations of the electron density or by local effects in the slant LoS. Indeed, particular geometric conditions may lead to unchanged or enhanced STEC values, as illustrated in figure 3.5.
As a conclusion, STEC measurements with GPS are biased by several effects mainly due to (1) the non-geostationary character of the GPS constellation, (2) the simpli-

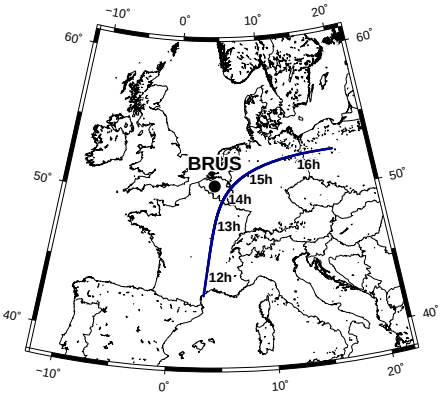

(a)

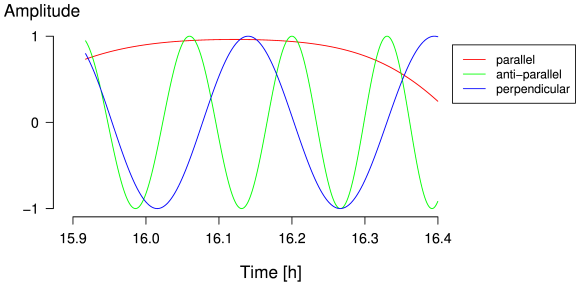

(b)

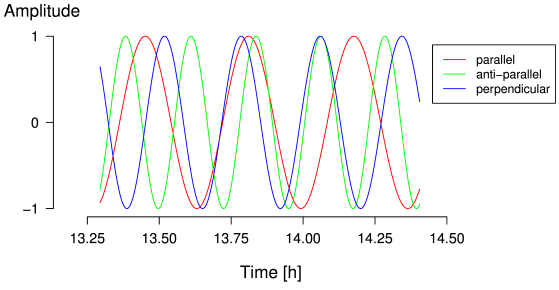

(c)

Figure 3.4 – Effect of the relative movement between a GPS satellite and an MSTID based on simulations. MSTID wavelength is 200 km, its velocity is 200 m/s and the ionospheric shell is at an altitude of 400 km height. (a) IPP trace of simulated PRN 13. (b) Time series of GF phase measurements while the satellite moves in the same, in the opposite or in a perpendicular direction than that of the MSTID. The time series corresponds to the end of the visibility period of PRN 13 (low elevation), which gives IPP velocity values of about 350 m/s. (c) Similar to (b) but for high elevation IPPs (close to the BRUS station), thus for IPP velocities of about 50 m/s. (Adapted from [102])

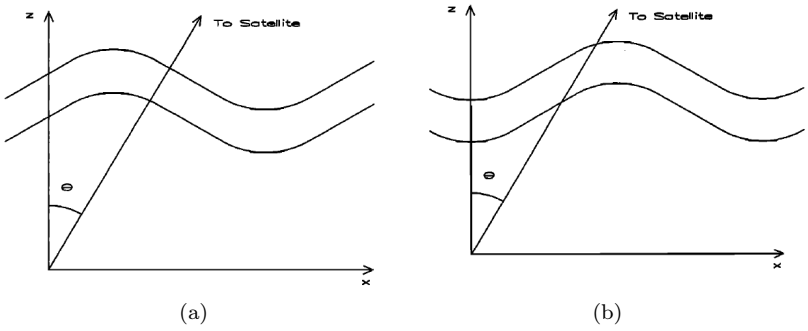

Figure 3.5 – Observational bias in STEC variations due to a propagating TID in the case of a geostationary LoS. Top and bottom lines correspond to the boundaries of the TID while the origin of axes is the observing ground station. When the disturbance is propagating in the X-axis direction (b) the resulting STEC value is larger than in the case of a stationary height disturbance (a). (From [5])

fied ionospheric model used and (3) the sampling rate of observations. These effects clearly distort the ionospheric disturbance parameters such as the wavelength, the period and the amplitude, so that their retrieval needs simultaneous observations at different ground stations. For example, Garrison et al. [32], Hernandez-Pajares et al. [43] exploited the added value of GPS networks to derive propagation parameters of ionospheric disturbances and performed some statistics of occurrence. However, it appears that such multi-station observations could be biased in favor of disturbances traveling in a direction roughly parallel to the satellite trajectory [32].

Chapter 4

Climatological study of ionospheric irregularities in Belgium

Contents

The ionosphere is generally considered as the main error source in precise positioning with the Global Positioning System (GPS). More particularly, the presence of small-scale structures and irregular patterns in time and space may be the origin of degraded positioning conditions. There is a growing demand from GPS user communities to be informed, if possible in advance, of the occurrence of irregularities that might impact on their positioning algorithm. For example, geomagnetic storm occurrence can be predicted about 7 hours in advance. On the contrary, the occurrence of irregularities which do not depend on space weather conditions are not easily forecasted: this is the case of Medium-Scale Traveling

Ionospheric Disturbances (MSTIDs) and of other irregularities whose origin is not totally understood yet.
In this chapter we will perform a climatological study of ionospheric irregularities observed at a mid-latitude GPS station. Their probability of occurrence with respect to solar cycle, seasons and time of day as well as their amplitude will be carefully analyzed and summarized. It should be stressed that, contrary to most of climatological studies focusing on a given irregularity type (e.g. MSTIDs, Es layers...), our approach gathers all irregularity types. As a consequence, there is no need to use complex mathematical tools to filter out (or select) specific behaviors, such as the Fourier transform broadly used to detect wave-like oscillations which are typical of MSTIDs.

4.1 Ionospheric irregularities detected at a single GPS station

4.1.1 Methodology

The ionospheric irregularities detection algorithm used in this chapter has been developed in Warnant [98] and is based on Total Electron Content (TEC) rate of change observations, *i.e.* time variations of TEC. We have seen that the Geometric-Free (GF) phase combination allows to obtain Slant TEC (STEC) (see equation 3.19):

$$\begin{aligned}\phi_{GF} &= \phi_1 - \phi_2 \\ &= \alpha\,\mathrm{STEC} + m_{GF} + c\,(d^s_{GF} + d_{r,GF}) + \mathrm{PCV}^s_{GF} \\ &\quad + \mathrm{PCV}_{r,GF} + N_{GF} + \varepsilon_{GF}\end{aligned}$$

Since we are interested in irregularities we compute the STEC rate of change, denoted ΔSTEC, between consecutive epochs t_k and t_{k-1}:

$$\Delta\mathrm{STEC} = \mathrm{STEC}(t_k) - \mathrm{STEC}(t_{k-1}) \tag{4.1}$$

Considering an elevation cut-off angle of 20°, the effect of multipath and noise can be considered as negligible with respect to the ionospheric signal. Moreover, the sampling rate of GPS measurements used in this thesis is 30 s, so that time differencing will eliminate all effects that are mostly stable with time (see section 3.2.2). As a consequence, phase hardware delays d and Phase Center Variations (PCV) appearing in equation (3.19) can also be neglected. Under these simplifications, equation (4.1) can be rewritten as:

$$\begin{aligned}\Delta\mathrm{STEC} &= \frac{1}{\alpha}\,(\phi_{GF}(t_k) - \phi_{GF}(t_{k-1})) \\ &= 9.5196\,(\phi_{GF}(t_k) - \phi_{GF}(t_{k-1}))\end{aligned} \tag{4.2}$$

ΔSTEC is then normalized to be expressed in TEC Unit (TECU)/min. As we are dealing with 30 s data, ΔSTEC value has therefore to be multiplied by a factor 2. Let us note that equation (4.2) is valid only if no cycle slip occurs on GF combination between epochs t_k and t_{k-1}, meaning that $N_{GF}(t_k) - N_{GF}(t_{k-1}) = 0$. Otherwise, any cycle slip on L_1 or L_2 (*i.e.* ΔN_1 and/or ΔN_2) will produce a jump in ΔSTEC equals to $(\lambda_1 \Delta N_1 + \lambda_2 \Delta N_2)$. This peak can be very large in comparison with the background level of the combination, allowing it therefore to be detected and removed during a dedicated step of the processing[1]. Let us also mention that a cycle slip detection algorithm has already been applied during the pre-processing step, making these jumps in ΔSTEC quite rare. This algorithm is based on the L_6 code-phase combination, also called Melbourne-Wübenna combination[2].

It is worth noting that ΔSTEC accuracy does not depend on TEC accuracy as it is derived from phase measurements only. This makes ΔSTEC observations much more precise than absolute TEC measurements[3].

ΔSTEC are then converted into vertical values by the mapping function, assuming a single ionospheric thin shell at an altitude of 400 km:

$$\Delta\text{VTEC} = \Delta\text{STEC} \,.\, \cos(z_{\text{IPP}}) \tag{4.3}$$

with z_{IPP} the zenith angle of the satellite at the Ionospheric Pierce Point (IPP). The choice of the shell height (400 km) and the elevation cut-off angle (20°) is discussed in the next section.

Considering the visibility period of a given satellite, or *arc*, we can observe that ΔVTEC time series exhibits a trend. This is due to a) the satellite motion on the ionosphere and b) the regular Vertical TEC (VTEC) variations with time and space. ΔVTEC series result therefore from the combined effects of constellation geometry and regular gradients of the ionosphere. To extract high-frequency variability in VTEC, such effects have to be filtered out: a polynomial fit of the third order is applied to each arc and then subtracted to ΔVTEC series. An example of polynomial fitting of ΔVTEC time series and their corresponding IPPs is shown in figure 4.1. Analysis of figure 4.1(a) shows a net eastward movement of the satellite; its zonal component being maximum around 0700 UT. This latter component is important since it is oriented against the apparent Sun motion on the ionosphere, enhancing the

[1] In this thesis, we use the efficient filtering algorithm developed by Wautelet [103]. Based on a statistical analysis of ΔSTEC time series, several filters identify and remove the outliers from the series. As a result, ΔSTEC series can be considered as clean series reflecting the true ionospheric conditions.

[2] Details concerning the cycle slip detection method using the L_6 combination can be found in [11, 47].

[3] An important step in the absolute TEC computation is the calibration of the receiver, or more precisely the computation of the Inter-Frequency Biases (IFB), which mainly depend on code accuracy. It is generally accepted that TEC accuracy is about 2-3 TECU while ΔSTEC measurements have an accuracy of about 0.01 TECU/min (see next section). Additional information about IFB and TEC computation can be found in [15, 44, 98].

regular VTEC gradients. In figure 4.1(b), the pattern observed for ΔVTEC series is the combination of these two factors: at the beginning of the arc, a moderate trend is observed because background nighttime gradients are low. In the middle of the arc (between 0500 and 0800 UT), ΔVTEC remains quite steady but rises quickly while approaching its end around 0900 UT, located in the dawn sector. One can observe that the third order polynomial provides a fairly good approximation of the ionospheric background, except during periods of irregularities, which can be identified around 0400 UT and between 0700 and 0830 UT.

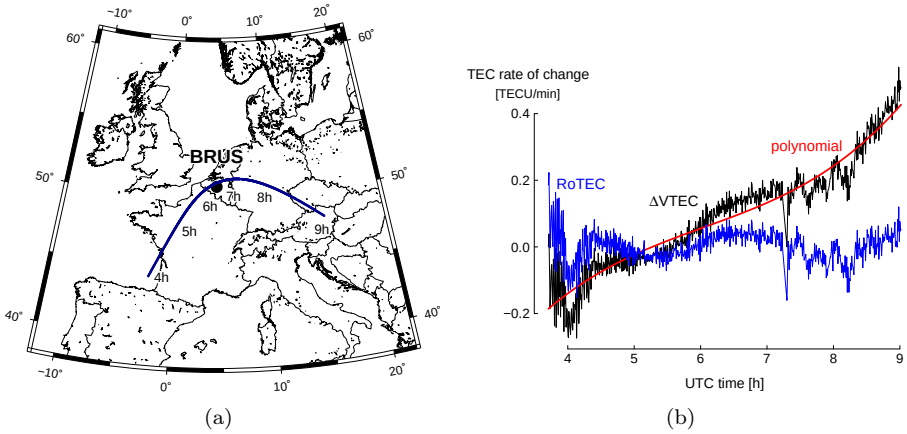

(a) (b)

Figure 4.1 – ΔVTEC, polynomial fit and RoTEC (b) related to PRN 12 on Day of Year 330 in 2011 (DOY 330/11). The corresponding IPPs are depicted in (a) together with their observation time, expressed in hours (UTC). Sunrise at BRUS occurs at 0816 UT.

Finally, residuals from the fitting procedure, denoted Rate of TEC (RoTEC), correspond to the basic observables used in this chapter to detect ionospheric irregularities. More precisely, the occurrence rate analysis detailed in section 4.2 will be based on the standard deviation of RoTEC computed over time windows of 15 min[4]. If this value, called σ_{RoTEC}, exceeds the detection threshold of 0.08 TECU/min, an "ionospheric event" is detected and added to the occurrence statistics. All details concerning this technique (including the choice of the thresholds) are discussed in Warnant [98], Warnant and Pottiaux [99].

[4]This time interval is suitable for MSTID detection as their corresponding period is generally ranging between ∼12 and 25 min [43].

4.1.2 Validity of the method

The methodology described in the previous section will be used to derive a climatological study of ionospheric irregularities over ten years of data. Therefore, all errors affecting the precision and the reliability of this study have been carefully assessed to validate our methodology.

- The climatological study which will be presented in the next chapter covers ten years of GPS data from 2002 to 2011. During this time interval, some satellites have been launched while some of them have been withdrawn from the constellation, leading to changes in the number of satellites with time. As a larger number of satellites implies a larger number of potential irregularities observed, the occurrence statistics have to take into account the evolution of the constellation. Figure 4.2(a) depicts the evolution of the number of GPS satellites from 2002 to 2011, corresponding to the time interval used in our analysis (see section 4.2).

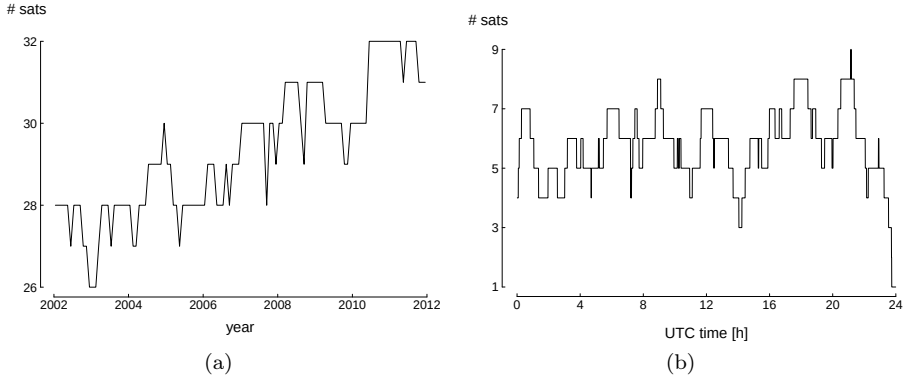

Figure 4.2 – Evolution of the GPS constellation. (a) Monthly mean number and (b) number of GPS satellites as a function of the time of the day, derived from RINEX observation files at BRUS station. Data depicted in (b) are related to DOY 001/02.

GPS constellation has globally seen its number of satellites to increase, starting from 28 in January 2002 to 31 satellites in December 2011. Of course, this number is fluctuating as some satellites are declared "unhealthy" during some maintenance periods, which explains the peaks observed in figure 4.2(a). As a consequence, the occurrence statistics described in the next section will include the evolution of the GPS constellation: the number of irregularity occurrence at a given epoch will be weighted by the number of satellites.

In addition to the long-term trend due to the evolution of the constellation, one should also pay attention to the daily variability of the number of satellites. Figure 4.2(b) illustrates the number of GPS satellites simultaneously

observed for a 24-hours period. This number oscillates generally between 4 and 8, with a mean number of about 6 satellites. As the constellation repeats itself every sidereal day, we can consider that daily variation in the number of satellites will not influence statistics built over long periods, which is the case for our climatological study. Therefore, only the long-term trend of the GPS constellation will be considered in the computation of our statistics.

- In equation (4.2) the effects of noise and multipath have been neglected with respect to the ionospheric signal. However, their precise assessment is needed to avoid that some periods of enhanced multipath and noise are identified as irregularities.

  One can assess the theoretical level of phase noise in the following way: considering that noise level of undifferenced phase measurements on L_1 and L_2 is respectively 2 and 2.5 mm (about 1/100 of the wavelength), variance propagation law predicts a noise level of 3.2 mm for the undifferenced GF combination. Considering equation (4.2), we obtain $\sigma_{\Delta \mathrm{STEC}} \simeq 0.009$ TECU/min. In addition, let us recall that slant values are mapped to vertical by the use of the Mapping Function (MF): $\Delta \mathrm{VTEC} = \Delta \mathrm{STEC} \cdot \mathrm{MF}^{-1}$, with $\mathrm{MF}^{-1} < 1$. As a consequence, theoretical noise on ΔVTEC, and therefore on RoTEC, is bounded by 0.009 TECU/min.

  Theoretical value of σ_{RoTEC} will then be compared with true data. Since the goal is to assess multipath and noise terms, we will select very quiet periods in terms of geomagnetic and solar activity. Moreover, to minimize dawn and dusk effects in TEC, only satellite arcs observed during nighttime (0000 - 0400 LT) will be considered. We chose a period of ten days during the very quiet summer 2009: from Day Of Year (DOY) 221 to 230, where TEC background level was about 2-3 TECU at night and less than 10 TECU during daytime. σ_{RoTEC} distribution is summarized in "box and whisker" plots for the three Belgian GPS stations that will be used in this chapter (figure 4.3): Brussels (BRUS), Dentergem (DENT) and Dourbes (DOUR). First, one can observe that medians do not exceed 0.025 TECU/min while 75% of the measurements are below 0.03. However, a slight variability of medians and InterQuartile Ranges (IQRs) between stations can be pointed out: for example, percentile 25 (P_{25}) at BRUS station is mostly equivalent to P_{75} related to DOUR station. These discrepancies can be explained by differences in receiving equipment (different receiver/antenna types imply different noise/multipath levels) but also by specific environmental conditions able to enhance the multipath effect at a given location. Comparing results from figure 4.3 with theoretical noise values, one can clearly observe that σ_{RoTEC} exceeds the expected values. As a conclusion, multipath effect can be interpreted as the major contribution to σ_{RoTEC} measurements, as long as the polynomial fit describes perfectly the long-term trend due to the combined geometry/quiet ionosphere and as true noise levels correspond to theoretical ones.

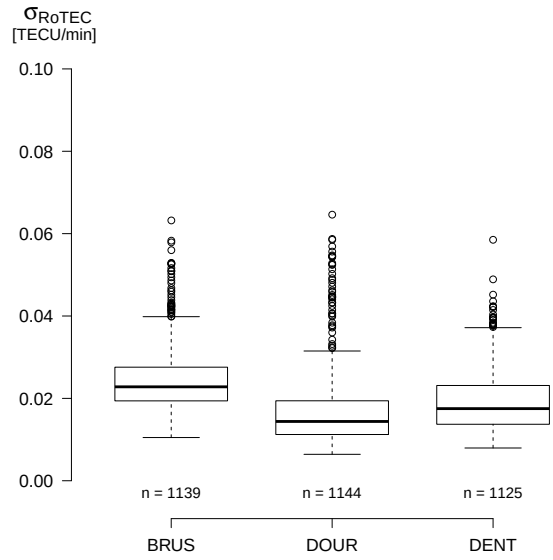

Figure 4.3 – Box and whisker plots of σ_{RoTEC} for BRUS (50.80°N,4.36°E), DOUR (50.09°N,4.59°E) and DENT (50.93°N,3.40°E) stations. Period analyzed covers DOY 221 to 230 in 2009. Box bounds correspond to quartiles (P_{25} and P_{75}) while the thick line is the median. Whiskers are located at $P_{25} - 1.5$ IQR (interquartile range) and at $P_{75} + 1.5$ IQR. If this value exceeds the minimum (maximum) of the dataset, the whisker is located at the minimum (maximum). Small circles correspond to outliers, *i.e.* values larger (smaller) than the upper (lower) whisker. The number "n" denotes the sample size, which is the number of 15 min periods used for each plot.

However, assessing multipath can also be achieved by using an interesting property of GPS constellation: its repeatability every sidereal day, which makes the "satellite-receiver" geometry to repeat every day minus 3 min and 56 sec. Considering a given satellite arc for several consecutive days and applying a time shift of about 4 min/day, superimposition of RoTEC time series will make appear multipath contribution. To better capture the multipath signature, noise is mitigated by using a 4 min (*i.e.* 9 measurement epochs) running average filter. Still based on the quiet period mentioned above (summer 2009), the chosen arc corresponds to Pseudo Random Noise (PRN) 20 as it exhibits a long period of visibility, allowing to assess noise/multipath effects for both low and high elevation values. RoTEC time series related to DOY 223 to 227 are depicted in figure 4.4, where a shift of 4 min/day has been applied. If some periodic effects and an enhanced variability at the end of the visibility period could support the contribution of multipath, it is not clear that it is the only explanation of the RoTEC variability. Indeed, an argument against multipath is that RoTEC series do not vary simultaneously and with the same pattern.

Let us also recall that the lack of fit of the polynomial (*i.e.* this latter does not exactly reproduce the combined effect of the geometry and of the TEC background) could also distort the RoTEC time series, even if its influence has been mitigated by selecting a very quiet TEC background. In conclusion, it is very difficult to isolate the multipath contribution from the RoTEC series, and *a fortiori* in σ_{RoTEC} measurements. Multipath, noise and the lack of fit due to the polynomial should be considered together while validating the detection threshold initially fixed to 0.08 TECU/min (see below).

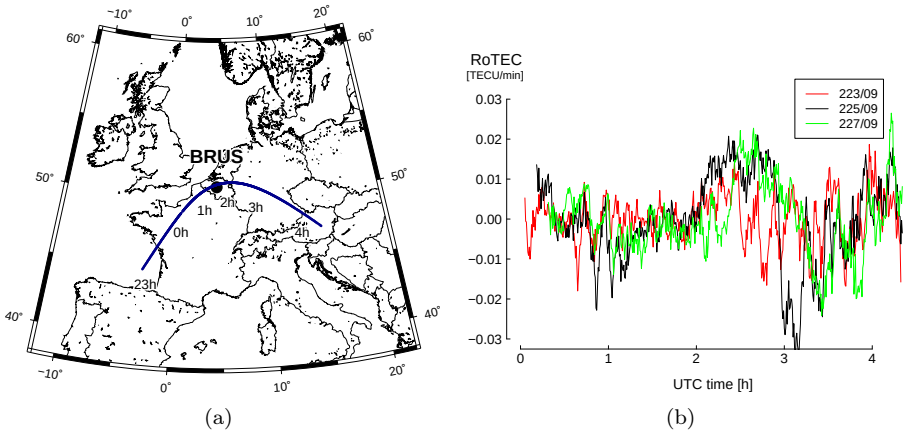

Figure 4.4 – Influence of multipath on a given satellite arc. (a) IPP trace of PRN 20 observed from BRUS station, DOY 225/09. (b) RoTEC for PRN 20, for DOY 223, 225 and 227 in 2009. Time series have been first shifted by $\sim$ 4 min/day before being smoothed by an running average filter (kernel 9) to highlight multipath influence.

- As discussed in the previous chapter, the use of a mapping function always introduces an error in the conversion from slant to vertical TEC values. Comparison between three different MFs has been performed in appendix A, where discrepancies between the different models can be considered as small enough (less or equal to 1.5%) to justify the use of the thin single layer model in the rest of this thesis. Furthermore, let us highlight the fact that using the same MF for all GPS observations makes our dataset self-consistent.

- If the choice of the MF has been justified, it is worth noting that both ionospheric shell height and elevation cut-off angle also play a role in the computation of RoTEC. Indeed, in addition to changes in the MF (see appendix A), variations of the cut-off angle induce changes in the polynomial computation since this latter depends on the number of observations constituting the RoTEC time series. In the aforementioned methodology, an ionospheric height

		Ionospheric shell height [km]					
		200	**300**	**400**	**500**	**600**	**700**
elevation [°]	**10**	8.677	8.770	8.859	8.944	9.024	9.101
	15	8.709	8.807	8.900	8.988	9.072	9.152
	20	8.739	8.839	8.933	9.023	9.108	9.189
	25	8.775	8.877	8.973	9.063	9.149	9.231
	30	8.810	8.912	9.008	9.100	9.186	9.268

Table 4.1 – Influence of ionospheric height and elevation cut-off angle on RoTEC values. The numbers correspond to the maximum RoTEC values (in TECU/min) observed at BRUS station on DOY 324/03. (From [101])

of 400 km and an elevation cut-off angle of 20° have been considered. The influence of these parameters on RoTEC computation has been investigated by comparing several ionospheric heights (from 200 to 700 km) and cut-off angles (from 10 to 30°). As a worst case study, we assessed the influence of those parameters on the extreme RoTEC value observed during the powerful geomagnetic storm of DOY 324 in 2003 (table 4.1). This storm, which will be investigated in the next section, was responsible for the largest RoTEC value of our GPS dataset.

One can observe from table 4.1 that RoTEC is proportional to both ionospheric height and cut-off angle. Discrepancies for a fixed height are the order of 1.5% while those due to cut-off angle variations are about 5%. If these errors are not negligible during the occurrence of extreme values, their contribution is the order of the combined multipath/noise error during moderate ionospheric disturbances. Indeed, considering a RoTEC value of about 1 TECU/min, which is a common value during the occurrence of a MSTID, one obtains errors of 0.015 and 0.05 TECU/min, respectively for ionospheric height and elevation cut-off errors.

- In the methodology described above, ionospheric variability σ_{RoTEC} is computed over time intervals of 15 min. However, the size of the time window affects the occurrence rate of ionospheric irregularities since most of them exhibit characteristic periodicities, like MSTIDs. The influence of the time window on the occurrence rate has been assessed in [101], where values from 5 to 30 min have been considered. It comes out that, if the number of "ionospheric events" is inversely proportional to the time window, occurrence statistics (*i.e.* the shape of the occurrence rate as a function of time) are not distorted by changes in the time window. As a conclusion, the time interval of 15 min originally proposed in our methodology has been kept for the climatological study described in the next section.

The validation step showed that, if the theoretical contribution of noise to the total error budget on σ_{RoTEC} is easy to compute, other effects like multipath or mapping function errors are really difficult to estimate. Indeed, their effect depends on several parameters such as satellite elevation, TEC background, satellite IPP trace... As a consequence, setting up a σ_{RoTEC} threshold valid in all circumstances and for several stations is very challenging and must rely on arbitrary decisions. Therefore, given the aforementioned sensitivity tests, it has been chosen to rise the initial threshold value of 0.08 TECU/min (as proposed by Warnant [98]) to 0.1 TECU/min.

4.1.3 Different types of irregularities

In the following sections we will investigate the occurrence rate and the amplitude of ionospheric irregularities based on a continuous period of GPS measurements in three Belgian stations (BRUS, DOUR and DENT), extending from January 2002 to December 2011. During this 10 years period which covers the declining phase of solar cycle 23 but also the rise of cycle 24, a large number of ionospheric irregularities have been detected. This section aims at illustrating the different RoTEC signatures encountered in our GPS time series by a detailed analysis of a few typical cases observed from BRUS station:

- a strong solar flare (X-flare);
- a major geomagnetic storm;
- a daytime MSTID;
- a nighttime disturbance.

4.1.3.1 Solar flare

As explained in section 2.3.1, Extreme Ultraviolet (EUV) and X photons travel the Sun–Earth distance in about 8 minutes. A burst in the EUV/X flux induces a rise in ionization for the whole sunlit hemisphere, and thus in the TEC values. As an example, let us analyze the ionospheric response to the X17.2 flare which occurred on DOY 301/03, around 1100 UT. All IPPs being located in the sunlit hemisphere, they were all subject to a Sudden Increase in TEC (SITEC) lasting several minutes, as illustrated in figure 4.5 for PRN 07. RoTEC behavior exhibits a double peak, with values reaching nearly 5 TECU/min. Let us note the short-lived signature of the flare in RoTEC compared with the slower recovering period for VTEC or X-ray flux. This is partially due to the extraction of high-frequencies by the polynomial fitting procedure. Let us also mention the superimposed wave-like pattern in RoTEC time series, which corresponds most likely to an MSTID (see below). It is worth mentioning that the MSTID was already observed before the occurrence of the solar flare; as a consequence, the origin of the Atmospheric Gravity Wave (AGW) can not be attributed to thermal gradients induced by solar radiation (*in situ* generation).

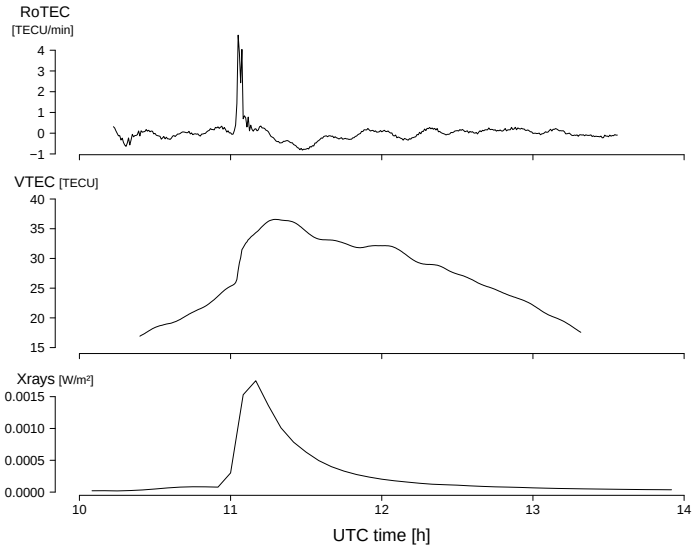

Figure 4.5 – Ionospheric effect of the X17.2 solar flare occurring on DOY 301/03. From top to bottom: time series of RoTEC, VTEC for PRN 07 observed from BRUS station and 5-min X-ray flux from GOES satellite in the 1-8Å band (credit: NOAA/SWPC).

4.1.3.2 Geomagnetic storm

The long-lasting geomagnetic storm occurring on DOYs 302–304/03 was the direct consequence of the extremely fast geoeffective Coronal Mass Ejection (CME), due to the aforementioned X17 flare which occurred the day before. The initial phase of the storm began at 0600 UT, when the Disturbance Storm Time (DST) index dropped quickly to about -150 nT, before a second storm phase made this value decrease to -353 nT around 2300 UT (figure 4.6). The recovery period started from about midnight and lasted until a new sharp decrease occurred in the late evening (1700 UT), with the minimum value of -383 nT observed at 2300 UT. Corresponding planetary K index (Kp) reached the value of 9 units (as large as possible); the periods of maximum being more or less simultaneous to large DST decreases. The ionospheric response to the CME impact has been studied for different regions by several authors, such as de Franceschi et al. [27], Ding et al. [30], Stankov et al. [89]. It has been shown that different phases (positive, negative) occurred, in addition to Large-Scale Traveling Ionospheric Disturbances (LSTIDs) and patches of ionization causing ionospheric scintillations. The panel of ionospheric patterns induced by ionospheric storms is therefore very large, and three specific RoTEC signatures have been chosen for illustrating purpose.

The first case is a TEC depletion (negative phase of the ionospheric storm), also called “moving ionospheric wall” [89], likely associated with a patch of higher ioni-

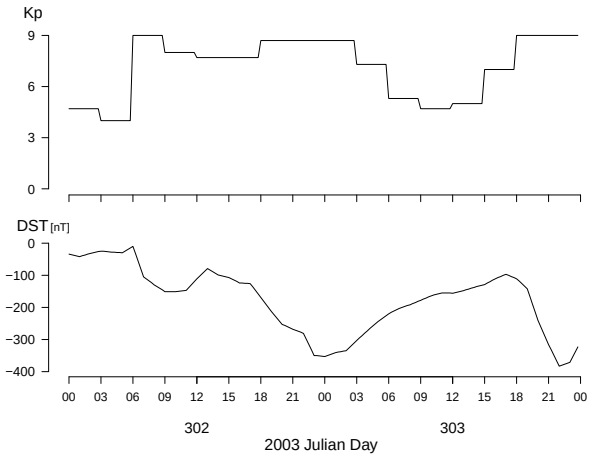

Figure 4.6 – Geomagnetic indices Kp (top) and DST (bottom) during the geomagnetic storm on DOYs 302-303 in 2003. (Credits: WDC for Geomagnetism, Kyoto for DST and NOAA for Kp index)

zation originating from high latitudes and propagating equatorwards. Figure 4.7(a) displays VTEC and RoTEC time series for PRN 05, which exhibits an IPP trace roughly oriented northwards, moving therefore in the opposite direction than that of the TEC wall. A decrease of about 20 TECU was observed in less than one hour, which is really unusual for the evening gradient. The corresponding RoTEC series follows the TEC decrease, exhibiting a "U" shape curve. However, maximum values observed in RoTEC are smaller than 1 TECU/min, which is four times less than during the X-flare event. In this case, the polynomial fit used in our methodology modeled not only the regular TEC gradients but also a significant part of the TEC depletion. In this first case, we can conclude that RoTEC measurements, characterizing high-frequency TEC changes, underestimate the extent and the severity of the corresponding ionospheric disturbance.

The second case occurred during the third DST depletion, between 1700 and 2100 UT the day after (DOY 303). In comparison with the first case, we can see from figure 4.7(b) that the ionospheric response is very sharp: VTEC values grew up to about 250% in a few minutes for PRN 31, with associated RoTEC values of nearly 10 TECU/min.

The third common pattern, also observed during moderate storms due to weak CMEs or Corotating Interaction Regions (CIRs), is the noisy signature observed for nearly all satellites in view, as illustrated for PRN 02 and PRN 23 in figures 4.7(c) and (d). RoTEC time series for PRN 02 exhibits a noisy pattern around 2030 UT and a very short variability cycle one hour later, almost simultaneously with the moderate VTEC increase observed for PRN 31. For PRN 23, the noisy behavior is clearly identified, with RoTEC values reaching 1 TECU/min. Once again, let us note

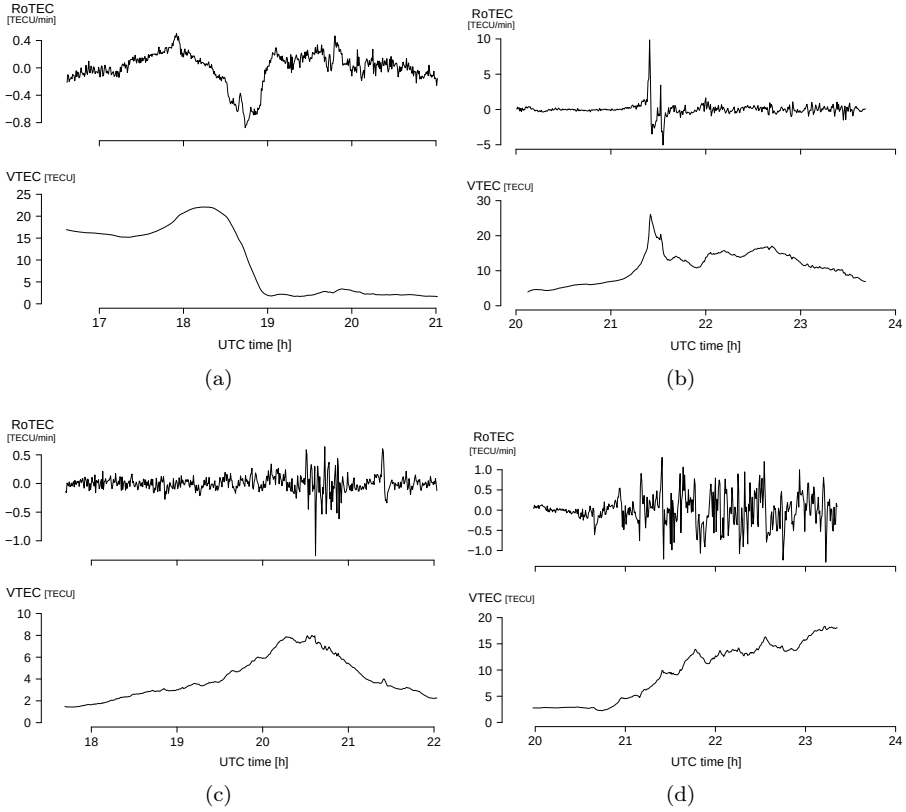

Figure 4.7 – Ionospheric effects in VTEC (bottom) and in the corresponding RoTEC (top) during the geomagnetic storm for (a) DOY 302/03, PRN 05, (b) DOY 303/03, PRN 31, (c) DOY 303/03, PRN 02 and (c) DOY 303/03, PRN 23. Observation station is Brussels (BRUS).

that RoTEC time series do not reflect the TEC behavior: for example, the single analysis of RoTEC does not allow to detect the positive phase of the geomagnetic storm appearing in figure 4.7(c).

In conclusion, we have seen that the ionospheric response to geomagnetic storms provides a lot of different RoTEC signatures whose order of magnitude can vary with a factor 10. As a consequence, it is not easy to isolate and recognize a unique, typical signature of geomagnetic storms in RoTEC measurements.

4.1.3.3 Daytime MSTID

The RoTEC pattern related to the occurrence of an MSTID is easily detected as wave-like fluctuations in the time series, as illustrated in figure 4.8(a). This lat-

ter corresponds to a winter daytime MSTID whose RoTEC amplitude is generally smaller than 1 TECU/min. As mentioned in section 3.3.2, apparent period does not correspond to the real one due to larger IPP velocity values at low elevations. Moreover, the amplitude is also generally larger for low elevations, probably due to geometric effects between the MSTID and the satellite Line of Sight (LoS). Let us highlight the fact that such disturbances generally occur during quiet geomagnetic periods.

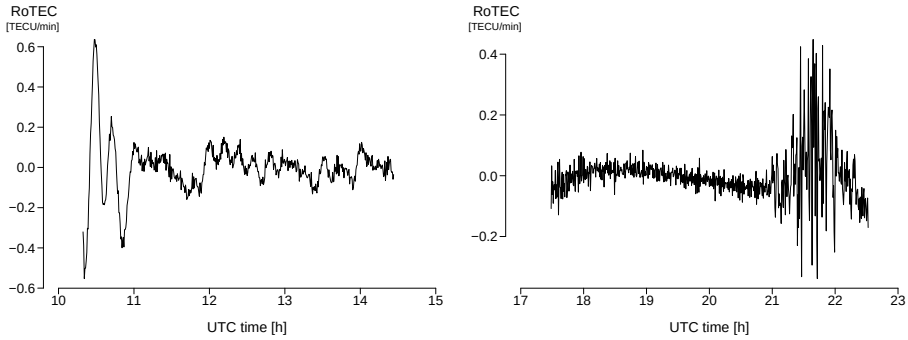

Figure 4.8 – RoTEC time series during (a) the occurrence of a typical winter daytime MSTID on DOY 328/11, PRN 22 and (b) during a summer nighttime disturbance on DOY 248/08, PRN 03 .

4.1.3.4 Nighttime disturbance

Finally, the last recurring pattern in RoTEC corresponds to disturbances detected during nighttime, for both winter and summer conditions (see the climatological study below for more details) and during quiet geomagnetic conditions. It corresponds to a noisy signature in RoTEC, similarly to that of figure 4.8(b); therefore, such disturbances are sometimes referred to as "noise-like structures". The noisy signature of nighttime disturbances in RoTEC has the same order of magnitude as those due to geomagnetic storms: peaks of about 1.5 TECU/min can sometimes be observed.

4.1.3.5 Conclusions

Different types of ionospheric irregularities imply different signatures in RoTEC, although similar signatures seem to correspond to different physical processes. From the analyzed cases we have seen that RoTEC amplitude is very large during geomagnetic storms or during X-flares while MSTIDs are generally responsible for irregularities of moderate amplitude. However, geomagnetic disturbances can be

forecasted as they generally result from solar flares; it comes that degraded ionospheric conditions can be expected in the 24 or 48 hours following the flare[5]. What about MSTID occurrence? Are their amplitude really negligible with respect to space weather induced phenomena?
The answer to these questions needs a precise climatological study of such phenomena. The knowledge of their occurrence rate and amplitude with respect to solar cycle, season and local time constitutes the first step of our approach, aiming at modeling and forecasting the ionospheric effects on precise GPS positioning.

4.2 Occurrence rate analysis

The climatological study of ionospheric irregularities performed in this section is based on the number of "ionospheric events", as defined in section 4.1. The occurrence rate will be related to space weather activity but will also be investigated as a function of solar cycle, season and local time. Statistics are based on GPS measurements performed at three Belgian stations (BRUS, DENT and DOUR) from 2002 to 2011. The use of three GPS stations allows to significantly reduce the influence of multipath, as this latter is a local effect and as we will assume that ionospheric conditions are identical for these stations. Geomagnetic indices are also part of our dataset, with hourly DST values coming from the World Data Center (WDC) for Geomagnetism, Kyoto[6] and Kp values provided by the NOAA National Geophysical Data Center (NGDC). The dataset also includes solar activity proxies, such as the sunspot number R_i (provided by the Solar Influences Data Analysis Center, Brussels) and the solar X-ray flux derived from NOAA/GOES measurements.

4.2.1 Space weather influence

As a preliminary study, let us assess the proportion of 15 min periods for which at least one irregularity has been detected with respect to the total number of observation periods. Yearly percentages are found in table 4.2 where one can see that proportion is slightly varying with the station, the largest values being often observed at BRUS while the lower ones are always observed at DOUR. This small bias in the number of irregularities detected is probably due to an enhanced multipath environment for BRUS and DENT in comparison with DOUR. Assuming an identical ionospheric activity for the three Belgian stations, these fluctuations prove that, even with a detection threshold large enough to filter out multipath effect, this latter

[5] In chapter 2 we have seen that CIRs can also produce geomagnetic disturbances. Even if they do not result from solar flares, it is however possible to forecast their occurrence as they are related to coronal holes, which are visible in X and EUV images.

[6] Let us precise that data related to 2002–2008 are final values, while those of 2009–2011 are classified by the WDC as "real-time" values. Although they can be used for climatological purposes, one would always prefer to use final values for analysis of specific cases.

	BRUS	DENT	DOUR	Belgian mean
2002	9.19	8.47	8.07	8.58
2003	4.21	4.12	3.54	3.96
2004	3.62	3.44	3.12	3.39
2005	2.13	2.03	1.84	2.00
2006	0.88	1.03	0.84	0.92
2007	0.84	0.78	0.62	0.75
2008	0.77	0.61	0.60	0.66
2009	0.36	0.33	0.29	0.33
2010	1.07	1.08	0.81	0.99
2011	3.90	3.42	3.37	3.56

Table 4.2 – Yearly proportion of 15 min epochs affected by the presence of one or several ionospheric irregularities (in %).

still slightly contaminates the results. Therefore, averaging over the three stations would allow to mitigate the influence of residual multipath.

It comes from Belgian mean values that, even during solar maximum, this proportion does not exceed 9% on average. This means that about 91% of observing epochs can be considered as quiet in terms of ionospheric irregularities during solar maximum, implying that nominal positioning accuracy for differential and relative techniques can be expected for 91% of the time[7]. Turning to low solar activity periods (e.g. years 2008 or 2009) this percentage rises up to 99.7%. Therefore, one has to keep in mind that if ionospheric delay represents the major error source in positioning with GPS, TEC high-frequency changes remain rather rare phenomena.

Given the clear solar cycle influence, one might also expect a relationship between geomagnetic activity and the occurrence of irregularities. Figure 4.9 depicts the cumulative percentage of the number of irregularities as a function of geomagnetic indices Kp and DST, all years taken together. It is usual practice to consider thresholds of $Kp \leq 4$ and $|DST| \leq 50$ nT to characterize quiet geomagnetic conditions, the more reliable geomagnetic filter being the combination of both[8]. It comes from figure 4.9 that about 90% of irregularities occur under such quiet conditions. We can also observe that the number of irregularities linearly increases with the geomag-

[7]This assumption is valid as long as the so-called irregularities are considered to be the only ionospheric contribution to the real-time positioning error in relative of differential mode. This will be discussed in more details in chapter 6.

[8]Considering both Kp and DST should always be preferred to a single index since they do not represent the same physical phenomenon. Examples of the added value of using both measurements are the recovering periods of geomagnetic storms, for which Kp values are low while DST is slowly recovering to pre-storm values. As a consequence, geomagnetic activity filter used in the frame of this work will always include both Kp and DST.

netic indices; this is particularly true for Kp where one can assess the slope to about 25%/Kp unit for Kp values ranging from 0 to 3. This linear behavior ends around the inflection points (Kp between 3 and 5, DST ranging from about -25 to -75 nT), where one can suspect changes in the irregularity type. Indeed, breakups in curve shapes seem to reveal the transition from the quiet to the disturbed regime.

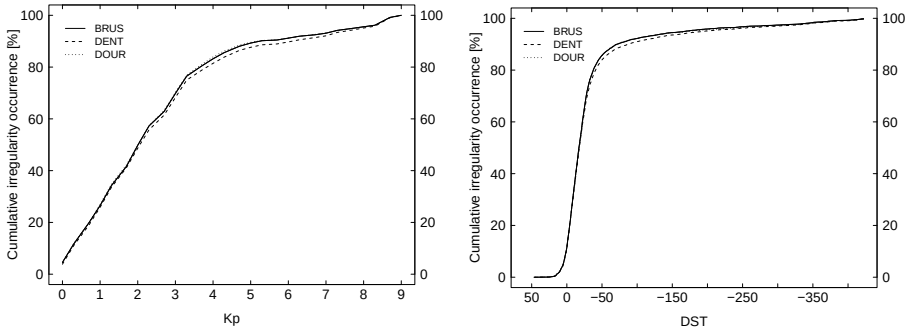

Figure 4.9 – Cumulative irregularity occurrence (in %) as a function of (a) Kp and (b) DST indices for the three Belgian stations BRUS, DENT and DOUR over the period 2002–2011. About 90% of irregularities are observed for Kp ≤ 4 or $|\text{DST}| \leq 50$ nT.

The influence of space weather phenomena on irregularity occurrence is highlighted in figure 4.10, where observations have been classified into two main categories: irregularities related to Space Weather (SW) and the others, qualified as "quiet-time". The first category includes all geomagnetically disturbed periods (*i.e.* showing $|\text{DST}| > 50$ nT and Kp > 4) but also the periods corresponding to the occurrence of solar flares[9], with X-ray flux larger than 10^{-5} W/m^2. Figure 4.10 displays yearly values of the number of ionospheric events, normalized by the number of GPS satellites, for BRUS station[10]. In parallel, monthly averages of the sunspot number R_i quantify the solar activity level. As expected, an increase in the occurrence rate is observed for high solar activity periods, such as years 2002 and 2003, where SW events may represent more than 25% of the total number of events. However, SW contribution remains very weak (less than 5%) during the rising phase of solar cycle 24 (*i.e.* years 2010 and 2011), despite a moderate solar activity level. Concerning quiet-time irregularities, we can observe that their occurrence rate is clearly correlated with solar activity. Indeed, figure 4.10 shows that their yearly number is

[9]For the sake of completeness, let us add that only flares occurring during sunlit hours in Belgium were taken into account, as the effect of a solar flare is null during nighttime.

[10]Since very similar results were found for DOUR and DENT stations, only those observed at BRUS have been displayed here.

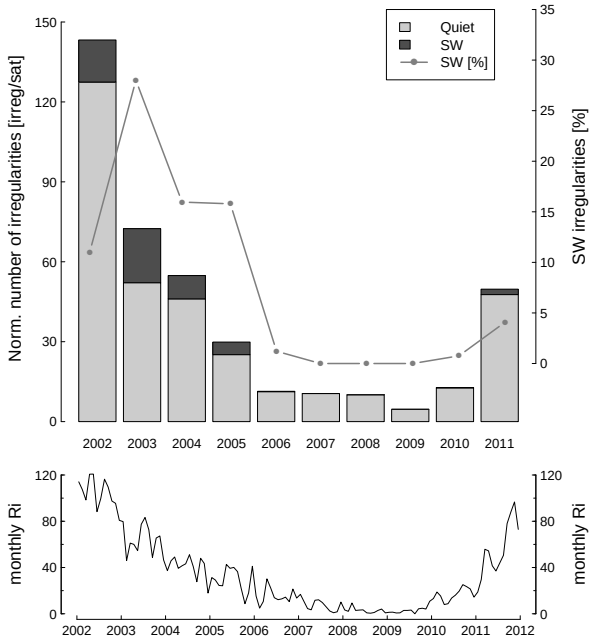

Figure 4.10 – *Top panel*: yearly number of irregularities per satellite at BRUS as a function of solar cycle and space weather activity. Irregularities are divided into two categories: those due to disturbed space weather conditions (denoted "SW") and the others, not related to SW activity and further referred to as "quiet-time irregularities" (denoted "Quiet"). *Bottom panel*: corresponding time series of monthly sunspot number R_i.

slightly equivalent for similar solar conditions: for example between years 2011 and 2003 or between years 2010 and 2006.

We have seen that irregularities induced by SW phenomena represent a small fraction of the total number that can be observed at a mid-latitude station. If their effects in terms of TEC rate of change are clearly larger than those of irregularities occurring during quiet conditions, their occurrence can though be forecast based on solar wind data and other satellite measurements. As a conclusion, we will investigate the occurrence rate of quiet-time irregularities, as they cannot be foreseen by models or other observations. Moreover, based on their recurrence patterns (solar, seasonal and local time dependence), we will attempt to explain the mechanisms responsible for their occurrence (see section 4.4).

4.2.2 Irregularities not due to space weather events

The occurrence of ionospheric irregularities related to quiet SW conditions, further referred to as "quiet-time irregularities", will be analyzed with respect to solar cycle,

season and local time. As already stated, quiet conditions are encountered if the following conditions are fulfilled:

- Kp ≤ 4 ;
- $|\text{DST}| \leq 50$ nT ;
- X-ray flux $< 5.10^{-5}$ W/m^2.

Statistics have been performed from 2002 to 2011 for the three Belgian stations BRUS, DENT and DOUR. Let us also remember that the evolution of the GPS satellite constellation is taken into account, as all measurements are normalized by the number of available satellites.

4.2.2.1 Solar and seasonal dependence

Seasonal dependence will be discussed based on monthly proportion of irregularity occurrence, computed as the ratio between the number of irregularities occurring during the given month and the total yearly number:

$$\%_{\text{month}} = \frac{\sum_{\text{month}}}{\sum_{\text{year}}} \cdot 100 \tag{4.4}$$

Figure 4.11 shows the occurrence frequency for years 2002 to 2011 at BRUS, DENT and DOUR stations. One can notice that the three stations give very similar occurrence rates, particularly for high solar activity periods. Discrepancies between stations during solar minimum can be explained by the weak number of irregularities. Indeed, a small variation in the number of irregularities detected induces a larger relative occurrence rate, and therefore a more variable behavior.
The most recurrent pattern in figure 4.11 lies in the maximum occurrence during late autumn and winter months. Peak values are observed during solar maximum where up to 35% of the annual irregularities can be observed within one particular month, mainly December or January. Seasonal means combining BRUS, DENT and DOUR data are given in table 4.3, where one can see that between 55 and 70% of yearly irregularities are observed during winter only, this values being subject to fluctuations with solar cycle. It is worth noting the unusual percentage of 63% observed for autumn 2011, which is due to a very fast increase of solar cycle 24 (as pointed out by R_i values, see figure 4.10). This is also visible in figure 4.11 where an asymmetrical pattern is observed for year 2011.
In the same figure, another recurrent feature seems to be the secondary maximum observed during summer, more particularly in July. This maximum is fluctuating between 5 (in 2005) and 25% (in 2006), with the corresponding Belgian means ranging from about 3 to 25%. Analysis of figure 4.11 and table 4.3 suggests that the ratio winter/summer occurrence rate is decreasing with solar activity. Indeed, the yearly percentage of summer irregularities is clearly larger during solar minimum.

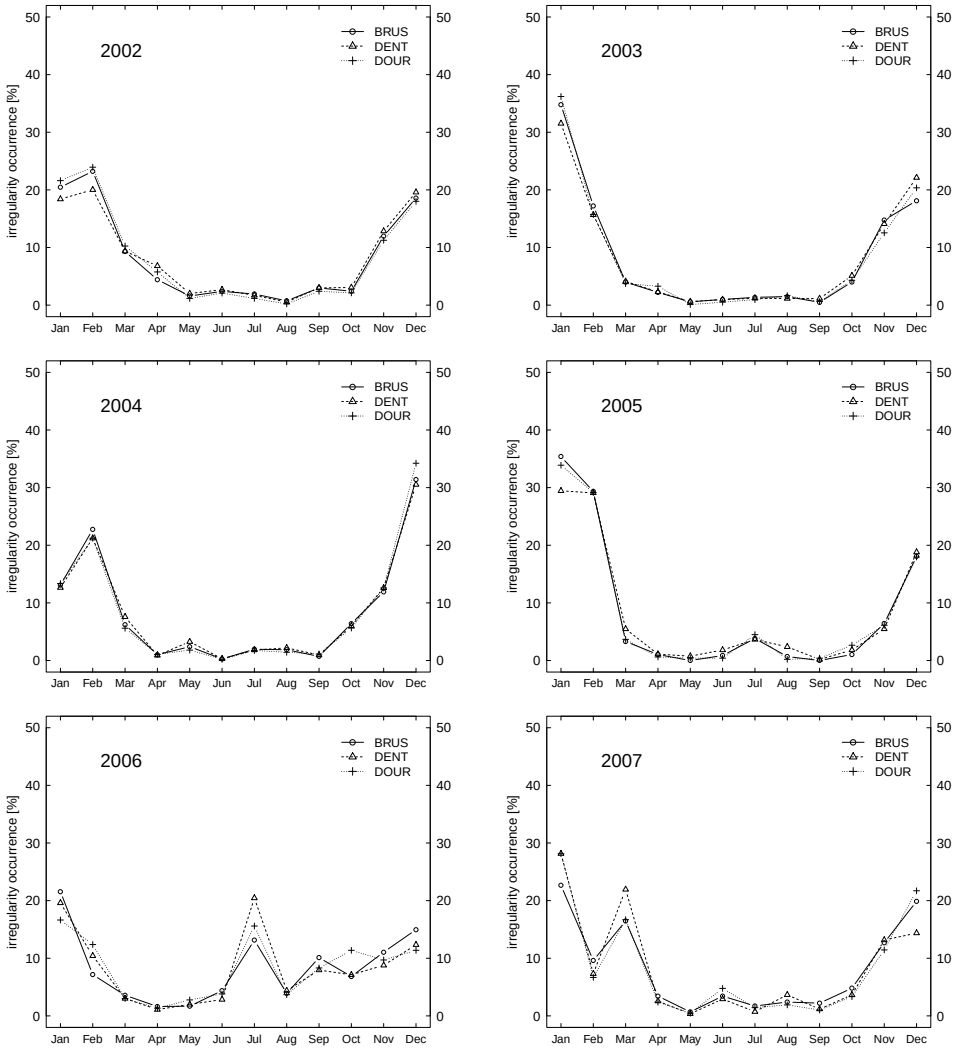

Figure 4.11 – Monthly proportions of quiet-time irregularities from 2002 to 2011 (first part).

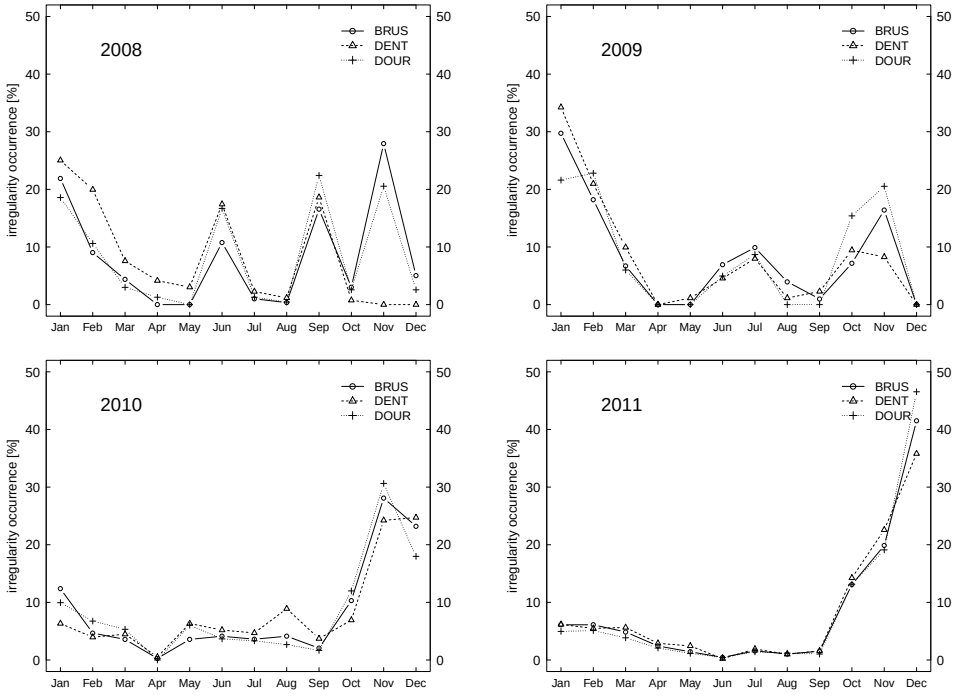

Figure 4.11 – Monthly proportions of quiet-time irregularities from 2002 to 2011 (second part).

This apparent anti-correlation with the solar cycle has to be confirmed by the analysis of the absolute number of irregularities, as illustrated in figure 4.12. This latter confirms the presence of the first maximum in autumn/winter but does not provide evidence for the secondary maximum in summer. Figure 4.12 shows that the number of summer irregularities is rather stable with solar activity, except for year 2002 (high solar activity). However, despite a relatively weak secondary maximum, the evolution of the ratio winter/summer with solar cycle constitutes an interesting feature that has to be highlighted, as it suggests the presence of two distinct physical phenomena.

Yearly minimum is mainly observed in May, with monthly percentages of barely 2%, except for 2010 where it reached about 6%. In general, spring is the less disturbed season with related occurrence rate ranging from 3 to 21%.

	Winter	Spring	Summer	Autumn
2002	55.9	11.0	4.7	28.3
2003	61.7	4.1	3.5	30.8
2004	55.5	5.4	4.4	34.7
2005	71.1	2.6	5.6	20.7
2006	35.3	7.1	24.6	33.1
2007	50.4	13.6	5.8	30.2
2008	35.8	20.6	22.0	21.6
2009	53.6	8.0	13.9	24.4
2010	23.4	9.6	12.7	54.3
2011	26.3	6.2	4.2	63.4

Table 4.3 – Seasonal occurrence rates (in %) as a function of year. Values correspond to Belgian means built upon BRUS, DENT and DOUR measurements.

4.2.2.2 Local time dependence

Similarly to seasonal dependence analysis, one can investigate local time dependence with the hourly occurrence rate for each of the four seasons:

$$\%_{\text{hour}} = \frac{\sum_{\text{hour}}}{\sum_{24 \text{ hours}}} \cdot 100 \tag{4.5}$$

As local time at the different IPPs differs from that at the GPS station, local time dependence can be computed in two different ways. However, one should remember that the goal of this climatological analysis is to retrieve and understand the most recurrent patterns for a single GPS station. Indeed, GPS users always refer to GPS time frame and do not consider ionospheric points. As a consequence, it would seem wise to base our occurrence statistics on local time at the receiving station.
As for monthly dependence, daily profiles coming from the three Belgian stations are very similar so that their average has been plotted, for each season, in figure 4.13. Average values allow to mitigate the multipath influence and get the most probable value, from a statistical point of view.
Figure 4.13 shows that autumn and winter profiles are very close to each other, displaying a large peak around noon. Daily maximum ranges between 12 and 20% and is generally observed between 1000 and 1400 LT. Spring profile also exhibits a maximum around 1200 LT which is observed during high or moderate solar activity only. Turning to low solar activity, spring profile gets closer to summer profile: a very weak occurrence rate during daytime and a maximum between 2000 and 2200 LT. Summer peaks are very variable: 5% were recorded for year 2002 while occurrence rates of 25% were reached in 2005.
Considering both seasonal and local time dependence, one can observe that two main occurrence patterns can be distinguished:

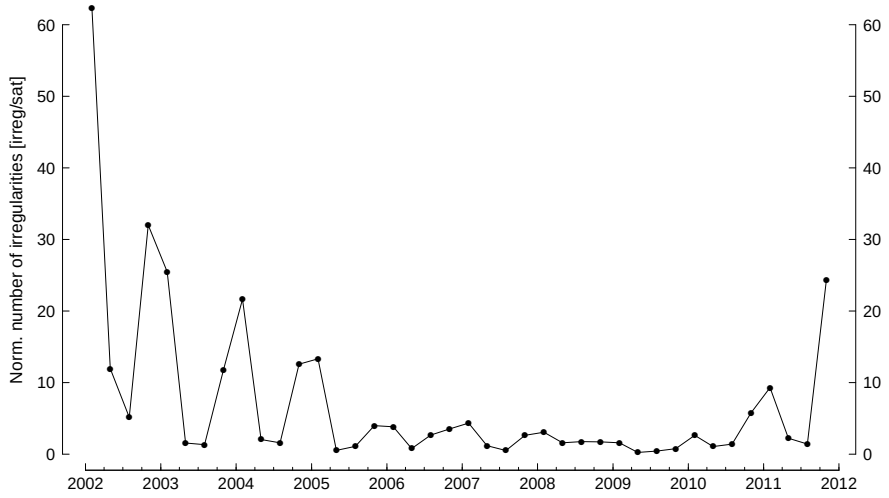

Figure 4.12 – Seasonal values of the absolute number of irregularities, normalized by the number of GPS satellites. Values correspond to Belgian means built upon BRUS, DENT and DOUR measurements.

- those occurring in winter and in late autumn, responsible for a maximum occurrence around 1200 LT and further referred to as Winter Daytime (WD) ;

- those occurring during summer nights, around 2000–2200 LT, further referred to as Summer Nighttime (SN).

Considering the aforementioned classification, let us refine our occurrence statistics by focusing only on these two main patterns, as illustrated in table 4.4 where occurrence rates are expressed as a function of the irregularity type. WD represent more than 50% of the yearly irregularities during moderate and high solar activity, with a maximum of 77% (in 2005). This proportion is globally decreasing with solar cycle to reach 31% in 2009, during the long-lasting solar minimum.

Despite a relatively clear pattern in yearly and daily profiles, SN phenomena are only responsible for a very small fraction of the yearly irregularities. As previously mentioned, they are more prevalent during solar minimum, with proportions between about 6 and 10%. Let us mention the unusual value of nearly 13% observed for year 2006.

Finally, even if the fraction of other irregularities (e.g. those not classified as SN or WD) remains relatively large (between 19 and 63%), their occurrence seems to be more or less homogeneously distributed with solar activity. This makes the retrieval of other typical behavior very difficult. As a consequence, only the two clear patterns SN and WD will be considered and analyzed from now on.

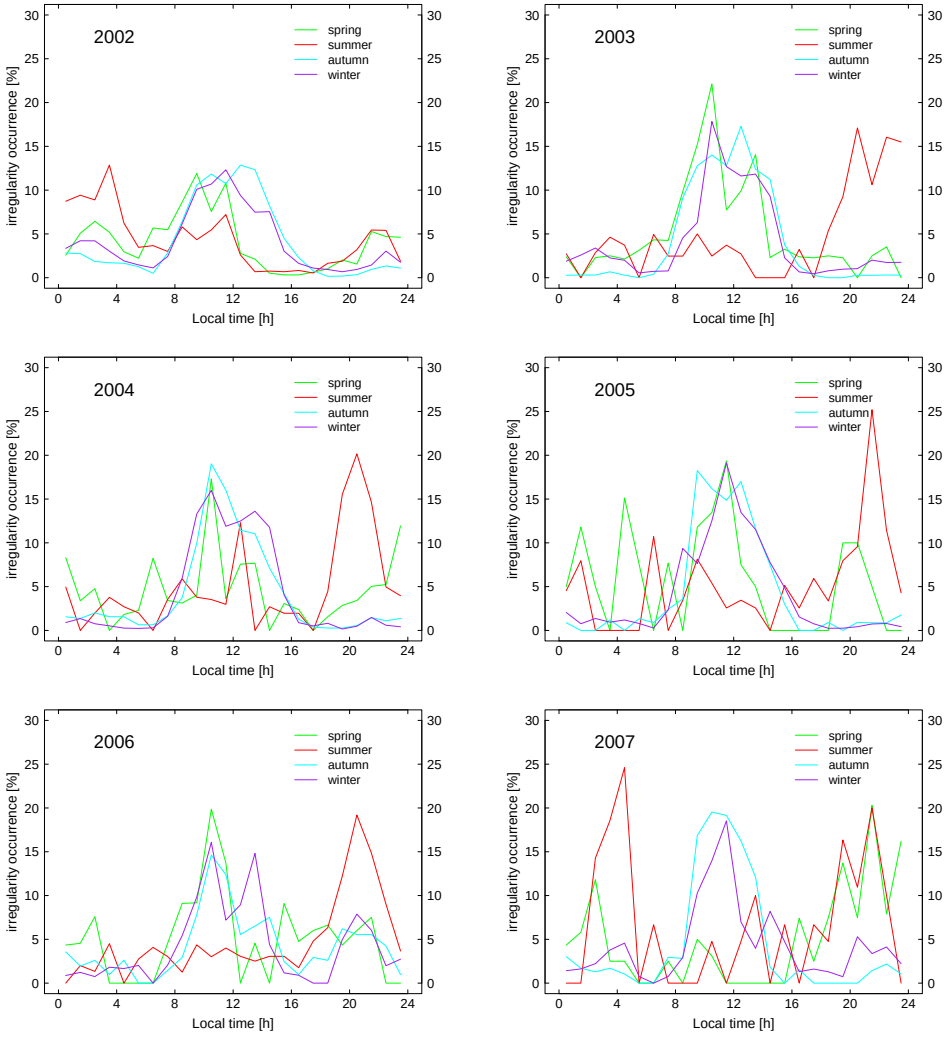

Figure 4.13 – Occurrence rate (in %) of quiet-time irregularities as a function of season and local time, from 2002 to 2011 (first part).

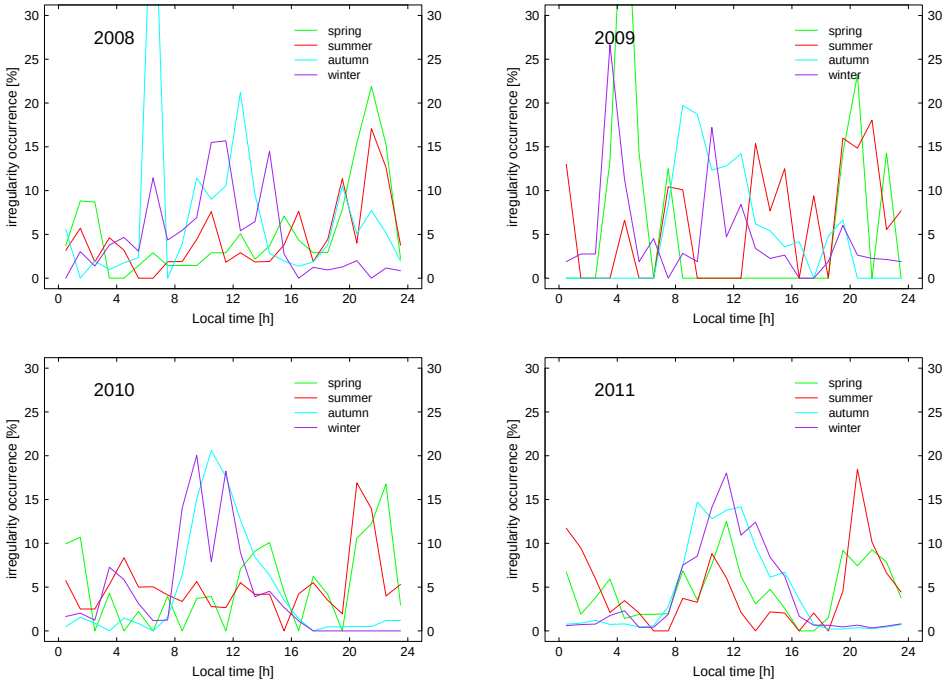

Figure 4.13 – Occurrence rate (in %) of quiet-time irregularities as a function of season and local time, from 2002 to 2011 (second part).

4.2.3 Summary

The occurrence rate of geomagnetic and quiet-time irregularities have been studied over a time period covering 10 years. The measurements related to three GPS stations have shown very close relative percentages, even if discrepancies could be observed in the absolute number, mainly due to local effects such as multipath. As expected, geomagnetic irregularities are more prevalent during periods of moderate and high solar activity where they can represent up to 30% of the total number of detected irregularities. Quiet-time irregularities, representing therefore 70 to 100% of the yearly irregularities, have been classified into two main categories: WD and SN. While the first ones are responsible for up to 75% of yearly quiet-time irregularities, the latter are quite rare as their respective part represents less than 10%. If WD occurrence rate is positively correlated with solar activity, this does not seem to be the case for SN. More particularly, the ratio between winter and summer relative occurrence rates seems to decrease with solar activity.

Based on RoTEC time series, a manual analysis of numerous WD and SN cases has been performed and tends to support the evidence that these latter correspond

	WD (0800-1600 LT)	**SN** (2000-0400 LT)	**Others**
2002	50.1	2.7	47.2
2003	68.7	2.4	28.9
2004	69.3	2.2	28.5
2005	77.6	3.1	19.3
2006	37.5	12.7	49.8
2007	54.4	2.6	43.0
2008	35.6	9.9	54.5
2009	31.1	6.1	62.8
2010	55.0	5.9	39.1
2011	63.8	2.3	33.9

Table 4.4 – Proportion of Winter Daytime (WD) and Summer Nighttime (SN) irregularities (in %) as a function of year. Considered observation period for WD is November to February, 0800-1600 LT while that related to SN is June 21 to September 21, 2000-0400 LT. Values correspond to Belgian means built upon BRUS, DENT and DOUR measurements.

respectively to daytime MSTIDs and nighttime disturbances, as presented in section 4.1.3. However, occurrence rate statistics have to be completed by the amplitude analysis in order to confirm these assumptions.

4.3 Amplitude analysis

The amplitude analysis developed in this section will assess the magnitude of quiet-time irregularities in terms of relative deviation of VTEC. In light of the previous occurrence rate analysis, our attention will be turned to WD and SN types only. Furthermore, because VTEC measurements are available for BRUS station only, the analysis will be carried out for this single station.
One defines the amplitude of an irregularity as the ratio between the extreme VTEC values observed within the 15 min interval, divided by the VTEC background value, which corresponds to the VTEC mean within the same 15 min period:

$$\begin{aligned} \mathrm{A}\,[\%] &= \frac{\Delta \mathrm{VTEC}_{15\,\mathrm{min}}}{\overline{\mathrm{VTEC}}_{15\,\mathrm{min}}} \cdot 100 \\ &= \frac{\mathrm{VTEC}_{\mathrm{max},15\,\mathrm{min}} - \mathrm{VTEC}_{\mathrm{min},15\,\mathrm{min}}}{\overline{\mathrm{VTEC}}_{15\,\mathrm{min}}} \cdot 100 \end{aligned} \tag{4.6}$$

Let us note that the computed amplitude corresponds to a given IPP, and therefore to a given satellite at the IPP local time, which differs from local time at the

observing station. Therefore, considering the local time **at the IPP**, irregularities have been classified as WD or SN and their corresponding amplitude has been computed. This differs from the previous study in which all irregularities were merged together to compute occurrence rate statistics and for which VTEC background was not needed.
Histograms of amplitude are displayed in figure 4.14 where we can observe that both WD and SN distributions are non-gaussian, uni-modal, with a peak between 5 and 10%. Given the asymmetrical pattern of the histograms, it has been chosen to summarize the distributions with boxplots instead of the commonly used mean and standard deviation. Boxplots have been computed for each year, allowing to discuss the evolution of the amplitude with the solar cycle.

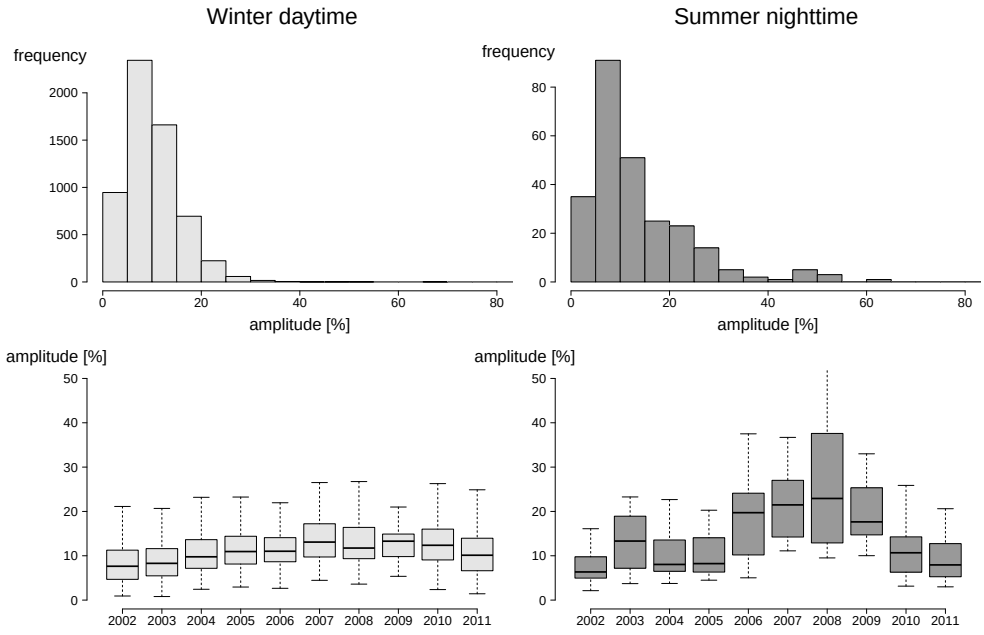

Figure 4.14 – Amplitude of ionospheric irregularities computed using equation (4.6). *Top*: amplitude histograms related to WD and SN irregularities observed at BRUS station. *Bottom*: yearly boxplots of the amplitude for WD and SN.

4.3.1 Winter daytime irregularities

The amplitude of WD irregularities shows little variation with solar conditions, with relatively steady medians ranging from 8 to 12%. However, one can observe that the largest values occur during solar minimum: this can be explained by a larger relative error during such periods. Indeed, VTEC background during low solar activity does

ΔVTEC [TECU]	**amplitude [%]**	$\sigma_{\mathbf{A}}$ **[%]**
0.1	2	1.0
0.2	4	2.0
0.3	6	3.0
0.4	8	4.0
0.5	10	5.0
0.6	12	6.0

Table 4.5 – Accuracy of amplitude measurement (σ_{A}) as a function of ΔVTEC, considering a VTEC background of 5 TECU and a related accuracy of 2.5 TECU.

not exceed 10 TECU, as shown in figure 2.9. As VTEC has an accuracy of 2–3 TECU, one could expect a larger relative error on the amplitude during solar minimum than during solar maximum, where VTEC background is much larger.
We can confirm this assumption by computing yearly statistics of $\overline{\mathrm{VTEC}}_{15\,\mathrm{min}}$ related to WD events. Results, depicted in figure 4.15, show that VTEC during winter daytime is clearly varying with solar cycle and is always smaller than 10 TECU during solar minimum: typical medians are about 5 TECU while their maximum is below 8–9 TECU and their minimum around 2 TECU.
Accuracy of amplitude measurement might be assessed if the error on VTEC measurement (2–3 TECU) can be considered as a random error. Then, using the error propagation law, we can compute the accuracy of a single amplitude value, which depends on the span $\Delta\mathrm{VTEC}_{15\,\mathrm{min}}$. Considering a VTEC background of 5 TECU with a related accuracy of 2.5 TECU, error on amplitude measurement σ_A has been computed and is summarized in table 4.5.
Taking into account that mean amplitude of WD irregularities are between 8 and 12%, one can deduce from table 4.5 that corresponding error lies in the range 4–6% during low solar activity periods. Given this uncertainty, the slight rise in amplitude observed for low solar activity is not statistically significant. Therefore, WD amplitude can be considered as a constant value oscillating around 10%, which suggests that $\Delta\mathrm{VTEC}_{15\,\mathrm{min}}$ grows linearly with VTEC background. Such VTEC background influence was already observed in the daily occurrence rate (daily profiles, see figure 4.13), which is in phase with absolute VTEC profiles (figure 2.9).
With amplitudes and occurrence rates strongly correlated with absolute VTEC values, one can assume that all WD irregularities detected are likely to be interpreted as MSTIDs. Indeed, our observations are in favor of the hypothesis that the ionospheric response to AGW is proportional to the number of passive tracers, *i.e.* to the VTEC at the IPP.
Our results have to be compared with external MSTID-related studies. To our knowledge, there is only one climatological study based on GPS measurements that can be used for comparative purposes. In this paper, Tsugawa et al. [92] propose a

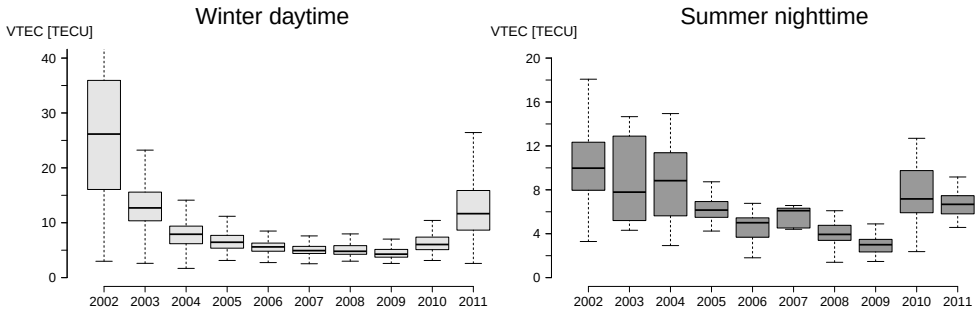

Figure 4.15 – Boxplots of VTEC values at the IPP for WD (left) and SN (right) irregularities as function of the year.

climatological study of daytime and nighttime MSTIDs based on a dense network of about 1200 GPS receivers in Japan. The analysis period covers eight years of data, whose minimum and maximum of cycle 23. Some of the results have been validated with radar and airglow measurements, which makes the study very reliable. Mean amplitudes for WD irregularities computed by Tsugawa et al. [92] are about 1–2%, which is quite lower than the results found in our study. However, the authors used a slightly different computation of the amplitude, defined as $\frac{\sigma_{\mathrm{VTEC}}}{\mathrm{VTEC}}$ within 1-hour periods, which prevent us to validate or invalidate our results.

As a consequence, it has been chosen to compute similar statistics, keeping the same 15 min time interval. Results, presented in the same way than previously, are displayed in figure 4.16. WD medians are varying between 1 and 3%, which is similar to the values of 1–2% mentioned by Tsugawa et al. [92]. It is worth noting that the values depicted in figure 4.16 would certainly be lowered if one would use a time interval of 1-hour, as originally proposed by Tsugawa et al. [92], instead of 15 min. Again, a certain anti-correlation with solar cycle can be noticed but the analysis of amplitude accuracy (around 1%, still for VTEC=5 TECU and σ_{VTEC}=2.5 TECU) leads to the same conclusions as before: there is no clear dependence of WD amplitude on solar activity.

In addition to the study developed by Tsugawa et al. [92], other authors have performed MSTID amplitude measurements, such as van Velthoven [95]. In his thesis, the author investigates the origin on MSTIDs based on radio interferometric measurements and on differential Doppler shift measurements related to Navy Navigation Satellite System (NNSS)[11] satellite passes. As the first method only allows to derive TEC gradients in the east–west direction, it is very hard to compare the related amplitudes with our results. However, the differential Doppler shift technique allows the computation of instantaneous relative TEC measurements in a similar

[11] NNSS is the forerunner of the modern GPS system developed in the 1960s. It was made up of several polar orbiting satellites allowing the computation of positions.

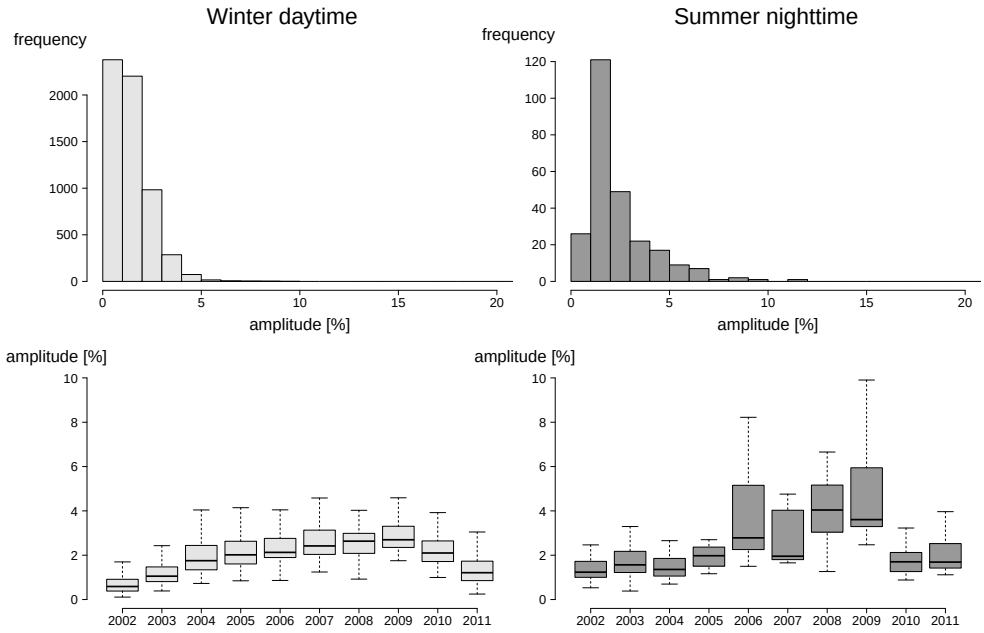

Figure 4.16 – Amplitude of ionospheric irregularities according to Tsugawa et al. [92] method for a 15 min time interval, which is $\frac{\sigma_{\mathrm{VTEC,\,15\,min}}}{\mathrm{VTEC}_{\mathrm{15\,min}}}$. *Top*: amplitude histograms related to WD and SN irregularities observed at BRUS station. *Bottom*: yearly boxplots of the amplitude for WD and SN.

way than for GPS measurements. The author found amplitudes values in the range 1–10%, with a corresponding average at 4%. Once again, one can observe that our amplitudes values are realistic and representative of MSTID behavior. However, despite a global agreement between our observations and those of van Velthoven [95], it should be stressed that the technique employed in the two cases is not identical, so that such comparisons have to be carefully considered[12].

Finally, we have seen that WD amplitude values are of the same order of magnitude than those relative to other studies, confirming the classical MSTID origin of these irregularities. Let us however point out that, as mentioned in section 3.3.2, observed amplitude does not correspond to the true amplitude because of the observational biases inherent to GPS measurements [5, 103].

[12] As an example, IPP velocity in the case of NNSS measurements is the order of 2000 m/s, which is more than six times faster than for GPS measurements. This leads to a larger observational bias which would certainly differ from that of GPS technique.

ΔVTEC [TECU]	**amplitude [%]**	$\sigma_{\mathbf{A}}$ **[%]**
0.2	5	3.1
0.4	10	6.2
0.6	15	9.4
0.8	20	12.5
1.0	25	15.6
1.2	30	18.7

Table 4.6 – Accuracy of amplitude measurement (σ_A) as a function of ΔVTEC, considering a VTEC background of 4 TECU with a related accuracy of 2.5 TECU.

4.3.2 Summer nighttime irregularities

Turning to SN irregularities, figure 4.14 shows that their histogram is more stretched towards larger values than for WD events: amplitudes reaching more than 20 or 30% occur more frequently during summer nighttime than during winter daytime. The non-gaussian character of the yearly distributions is also visible in the boxplots, where some medians are much closer to the lower quartile. During solar maximum, amplitudes range between 8 and 15% while the largest values are observed during solar minimum, with medians around 20%, *i.e.* twice as large as for WD. Related VTEC background can be read from figure 4.15, where one can see that it reaches about 10 TECU during solar maximum but rarely exceeds 6 for solar minimum (years 2006 to 2009). Contrary to winter daytime values, SN VTEC does not follow the smooth curve of solar activity so that differences between solar maximum and minimum are lower and more variable.

We showed that WD amplitude does not seem to depend on solar activity because of the large relative error on amplitude measurement during solar minimum. Similar computations have been achieved for SN events, where VTEC background of 4 TECU has been assumed, with the same accuracy for VTEC (σ_{VTEC}=2.5 TECU). Results are displayed in table 4.6 where it comes that σ_{A} associated with an amplitude of 20% is about 12%. Therefore, this means that, from a statistical point of view, one can not demonstrate any relationship between SN amplitude and solar activity. It is worth mentioning that the same conclusions can be drawn from amplitudes derived from Tsugawa's definition of the amplitude, which is $\frac{\sigma_{\mathrm{VTEC}}}{\mathrm{VTEC}}$.

In addition to winter daytime MSTIDs, Tsugawa et al. [92] have also investigated the occurrence and the amplitude of nighttime MSTIDs. He observed that they generally appear during summer but also during winter, though with a weaker occurrence rate. Corresponding amplitudes are the order of 1–5% and are negatively correlated with solar activity. Comparison of Tsugawa's results and our statistics (figure 4.16) would indicate the MSTID nature of SN irregularities. However, this does not seem to be the case as we can point out two main inconsistencies between the two studies:

1. Most of RoTEC patterns related to SN irregularities do not correspond to the wave-like pattern typical of MSTIDs, as they are rather associated with a noise-like behavior.

2. Tsugawa et al. [92] observed a negative correlation between SN amplitude and solar activity, which could not been demonstrated here.

As a conclusion, if the amplitude analysis has clearly confirmed the MSTID origin for WD irregularities, it is not the case for SN ones. Indeed, even if some points of convergence (such as occurrence rates and amplitudes) with the existing literature can be highlighted, RoTEC signature of SN events does not correspond to MSTIDs for most of cases. This latter point is the main obstacle to the identification of the SN origin, which will be further investigated in section 4.4.

4.4 The origin of quiet-time irregularities

Several mechanisms have been suggested by the scientific community to explain the origin of quiet-time irregularities, as summarized in section 2.3. Here we propose to compare the existing theories with our GPS dataset, taking into account the specificity of GPS measurements (observational bias). For that purpose, some external data sources have been used, such as atmospheric datasets or ionograms originating from Dourbes ionosonde station (south of Belgium).

4.4.1 Winter daytime irregularities

4.4.1.1 MSTIDs observation with GPS

As demonstrated in the previous section, WD irregularities correspond to classical MSTIDs, whose propagation parameters and properties are biased by the GPS observation conditions (see section 3.3.2). It has been shown that IPP velocity was varying with satellite elevation, and that relative velocity between the Traveling Ionospheric Disturbance (TID) and the IPP stretched the apparent period in RoTEC time series. Moreover, low elevation angles are responsible for another type of bias, related to the finite thickness of the TID slab of plasma (figure 3.5). Indeed, low elevations make the LoS to cross the TID slab over a longer path, so that STEC is highly increased. Consequently, corresponding amplitudes are enhanced.
This section aims at investigating the role of these observational biases in the detection of MSTIDs. For example, let us analyze the occurrence of quiet-time irregularities in 2002, during the solar maximum of cycle 23. One can summarize the information by displaying the number of ionospheric events as a function of DOY and local time, for each of the 96 time intervals (figure 4.17).
As previously observed, figure 4.17 shows that most of irregularities are detected during winter daytime. However, some winter nighttime events also appear in figure 4.17, which was not mentioned in the occurrence rate analysis. The interesting

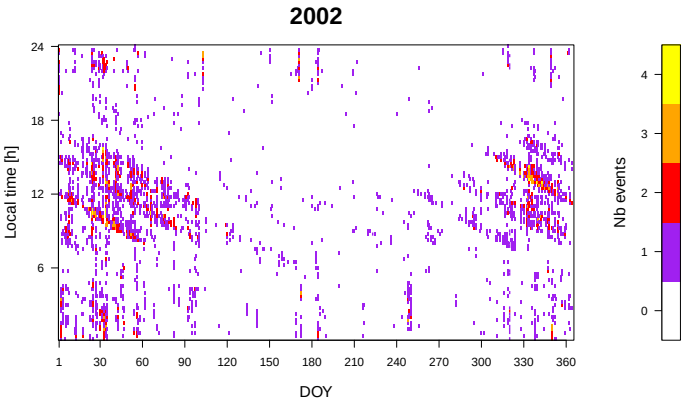

Figure 4.17 – Number of ionospheric irregularities detected at BRUS in 2002 (15 min resolution) expressed as a function of DOY and local time. The slopes related to winter daytime events are about 4 min/day.

feature of figure 4.17 lies in the fact that irregularities seem to be detected about 4 min earlier each day, indicating the influence of the GPS constellation. Indeed, let us remind that satellite configuration repeats itself every sidereal day, which is about 4 min earlier than the day before. Irregularity slopes appearing in figure 4.17 allow therefore to formulate two hypotheses:

1. irregularities are not physical phenomena but correspond to multipath, enhanced at low elevations;

2. irregularities are recurrent phenomena which are mostly detected under specific observational conditions, related to satellite geometry.

The first hypothesis can be tested by selecting several consecutive days where similar irregularities occurred on the same satellite and comparing their RoTEC time series, after shifting them by -4 min/day. Such example is illustrated in figure 4.18, where IPP trace of PRN 17 and RoTEC time series for DOY 041 to 044 are depicted. IPP trace is oriented northwards, which is parallel to geomagnetic field lines. If one remembers that MSTIDs propagate mostly equatorwards (*i.e.* along the magnetic meridians), one can expect an enhanced observational bias due to the opposite velocities of the MSTID and the IPPs. This allows the MSTID to be easily detected in the RoTEC time series where clear wave-like patterns can be identified for the consecutive days.
Superimposing the several RoTEC time series demonstrates that wave-like variability is not due to local multipath effects, as the phase and the amplitude of cycles differ from day to day. As a consequence, we can exclude multipath as the primary cause of this geometry-dependent effect.

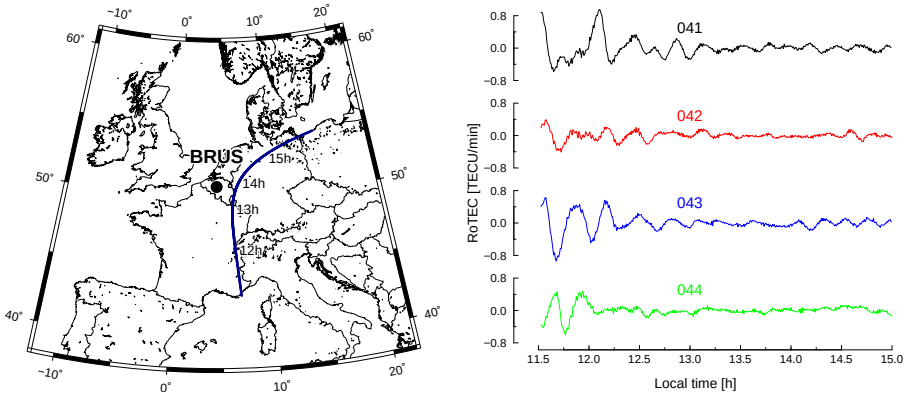

(a) (b)

Figure 4.18 – Assessment of multipath for a given IPP trace related to PRN 17 during four consecutive days. (a) IPP map on DOY 042/02, BRUS station. Local time is labeled in black (hours). (b) RoTEC time series for PRN 17 from DOY 041 to 044, shifted by -4 min/day.

As already mentioned, an MSTID is easily detected by a GPS satellite if its propagation vector is anti-parallel to the IPP trace of the satellite. Therefore, one can expect that most of WD irregularities might be detected by satellites whose IPP trace has a positive northward component. Indeed, let us recall that MSTIDs propagate mostly southwards in the northern hemisphere as they follow the topology of the magnetic field lines. The results confirm this assumption: approximately 96% of the IPP traces having detected an MSTID are oriented northwards.
In conclusion, we have seen that the very large majority of MSTIDs detected by GPS obey some conditions, where observational bias is enhanced. One can summarize them as follows:

- VTEC background must be large enough to allow the AGW to be detected as an MSTID. The larger the VTEC is, the larger the MSTID amplitude will be (see section 4.3).
- The AGW must propagate in the opposite direction than that of the observing satellite. In the northern hemisphere, winter daytime MSTIDs propagate southwards, so that satellites whose IPP trace is oriented northwards fulfill this condition.
- Large amplitudes are generally observed at low elevation, due to the larger part of the plasma slab crossed by the LoS.

Based on these results, it is therefore possible to identify the satellites prone to detect MSTIDs, which constitute thus a threat for precise GPS applications. However, if

one can theoretically predict such situations, it is not the case for the occurrence of AGW whose origin is still to be investigated.

4.4.1.2 The origin of AGWs

The occurrence rate of classical MSTIDs shows a large seasonal and local time dependence and their detection with GPS results from the combined effect of satellite geometry and background VTEC. Therefore, the following questions arise:

- Are the seasonal/local time patterns only due to the background VTEC, which is generally larger during daytime in autumn and winter? If so, AGWs can be generated all the time but would only be detected when a minimum background VTEC is observed.
- Are the AGWs generated all the time and their seasonal pattern only due to the atmospheric filtering or to specific atmospheric conditions that are also season-dependent?
- On the contrary, are AGWs mainly generated during daytime in autumn and winter?
- What are the physical phenomena responsible for the AGW generation?

As a starting point of the investigation, let us come back to the two main mechanisms proposed by the literature to explain the generation of AGWs.

1. **The solar terminator**. Thermal gradients due to the passage of the terminator in the F-region might produce AGWs which, by ion-neutral collisions, are detected in the ionospheric plasma as MSTIDs. In this first mechanism, the generation is done *in situ*, *i.e.* directly in the thermospheric layer, by absorption of solar radiation by neutral constituents. This means that atmospheric filtering processes can be considered as negligible, although a certain propagation has to be considered in some cases. Indeed, if the AGW generation takes place in the lower thermosphere, a significant time interval is needed for the wave propagation up to the maximum electron density region.
2. **Generation from below and upward propagation**. It has been shown that multiple phenomena occurring in the troposphere or in the stratosphere were responsible for the generation of AGWs, such as tropospheric weather systems, orography, jetstreams, storms... Contrary to the *in situ* generation by the terminator, the question of their propagation up to the ionospheric layer has to be taken into account. As a matter of example, directional filtering by background neutral wind [95] or steep temperature gradients [13, 54] are some filtering processes that could prevent AGWs to propagate upwards.

Generation of AGWs by the solar terminator can be discussed by comparing the occurrence time of MSTIDs with time of sunrise and sunset. If AGWs are generated *in situ*, one could expect a double peak in the daily occurrence rate, just after sunrise and sunset. Figure 4.19 depicts the occurrence of ionospheric events and σ_{RoTEC} as a function of local time at the IPP for the autumn/winter period. A peak between 1000 and 1200 LT is observed in the occurrence rate while maximum σ_{RoTEC} values are symmetrically distributed around noon, which clearly indicates the response to VTEC background. The striking feature of figure 4.19 is that MSTID occurrence and sunrise/sunset are not synchronous. Although, it is likely that AGWs observed within the hour following the passage of the morning terminator would be related to sunrise. Indeed, let us remind that MSTIDs are propagating phenomena that can last for several hours, so that their detection several hours after their generation is still possible. However, this hypothesis becomes unlikely if one considers MSTIDs observed around 1200 LT or during the afternoon. Turning to the evening terminator, it is observed that irregularities occurring after sunset are relatively scarce, which could be attributed to the low VTEC values observed in the evening hours. Nevertheless, the detected MSTIDs are once again not synchronous with the evening terminator, weakening a bit more this hypothesis.

In conclusion, even if one cannot exclude the solar terminator as a secondary source of MSTIDs, there is some observational evidence that it is not the main cause of the MSTIDs observed by GPS, particularly for those detected several hours after sunrise. Let us highlight that the study of van Velthoven [95] already led to similar conclusions, with results based on models of AGWs and of the thermospheric layer. However, our results do not agree with those of Hernandez-Pajares et al. [43] which concluded that occurrence of MSTIDs detected by GPS are mainly confined by the solar terminator. Multi-instrument approach and atmospheric data related to low thermosphere would certainly contribute to quantify the effective part of AGWs due to the solar terminator.

As a consequence, let us investigate the second possible mechanism for the generation of AGWs: phenomena of tropospheric/mesospheric origin. As most of ionospheric events are observed during autumn and winter, we have focused our analysis on an atmospheric structure mainly occurring during these periods: the jetstream. Jetstreams are fast air fluxes generally located below the tropopause, at an altitude ranging between 9 and 12 km. Assimilated to narrow flux tubes of a few kilometers thick, they are responsible for horizontal wind speeds of about 25 m/s that can reach more than 100 m/s in the center. Even if jetstreams are present all the time at mid-latitudes, polar jetstreams mostly occur during autumn/winter where large speed values are observed, together with cold fronts. Strong wind shears are associated with jetstreams, which makes them ideal candidates for AGW generation [63]. Previous studies have investigated the relationship between jetstream and MSTIDs occurrence. For example, Bertin et al. [10] suggest that MSTIDs might result from non-linear interactions between different wave modes generated by the jetstream.

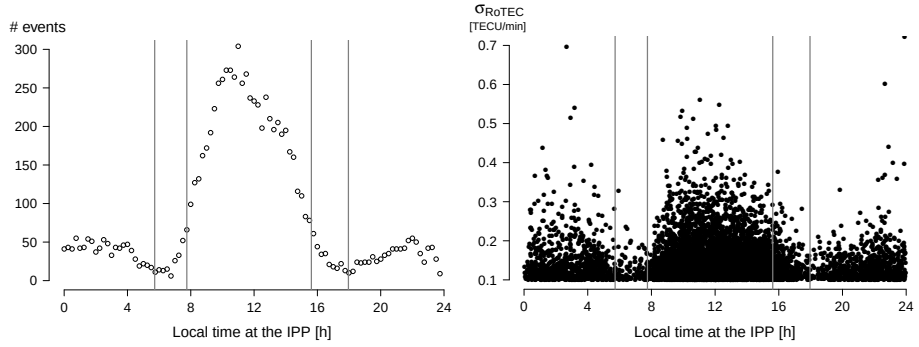

Figure 4.19 – Relationship between occurrence time of MSTIDs and solar terminator. (a) Number of events and (b) σ_{RoTEC} observed at BRUS as a function of the local time at the IPP between November 1 and March 21, from 2002 to 2011. Vertical lines correspond to the earliest and the latest sunrises and sunsets for BRUS latitude during the autumn/winter period.

In order to check whether MSTIDs are related to powerful jetstreams, one proposes to spatially correlate wind velocity at jetstream heights with IPP locations. MSTIDs and jetstream taking place in different atmospheric layers, propagation up to the F-layer has therefore to be taken into account for the spatial correlation. If jetstream-originating AGWs propagate upwards with a non-null horizontal velocity, they would be detected in a cone centered on the AGW source. At ionospheric heights, the intersection of the cone and the spherical shell gives a circle centered on the AGW source and whose radius depends on horizontal velocity. Let us highlight that this assumption is valid only if the background wind is negligible. Otherwise, this latter would tilt the cone so that the center of the ionospheric circle would not be located at the vertical of the AGW source anymore. Unfortunately, very little is known about the opening angle of the cone, which depends on propagation conditions along the whole path (neutral density, temperature...). As a result, it is extremely difficult to compute realistic values of the cone diameter. Therefore, spatial correlation shall be simply expressed in terms of proximity between the IPP and the jetstream. In our study, there will be three correlation levels: 1) the IPP is located at the vertical of the jetstream, 2) the jetstream is located at less than 1000 km far from the IPP (ionospheric circle centered on the IPP and radius equals 1000 km) and 3) the jetstream is located at more than 1000 km far from the IPP or there is no jetstream over the European region. The correlation between the two phenomena will be denoted as “strong” for the first case, “weak” for the second while the absence of spatial correlation will be further referred to as “none”.

Horizontal wind data come from the "ERA-interim" re-analysis [94] provided by the European Center for Medium-range Weather Forecasts (ECMWF)[13]. The pressure level has been fixed to 250 hPa, which corresponds to an altitude of 8–9 km. Wind speeds smaller than 50 m/s (*i.e.* 180 km/h) have been filtered out to highlight zones of strong wind shears. Figure 4.20 gives an illustration of the maps that will be used for the spatial correlation analysis. The figure displays σ_{RoTEC} related to the IPPs (15 min time resolution), for all satellites in view from BRUS station within a time interval of two hours (see figure caption for more details). Wind speed is superimposed to IPP map, with a spatial resolution of 1.5°x1.5° and a time resolution of 6 hours.

The case displayed in figure 4.20 corresponds to a classical MSTID detected with a satellite (PRN 17) whose IPP trace is oriented northwards, that is anti-parallel to the assumed equatorwards propagation of the wave. This latter can be confirmed by comparing RoTEC time series of PRN 17 between several stations (see figure 4.20 displaying RoTEC time series for BRUS, DENT and DOUR stations). Indeed, one can observe that the MSTID crests are nearly simultaneously observed at DENT and BRUS while they are delayed by a few minutes at DOUR station. This is particularly true for the first observation hour (1130 – 1230 LT). As the time lag is due to wave propagation, one can deduce that the MSTID wave vector is mostly oriented along the axis BRUS–DOUR, what confirms the equatorwards propagation.

Maximum σ_{RoTEC} observed in figure 4.20 occurs at low elevation, which proves once again the importance of the observational context in the detection of MSTIDs with GPS. The IPPs related to PRN 17 are nearly all located at the vertical of the jetstream flux tube, where speeds are ranging between 50 and 60 m/s. As a consequence, spatial correlation would be qualified as "strong" in this case. Conversely, the first IPP related to PRN 15 is not located at the vertical of the jetstream; in this case the spatial correlation would be qualified as "weak". Let us point out that the absence of MSTID detection with GPS does not mean that the spatial correlation does not exist. For example, let us consider the case of PRN 06 for which the IPP trace is mainly oriented eastwards. Even if this satellite is clearly located above the jetstream flux tube, it does not observe any irregularity. This could be explained by the relatively large elevation values of the IPPs or by the eastwards motion of the satellite trace. As a consequence, the amplitude of the (if existing) MSTID should be too small to be detected by our algorithm. Of course, it is also possible that no AGW was generated in this region. Another example of the observational bias is the absence of irregularity for PRN 30, although a clear spatial correlation with the jetstream and the MSTID detected for PRN 15 and 17. Explanation lies certainly in the relative motion between the MSTID and the satellite: this latter moves in the same direction as that of the MSTID, which makes its detection very difficult.

[13]The ERA-interim product is a set of global analyses (dataset) describing the state of the atmosphere and land and ocean-wave conditions.

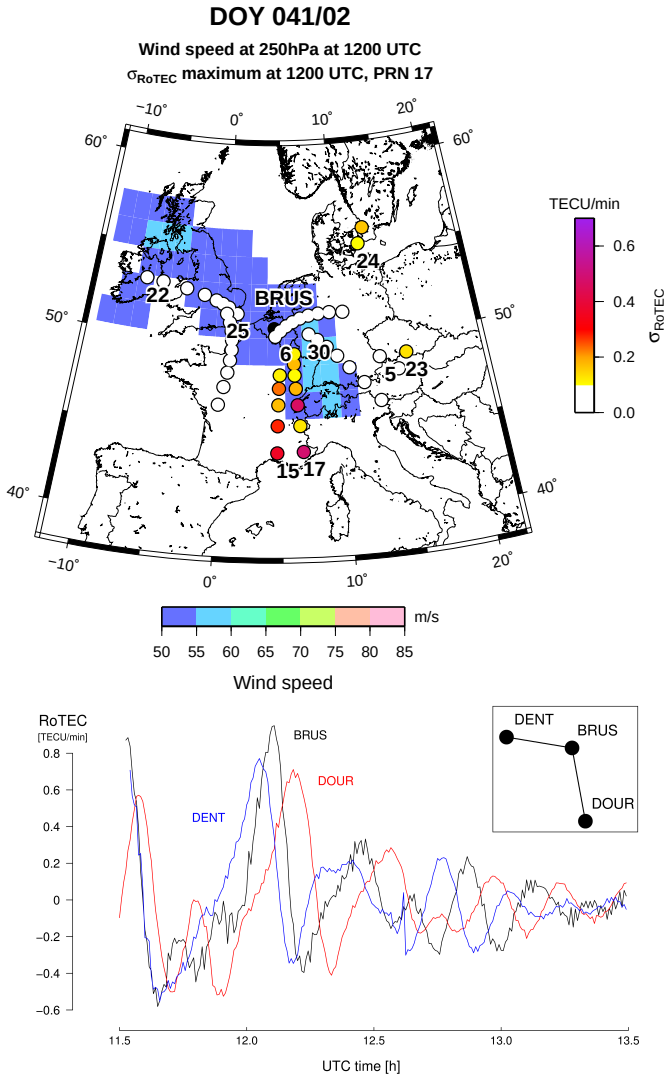

Figure 4.20 – Example of map used to investigate the spatial correlation between MSTIDs and tropospheric jetstream. *Top*: σ_{RoTEC} related to IPPs observed at BRUS station, with a time resolution of 15 min. Time interval for IPPs covers one hour before and after the maximum σ_{RoTEC} observed (here at 1200 UTC). PRN numbers always indicate the first 15 min period of the satellite, allowing to deduce its direction. Background horizontal winds are related to a pressure level of 250 hPa (source: ERA-interim re-analysis, ECMWF). Velocities smaller than 50 m/s are not mapped. Wind data are available four times a day: 0000, 0600, 1200 and 1800 UTC with a spatial resolution of 1.5°x1.5°. *Bottom*: RoTEC time series for PRN 17 observed from BRUS, DOUR and DENT stations (time resolution of 30 s). Geographic position of these stations is depicted in the frame located at the top right corner.

Let us stress that most of disturbed periods of figure 4.20 are located close to a mountainous region: the Alps. As orography is also known to be a potential source of AGWs, spatial correlation between MSTIDs and orography will also be investigated. If one considers that such AGWs are also propagating inside a cone, we can use the same methodology than for qualifying the correlation between jetstream and MSTID occurrence. For orography, the spatial correlation would also be qualified as "strong" or "weak" depending on the distance separating the IPP and the mountainous region. Regions that will be considered as "mountainous" are arbitrary defined as regions where altitude exceeds the threshold of 2000 m, which corresponds to the Alps and the Pyrenees. Spatial correlation between jetstream, orography and MSTID occurrence is manually checked (visual interpretation) on a limited number of cases. The dataset analyzed in this thesis is made up of 20 cases, chosen as follows:

- the ten most disturbed 15 min periods in terms of σ_{RoTEC}, for the interval 2002-2011;
- ten other periods, randomly selected.

Let us mention that the |DST| threshold has been lowered to 25 nT instead of 50 nT previously, to guarantee the non-geomagnetic origin of the selected cases.
Tables 4.7 and 4.8 detail the analysis of the 20 cases which are illustrated in appendix B and which can be summarized as follows:

- Considering the ten most disturbed events, a strong spatial correlation between MSTID and jetstream is observed in 40% of the cases, while weak correlation appears for 30% of cases. For the remaining 30%, no correlation is found.
- Results related to randomly selected cases show that 80% of the MSTID cases do not suggest any relationship with jetstream, while a weak and a strong spatial correlation are found only one time each (10%).
- Spatial correlation with orography is always observed, with similar proportions for the two datasets: 60% for strong correlation and 40% for weak correlation.

It can be concluded that the correlation between jetstream and MSTID occurrence is quite weak, as it has been observed for less than half of the cases. The clearer correlations were found for large amplitude MSTIDs (*i.e.* large σ_{RoTEC} values). However, it should be stressed that only 20 from a total of 4501 cases were selected for this manual analysis, which represents only about 0.4%. A further step would be the implementation of an automatic correlation algorithm analyzing all MSTID cases, that might refine and improve our statistics. Moreover, let us note that fixing a pressure level (here 250 hPa) does only provide a partial view of the three-dimensional structure of the jetstream rope. It would therefore be relevant to investigate several pressure levels at the same time. In addition, an arbitrary threshold of 50 m/s was used to detect jetstream regions. Therefore, similarly to pressure

DOY	Hour	PRN	$\sigma_{\mathbf{RoTEC}}$	jetstr.	orogr.
063/02	1030	17	0.56	none	strong
359/04	1145	21	0.55	weak	strong
049/02	0845	24	0.52	none	weak
036/02	0930	24	0.51	weak	weak
043/02	1130	17	0.50	weak	strong
041/02	1130	17	0.48	strong	strong
025/02	1030	24	0.47	strong	weak
041/02	1200	17	0.46	strong	strong
343/11	0930	18	0.46	strong	weak
295/02	0900	28	0.46	none	strong

Table 4.7 – Ten most disturbed 15 min periods observed during autumn/winter daytime. Spatial correlation between the occurrence of an MSTID and the jetstream ("jetstr.") and the orography ("orogr.") is assessed by one of the three levels: "none", "weak" or "strong", according to the methodology.

DOY	Hour	PRN	$\sigma_{\mathbf{RoTEC}}$	jetstr.	orogr.
035/11	1500	07	0.11	none	strong
011/05	1215	15	0.13	none	weak
009/11	1330	23	0.20	none	weak
053/02	1430	21	0.21	weak	strong
337/05	1000	06	0.14	none	weak
076/02	1145	18	0.20	none	strong
047/03	1030	17	0.25	none	strong
346/07	0745	02	0.14	none	weak
005/02	1415	17	0.11	none	strong
041/02	1215	17	0.18	strong	strong

Table 4.8 – Similar to table 4.7, but related to the ten randomly selected periods.

levels, several thresholds should be considered in a more sophisticated analysis. In general, further analysis should include other atmospheric parameters that are also available in the ERA-Interim dataset. For example, potential vorticity might also indicate the presence of strong wind shears associated with jetstreams.
Contrary to jetstream, orographic influence is clearly visible in our results, as 60% of IPPs are located above mountainous regions. This conclusion has however to be tempered as GPS constellation imposes some observational conditions to allow the detection of MSTIDs. Indeed, the large majority of regions where observational conditions are favorable to MSTID observation (*i.e.* trace oriented mainly northwards and low elevation) are located south/southeast of the observing station. For a Belgian site, this corresponds mainly to the alpine region. Therefore, it comes out that the apparent spatial correlation between orography and MSTID occurrence might only result from the observational conditions imposed by the GPS constellation. The analysis of data related to another station located east from the Alps would certainly confirm or invalidate the orographic origin of AGWs.
We have seen that GPS offers a very incomplete view of the ionospheric physics, as observational bias plays an important role by fixing MSTID observational conditions. In the future, investigation on AGW origin should be completed by additional measurements, such as those provided by geostationary satellites. Indeed, as they are related to a static IPP, they are not prone to distort MSTID period and amplitude. More particularly, it might be relevant to perform similar RoTEC measurements on GPS signals transmitted by Satellite-Based Augmentation System (SBAS) systems[14], such as the European EGNOS or the American system WAAS.

4.4.2 Summer nighttime irregularities

Observational conditions related to SN irregularities are quite different from those of WD ones, as illustrated in figure 4.21. Indeed, while WD IPPs are generally observed at low elevation; this is not the case for SN ones where the majority of IPPs are located relatively close to the station. Spatial distribution of IPPs exhibits also some differences: WD events are mainly observed south to east of the station (where they satisfy the "observational bias" conditions) and SN irregularities occur in the region extending from southwest to southeast. Such differences suggest that the mechanism responsible for SN irregularities does not correspond to a classical MSTID, as expected.
Figure 4.22 shows an example of SN event during which irregularities were detected for six satellites. A quick look at the IPP map shows that all irregularities are located within the same latitudinal band between 46 and 49°. It is worth mentioning that they were detected for satellite traces oriented not only northwards (PRN 20 and 32) but also southwards (PRN 19, 03 and 06), contrary to daytime MSTIDs for

[14]SBAS systems are originally developed for positioning purposes, allowing to improve positioning accuracy and to provide integrity messages to users.

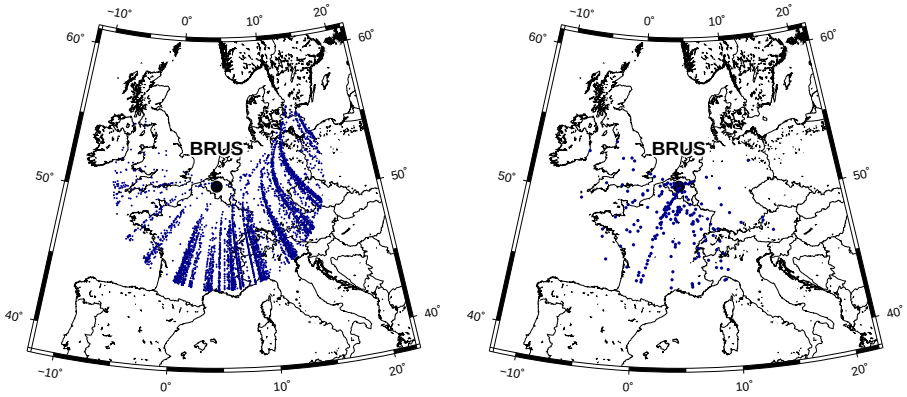

(a) (b)

Figure 4.21 – IPPs related to (a) WD irregularities and (b) SN irregularities, for the 2002-2011 time interval. Number of irregularities is 4501 for WD and 188 for SN. Elevation cut-off is 20° and h=400 km.

which the traces were nearly always oriented towards the north. RoTEC time series exhibit noisy signatures between 2030 and 2330 LT, with a mean variability around 0.5 and peaks reaching about 1 TECU/min for PRN 32.

It is generally admitted that SN irregularities correspond to MSTIDs of electrical origin. Although some authors are still debating on the physical origin of these disturbances, their physical properties have been accurately measured (see section 2.3). The presence of such periodic phenomenon has been detected in some[15] of the SN cases, as illustrated in figure 4.23. The two examples appearing in this figure exhibit a time series modulated by an harmonic component, whose signature can be attributed to an MSTID. A deeper examination of figure 4.23 shows that a noise-like pattern is superimposed to the MSTID, which was not the case of WD irregularities. If the causes of nighttime MSTIDs are well documented, the origin of this noisy pattern is still to be discovered. In the next paragraphs, we will attempt to provide such a physical explanation.

A typical feature of summer nights is the appearance of sporadic E-layers (Es) that are understood as patchy layers of a few kilometers thick. These layers are known to be responsible for a moderate to intense ionization level, as critical frequency in the E-layer can reach up to 30 MHz in equatorial regions. Es layers are not opaque, so that the satellite LoS crosses alternately regions of enhanced ionization (presence of patches) and region of gaps (absence of patches), which might explain the noise-like

[15]Let us note that the presence of the wave-like pattern typical of MSTIDs is sometimes absent from the RoTEC time series; this is the case of the example illustrated in figure 4.22.

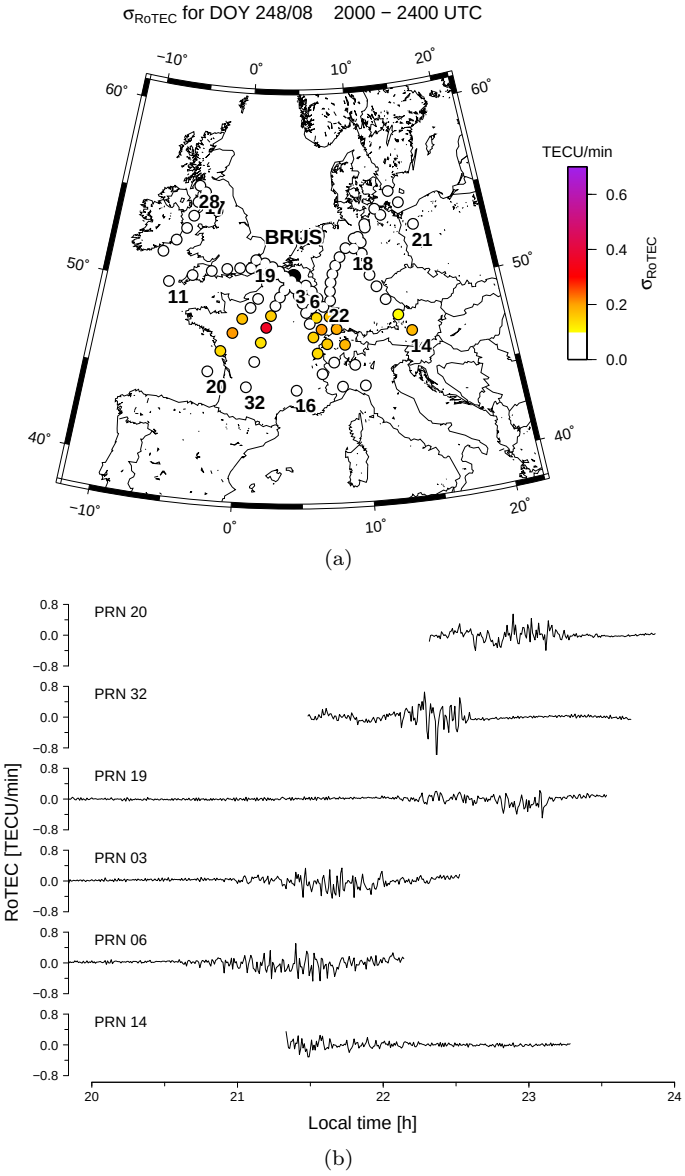

Figure 4.22 – Example of SN irregularity observed for six satellites. (a) IPP map and their related σ_{RoTEC} for period 2000-2400 UTC. (b) RoTEC time series related to the six satellites experiencing SN irregularities.

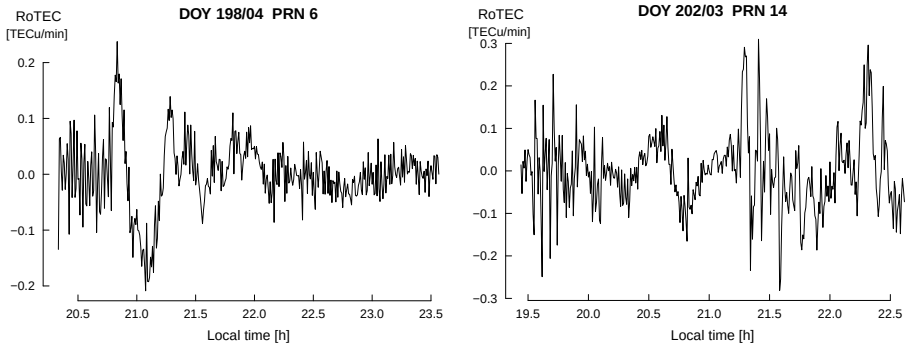

Figure 4.23 – Two examples of wave-like patterns in RoTEC related to SN irregularities. Let us highlight the superimposition of a noisy pattern responsible for a peak-to-peak RoTEC larger than 0.5 TECU/min.

variability observed in RoTEC time series. Therefore, let us assess the contribution of a Es layer to the VTEC by assuming a 5 km thick layer, which can be considered as the maximum thickness of an Es (see section 2.3.2). According to equation (2.7), Es contribution (denoted $\mathrm{VTEC_{Es}}$) depends on its critical frequency f_0Es, which is summarized in table 4.9:

f_0Es	$\mathbf{VTEC_{Es}}$
2	0.02
4	0.10
6	0.22
8	0.40
10	0.62
12	0.89
14	1.22
16	1.59

Table 4.9 – Theoretical VTEC contribution (in TECU) of a 5 km thick Es layer, as a function of its critical frequency f_0Es (expressed in MHz).

Values displayed in table 4.9 show that Es layers for which f_0Es is smaller than 4 MHz do not contribute significantly to VTEC, as the corresponding $\mathrm{VTEC_{Es}}$ is the same order of magnitude than RoTEC accuracy level (about 0.1 TECU). Coming back to the example of figure 4.22 and according to table 4.9, it comes that f_0Es would be the order of 10–15 MHz to support the hypothesis that noise-like patterns in RoTEC are due to the single presence of an Es layer. Such theoretical values have to be compared with real f_0Es data coming from the ionospheric sounder of

Dourbes, located 80 km south of BRUS station. As we are dealing with ionosonde data, let us remind some basic principles.

1. The study of ionospheric phenomena based on ionograms is mainly achieved through the analysis of a sequence of several ionograms. This allows to understand the underlying dynamics in (and between) the different layers.

2. Routine soundings are generally performed every hour, even if the preferred schedule is quarter-hourly. In the case of Dourbes station, ionograms are generally available every 20 min.

3. An ionogram depicts the ionospheric structure above the sounding station. The derived characteristics and parameters (such as f_0F_2, f_0E, $h'F$...) are generally assumed to be valid within a circle of 100 km radius around the station, as spatial autocorrelation of N_e decreases with distance.

4. While comparing GPS and ionosonde measurements, one has to adapt the ionospheric shell height (in the thin single layer model) to the altitude of the layer of interest. As an example, considering a given LoS, the IPP related to the E-layer is located nearly four times closer to the observing station than the usual IPP located at $h = 400$ km (see appendix D).
   In this context, the ionogram would reliably represent the E-layer crossed by the LoS if the $\mathrm{IPP}_{\mathrm{E-layer}}$ is located inside the 100 km circle around the ionosonde, as illustrated in figure 4.24. Let us note that it is generally not the case for the F-region, as $\mathrm{IPP}_{\mathrm{F-layer}}$ are located outside the aforementioned circle.

The sequence of six ionograms related to the example of figure 4.22 shows the development of a semi-transparent Es layer (figure 4.25). The formation starts at 1800 UT where coexist two separate Es layers located at an altitude of 100 and 120 km, in addition to multiple echo traces sustained over the following couple of hours. From 1900 to 2100, the lower layer disappears and the upper one slowly descends, together with an increasing f_0Es value. Maximum f_0Es value of about 4 MHz is observed at 2000, when frequency spread in the F-layer started to develop. This spread will continue until the end of the sequence, where a residual Es trace is still visible. The intermediate trace in the altitude range of 130–230 km visible on 2200 ionogram might be due to reflection on the dissipating Es layer.
If a positive correlation between Es occurrence and SN irregularities can be found in this example, it comes from table 4.9 that the low f_0Es values cannot explain the large RoTEC values observed in the time series of figure 4.22(b)[16]. A possible explanation arises from the spread-F phenomenon, which is generally associated with the

[16]Moreover, let us recall that values appearing in table 4.9 can be considered as the largest contribution of an Es layer, as we fixed its thickness to the maximum value of 5 km.

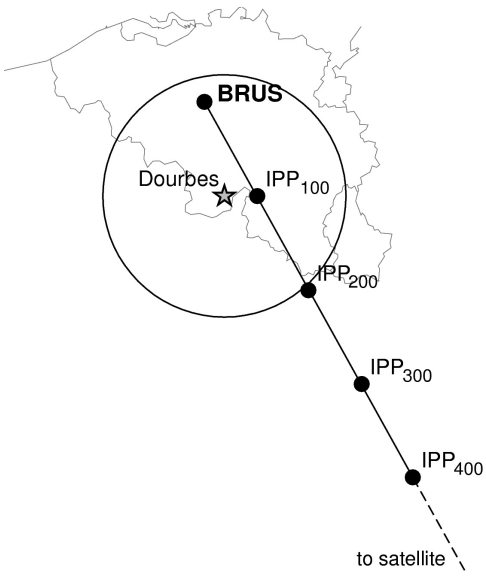

Figure 4.24 – For a given line of sight (LoS), the IPP is varying with the ionospheric shell height. The IPP related to $h = 100$ km (denoted IPP_{100}) is located inside the circle of 100 km radius centered on Dourbes station. As a consequence, one can consider that the morphology of the E-layer crossed by the satellite LoS (located at IPP_{100}) is similar to that depicted in Dourbes ionograms. This is not the case for the other IPPs which are located too far from Dourbes station. As a consequence, the morphology of the F-region crossed by the LoS (represented by IPP_{300} and IPP_{400}) may strongly differ from that observed in Dourbes ionograms. In tables 4.10 and 4.11, an asterisk appearing in the respective column (Es and/or spread-F) will indicate that the corresponding IPP is outside the 100 km circle around Dourbes.

occurrence of Es layers. As they are located in the F-region, the Field-Aligned Irregularitiess (FAIs) associated with spread-F might give a VTEC contribution much larger than that of Es layers and explain the amplitude of RoTEC fluctuations. The coupling mechanism between the two layers may be found in the mapping of E-layer irregularities (patches) into the F-layer along the geomagnetic field lines, which results in FAIs. This is in good agreement with other studies in which the authors observed that (unstable) Es layers and FAIs are generally observed over mid-latitudes during nighttime [40].

As a consequence, we propose to investigate the relationship between SN noisy patterns and the occurrence of coupled Es layer/spread-F phenomena. Similarly to WD irregularities, we will analyze 20 cases of SN irregularities. The ten most disturbed cases in terms of σ_{RoTEC} and ten randomly selected cases have been carefully investigated; the related observations are given in tables 4.10 and 4.11. All IPP maps

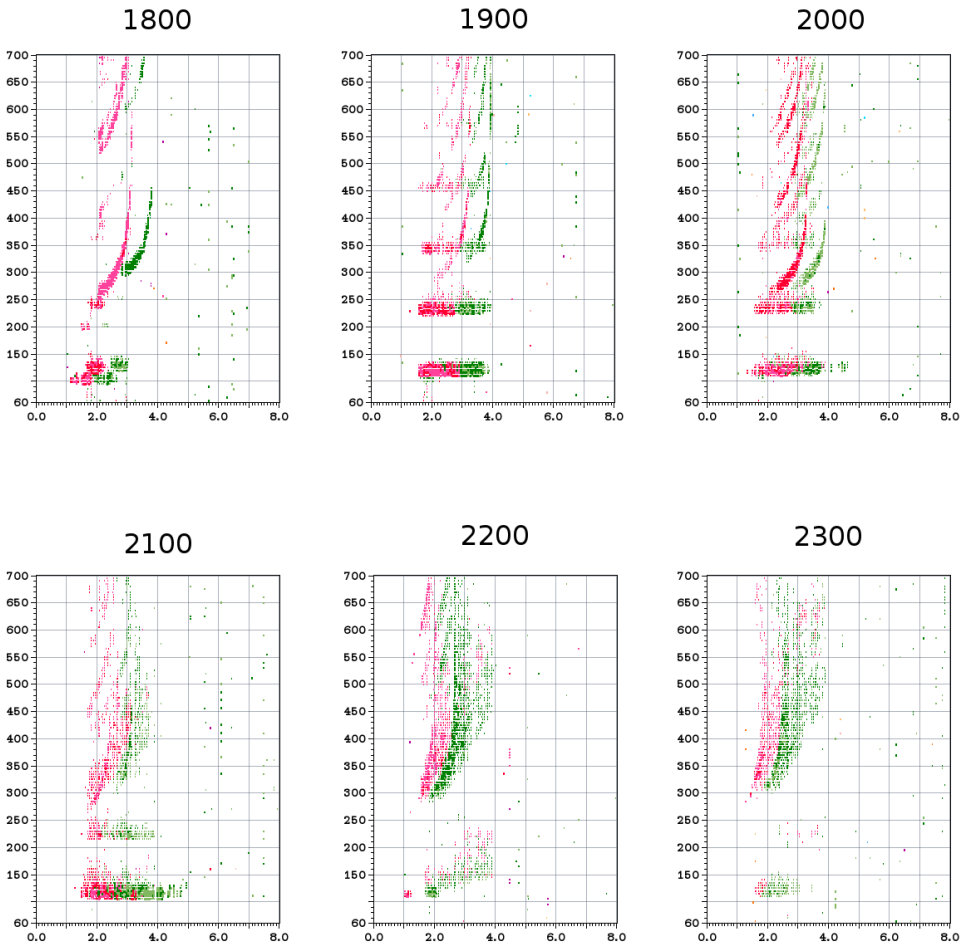

Figure 4.25 – Sequence of ionograms related to Dourbes station for DOY 248/08, from 1800 to 2300 UTC.

related to the analyzed cases are depicted in appendix C. Each of the 20 SN irregularities has been examined according to the following rules:

- If an Es layer is observed, one will mention the range of f_0Es values observed within the two hours interval around the occurrence of the SN irregularity.

- The amplitude of spread-F phenomenon is generally assessed based on the dfS parameter, which measures the total frequency width of frequency spread

traces for the F-layer [76][17]. In the frame of this thesis, one has quantified the amplitude of spread-F by using a simple qualitative scale consisting in three levels: "none", "weak" and "strong". The latter two levels represent frequency spread classes based on ordinary mode measurements. "Weak" level corresponds to a spread between 0.2 and 0.5 MHz while "strong" denotes a spread larger than 0.5 MHz. As for Es layer, spread-F measurements refer to the time interval $[t - 1\text{h}, t + 1\text{h}]$, where t denotes the time at which the SN irregularity occurred.

- As previously mentioned, the IPP related to the E- or F-layer may be located too far from the Dourbes ionosonde station (distance larger than 100 km), implying that ionosonde measurements could not be representative of the ionospheric layer crossed by the LoS. In this case, an asterisk will appear in the corresponding column (Es and/or spread-F).

- RoTEC time series may exhibit a wave-like or a noise-like pattern, or both. These three features have been distinguished in our analysis, where three different codes would correspond to a given category. The first corresponds to the simple, smooth, wavy pattern typical of classical MSTIDs. The second case is characterized by a noise-like pattern (NLP) without any harmonic component, similarly to figure 4.22(b). The last case is the superimposition of both, as it was observed in figure 4.23. The corresponding codes found in tables 4.10 and 4.11 will be respectively "MSTID", "NLP" and "both".

Different conclusions can be drawn from the analysis of tables 4.10 and 4.11 and of their related IPP maps, depicted in appendix C. According to their RoTEC signature, two different types of irregularities have been observed in our SN dataset. The first ones, observed in 30% of the cases, exhibit a RoTEC behavior similar to that of WD MSTIDs. Some of them obey the WD observational conditions discovered in the previous section while others do not. For example, the MSTID occurring on DOY 190/05 has been detected at high elevation by two satellites moving in opposite directions. For this particular case, it is likely that the physical origin of such MSTID would be different from the classical interaction between an AGW and the ionospheric plasma. As suggested in the literature, some of these MSTIDs may correspond to electrical MSTIDs, for which key properties are quite different from WD ones.
The second type of irregularity is the noise-like pattern (NLP), observed either alone (in 50% of the cases) or superimposed to an MSTID background (remaining 20%). They are observed at medium or high elevation and their physical origin has been

[17] More precisely, the dfS parameter is defined as the frequency difference between the lower boundary, related to the ordinary mode, and the upper boundary, related to the extraordinary mode.

DOY	Hour	PRN	$\sigma_{\mathbf{RoTEC}}$	RoTEC	Es [MHz]	spread-F
248/08	2215	32	0.36	both	2 – 3.2	strong*
184/06	2145	21	0.36	MSTID	2.5 – 5*	weak*
262/06	0345	13	0.25	NLP	none	strong
190/05	0130	16	0.25	MSTID	1.4 – 3.8	strong
248/08	1930	16	0.24	NLP	2.4 – 4.9	strong*
249/08	0145	13	0.23	NLP	0 – 1.9	strong*
172/02	0100	06	0.23	NLP	0 – 3.2	strong*
248/08	1845	22	0.22	NLP	2.2 – 4.9	weak*
184/02	0100	06	0.22	both	1.9 – 3.9	strong
189/10	2030	22	0.21	MSTID	N.A.*	N.A.*

Table 4.10 – Ten most disturbed 15 min periods observed during summer nighttime. The asterisk (*) denotes that the IPP corresponding to the layer of interest (e.g. E or F-layer) is outside the 100 km circle around the Dourbes station. "N.A." means that the ionogram sequence was not available.

DOY	Hour	PRN	$\sigma_{\mathbf{RoTEC}}$	RoTEC	Es [MHz]	spread-F
248/08	2245	19	0.15	NLP	0 – 1.5	strong*
184/02	0015	06	0.17	both	1.9 – 3.9	strong*
207/06	2015	21	0.11	both	4.5 – 9.0	weak*
189/02	0145	17	0.13	NLP	none	strong*
262/06	0315	13	0.20	NLP	none	strong*
209/02	2130	06	0.13	MSTID	3.2 – 5*	none*
202/03	2215	06	0.16	MSTID	4.8 – 8.9	weak*
209/05	2130	21	0.13	NLP	3.6 – 5.6	strong*
190/05	0045	15	0.13	both	1.4 – 3.8	strong*
259/03	2330	02	0.19	NLP	none	strong*

Table 4.11 – Similar to table 4.10, but related to the ten randomly selected periods.

investigated based on Dourbes ionograms. In practice, ionograms are valid for the E-region but not for the F-region, as the corresponding IPP ($IPP_{400\ km}$) is generally outside the 100 km circle around Dourbes. However, it is worth recalling that the phenomena which could be responsible for SN irregularities (either Es/spread-F or MSTIDs) exhibit a spatial extent exceeding several hundreds of kilometers. As a consequence, the ionospheric features observed in Dourbes ionograms should also be observed within a radius of more than the assumed 100 km, making our ionogram analysis rather reliable with respect to the size of the considered irregularities. Ionogram analysis reveals that Es layers and NLP are observed simultaneously nearly all the time. The corresponding f_0Es value rarely exceeds 5 MHz and does not seem to be correlated with the amplitude of σ_{RoTEC}: largest σ_{RoTEC} values do not correspond to large f_0Es values.

If Es layers do not seem to be responsible for the amplitude of the observed σ_{RoTEC} values, tables 4.10 and 4.11 show that spread-F phenomenon occurred in all cases, except one. Moreover, the so-called "strong" spread-F seems to be associated with large σ_{RoTEC} values, even in the absence of Es layer.

In conclusion, we have highlighted the close relationship between Es occurrence and spread-F phenomenon, as suggested in the literature [40]. F-region irregularity patches, also called FAIs, could be the origin of most of SN irregularities presenting a noise-like behavior in the RoTEC. However, additional measurements at the concerned IPPs are needed to confirm this mechanism. As an example, GPS scintillation measurements performed in the same area may help to confirm the scattering nature of spread-F irregularities, understood as the result of the mapping of Es patches along the geomagnetic field lines.

4.5 Summary and perspectives

A climatological study of ionospheric irregularities has been carried out based on 10 years of GPS data in Belgium. The detection algorithm comes from the method developed by Warnant and Pottiaux [99], with a slight adaptation allowing to mitigate data contamination by multipath and noise. The occurrence rate analysis reveals that the yearly proportion of 15 min periods qualified as "disturbed" does not exceed 9% (solar maximum), which implies that irregularities are not frequently observed, even during high solar activity periods. This proportion lowers to about 0.3% during solar minimum. These annual values are modulated by the seasonal and local time dependence of the occurrence rate.

Ionospheric irregularities have been divided into two main categories: those related to Space Weather (SW) events and the others, referred to as "quiet-time" irregularities. Even if SW irregularities are responsible for the largest RoTEC values, their contribution oscillates between 0 (solar minimum) and 25% (solar maximum) of the yearly total number. Therefore, the occurrence rate as well as the amplitude analysis have been focused on quiet-time irregularities, which constitute the major part of

irregularities detected over mid-latitudes. These latter have been classified into two groups, denoted Winter Daytime (WD) and Summer Nighttime (SN).

- **WD** are mainly observed during autumn and winter months, generally between 0800 and 1600 LT with a maximum of occurrence around 1100–1200 LT. Their amplitude, peaking at noon, is about 10% of the VTEC background and does not seem to vary with solar cycle while their RoTEC time series exhibits a clear, smooth, wave-like pattern. WD are preferentially observed at low elevation for satellites whose IPP trace is oriented northwards. This observational bias is the direct consequence of the moving character of the GPS constellation, the assumed southwards propagation of WD irregularities and of the non-vertical character of GPS measurements. Comparing these characteristics with the literature led us to support the evidence that WD irregularities correspond to classical MSTIDs, which consist in interactions between AGWs and the ionospheric plasma.
  The origin of the AGWs has been investigated by considering two main mechanisms: generation a) *in situ* by the solar terminator and b) in the lower atmosphere, followed by their propagation up to the ionospheric layer. The comparison of the time of WD occurrence and that of the passage of the terminator suggested us that the solar terminator may act as a secondary source of AGWs, while primary source is believed to be from orographic, tropospheric or stratospheric origin. Investigation of the spatial correlation between tropospheric jetstream and the occurrence WD irregularities shows little significance, the two phenomena being observed simultaneously for about 30% of the cases. The orography has also been considered as a potential source of AGWs and the spatial correlation with WD irregularities was rather positive, with a one-to-one correspondence in 60% of cases. These latter results have however to be tempered as IPPs satisfying the observational bias are mainly located above mountainous regions.
  As a result, the question on the AGW generation remains open and the most promising perspectives come from the multi-instrument approach. Indeed, it is believed that the question would be answered by combining techniques allowing to retrieve the vertical structure of the ionosphere (like sounders or radars), together with integral measurements such as TEC provided by the Global Navigation Satellite Systems (GNSS) technique. Another interesting perspective is the ionospheric tomography, which yields to a 3-D view of the plasma based on GNSS signals only. The use of mesospheric and thermospheric circulation models would also bring new elements, by allowing the computation of the propagation of AGW – generated in the low atmosphere – up to the ionospheric F-layer (atmospheric directional filtering). Indeed, during their propagation, AGW are subject to drifts due to the background neutral wind so that their effect in the ionosphere may be observed far from the source where they were generated. At last, one can also point out that our detection

algorithm should be applied to geostationary GPS signals, such as those sent by EGNOS or WAAS constellations. As such satellites appear as fixed points in the sky, the relative motion between the MSTID and the observer becomes absolute, allowing to perform wavelength and period measurements.

- **SN** occurrence takes place in summer, where they are more prevalent between 2000 and 2200 LT. Amplitude of SN irregularities is strongly varying from year to year, with values ranging between 8 and 15% during solar maximum and reaching 20% during solar minimum. However, the absolute error on VTEC measurements did not allow to prove the apparent anti-correlation between the amplitude and the solar activity, which is argued by some authors. In addition, these latter state that SN irregularities correspond to MSTIDs of electrical origin, whose parameters have been well established (see section 2.3). From the different RoTEC time series analyzed, it comes that only half of them exhibit a wave-like pattern typical of MSTIDs. As a consequence, it is believed that the remaining 50% of SN irregularities, which present a noise-like pattern, are due to small-scale irregularities in the F-region known as FAIs. These latter are generally associated with the occurrence of Es layers, which was confirmed in our study based on 20 cases of SN irregularities and their related ionograms from Dourbes station. In all the cases, the presence of frequency spread was clearly visible on ionograms, indicating that FAIs in the F-layer were strongly related to the noise-like pattern identified in the SN RoTEC time series.
  However, one cannot exclude that the absence of oscillatory behavior in 50% of cases imply the absence of electrified MSTID. Indeed, it is known that GPS measurements bias the detection of MSTIDs and that this latter depends on the relative motion between the MSTID and the IPP. Keeping in mind that the so-called nighttime MSTIDs have larger wavelengths and periods than classical MSTIDs, it is therefore possible that the lack of wave-like pattern in RoTEC time series would be due to this observational bias.
  Again, confirmation of the nature of the irregularity might be achieved using different measurement types, together with the GPS technique. As an example, the MSTID behavior could be confirmed based on airglow measurements or on ion/electron drifts derived from the new generation of ionospheric sounders. The new ionosonde of Dourbes is one of these new devices and could be, in the future, a very useful source of GPS-independent measurements. In addition, let us also mention that the presence of spread-F is generally associated with scintillation events, which correspond to signal fadings together with high-rate variations of the GPS phase measurements. A careful analysis of the carrier-to-noise ratio, also denoted C/N_0, during SN events would help to reveal the presence of ionospheric diffraction, which is the physical process responsible for scintillations. Let us conclude that this latter can also be confirmed by using dedicated scintillation receivers, allowing to perform precise measurements of the variations in phase and amplitude.

Chapter 5

Local climatological model of ionospheric irregularities

Contents

The climatological study performed in the previous chapter allowed to identify the different types of ionospheric irregularities observed from a typical Global Positioning System (GPS) station in Belgium. More particularly, it has been shown that the occurrence rate of quiet-time irregularities was smoothly varying with local time, season and solar activity, contrary to Space Weather (SW) induced irregularities which are transient by nature. Quiet-time irregularities represent between ∼75% and 100% of the yearly number of irregularities and constitute the major error source in precise (relative and differential) positioning[1].

In this chapter we present an original technique to analyze and model an ionospheric irregularity time series covering ten years of GPS data in Belgium. We use a Principal Component Analysis (PCA) to extract the most regular patterns from the series and build a local climatological model based on a limited number of principal components coming from the PCA. In section 5.1 we explain the methodology used: after the retrieval of the ionospheric irregularity time series, the principles relative to its analysis are described. In section 5.2, PCA results are detailed and lead to the elaboration of a PCA model representing the most recurrent daily patterns in

[1]Their impact on relative positioning technique will be investigated in details in the frame of the next chapter.

the series. Furthermore, a second model based on harmonic decomposition and autoregressive functions has been developed to take into account the day-to-day mean level, which is mainly due to secular variations of solar conditions. The final model, called climatological model, is then computed as the sum of these two models and validated over low and active solar activity periods. This final model can be considered as a local model since its computation and validation have been achieved based on Belgian data only. The present chapter is adapted from Wautelet and Warnant [104].

5.1 Methodology

The climatological study presented in this chapter relies on a dataset covering ten years of GPS data in Belgium. The first part of this section describes the setting up of the ionospheric irregularity time series based on Rate of TEC (RoTEC) measurements. In a second part the main concepts of the PCA are explained, followed by the reconstruction technique based on a subset of principal components.

5.1.1 Irregularity detection by GPS: setting up the time series

The detection of ionospheric irregularities has already been detailed in chapters 3 and 4. It is based on σ_{RoTEC} measurements performed at a single GPS station, as expressed by equations (4.1) to (4.3). Values of σ_{RoTEC} have a time resolution of 15 min and are computed for every satellite in view. The sampling rate of GPS measurements being 30 s, each standard deviation value is based on 30 observations. As we observe several GPS satellites at the same time, we average out all σ_{RoTEC} values occurring simultaneously. Moreover, we also use observations related to three Belgian stations: BRUS (50°47'N, 04°21'E), DENT (50°56'N, 03°23'E) and DOUR (50°05'N, 04°35'E). These stations being relatively close to each other (distance between them ranges from 70 to 125 km), σ_{RoTEC} values are highly correlated and averaging these three measurements provides a reliable series without any data gap and minimizes the influence of multipath and possible outliers[2]. The time span extends from January 2002 to December 2011, which covers the declining phase of solar cycle 23 and the rise of cycle 24.

Finally, a weighted moving average has been applied to the whole series to minimize the noise level and highlight the ionospheric signal. The sample window covers 45 minutes on either side of the central value, which corresponds to three observation epochs. The time series, further referred to as $\overline{\sigma_{\mathrm{RoTEC}}}$, is depicted together with the monthly sunspot number in figure 5.1. One can observe that the amplitude

[2]Moreover, to prevent enhanced multipath contamination, the elevation cut-off angle has been fixed to 20°.

of irregularities is in phase with solar activity, showing a maximum around 2002 and a long minimum in 2008–2009. Let us also note the rapid rise of solar cycle 24 at the end of 2011, followed by the irregularity time series. Seasonal patterns can also be identified: large irregularity values occur mostly during winter, reflecting the presence of Winter Daytime (WD) irregularities, while few of them take place in summer, corresponding to Summer Nighttime (SN) irregularities. We can also observe some peaks, especially in late 2003: these outliers correspond to high ionospheric variability periods due to powerful geomagnetic storms. For example, the maximum RoTEC value observed at BRUS station during November 20, 2003 storm (DOY 324/03) was about 10 TEC Unit (TECU)/min, which represents an extremely large variability value for mid-latitude regions. A deeper analysis of the series, although impossible to discriminate from figure 5.1, concerns daily variability that has already been detailed in the climatological study of chapter 4. Two main patterns have been identified: a rise of variability during winter daytime and in the late afternoon (around 2000 LT) during summer.

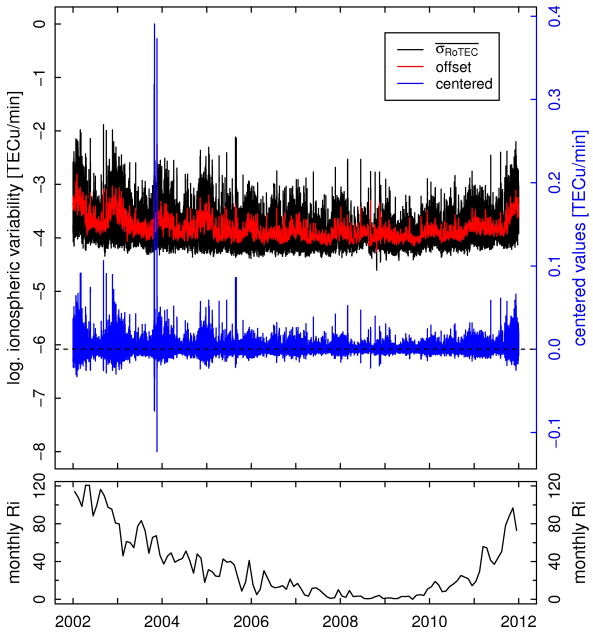

Figure 5.1 – *Top panel:* $\overline{\sigma_{\mathrm{RoTEC}}}$ and offset time series. Both series have been log-transformed because of the dynamics of the values. The centered series, which corresponds to $\overline{\sigma_{\mathrm{RoTEC}}}$ subtracted by the offset, is depicted with a normal scale. *Bottom panel:* monthly sunspot number *Ri*.

In the next sections we carefully analyze the $\overline{\sigma_{\mathrm{RoTEC}}}$ time series to retrieve and detail its principal climatological patterns.

5.1.2 Time series analysis and PCA

The most common technique used in time series analysis is the well-known Fourier transform, which allows to identify the most important periods in the series, together with their associated amplitude. In this chapter, we present another way of extracting such information: the PCA, also known as Empirical Orthogonal Function (EOF) analysis. This method has already been successfully used to analyze long time series or to forecast ionospheric parameters such as f_0F_2 [16, 109]. PCA is a multivariate analysis which consists in transforming an original space of correlated variables into another space of uncorrelated variables, called Principal Components (PCs). After this change of base, the greatest part of the information contained in the original space can be summarized using a few PCs only, others being associated with noise. The limited number of dimensions allows therefore an easy interpretation of data features.
In the frame of this chapter, the 3652 days constituting the $\overline{\sigma_{\mathrm{RoTEC}}}$ time series are considered as the correlated variables and the 96 quarter-hours play the role of the observations. By doing this way, the goal is the analysis of similar daily patterns in order to retrieve the most typical patterns of the series. The original time series is therefore reshaped in a matrix form whose structure is shown in table 5.1.

	01/01/02	**01/02/02**	**...**	**12/31/11**
00:00	0.023	0.057	...	-0.004
00:15	0.023	0.064	...	-0.004
00:30	0.023	0.070	...	-0.005
...	...	...	...	...
23:45	0.052	0.018	...	-0.005

Table 5.1 – Original time series of $\overline{\sigma_{\mathrm{RoTEC}}}$ reshaped in a matrix form containing 96 rows and 3652 columns, corresponding respectively to the quarter-hours and the days.

A preliminary step to PCA is to translate the origin of the observations to their centroid, which will ease PCA processing. In this context, the transformation consists in subtracting the mean for each of the columns to obtain centered values. From now, the series is then divided into two components: the first corresponds to the centered values on which the PCA will be applied and the second is the daily mean series, which will be referred to as "offset" series. Let us mention that the length of the offset series is 96 times shorter than that of the centered series, as we have only one value per day. Summing these two components leads to the original series $\overline{\sigma_{\mathrm{RoTEC}}}$. Both original and offset series are shown in figure 5.1 where we can observe solar cycle influence and seasonal patterns in the offset series. In its matrix form, centered series will be referred to as A.
The inertial matrix used in PCA algorithm must contain all the redundant information that will be summarized in a few PCs. In the frame of this work, the correlation matrix C has been chosen to play that role.

PCA consists in computing the 3652 eigenvectors X_i, which will be referred to as PCs, and their associated eigenvalues λ_i of the inertial matrix C:

$$C\,X_i = \lambda_i\,X_i \tag{5.1}$$

Each PC is associated with a percentage of the total variance σ^2_{tot} contained in the inertial matrix, σ^2_i, which represents the fraction of the total variance explained by the ith PC:

$$\sigma^2_i = \lambda_i/\sigma^2_{tot} = \lambda_i/\mathrm{tr}(C)\ \ [\%] \tag{5.2}$$

with $\mathrm{tr}(C)$ the trace of the correlation matrix C, which corresponds to the matrix dimension (*i.e.* 3652).
PCs are generally sorted in order of decreasing importance, so that we can easily identify the few ones representing the bulk of the total variance. Others can be associated with noise as they represent a small part of the signal. PCs consist in linear combinations of the original variables and their correlations with these latter are called "loadings".
The coordinates of the observations into the new space formed by the PCs are called "scores" and their computation is done through equation (5.3):

$$S' = X'\,A' \tag{5.3}$$

with

S' the transpose of the score matrix S;

X' the transpose of the principal component matrix X, set up by all PCs arranged in columns;

A' the transpose of matrix A.

Original data retrieval is achieved by inverting equation (5.3) and X being an orthogonal matrix, we have $X'^{-1} = X$ so the inversion takes the following form:

$$A' = X\,S' \tag{5.4}$$

As the aim of PCA is to reduce the number of dimensions, it is usual practice to keep only PCs which have been associated with signal pattern; others are considered as non-significant since they correspond to noise. Matrix X is therefore constituted with only a small number of columns and X becomes a (3652 x n) matrix, with n the number of PCs kept. We also have to truncate the S matrix in the same way to select only scores relative to the n PCs chosen. These truncations make the equation (5.4) compatible again and we are able to reconstruct the data in the original space. The loss of precision is proportional to the percentage of variance lost by not considering all PCs in the computation.

The reconstruction based on a small number of PCs has the advantage to extract the most recurrent patterns present in the original signal and to discard the signature of transient events, such as the effects of geomagnetic storms.

As the rest of the methodology follows from results, it will be explained and discussed in the next section. The processing diagram shown in figure 5.2 depicts the methodology used in this chapter.

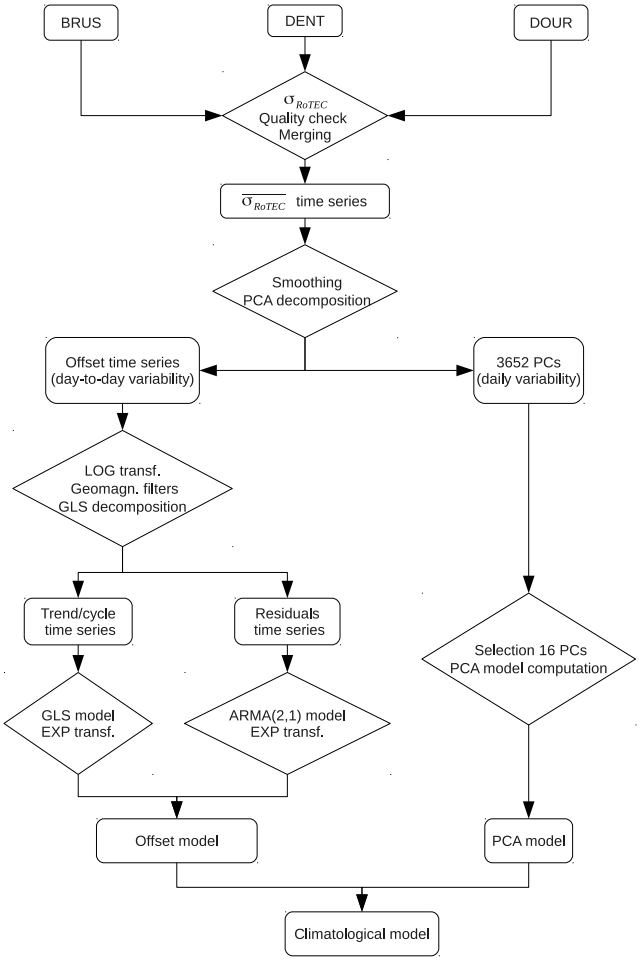

Figure 5.2 – Processing diagram. Data are represented as boxes while methods and transformations are illustrated by diamonds.

5.2 Results

We first present the principal component analysis of $\overline{\sigma_{\mathrm{RoTEC}}}$ series whose results lead to a daily variability model, further referred to as "PCA model". Then, we tackle the setting up of the model related to the offset series (daily means) which, once added to the PCA model, defines the final "climatological model". Finally, performance of this latter is assessed through a validation step considering data related to low and active solar activity periods.

5.2.1 PCA analysis and modeling

PCA on centered series leads to 3652 PCs whose ten most important are displayed in table 5.2, sorted by decreasing percentage of the explained total variance.

PC	λ_i	σ_i^2 [%]	$\sum \sigma_i^2$ [%]
1	1215.69	33.29	33.29
2	676.12	18.51	51.80
3	287.91	7.88	59.69
4	270.67	7.41	67.10
5	183.99	5.04	72.13
6	138.35	3.79	75.92
7	129.40	3.54	79.47
8	115.80	3.17	82.64
9	84.14	2.30	84.94
10	82.19	2.25	87.19

Table 5.2 – Eigenvalues, explained variance and cumulative explained variance (expressed in %) for the first ten principal components.

In figure 5.3, the cumulative explained variance is plotted with respect to the number of PCs considered. Together with the analysis of table 5.2 we can state that the first two PCs represent most of the regular patterns contained in the series, despite a cumulative variance of only about 52%. This relatively weak value is likely associated with the smooth character of $\overline{\sigma_{\mathrm{RoTEC}}}$ series (see previous section). To confirm these hypothesis, PCA was also performed on the centered series before being smoothed by the moving average filter: percentages of explained variance for the first three PCs were respectively 23.8%, 12.5% and 5.5% for a cumulative value of 41.7%. Comparison between these percentages and values displayed in table 5.2 shows that smoothing is needed if one wants to get the most significant PCs in terms of explained variance.
Scores and loadings relative to the first four PCs are depicted in figures 5.4 and 5.5. Their analysis reveals different patterns essentially associated with the first three PCs.

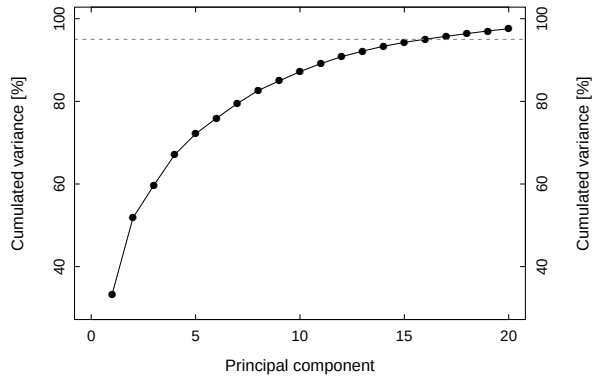

Figure 5.3 – Cumulative explained variance as a function of PC. The dotted line corresponds to the 95% threshold.

PC1 presents a scores pattern clearly related to a 24-hour cycle, due to day-night alternation. It shows a sharp decrease in $\overline{\sigma_{\mathrm{RoTEC}}}$ before noon and a longer increase in the afternoon, which is contrary to the regular daily pattern consisting in a rise of ionospheric activity during sunlit hours. Having a closer look to the associated loadings, we can observe a very strong negative correlation (almost -1) during winter days and a rather weak correlation (around 0.5) during summer. The behavior of this PC1 corresponds therefore to an increase of ionospheric variability during daytime in winter, between approximately 0800 and 1600 LT, which corresponds to WD irregularities. During nighttime, variability remains more or less constant, with values around 0.15 TECU/min. It is worth noting that this pattern represents about one third of the total ionospheric variability ($\sigma^2_{PC1} \approx 33\%$).

PC2 scores show an asymmetrical pattern: activity decrease between midnight and 0800 LT, followed by a nearly null value during daytime to end with a peak around 2000 LT. Correlations are strong to very strong (0.8–0.9) during summer days, meaning that an increase of evening ionospheric variability in summer is another recurrent pattern in our time series. During winter, days do not seem to respond to PC2 quite well as the correlation values are very variable, reaching sometimes 0.9 but oscillating around zero on average. This also confirms the results of the climatological study, during which nighttime irregularities have been observed mostly in summer (SN) but also during winter. The periodicity in loadings is once again annual.

Scores relative to PC3 show a cyclic signal with a period of about 12 hours: the two crests of activity occur around noon and 2300 LT. The series of loadings still consists in an annual cycle but shows sharp transitions around fall equinoxes while a large variability around spring equinoxes can be observed in the correlations. In summer, where correlations are rather negative (around -0.5),

this PC can be translated as pre-sunset and pre-sunrise bursts of ionospheric activity. During winter months correlations are rather positive (around 0.5) and PC3 not only strengthens the noon peak related to PC1 but also adds a secondary peak around midnight. Moreover, PC3 tends to lower the activity level during the early hours and in the late afternoon.

Loadings of all other PCs are similar to that of PC4 (figure 5.5): no clear pattern in correlations can be observed, which makes the interpretation of these components very difficult. To summarize, when considering the first three significant PCs, winter recurrent pattern corresponds to a peak of WD irregularities around noon, linked to sunshine duration. A more detailed analysis of PC1 scores shows that peak slopes are not identical: a rapid rise is observed between 0700 and 1100 LT while the decay period in the afternoon is longer (between noon and 1800 LT). This behavior is quite similar to vertical Total Electron Content (TEC) daily curve at mid-latitudes, which confirms the role played by background TEC in the detection of WD irregularities.

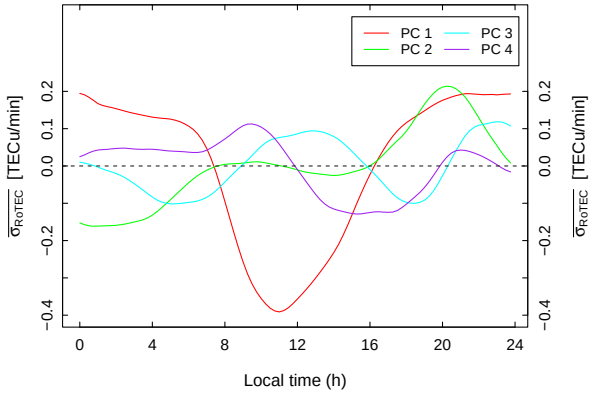

Figure 5.4 – Scores for the first four PCs.

We have seen that the first three PCs were responsible for about 60% of the total variance. However, it is usual practice to reconstruct 95% of the original variance. We need therefore to include some non-significant PCs to reach this threshold. According to figure 5.3, we need to use the first 16 PCs to reconstruct the data; the differences between original and reconstructed data, called residuals, are presented for years 2003 and 2008 in figure 5.6.

The main feature in figure 5.6 is the presence of large residuals for specific days, especially for year 2003: these are due to large RoTEC values observed during geomagnetic storms. In that sense, one can confirm that PCA reconstruction allows to filter out all days whose daily behavior differs significantly from the typical patterns. Analysis of figure 5.6 also shows that, for year 2003, residuals are larger in winter than for the rest of the year, which means that winter days differ on average more from PCA regular pattern than other periods of the year. This is probably due to a)

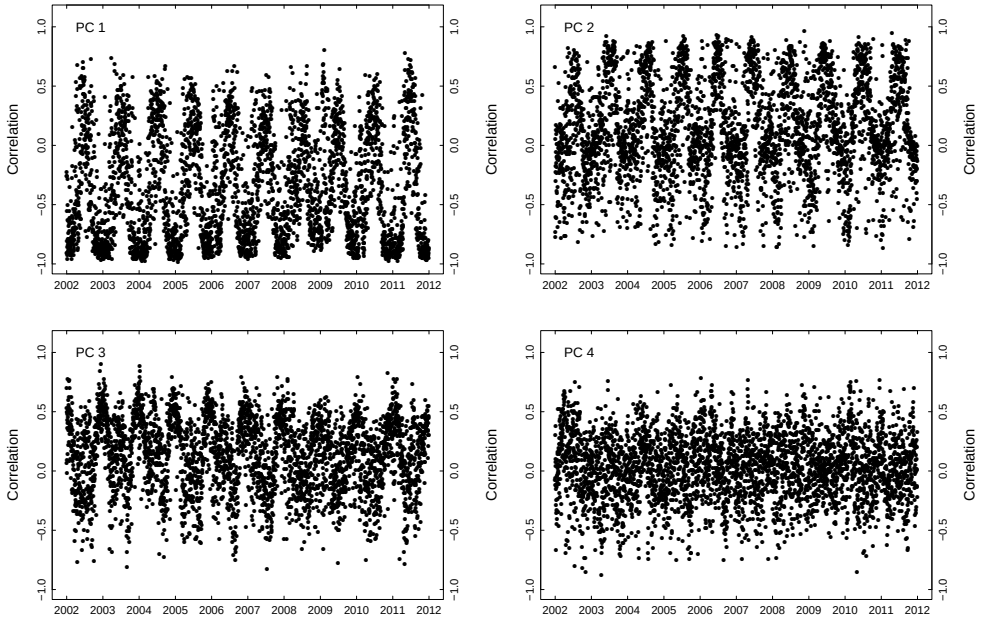

Figure 5.5 – Loadings for the first four PCs.

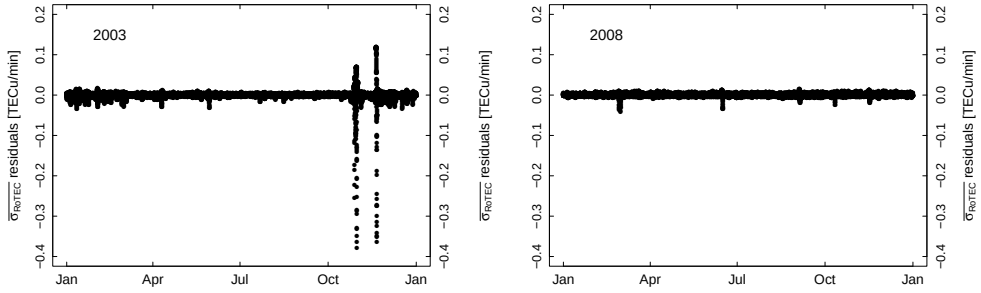

Figure 5.6 – Residuals of PCA reconstruction considering the first 16 PCs for years 2003 (left) and 2008 (right).

high solar activity conditions in terms of Extreme Ultraviolet (EUV) radiation and b) combined winter/December anomaly, which makes TEC annual maximum occur in winter, despite of a smaller ion production rate than during summer [24]. In 2008 (low solar activity period), PCA reconstruction seems to produce uniform residuals along the whole year, as geomagnetic storms were rarely occurring and TEC values were usually not larger than 10 TECU.
In this chapter, we will use PCA results to build an annual model of centered values. This model will result from averaging several years of data to obtain smooth and continuous daily patterns. Validation will be performed over low and active solar activity periods (see section 5.2.3). Therefore, two different PCA models will be built and validated separately. For validation during solar minimum (year 2008), PCA model will be based upon periods 2002–2007 and 2009–2011 while validation during active solar conditions (year 2011) will use a model built from 2002–2010 period (see figure 5.1 for solar activity levels).
Analysis of figure 5.5 shows that loadings relative to the first three PCs do not vary much with solar cycle. This is due to the fact that these results are related to centered value and that most effects due to solar cycle (as well as part of seasonal pattern) have already been taken into account in the offset series (see section 5.1.2). The annual cycles in loadings can therefore be averaged to get an eigenvector matrix X of size (365x16). Scores matrix S being already truncated to the first 16 PCs, the reconstruction can be achieved and the result is called "PCA model". This model corresponds to a (96x365) matrix expressing centered $\overline{\sigma_{\mathrm{RoTEC}}}$ every 15 min for a mean year.
For example, the comparison between the PCA model built over 2002-2010 and the original centered values is illustrated in figure 5.7. We can observe that climatological features which have been identified in the previous sections are correctly reproduced by this model: a main rise during winter daytime and a small peak in the late afternoon for summer days. Data related to 2002 show the largest variability with respect to the model: that is a direct consequence of high solar activity encountered in 2002. Considering periods of moderate or low solar activity, one can notice that the PCA model is in good agreement with data. Since an important part of solar cycle influence has been removed by the use of centered values, the PCA model can be repeated from year to year to forecast daily variability due to ionospheric irregularities.

5.2.2 Offset time series modeling

The PCA model has to be added to the offset time series model to create the final climatological model (figure 5.2). As the goal is to retrieve and model the main patterns, we also need to exclude geomagnetically active periods from our series, which can be clearly identified as spikes in figure 5.1. This is done through the use of geomagnetic filters which were already used in the frame of chapter 4: Kp ≤ 4 and |DST| $\leq$ -50 nT.

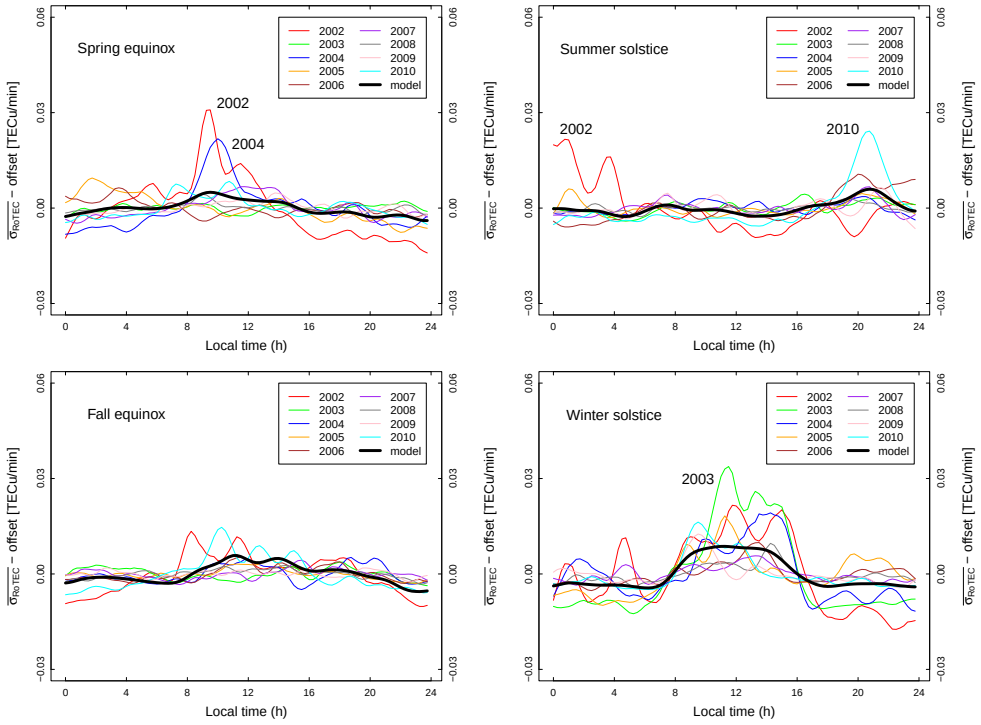

Figure 5.7 – Comparison between original (centered) data and the PCA model for solstices and equinoxes.

As for the PCA model, two offset models will be computed in order to validate the method over two different years corresponding to different solar conditions. The model based on 2002–2007 period will be validated over year 2008, during solar minimum. The validation of the active solar activity period will be performed over the year 2011, the related model being derived from 2002–2010 period.
Figure 5.1 shows that offset variability in not constant with time: variance during low solar activity periods (2008–2009) is clearly smaller than variance during solar maximum (2002). Stabilization is achieved through log-transformation (natural logarithm) of the series, which gives a steadier series also depicted in figure 5.1. This transformation will ease model processing, which can be divided into two main steps:

1. Modeling of annual cycle(s) and long-term trend due to solar activity in a least-squares adjustment. The model coming from this procedure is purely mathematical, resulting in a very simple forecast computation.

2. Modeling of the residuals coming from the least-squares adjustment processed in the first step. As this time series is more or less similar to a noisy pattern, specific statistical tools have to be applied for modeling purposes.

5.2.2.1 Modeling trend and cycles: generalized least-squares

Time series analysis suggests lots of ways of extracting trends and cycles: exponential smoothing, Holt-Winters method, additive and multiplicative decompositions, least-squares method [14, 21]. Many of them have been investigated and the method presented here is the one giving the most satisfactory results. The shape of the log-transformed offset series suggests to model the trend with a low order polynomial while cycles can be reproduced with harmonic functions. To accurately model the solar cycle influence, a third order polynomial trend has been chosen. To retrieve frequencies of the series, a Fourier transform is applied to the detrended offset series and detects periods of 182.5 and 365 days, as expected. Annual and semi-annual periodicity, added to the long-term trend can therefore be modeled as follows:

$$\begin{aligned} \text{Offsets}(t) &= a_0 + a_1 t + a_2 t^2 + a_3 t^3 + a_4 \sin\left(\frac{2\pi t}{T_1}\right) \\ &\quad + a_5 \cos\left(\frac{2\pi t}{T_1}\right) + a_6 \sin\left(\frac{2\pi t}{T_2}\right) \\ &\quad + a_7 \cos\left(\frac{2\pi t}{T_2}\right) \end{aligned} \tag{5.5}$$

with

a_i some numerical coefficients to be computed from the least-squares procedure;

T_1 and T_2 the two harmonic periods, respectively 182.5 and 365 days.

Partial autocorrelograms obtained from offset time series show strong autocorrelation within the series and, from a statistical point of view, an ordinary least-squares procedure is not suitable in this case. To take this autocorrelation into account, we first need to assess it and then feed a Generalized Least-Squares (GLS) adjustment with such information. Autocorrelation is estimated by fitting the series with a first order autoregressive model – AR(1) – whose principles can be summarized as follows: an observation made at epoch t can be expressed as a fraction of the previous observation added to a white noise term ε_t : $A_t = \alpha A_{t-1} + \varepsilon_t$. AR(1) model leads to $\alpha = 0.85$, that corresponds to a strong autocorrelation, and GLS fitting can therefore be computed using this information. As details of the computing method are out of the scope of this thesis, we invite the interested reader to consult the following references: Box and Jenkins [12], Brockwell and Davis [14].
GLS fitting described in equation (5.5) leads to three coefficients a_3, a_4 and a_6 statistically non-significant as their value is not statistically different from zero. Trend formulation is thus simplified by a second order polynomial and the cycle component relies on a pure cosine model nearly in phase with winter/summer alternation. Equation (5.5) can therefore be simplified as:

$$\begin{aligned} \text{Offsets}(t) &= a_0 + a_1 t + a_2 t^2 + a_3 \cos\left(\frac{2\pi t}{T_1}\right) \\ &\quad + a_4 \cos\left(\frac{2\pi t}{T_2}\right) \end{aligned} \tag{5.6}$$

Data and GLS model are both depicted in figure 5.8 (top panel) where extrapolation (forecast) for year 2011 and its related confidence interval are depicted. A more detailed view of 2011 (active conditions) and 2008 (low solar activity) forecasts is depicted in figures 5.9, where one can observe the increase due to the polynomial model, translating the rising activity of solar cycle 24.

5.2.2.2 Modeling residuals: ARMA model

Subtracting the GLS model from the offset observations leads to the residual time series depicted in figure 5.8 (middle panel). Although this series presents a null mean average, one can identify some periods where values do not vary around zero. In addition, analysis of total and partial autocorrelograms reveals the presence of autocorrelation within the series. Therefore, an AutoRegressive and Moving Average (ARMA) method is used to fit the residual series. This algorithm implies not only autoregressive terms, as used for trend/cycle modeling in the previous paragraph, but also moving average terms whose effects correspond to a smoothing of the error modeling and a better fitting than with a pure autoregressive model. Once again, all details about the implementation and the computation can be found in [12, 14]. The physical meaning of the autoregressive terms in the residual model lies in the presence of relatively long-lived phenomena lasting several days. For instance, the presence of a given sunspot group rises TEC values due to an enhancement of EUV and soft X-rays. This leads to a larger TEC background, which implies larger amplitudes of ionospheric irregularities.

Residual time series modeling consists in computing several ARMA candidate models, each of them being characterized by a given order for autoregressive and moving average terms. Then, we compare the different models on the basis of the Akaike Information Criterion (AIC), which is an indicator of the goodness of fit. The candidate exhibiting the lower AIC becomes the selected model, except if another candidate gives a similar AIC value with smaller orders, in which case the latter is chosen.

The ARMA model selected is an ARMA(2,1), which means that the autoregressive component is of order 2 (*i.e.* previous two days influence) and the moving average component is of order 1. It is depicted in figure 5.8, where forecast values for year 2011 are also presented. As we can observe, forecast values quickly tend to zero, which is due to the fact that the influence of the last days of 2010 vanishes with time. A more detailed analysis of the ARMA model is presented in the next section

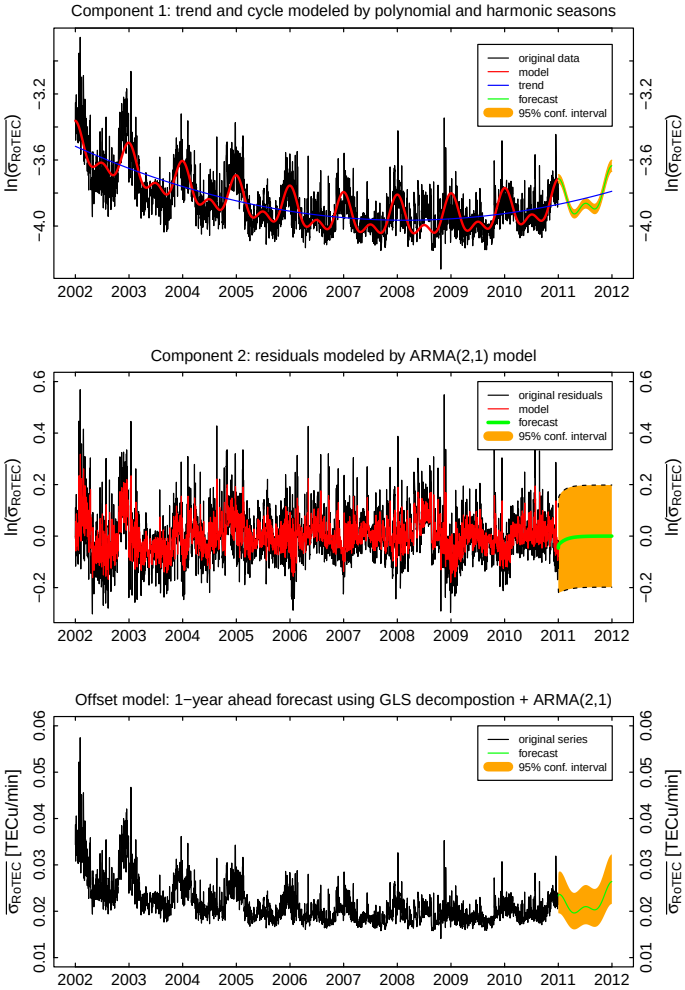

Figure 5.8 – Model (2002-2010) and forecast (2011) of the offset series. *Top panel*: trend and cycle are fitted by using Generalized Least-Squares (GLS) procedure, which features harmonic seasons and a second order polynomial for the trend. *Middle panel*: residuals from this fit are modeled by AutoRegressive and Moving Average (ARMA) method. *Bottom panel*: offset model is constituted by summing the two aforementioned components.

where validation dataset (*i.e.* data related to years 2008 and 2011) has been taken into account.

Finally, we get the offset model by summing both GLS and ARMA models and then applying an exponential transformation to retrieve the original units. Forecast values and their corresponding confidence interval for year 2011 are shown in figure 5.8. Let us note that the most important contribution to the final model confidence interval

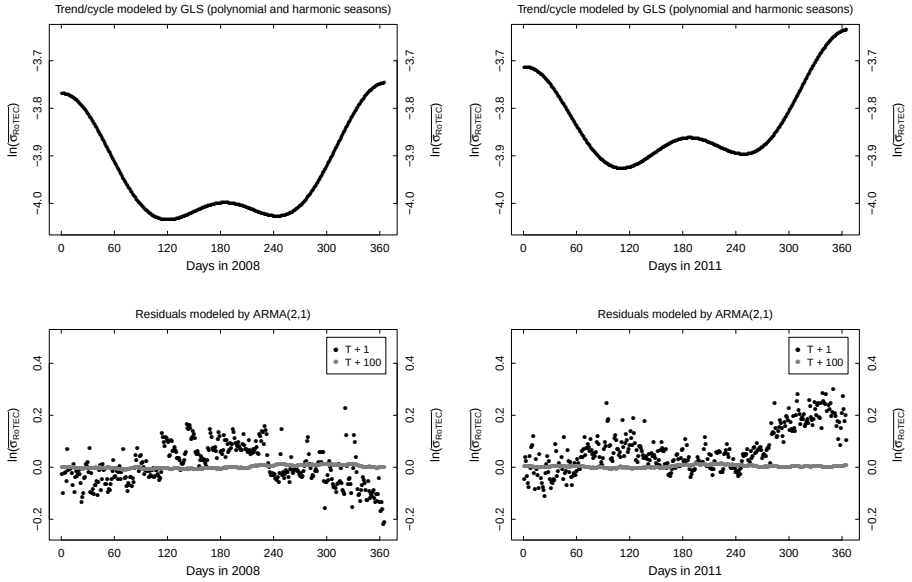

(a) (b)

Figure 5.9 – *Top panel*: determinist forecast of trend/cycle component for years 2008 (a) and 2011 (b). *Bottom panel*: residual forecast using ARMA(2,1) model for prediction steps T+1 and T+100.

comes from the residual modeling.

5.2.3 Validation

This section aims to validate the final model, called climatological model, made up of PCA and offset models (figure 5.2). As the validation dataset covers two periods (2008 for solar minimum and 2011 for active conditions), we have to compare two forecasts with their related true values. These forecasts, featuring a time resolution of 15 minutes, have been computed for prediction steps (*i.e.* future epochs) of 1 day (T+1) and 100 days (T+100). As PCA and trend/cycle models do not depend on prediction step, difference between epochs T+1 and T+100 lies in the ARMA component. In figure 5.9 we present ARMA residual forecasts for prediction steps T+1 and T+100. Considering T+100, we can observe that ARMA forecast is not markedly different from zero for both 2008 and 2011. For this timestep one can therefore state that ARMA model does not provide any added value to the climatological model. Conversely, forecast values are significantly different from zero considering the T+1 timestep. For year 2008, ARMA model lowers the forecast values until day 100 (spring equinox). Then, it tends to increase the forecast during the whole summer and finally to lower again at the end of 2008 (fall and winter). From

these observations we can conclude that trend/cycle model underestimates summer $\overline{\sigma_{\mathrm{RoTEC}}}$ values and overestimates the winter behavior. This latter point is certainly due to the fact that, according to the trend/cycle model, a new solar cycle should have appeared around August 2008. In practice, this did not happen and residual values tend to remain negative. In that sense, the ARMA residual model can be considered as an adaptive model. Considering year 2011, similar observations can be made: ARMA forecast tends to adapt the residual level, especially during fall and winter where the trend/cycle model clearly underestimates $\overline{\sigma_{\mathrm{RoTEC}}}$ values.
Validation of the climatological model can also be done through the computation of the Root Mean Square (RMS) of differences between observations and forecast values for years 2008 and 2011. Absolute RMS is computed daily and is expressed as follows:

$$RMS_i = \sqrt{\langle (X_{ij} - M_{ij})^2 \rangle} \tag{5.7}$$

with

i the day identifier, from 1 to 365;

X_{ij} the observation for day i at epoch j;

M_{ij} the model value for day i at epoch j.

Relative RMS values are obtained by dividing absolute RMS by the daily mean of absolute $\overline{\sigma_{\mathrm{RoTEC}}}$ values. Both relative and absolute values are depicted in figure 5.10 where prediction steps T+1 and T+100 have been represented. From the previous conclusions, we can consider that T+100 RMS values correspond to a PCA + trend/cycle model, without any residual modeling.
The common feature between the four graphs of figure 5.10 lies in a larger RMS in winter than in summer. Typically, relative RMS is around 10–15% in summer for both solar conditions (2008 and 2011). During winter, this value oscillates around 20–25% during solar minimum, reaching rarely more than 40%. Under active conditions (2011), RMS values also oscillate around 25% but with a larger variability than for solar minimum, reaching up to 60%. As explained above, the main difference between T+1 and T+100 is due to residual modeling. ARMA model allows to improve the model accuracy during summer and for the end of the year, where it brings corrections for a too optimistic trend/cycle model in 2008 and a too pessimistic trend/cycle model in 2011. Translated into relative RMS, figure 5.10 shows that, for end of 2008, values stay around 25% for T+1 model while they can exceed 35 to 40% when no ARMA model is considered. In 2011, mean RMS values oscillate around 30–35% in winter when the T+100 model is taken into account.
Residual model using the ARMA method is therefore a convenient way to make the final model adaptive to current conditions if the prediction step is not too far from the last observed epoch. We can assess the added value of residual modeling through the computation of the yearly average of daily RMS for different timesteps.

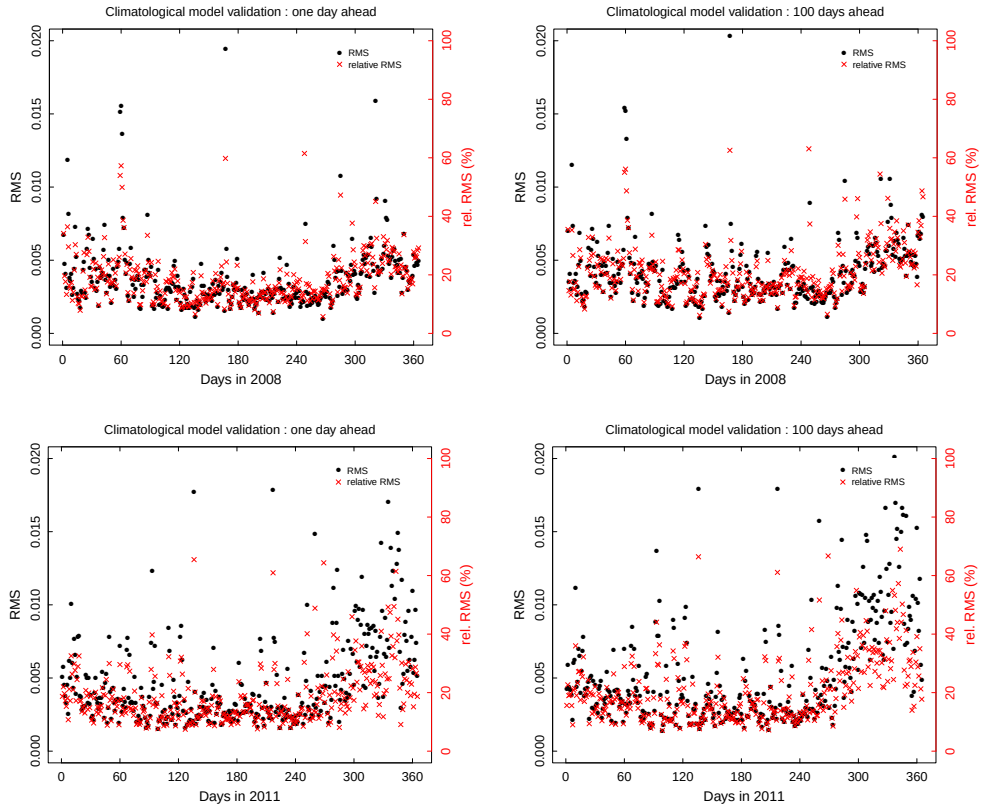

Figure 5.10 – Validation of climatological model. Absolute (*dots*) and relative (*crosses*) RMS values for years 2008 (top) and 2011 (bottom) are shown for a prediction step of 1 day (left) and 100 days (right).

More particularly, we have considered the prediction steps from T+1 to T+100 and we have observed that residual modeling was null on average for the latter case. Results, depicted in figure 5.11, show that mean RMS significantly increases in the first four or five days, after which it tends to an asymptotic RMS value due to the only deterministic part of the model. From this figure, we can state that the climatological model reliability is about four or five days, being the timestep from which the ARMA contribution tends to be negligible. It is worth adding that the mean RMS values are larger for year 2011 than for 2008 due to the larger RMS values observed during fall and winter. Moreover, we can also observe from figure 5.11 that the convergence speed during 2011 is slower than for 2008. This behavior is most probably due to a larger influence of the residual modeling in 2011.

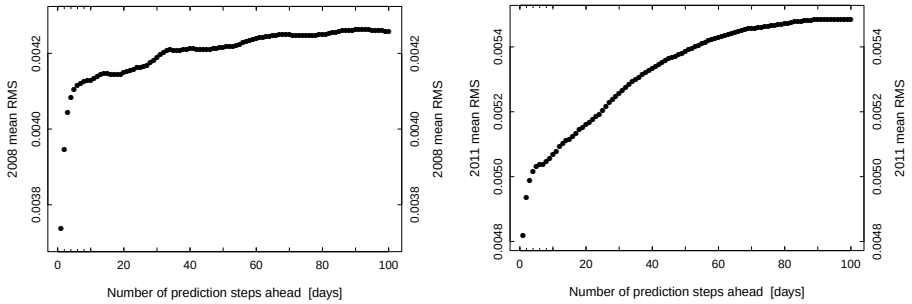

(a) (b)

Figure 5.11 – Yearly mean of daily RMS values for prediction steps T+1 to T+100 days for years 2008 (a) and 2011 (b).

5.3 Discussion and perspectives

We have presented a climatological model of ionospheric irregularities valid for the Belgian region. This model does not consider transient events due to disturbed SW conditions, such as geomagnetic storms or solar flares. For operational forecasting, geomagnetic activity has to be taken into account as these disturbed conditions are part of the observations from which the model is built. On the one hand, residuals modeled by ARMA will reflect the increase in ionospheric activity due to active conditions and the model will therefore undergo an increase in its offset value. This is true when considering geomagnetic storms whose time span can extend up to several days. On the other hand, ARMA(2,1) is certainly not the best model to describe rapid changes in ionospheric plasma induced by SW events. Indeed, the offset model has a daily time resolution while time scale of SW events can be significantly shorter. In this context, a specific SW model with a time resolution of about one hour should be developed and added to the climatological model for real-time forecasting.

In the offset model, solar cycle influence has been modeled by a second order polynomial. If this model gives satisfactory results while considering the time span analyzed in the frame of this work, it could not be the case during solar maximum periods. For real-time modeling and forecasting, several mathematical functions should be tested to better capture the solar cycle influence on ionospheric irregularity occurrence.

The main drawback of a climatological model is its continuity: it does not characterize inter-daily variability at all. Moreover, it does not provide any explanation about the difference between winter and summer behaviors as the model is purely statistical. The next step is to develop a semi-empirical model still based on statistics but which can assimilate information coming from proxies of ionospheric irregularities. In the previous chapter, it has been shown that some meteorological features like jetstream or the occurrence of Es layers could be related to WD or SN irregularities. As a consequence, forecasting of such parameters (if available) might be integrated

into a next generation of models to modulate the climatological forecast background. Finally, as the area of validity of the climatological model is limited to the Belgian region, some additional validation over other mid-latitude stations should be carried out to make the model applicable to the whole mid-latitude region.

5.4 Conclusions

Ionospheric irregularities represent an important threat to GPS high-precision positioning techniques, used mainly by surveyors, civil engineers and farmers. To monitor and forecast this activity, a climatological model has been set up on the basis of an irregularity time series in Belgium between 2002 and 2011. This local model is divided into two main components.

The first models daily variability of irregularities. Resulting from a statistical method called PCA, it allows to reproduce the main patterns of the time series which has a time resolution of 15 minutes. Among them are the activity maximum observed during winter days and the slight maximum during nighttime in summer, in agreement with the climatological study performed in the previous chapter. As the PCA model shows a null daily average, it has to be leveled by the offsets, which correspond to daily mean values. This series, whose behavior describes solar cycle and seasonal influences on ionospheric irregularity occurrence, is the second component of the model. It has been modeled by a quadratic trend and harmonic functions, computed together in a GLS adjustment. Residuals are fitted by an ARMA(2,1) model, which is a statistical autoregressive model. In this context, ARMA allows to correct GLS forecast values by taking into account the previous residual values.

The climatological model, constituted by adding both PCA and offset models, has been validated on the whole years 2008 and 2011. Its accuracy, expressed in terms of RMS, depends on the season: mean RMS values oscillate around 10–15% during summer while winter values are ranging between 20 and 25%. Moreover, the added value of ARMA modeling has been assessed: the use of the ARMA method significantly improves the forecast up to four or five days after the last observation, epoch from which its contribution can be considered as negligible.

In the future, several model improvements should be considered. First, the solar cycle modeling function, which corresponds at the present time to a second order polynomial, might take another form, depending on the solar cycle phase considered. Another major improvement would be the addition of a space weather component, which will allow to take into account ionospheric irregularities due to transient events such as geomagnetic storms. More particularly, these latter are known to be forecasted several hours in advance. Thirdly, the PCA model is a mean model repeated year after year; as a consequence it does not take into account the larger values observed during solar maximum. In this context, future work should focus on the model adaptation to current solar conditions by multiplying the mean model by a stretching parameter, smaller or larger than 1. At last, as the model proposed

in the frame of this thesis is climatological, it does not reproduce the day-to-day variability observed in $\overline{\sigma_{\mathrm{RoTEC}}}$ values. The only adaptive part is the ARMA component which only acts on the daily mean; therefore, future developments should be oriented towards a semi-empirical modeling. By assimilating proxies of ionospheric irregularities, it is thought that such model would improve the day-to-day variability. However, if this solution seems to be the best way to forecast irregularities, let us recall that their origin is still under investigation (see previous chapter), so that development of such models has to be considered over the long term.

Chapter 6

Ionospheric irregularities and relative positioning

Contents

Over the last decade came major breakthroughs in satellite navigation and positioning, mainly due to the development of precise positioning techniques based on Global Positioning System (GPS) signals. The number of application fields is continuously increasing and new user groups, such as surveyors or farmers, joined the community. At the present time, only differential and relative positioning techniques guarantee a real-time, precise, positioning service[1]. If they are based on phase measurements, they allow to measure the user position in real-time with a centimeter-level accuracy, for each of the three components (North, East, Height). The most widespread technique is the so-called Real-Time Kinematics (RTK), working in both differential and relative modes. The user, equipped with his own Global Navigation Satellite Systems (GNSS) receiver, needs to be in permanent radio link

[1]Let us point out that Precise Point Positioning (PPP) allows the same accuracy level than differential or relative mode but is more difficult to carry out, as being an absolute positioning method. Indeed, the need of precise satellite orbits and clocks as well as accurate atmospheric, earth tides and ocean models makes the computation much more complicated than in differential or relative modes.

with his data provider to allow real-time positioning. RTK is generally used within networks of Continuously Operating Reference Stations (CORS), for which the position is accurately known. The basic principle of classical RTK, *i.e.* considering a user and a single reference station, relies on the fact that all errors common to the two stations are mitigated or canceled, as algorithms are based on differential/relative measurements. In the case of the ionospheric refraction, the error source in RTK corresponds to the residual term due to the spatial decorrelation of the ionospheric plasma. During quiet periods, *i.e.* in the absence of ionospheric irregularities, such error term can be neglected if the baseline, which is the vector linking the two receivers, is ideally smaller than 20 km.

Ionospheric irregularities, which have been investigated in the previous chapters, are the major error source for RTK measurements as they are responsible for moderate to severe Total Electron Content (TEC) gradients. In the absence of integrity monitoring[2], the user is not aware of the presence of irregularities and will trust positioning solutions provided by the GNSS receiver. These latter are affected by errors that can reach several meters, while the nominal accuracy of the technique is about 1 cm [59]. In practice, the residual ionospheric error acts on the real-time GNSS processing software in two ways. On the one hand, it affects the ambiguity resolution algorithm, which can fail or, even dangerous, fix the ambiguities to wrong integer values, resulting in a bias in the positioning solution. On the other hand, even after a successful ambiguity resolution, the ionospheric error affects the least-squares adjustement, and thus the estimation of the user position.

In the recent years, GNSS manufacturers have developed positioning solutions based on a network approach. Using a sub-network of CORS stations around the user, sophisticated algorithms embedded in the user's receiver (or computed by a dedicated center) provide robust positioning solutions with mitigated ionospheric effects, taking benefit of the network computation. However, those algorithms such as Virtual Reference Station (VRS) or Flachen Korrectur Parameter (FKP) are developed by private companies and are therefore proprietary. This leads to non-standard procedures that are very difficult to reproduce to correctly assess the influence of ionospheric irregularities on positioning. Therefore, it has been decided to focus our analysis on "classical" relative positioning technique.

In a first step, we describe the algorithm allowing to compute the positioning error due to the ionosphere (further referred to as "ionospheric positioning error") in the case of relative positioning. Next, the effects of baseline length and orientation on ionospheric positioning error are assessed for three different levels of ionospheric activity: quiet conditions, occurrence of quiet-time irregularities – basically a Medium-Scale Traveling Ionospheric Disturbance (MSTID) – and during a powerful geomagnetic storm. In a final step, we attempt to correlate ionospheric

[2]Integrity can be defined as a measure of the reliability of a computed result. In the case of the ionospheric threat, integrity could be based on the monitoring of ionospheric irregularities, for example with the single-station algorithm described in chapter 4.

activity detected at a single station – through Rate of TEC (RoTEC) measurements – with the ionospheric positioning error experienced by a typical RTK baseline. If this latter correlation is significant, we would be able to translate RoTEC (or its variability over a given time interval) into positioning error, expressed with units easily understandable for users (*i.e.* in meters). This latter point is particularly important as it would make the link between "GNSS-ionosphere" and "user" communities. Let us mention that the content of this chapter has been partially adapted from the original article of Lejeune et al. [60].

6.1 Ionospheric positioning error

This section aims at explaining the methodology used to compute the ionospheric positioning error in the case of relative positioning. The algorithms described below have been implemented in the Software for Determining the Ionospheric Positioning Error on RTK (SoDIPE-RTK). Using Receiver INdependent EXchange (RINEX) observation and navigation files as input, it computes the positioning error (in meters) only due to the ionosphere for a given baseline.

6.1.1 Methodology

In relative mode, RTK users form Double Differences (DDs) of their own phase measurements (mobile station - B) with measurements made by a reference station (A) for which the position is accurately known (see section 3.2.2). In a first step, SoDIPE-RTK computes DD for every epoch (conventional sample rate of 30 s is used in the frame of this work), based on all visible satellites in both stations for the given epoch. If ϕ^i_A, ϕ^i_B, ϕ^j_A and ϕ^j_B are the four simultaneous "one-way" phase measurements between receivers A, B and satellites i, j, double difference $\phi^{ij}_{AB,k}$ on L_k carrier is computed as follows (see equation 3.4):

$$\begin{aligned} \phi^{ij}_{AB,k} &= (\phi^i_{A,k} - \phi^i_{B,k}) - (\phi^j_{A,k} - \phi^j_{B,k}) \quad \text{[m]} \\ &= \rho^{ij}_{AB} + \Delta\rho^{ij}_{AB} - I^{ij}_{AB,k} + T^{ij}_{AB} \\ &\quad + m^{ij}_{AB,k} + \mathrm{PCV}^{ij}_{AB,k} + \lambda_k N^{ij}_{AB,k} + \varepsilon^{ij}_{AB,k} \end{aligned} \tag{6.1}$$

with ρ^{ij}_{AB} the distance term between the different satellites and stations, $\Delta\rho^{ij}_{AB}$ the residual orbit error, $I^{ij}_{AB,k}$ the residual ionospheric error, T^{ij}_{AB} the residual tropospheric error, $m^{ij}_{AB,k}$ the residual multipath term, PCV^{ij}_{AB} the DD combination of satellite and receiver Phase Center Variations (PCV), λ_k the wavelength, $N^{ij}_{AB,k}$ the ambiguity term and $\varepsilon^{ij}_{AB,k}$ the noise on the DD. In accordance with the definition of the double difference in section 3.2.2, the notation $*^{ij}_{AB}$ refers to $(*^i_A - *^i_B) - (*^j_A - *^j_B)$.

In a second step, we extract the ionospheric residual term in DDs by computing the Geometric-Free (GF) phase combination $\phi^{ij}_{AB,GF}$. Indeed, neglecting multipath[3] and noise terms and correcting for PCVs[4], we obtain from equation (6.1):

$$\begin{aligned} \phi^{ij}_{AB,GF} &= \phi^{ij}_{AB,L1} - \phi^{ij}_{AB,L2} \qquad [\text{m}] \\ &= \alpha\, \text{STEC}^{ij}_{AB} + \lambda_k\, N^{ij}_{AB,GF} \end{aligned} \tag{6.2}$$

with $\alpha = -1.05046\ 10^{-17}$ [m^3/e$^-$] and STEC^{ij}_{AB} the combination of the four Slant TEC (STEC) measurements.
For each DD, the float ambiguity $N^{ij}_{AB,GF}$ is solved using the whole observation period, so that the resolution process can not be considered as a real-time one[5]. Therefore, the ambiguity resolution algorithm implemented in SoDIPE-RTK is very reliable and the computed ambiguities can be considered as the true integer values. This constitutes an important difference with real-time processing softwares run by GPS users in the field.
After ambiguity resolution, STEC^{ij}_{AB} can be computed to reconstruct the ionospheric residual term on each GPS carrier $I^{ij}_{AB,k}$:

$$I^{ij}_{AB,k} = 40.3\, \frac{\text{STEC}^{ij}_{AB}}{f_k^2} \qquad [\text{m}] \tag{6.3}$$

with f_k the kth GPS frequency.

Then, we are now able to compute the three components (North, East, Height) of the positioning error for every epoch using a least-squares adjustment on L_1 DDs. The positioning method in SoDIPE-RTK is therefore based on single-frequency measurements, but uses ambiguities estimated previously from dual-frequency measurements. The L_1 carrier was chosen because it offers more precise and reliable observations than L_2. The least-squares adjustment is based on a set of linearized observation equations which can be expressed in a familiar matrix-vector notation [47]:

$$\underline{l} = A\, \underline{x} \tag{6.4}$$

with $\underline{l}$ the vector of observations, A the design matrix containing geometric constants and $\underline{x}$ the vector of unknowns, which are the three components of the positioning error.

[3]This assumption will be verified in the next section.
[4]PCV absolute values are provided by the International GNSS Service (IGS) in the ANTEX format.
[5]The algorithm uses both Wide-Lane (WL) and GF combinations to solve integer ambiguities on L_1 and L_2 carriers, which allows to determine $N^{ij}_{AB,GF}$. More information about its computation can be found in [105].

The solution of this system is unique considering the least-squares principle $\underline{\nu}^T\ P\ \underline{\nu}$ *minimum*, with $\underline{\nu}$ the vector of residuals between observations and adjusted values and P the weight matrix, reflecting the non-null correlation between the DDs [47]. Applying this minimization principle on equation (6.4) leads to the estimate of the unknowns:

$$\underline{x} = (A^T P A)^{-1}\ A^T P\ \underline{l} \tag{6.5}$$

Developing the distance term ρ_{AB}^{ij} of equation (6.1) and ommitting the $*_{AB}^{ij}$ notation, the observation equations appearing in (6.4) can be expressed as follows:

$$\begin{aligned} l = \phi_1 - \rho_0 - \lambda_1\, N_1 - \mathrm{PCV}_1 \quad &= \quad a_1 \Delta\mathrm{N} + a_2 \Delta\mathrm{E} + a_3 \Delta\mathrm{H} - I_1 \\ &\quad + T + \Delta\rho + m_1 + \varepsilon_1 \end{aligned} \tag{6.6}$$

where ρ_0 is an approximate value to the distance term ρ_{AB}^{ij}; a_1, a_2, a_3 are three geometric constants and $\Delta\mathrm{N}, \Delta\mathrm{E}, \Delta\mathrm{H}$ are the three components (North, East, Height) of the positioning error.

In our study, GPS permanent stations will play the role of both reference (A) and user (B) stations; their position is thus known with a millimeter accuracy. Since the "nominal" RTK accuracy is usually the order of 1 cm for each component, we will further consider that the position of the permanent stations is perfectly known and we will refer to it as the "true" position of the station. As a consequence, ρ_0 is a known quantity, as well as the ambiguity N_1, the ionospheric term I_1 and the PCV term. In equation (6.6), the known parameters figure therefore on the left side (except for I_1) while the three unknowns and the unmodeled parameters figure on the right side. The positioning error $(\Delta\mathrm{N}, \Delta\mathrm{E}, \Delta\mathrm{H})$ computed based on (6.6) will reflect the influence of the unmodeled parameters, which are not only the ionospheric effect but also the troposphere, orbit error, multipath and noise. As our study aims at assessing the positioning error due to the ionosphere only, the formulation of the observation equation has been quite simplified. The vector of observations implemented in SoDIPE-RTK corresponds to the single ionospheric term, while matrix A contains the aforementioned geometric constants a_i. If there are n visible satellites, the system of $(n-1)$ observation equations takes therefore the following form:

$$\underline{l} = -\underline{I}_{AB,1}^{ij} \qquad \Rightarrow \qquad \begin{pmatrix} I_{AB,1}^{12} \\ I_{AB,1}^{13} \\ \vdots \\ I_{AB,1}^{1n} \end{pmatrix} = \begin{pmatrix} a_1^{12} & a_2^{12} & a_3^{12} \\ a_1^{13} & a_2^{13} & a_3^{13} \\ \vdots & \vdots & \vdots \\ a_1^{1n} & a_2^{1n} & a_3^{1n} \end{pmatrix} \begin{pmatrix} \Delta\mathrm{N} \\ \Delta\mathrm{E} \\ \Delta\mathrm{H} \end{pmatrix} \tag{6.7}$$

Considering equation (6.5), the positioning error resulting from the least-squares adjustment of (6.7), further referred to as the "positioning error", is, in this manner,

only affected by the ionospheric residual term and can be expressed for the three components North, East, Height (ΔN, ΔE, ΔH). We also computed the positioning error in terms of distance, corresponding to the error on the baseline measurement: $\Delta B = \sqrt{\Delta N^2 + \Delta E^2 + \Delta H^2}$. Let us draw the reader's attention on the fact that the positioning error computed by SoDIPE-RTK does not reflect the potential troubles that could occur in a real-time ambiguity resolution process due to the presence of enhanced ionospheric variability. Indeed, let us recall that L_1 and L_2 ambiguities are assumed to be fixed to their true integer value. As a consequence, the real-time positioning error experienced by users in the field can widely exceed the values presented in the frame of this work. More details about the algorithms used in SoDIPE-RTK software can be found in Lejeune [58].

6.1.2 Validation of the method

In the previous section, the influence of the multipath error on I_{AB}^{ij} computation has been neglected; it is therefore needed to assess its contribution to confirm the ionospheric origin of the positioning error. In the case of quiet ionospheric conditions, one can expect that multipath is the main remaining error source (except for noise) in the $I_{AB,1}^{ij}$ term used in SoDIPE-RTK computations. As a consequence, let us try to detect a day-to-day correlation in $I_{AB,1}^{ij}$ time series by applying shifts of about 4 minutes between consecutive days. We considered 113 baselines belonging to the Belgian Dense Network (BDN)[6] and two days characterized by very quiet ionospheric conditions (*i.e.* the absence of ionospheric irregularities and low background TEC values): Day Of Year (DOY) 233 and 234/08[7]. For each baseline, we have computed the correlation coefficient (r) between $I_{AB,1}^{ij}$ time series, considering similar satellite pairs and corresponding epochs. Results are illustrated in figure 6.1, where r is expressed as a function of baseline length.
The square of the correlation coefficient, r^2, can be considered as a measure of the part of the total variance of $I_{AB,1}^{ij}$ "explained" by a similar day-to-day behavior. Assuming that the residual ionospheric term is very close to zero because of the small TEC values and the absence of irregularities, one can estimate that such a day-to-day behavior corresponds to the signature of multipath. The analysis of figure 6.1 shows that the correlation level is rather different from a baseline to another, with r values ranging from 0.1 to 0.65, meaning that multipath can explain from 1 to about 42% of the total variance. As pointed out by the regression line, the correlation seems to depend on baseline length, the largest values being observed for the shortest baselines. This could be explained by the increase of the residual ionospheric term with baseline length, due to the a larger spatial decorrelation for larger baselines. However, let us point out the large discrepancies between baselines of similar length.

[6]The BDN will be presented in details in the next section.
[7]Vertical TEC (VTEC) did not exceed 8 and 9 TEC Unit (TECU) on DOY 233 and 234, respectively.

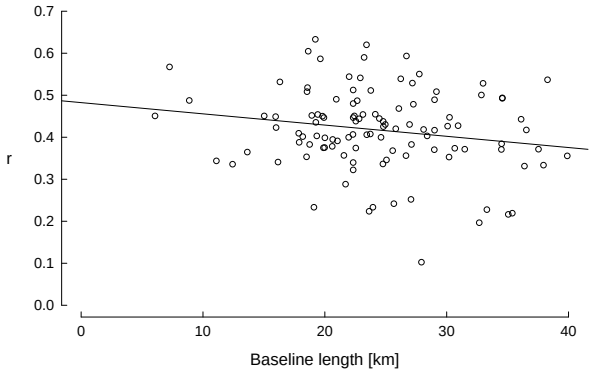

Figure 6.1 – Correlation coefficient r between $I^{ij}_{AB,1}$ time series corresponding to two consecutive days (DOY 233 and 234 in 2008), for 113 baselines belonging to the Belgian Dense Network (BDN). A shift of 4 min/day has been applied to take into account the difference between the solar day and the sidereal day.

As an example, r is ranging from 0.2 to 0.65 for a ∼20 km baseline. It is believed that such disagreement is due to the large variability of environments surrounding the different observation stations. Indeed, let us recall that multipath is a local effect which is enhanced by the presence of trees, walls or other reflecting surfaces around the antenna.

Therefore, the influence of multipath in $I^{ij}_{AB,1}$ term is non negligible in the case of very quiet ionospheric conditions, as expected. However, it does not constitute the major contribution as multipath could explain less than ∼40% of the total variance contained in a $I^{ij}_{AB,1}$ time series. The remaining variability is therefore due either to the measurement noise or to unmodeled effects whose magnitude could depend on baseline length and which are not correlated from day-to-day. This latter statement will be investigated in section 6.2.1.

Independently of DD accuracy, another effect influencing the positioning error accuracy is the geometry of the GPS constellation. Indeed, poor geometric conditions induce large positioning errors, even if the accuracy of all DDs is acceptable. In absolute positioning, the effect of the constellation is easily translated by the Dilution Of Precision (DOP) parameter[8], which acts as an "amplifier" of the variance related to one-way measurements:

$$\sigma_{\text{pos}} = \text{DOP}\ \sigma_{\text{obs}} \tag{6.8}$$

[8]For the sake of completeness, it is worth mentioning that DOP is a generic term expressing the geometric contribution to the total error budget on the computed position. For 3-D absolute positioning, the exact term to be considered in equation (6.8) is the Positioning DOP (PDOP), which considers the geometric influence in the three dimensions.

with σ_{pos} the absolute positioning error (standard deviation) and σ_{obs} the accuracy of a one-way measurement. In relative positioning, an equation similar to (6.8) can be written, expressing the error on the relative positioning error $\sigma_{\Delta \text{i}}$ (i being either the E, N or H component) as a function of a geometric parameter denoted Relative DOP (RDOP) and of the accuracy on DD measurements σ_{DD}:

$$\sigma_{\Delta \text{i}} = \text{RDOP}\ \sigma_{\text{DD}} \tag{6.9}$$

Similarly to DOP parameter for absolute positioning, RDOP characterizes the quality of geometric conditions in the case of relative positioning. RDOP can be computed based on equation (6.5), since it corresponds to the trace of the cofactor matrix $Q = N^{-1} = (A^T P A)^{-1}$:

$$\text{RDOP} = \text{tr}(Q) = \text{tr}\left((A^T P A)^{-1}\right) \tag{6.10}$$

Considering short baselines (less than 50 km), it has been demonstrated that RDOP and DOP at the rover station are closely correlated [61]. This is illustrated in figure 6.2 depicting the positioning error ΔB as a function of GPS time, together with RDOP and DOP at the rover station. One can observe that peaks in ΔB correspond to periods where both RDOP and DOP are large, due to poor geometric conditions. RDOP and DOP curves are varying together, and it can be demonstrated that, for RTK baselines used in the frame of this thesis, the correlation between these two indicators is very close to 1.

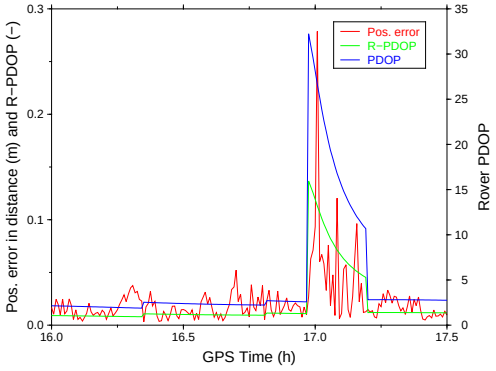

Figure 6.2 – Peaks in positioning error ΔB are closely correlated to large (R)DOP values. Data are related to GILL-LEEU baseline (11 km), for DOY 309/08.

In figure 6.3(a), there is evidence for the geometric origin of some peaks in positioning, as their occurrence is lagged by about 4 min/day. Because such peaks are not reflecting the ionospheric activity – the analyzed period corresponds to a very quiet ionospheric activity period – they have to be removed from the dataset using a

threshold value of either DOP or RDOP, both indicators being perfectly correlated. Even if RDOP seems to be the more appropriate indicator (we are dealing with relative measurements), its main drawback lies in the fact that its value depends on the weight matrix, as shown in equation (6.10)[9]. Therefore, all periods exhibiting a DOP value larger than 5 have been removed from the dataset to filter out geometric outliers[10]. Results of such filtering is shown in figure 6.3(b) where cleaned time series are displayed.

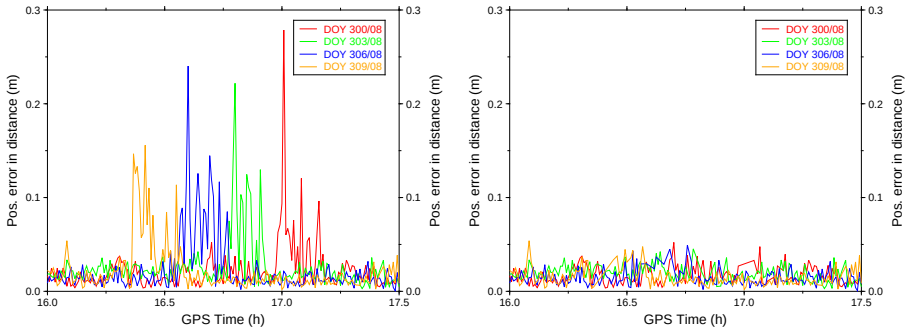

Figure 6.3 – Geometry-originated peaks appearing in ΔB (a) are filtered out by applying a DOP filter (b). Data are related to DOY 300, 303, 306 and 309/08 for baseline GILL-LEEU (11.3 km).

Finally, one can conclude that the ionospheric positioning error computed by SoDIPE-RTK software reflects the true ionospheric conditions in the case of relative positioning.

6.1.3 Dataset

The aim of this chapter is to analyze and assess the effect of ionospheric irregularities on relative positioning. In the previous section, it was suggested that baseline length would influence the $I^{ij}_{AB,1}$ term, and thus the positioning error. Indeed, the residual ionospheric term is directly proportional to the spatial decorrelation of the TEC which depends on the distance between the two stations. In the same manner, it is also believed that baseline orientation might influence the positioning error in the case of irregularities, as these latter are responsible for anisotropic TEC patterns. For example, TEC gradients observed during the occurrence of daytime

[9]The weight matrix depends on the number of DD in view at the given epoch, which implies that RDOP is varying with time.

[10]In absolute positioning, the user generally applies a DOP threshold of 5 to filter out poor geometric conditions.

MSTIDs are propagating along the magnetic meridians, which leads to a clear spatial heterogeneity of the ionospheric plasma. Therefore, the influence of both baseline length and orientation on the ionospheric positioning error will be assessed in the frame of this section.
As such a study needs a large range of baseline lengths and orientations, we decided to run SoDIPE-RTK software on the Belgian network of CORS stations, denoted BDN. This latter is made up of 66 GPS (dual-frequency) stations belonging to three different institutions: FLEPOS (Flemish part, 40 stations), WALCORS (Walloon part, 23 stations) and the Royal Observatory of Belgium, ROB (3 stations). The commissioning of these networks has not been synchronous since FLEPOS started in October 2002, WALCORS in September 2003 while the ROB stations were already operational in the 90's.
Since we are dealing with relative positioning, we have to form baselines between these 66 receivers. A common approach in selecting the baselines is the Delaunay triangulation [38]. In RTK networks designed for the use of VRS or FKP techniques, rover and reference stations are not separated by more than 25–30 km. In our study, we decided to select all baselines less than 40 km. The total number of baselines created by the Delaunay triangulation which are less than 40 km is 161 (figure 6.4). Mean baseline length in the BDN is 24.7 km while 95% of the baselines are less than 36.1 km. There is a slight difference in density between the two sub-networks FLEPOS and WALCORS, with a mean baseline length of 23.5 km and 28.7 km, respectively. In order to identify the effects of ionospheric irregularities on relative positioning, three particular days were analyzed in detail, based on their typical ionospheric conditions.

DOY 359/04: a typical MSTID On December 24, 2004 (DOY 359/04), a medium-amplitude MSTID has been detected between 0900 and 1500 UT in RoTEC time series. Maximal RoTEC value was about 0.8 TECU/min around noon at BRUS station. As MSTIDs are generally not linked to geomagnetic activity, geomagnetic indices displayed in figure 6.5(a) show, as expected, very quiet conditions: $\mathrm{Kp}_{\max} = 2$ and Disturbance Storm Time $(\mathrm{DST})_{\min} = -26$ nT. Background VTEC for DOY 359/04 is also quiet, with a maximum of about 10 TECU, which corresponds to solar quiet conditions (monthly sunspot number Rd = 17.9). As pointed out by the "RTK intensity" index[11], the MSTID occurred mostly between 0900 and 1500 UT, so that we will only consider this time interval in further computations.

DOY 324/03: a powerful geomagnetic storm On November 20, 2003 (DOY 324/03), a huge Coronal Mass Ejection (CME) coming from a giant sunspot group hit the Earth's magnetosphere, which led to a severe geomagnetic storm,

[11] The RTK intensity index is an hourly index developed in Warnant and Pottiaux [99] to monitor ionospheric irregularities at a single GPS station. It depends on the number and on the amplitude of ionospheric irregularities, which are based on σ_{RoTEC} measurements performed every 15 min.

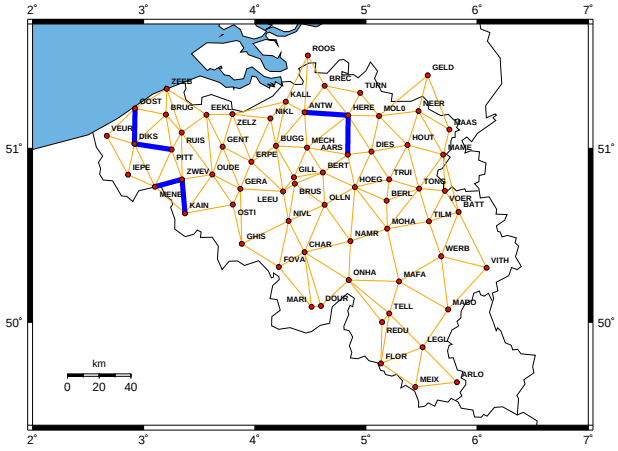

Figure 6.4 – The Belgian Dense Network (BDN), with baselines selected for the baseline orientation analysis (in blue).

as shown in figure 6.5(b). It was one of the most powerful geomagnetic storm ever observed since the commissioning of the GPS system. Indeed, DST values reached -422 nT around 2000 UT while Kp index was 8.7 during 6 hours. The ionospheric background of DOY 324/03 was relatively high, due to the large value of the sunspot number (Rd = 67.3) but also to the positive phase of the ionospheric storm beginning in the early morning hours. Indeed, a maximum of about 50 TECU was observed around noon, which represents an increase of 150% of the VTEC background comparing with the previous day. A secondary maximum of about 30 TECU was also observed around 2000 UT, in phase with the large increase of RTK intensity index and with the increasing geomagnetic activity. Maximum RoTEC value at BRUS stations was about 9 TECU/min at 1900 UT.

Since the effects of the geomagnetic storm become very large from 1500 UT – see RTK intensity values in figure 6.5(b) – we will only consider the data relative to the time interval [1500 – 2400 UT] in further computations.

DOY 310/08: a quiet day Finally, we selected November 5, 2008 (DOY 310/08) as the quiet reference day. This day is characterized by a quiet VTEC background (less than 10 TECU) and quiet geomagnetic activity (Kp values of 0.3), as shown in figure 6.5(c). Furthermore, almost no ionospheric event was detected by the single-station method. DOY 310/08 is therefore considered as representative of a quiet and regular ionosphere.

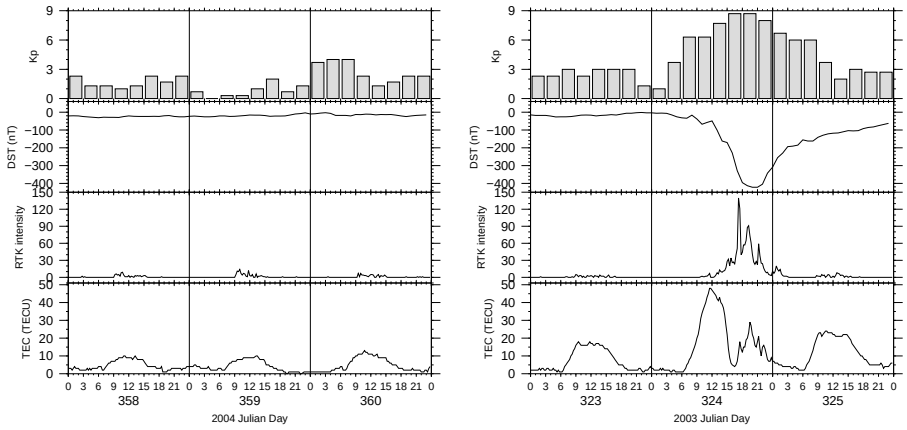

(a) (b)

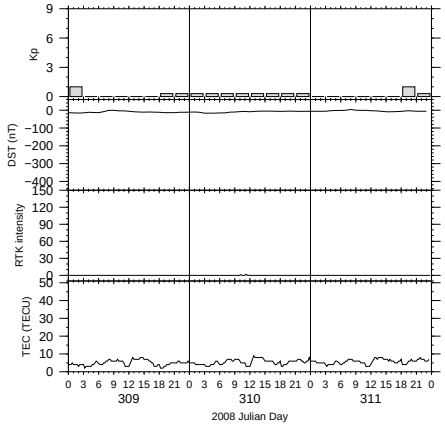

(c)

Figure 6.5 – Geomagnetic and ionospheric indices for the three typical cases. DOY 359/04 corresponds to a winter daytime MSTID, 324/03 to a powerful geomagnetic storm while 310/08 constitutes the quiet reference day. "RTK intensity" corresponds to an ionospheric activity index developed in Warnant and Pottiaux [99] and characterizing the number and the amplitude of ionospheric irregularities at a single GPS station.

6.2 Ionospheric irregularities and relative positioning

In order to assess the ionospheric effects on positioning error under disturbed conditions, it is crucial to have a reference dataset where positioning errors correspond to quiet ionospheric conditions. As a first step, this section thus provides the results related to nominal accuracy within the BDN. Next, we focus on the effects of ionospheric irregularities on positioning.

6.2.1 BDN nominal conditions

Quiet ionospheric conditions will be used to validate the SoDIPE-RTK algorithm and to decide when non-nominal conditions occur. Moreover, it will allow to answer two questions: (1) is the influence of residual ionosphere still negligible when increasing the baseline length and (2) is there a maximum usable length?
We compute all BDN baselines to extract the ionospheric residual term on DD and the positioning error (ΔN, ΔE, ΔH and ΔB). All baselines containing residual cycle slips, data gaps, and outliers have been manually filtered out from the dataset. For example, the number of appropriate baselines dropped from 146 to 131 for the quiet reference day 310/08. This means that about 10% of the baselines underwent problems and were therefore removed from the results. Next, the daily average ($\bar{x}$) and standard deviation (σ) are computed for each component (and for ΔB) and for each baseline (figure 6.6). Since the sampling rate is 30 s, the number of observations for each baseline is 2880.
The relationship between $\bar{x}$ or σ and the baseline length are investigated with linear regressions. Baseline length being known with a millimeter accuracy, we assume that there is no error on this parameter so that it can be considered as the independent variable. On the contrary, $\bar{x}$ and σ values cannot be considered as perfect measurements, which implies that linear regression on both variables will be computed with a weighted least-squares fit[12]. The slopes of regression lines relative to $\bar{x}$ (figure 6.6) are very close to zero for ΔN, ΔE and ΔH while that of ΔB seems to be positive. Confirmation of these assumptions is achieved by statistical tests on linear regressions. These tests have been performed for a significance level $\alpha = 0.1\%$ and confirm our hypotheses: ΔN, ΔE and ΔH slopes are statistically null, while the one related to ΔB is not. A similar analysis has been performed for the slopes related to σ values (figure 6.6); the statistical tests prove that they are all significantly positive. Therefore, one can summarize the results as follows: for the three components, $\bar{x}$ does not increase with baseline length, while σ does. In other words, residual ionosphere in DD results in a larger variability on positioning error, but

[12]In a weighted least-squares algorithm, the weight of the observations is inversely proportional to the variance of observations.

does not induce any bias. This conclusion is not valid for ΔB for which a positive trend with baseline length has been found for both $\bar{x}$ and σ.

In the previous section, we concluded that multipath was not the major error source on the positioning error, even during quiet ionospheric conditions. This assumption can also be confirmed using results displayed in figure 6.6. Indeed, if multipath would constitute the major part of the positioning error, the standard deviation σ would remain constant with baseline length, as multipath is not spatially correlated. On the contrary, we have statistically demonstrated that σ was increasing with baseline length for each component. As a consequence, it strongly suggests that regression slopes are due to the ionosphere, and more particularly to the spatial decorrelation increasing with baseline length. However, let us point out that multipath constitutes a realistic explanation of the variability observed between similar baseline lengths during quiet conditions, as already suggested.

From a numerical point of view, one can see that the slope related to σ is 0.2 mm/km (or 0.2 ppm) for ΔE and ΔN, whereas it reaches 0.4 ppm for ΔH. For the quantity ΔB, the value of σ equals 0.2 ppm, which is half the value of ΔH. This is easily explained by the fact that all ΔB values are always positive. Therefore, one can say that ΔB is not really representative of the effects on each component, but constitutes a synthetic index to quantify and compare the different trends and effects. Considering that the typical accuracy for real-time relative positioning is of the order of 1 cm for each component, we can see that this limit is reached for a 50 km baseline in both ΔN and ΔE components (2-D positioning) and for a 25 km baseline for ΔH component (3-D positioning). This means that, considering a cm-level accuracy, the influence of the ionosphere can be neglected during quiet conditions if the baseline length does not exceed 25 km. 25 km can therefore be considered as the maximum usable length for relative positioning, while assuming $\sigma = 1$ cm on each component. More precisely, this means that about 67% of the measurements are within the interval $[\bar{x} \pm \sigma]$. If the cm-level accuracy has to be achieved in 95% of cases, one has to extend the interval to $[\bar{x} \pm 1.96\sigma]$. In this latter case, the maximum baseline length has to be reduced by a factor 2. This means that, considering $\sigma = 1$ cm for all components in 95% of cases, the maximum usable length for 3-D positioning is about 13 km. These results complete the validation of the methodology. Indeed, σ values and the maximum usable length are of the same order of magnitude that those generally admitted for relative positioning technique.

6.2.2 Effect of baseline length

In the previous section, we have seen that positioning error depends on baseline length, even during quiet ionospheric activity periods. Using the same methodology than for DOY 310/08, we propose to study this influence during two disturbed periods previously identified: [0900–1500 UT] for DOY 359/04 (MSTID) and [1500–2400 UT] for DOY 324/03 (geomagnetic storm).

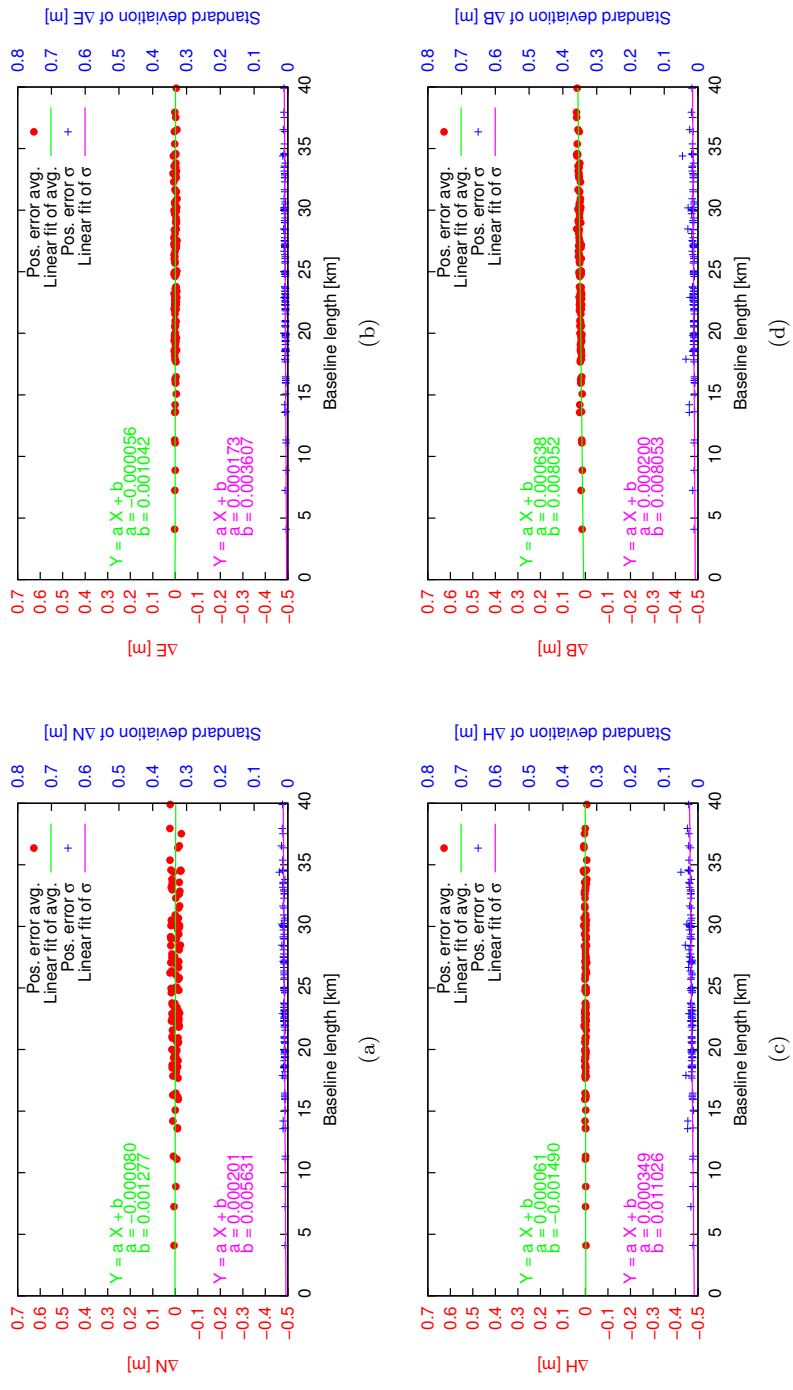

Figure 6.6 – Average ($\bar{x}$) and standard deviation (σ) of the positioning error as a function of baseline length for DOY 310/08. The three components (a) North, (b) East, (c) Height as well as (d) the positioning error in terms of distance are respectively denoted ΔN, ΔE, ΔH and ΔB.

DOY 359/04 As for quiet conditions, a statistical analysis of regression slopes related to $\bar{x}$ values shows that they do not differ significantly from zero, except for ΔB which exhibits a non-null slope (figure 6.7). However, it is worth noting that, considering a given baseline length, residuals of the regression are generally larger during the MSTID occurrence than during the quiet reference day. Such an increase in variability around the regression line, not linked with the baseline length, can be understood as an effect of baseline orientation. This hypothesis will be verified in the next section.

Concerning σ values, we can observe and confirm statistically that the variability increases with baseline length for all components, including ΔB. From a numerical point of view, residual ionospheric error is responsible for $\sigma = 1.5$ ppm for ΔN, 1 ppm for ΔE, 2.5 ppm for ΔH, and 1.5 ppm for ΔB. Once again, the largest value corresponds to the Height component, while the smallest one is the East component. Under such circumstances, the cm-level accuracy is reached for a baseline not longer than 4 km, considering a 3-D positioning with a 67% confidence interval. If $\sigma = 1$ cm has to be achieved in 95% of cases, the maximum usable length in this context drops to 2 km.

DOY 324/03 The analysis of figure 6.8 leads to similar conclusions, namely (1) an increasing variability with the baseline length and (2) the absence of bias for the average positioning error in ΔN, ΔE and ΔH. Nevertheless, residuals are much larger during the geomagnetic storm than during the MSTID and the quiet reference day. Numerical values of the variability on positioning error are 3.5, 2.5, 6.5, and 5.5 ppm, respectively for ΔN, ΔE, ΔH, and ΔB. On this basis, the maximum baseline length for a cm-level accuracy in 67% of cases is less than 2 km. This value drops to about 1 km considering a 95% confidence interval. Again, let us point out the large discrepancies in $\bar{x}$ and σ values between baselines of similar length. As already stated, this suggests that baseline orientation also influences the ionospheric positioning error, which will be examined in the next section.

6.2.3 Effect of baseline orientation

The analysis of the effect of baseline orientation on positioning error will be achieved using polar plots. For each selected day, they depict σ of ΔB component ($\sigma_{\Delta B}$) as a function of baseline azimuth (figure 6.9). Since the aim is to compare all baselines with each other, it is necessary to eliminate the length effect. Therefore, $\sigma_{\Delta B}$ has been normalized by the baseline length. As for the previous section, polar plots contain all cleaned BDN baselines, with no gap nor residual cycle slip. Analysis of figure 6.9 shows that, for DOY 310/08, $\sigma_{\Delta B}$ values are, for each baseline, rather low and the polar plot shape is almost isotropic. On the contrary, $\sigma_{\Delta B}$ values related to DOY 359/04 exhibit a dependence on baseline orientation. Indeed, the polar plot

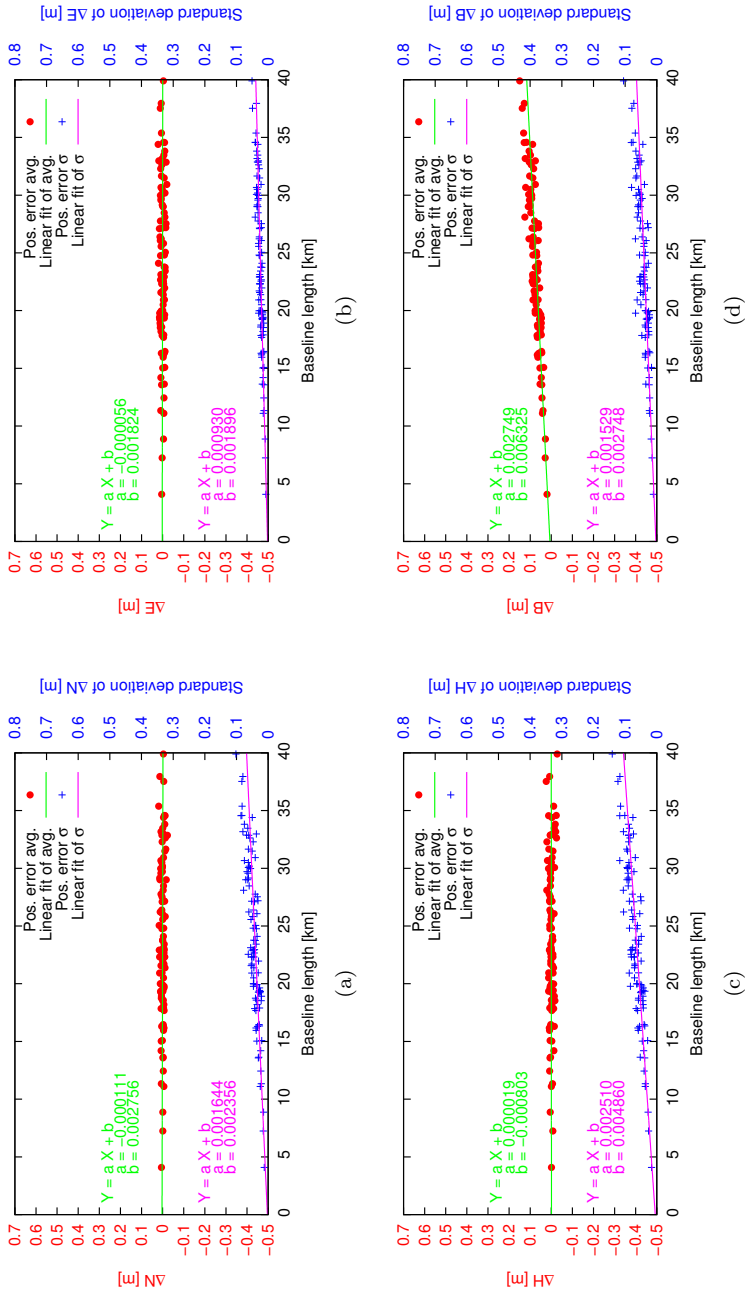

Figure 6.7 – Similar to figure 6.6 but for DOY 359/04.

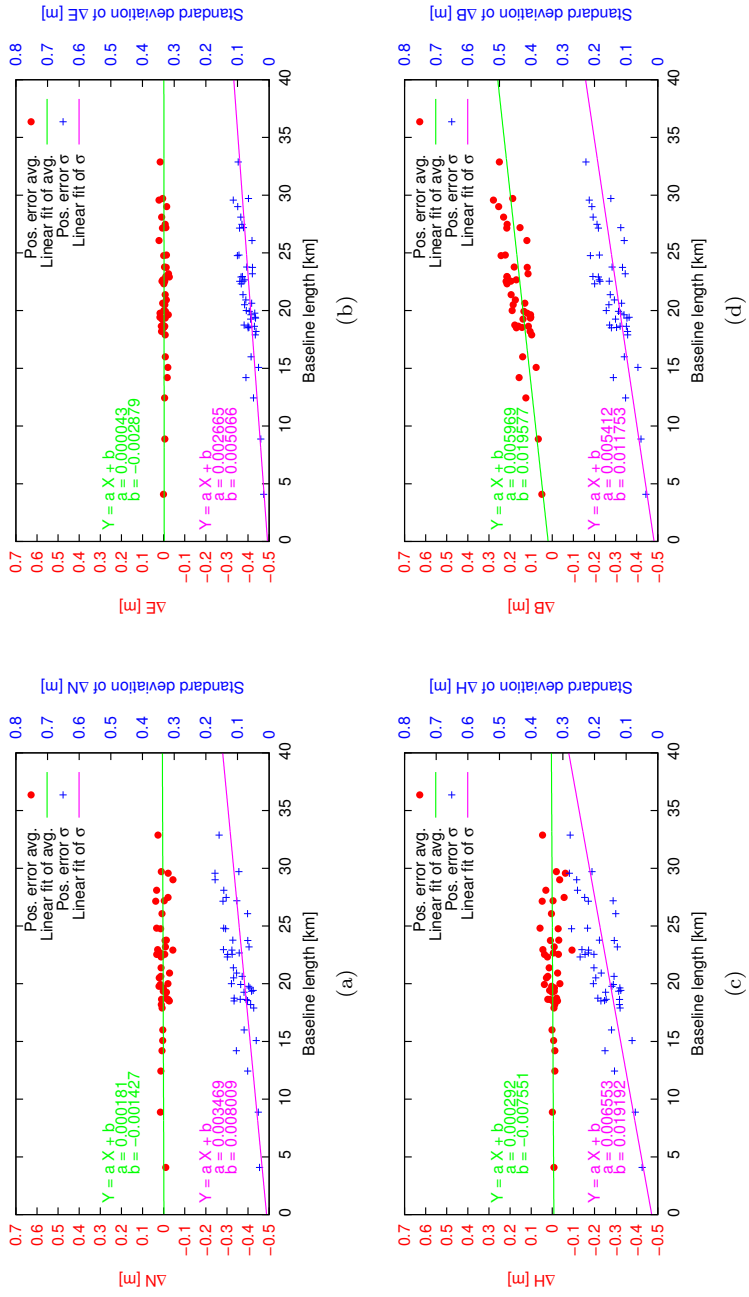

Figure 6.8 – Similar to figure 6.6 but for DOY 324/03.

shape presents a preferential north–south orientation: this direction is generally affected by errors larger than for baselines oriented west–east. This orientation effect is also clearly visible for DOY 324/03, with σ values larger than during the occurrence of the MSTID. In the case of the MSTID, one can observe that the MSTID is responsible for positioning errors 30 to 50% larger in the north–south direction than in the west–east direction. The sharp TEC gradients due to the geomagnetic storm of DOY 324/03 induced similar differences between the most and the less affected baselines.

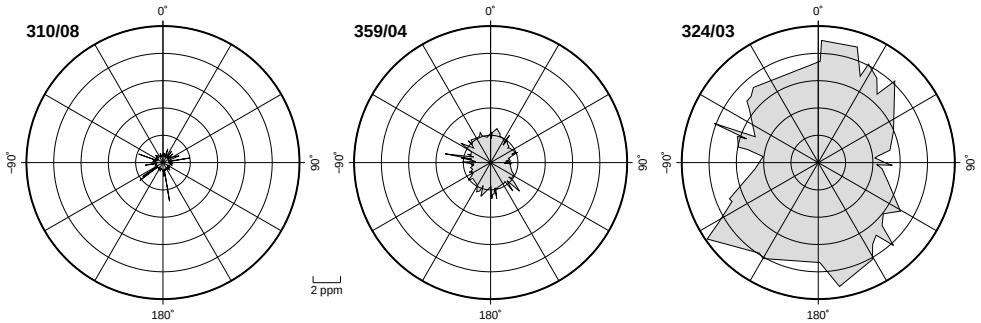

Figure 6.9 – $\sigma_{\Delta B}$ normalized by the baseline length for DOY 310/08 (0000–2400 UT), DOY 359/04 (0900–1500 UT), and DOY 324/03 (1500–2400 UT), considering all BDN baselines. Values are expressed in ppm.

To complete the analysis of polar plots, some specific cases will also be investigated. Three pairs of baselines sharing one common station were chosen to form small sub-networks (figure 6.4). These pairs are roughly characterized by the same length, but have different orientation, which have been chosen north–south and east–west. They are: (a) AARS–HERE (25 km) and ANTW–HERE (28 km), (b) DIKS–OOST (22 km) and DIKS–PITT (24 km), and (c) KAIN–ZWEV (22 km) and MENE–ZWEV (18 km), respectively. These baselines form a set of triangles required in the computation of the I_{95} index[13], allowing a direct comparison with the results of SoDIPE-RTK. Maximum (MAX) and σ values of positioning error related to these triangles of stations are given in table 6.1.

DOY 310/08 Table 6.1 shows that σ varies between 0.006 m and 0.021 m, depending on the considered component. As already seen, the East component presents the lowest values, while the Height component shows the largest. No clear effects of baseline orientation can be found since σ differences between baselines are the same order of magnitude than measurement noise. In conclusion, one cannot state that there is any effect of baseline orientation on

[13]The I_{95} index is an ionospheric activity index developed by Wanninger [97] whose computation relies on a triangle of stations. Additional information will be given in the next section.

Baseline	Dist [km]	Day	Period [UT]	North [m]		East [m]		Height [m]		Distance [m]	
				SD	MAX	SD	MAX	SD	MAX	SD	MAX
AARS - HERE	24.8	310/08	0000–2400	0.012	0.033	0.008	0.025	0.020	0.084	0.013	0.104
N-S		359/04	0900–1500	0.047	0.114	0.029	0.071	0.086	0.268	0.054	0.278
		324/03	1500–2400	0.143	0.686	0.095	0.552	0.221	1.936	0.184	2.069
ANTW - HERE	27.5	310/08	0000–2400	0.013	0.048	0.009	0.021	0.021	0.079	0.014	0.100
W-E		359/04	0900–1500	0.034	0.116	0.021	0.034	0.051	0.139	0.029	0.160
DIKS - OOST	22.3	310/08	0000–2400	0.010	0.030	0.007	0.030	0.019	0.085	0.012	0.124
N-S		359/04	0900–1500	0.046	0.128	0.027	0.075	0.071	0.199	0.042	0.251
		324/03	1500–2400	0.136	0.864	0.083	0.497	0.239	1.809	0.199	2.061
DIKS - PITT	23.7	310/08	0000–2400	0.010	0.052	0.007	0.035	0.021	0.150	0.016	0.159
W-E		359/04	0900–1500	0.041	0.142	0.019	0.047	0.057	0.185	0.034	0.195
		324/03	1500–2400	0.067	0.389	0.053	0.186	0.142	0.914	0.115	1.303
KAIN - ZWEV	21.7	310/08	0000–2400	0.011	0.035	0.009	0.66	0.020	0.129	0.017	0.137
N-S		359/04	0900–1500	0.051	0.176	0.028	0.069	0.069	0.228	0.040	0.236
MENE - ZWEV	17.9	310/08	0000–2400	0.008	0.033	0.006	0.019	0.015	0.093	0.009	0.094
W-E		359/04	0900–1500	0.027	0.066	0.016	0.034	0.042	0.111	0.025	0.152
		324/03	1500–2400	0.048	0.299	0.042	0.146	0.121	0.769	0.096	0.830

Table 6.1 – σ (SD) and maximum (MAX) values of the ionospheric positioning error for the selected baselines (see figure 6.4).

positioning error for this reference day.

DOY 359/04 The σ values are at least two times larger than for DOY 310/08 (table 6.1). Moreover, they confirm the influence of baseline orientation previously observed in the polar plots. Indeed, the σ and MAX values for baselines with a north–south orientation (*i.e.* AARS–HERE, DIKS–OOST and KAIN–ZWEV) are, for each component, larger than those related to other baselines with an west–east orientation. These numerical observations are also presented for AARS–HERE and ANTW–HERE in figure 6.10(a), where one can observe that, even though the error values are similar during most of the day, it is not the case during the MSTID occurrence (0900–1500 UT). Indeed, a maximum value of 0.278 m is observed for AARS–HERE (north–south orientation) while ANTW–HERE baseline reaches simultaneously a maximum value of 0.160 m. Since the difference cannot be attributed to the length difference of 2.7 km between the two baselines, it is suggested that such effect is due to the direction of propagation of the MSTID. In theory, a planar wave propagating in a given direction induces a smaller TEC gradient for a baseline oriented parallel to the wave front than for a perpendicular one. Since winter daytime MSTIDs propagate mostly southwards or southeastwards, one can therefore assume that baselines with east–west orientation would experience smaller errors than north–south ones. The analysis of RoTEC at the aforementioned stations confirms our hypothesis (figure 6.11). One can observe that RoTEC is generally in phase for stations ANTW and HERE constituting the baseline with the smallest positioning error values. On the contrary, RoTEC is lagged between AARS and HERE stations, which proves that the wave vector (direction of propagation) is oriented southwards. As MSTIDs are moving structures, TEC rate of change corresponds to TEC gradients which affect the relative positioning algorithm by introducing a larger ionospheric residual term (STEC_{AB}^{ij}) for baselines oriented parallel to the wave vector. Therefore, one can reasonably admit that differences in positioning error between the analyzed baselines are explained by their difference in azimuth.

DOY 324/03 Table 6.1 and figure 6.10(b) confirm the results related to the polar plot analysis: baselines oriented north–south (e.g. DIKS–OOST) present larger σ and MAX values than those oriented east–west (e.g. DIKS–PITT), with peaks larger than 2 m. As explained previously, north–south orientation coincides with the preferential orientation of ionospheric walls observed during geomagnetic storms [27, 89]. These walls, whose signature can be found in the positive phase of the ionospheric storm occurring between 1700 and 2400 UT (figure 6.8), correspond to the passage of patches of higher ionization propagating equatorwards. However, the signature of TEC walls cannot be easily derived from RoTEC time series as it was the case for MSTIDs. Indeed, let us recall that RoTEC monitors high-frequency changes in TEC by filtering out all smooth behaviors. As a consequence, a part of the ionospheric increase in

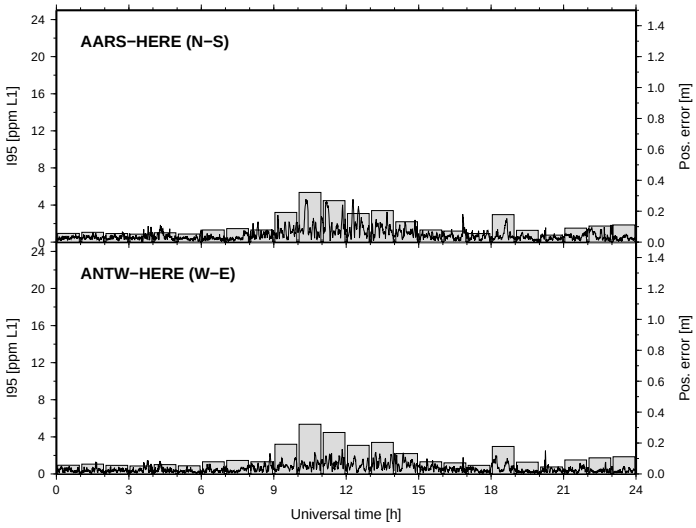

(a)

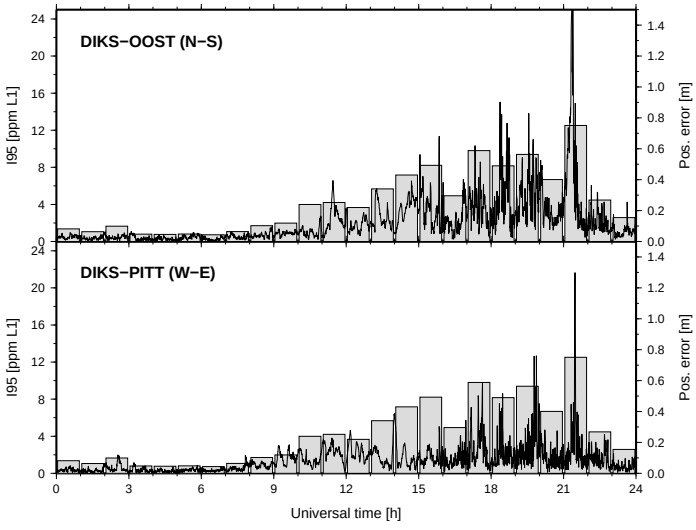

(b)

Figure 6.10 – I_{95}-index (grey boxes) and ΔB during the occurrence of (a) an MSTID (DOY 359/04) and (b) a geomagnetic storm (DOY 324/03).

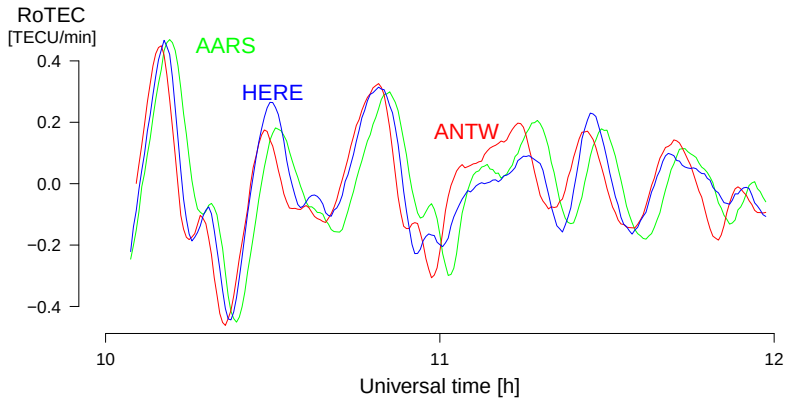

(a)

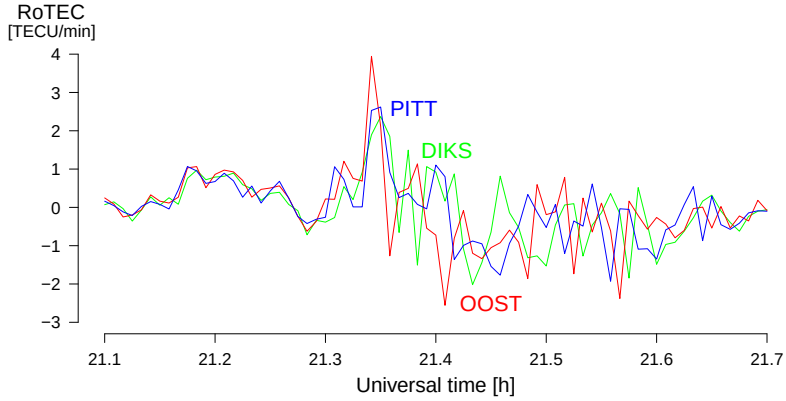

(b)

Figure 6.11 – Time series related to (a) the MSTID of DOY 359/04 (3 min running average) for stations AARS, ANTW, and HERE, PRN 17 and (b) the geomagnetic storm of DOY 324/03 for stations DIKS, PITT and OOST, PRN 31.

TEC would not be detected in RoTEC, as mentioned in section 4.1.3. This is illustrated in figure 6.11(b) where a good agreement between the three stations PITT, DIKS and OOST can be found. Even if the variability is very large for each station, one cannot deduce a time lag typical of an ionospheric wall.

6.2.4 Comparing with I_{95} index

Figures 6.10(a) and 6.10(b) give, in addition to ΔB, the I_{95} index values developed by Wanninger [97]. This index, expressed in ppm on L_1, merges into a single number all the ionospheric residual terms I^{ij}_{AB,L_1} related to DDs in view within a triangle of

GPS permanent stations. This value, valid for all stations located inside the triangle, gives therefore not only the same value for the two baselines – figures 6.10(a) or 6.10(b) – but also for any other baseline located within the considered triangle. On the contrary, SoDIPE-RTK computes positioning errors for each baseline, revealing the effect of baseline orientation. Indeed, despite a general agreement between the two quantities during disturbed conditions, the direction of propagation of ionospheric gradients cannot be retrieved with the I_{95} index. In addition, SoDIPE-RTK offers a better temporal resolution: I_{95} index values are obtained on a hourly basis while $I^{ij}_{AB,k}$ and the positioning error are computed every 30 s. Therefore, SoDIPE-RTK does not only constitute an interesting alternative to I_{95} index, but also offers a better spatial and temporal resolution allowing to derive propagation direction of ionospheric irregularities.

6.3 Correlating RoTEC with the ionospheric positioning error

The detection of ionospheric irregularities with GPS has been detailed in chapter 4. The method, which relies on GPS measurements performed at a single station and further referred to as "single-station measurements"[14], allowed to derive a climatological study of such irregularities. Their effect on relative positioning has been carefully analyzed in the frame of this chapter. In this context, a question arises: are the ionospheric irregularities detected based on σ_{RoTEC} correlated with the ionospheric positioning error given by SoDIPE-RTK?
Below is the methodology used to correlate single-station measurements and the ionospheric positioning error.

1. To ensure that all irregularity types are included in our statistics, it was decided to process a given baseline for a very long time interval, similarly to a climatological study. Thus, we have computed the ionospheric positioning error for a baseline with a typical length of 11.3 km. The GILL–LEEU baseline belongs to the FLEPOS network and GPS observations are available from May 4, 2003 (DOY 124/03) to December 31, 2008 (DOY 365/08). This time interval covers therefore periods of moderate to strong solar activity (2003 and 2004) as well as quiet conditions (solar minimum in 2008).

2. In section 6.1, it has been pointed out that geometric conditions amplify the ionospheric error observed in double differences (equation 6.9). As we are interested in ionospheric effects only, we have to make the positioning error independent of this effect. Here we propose to normalize the ΔB by the PDOP observed at the rover station; the result can therefore be understood as a

[14] Considering the related methodology, we will also refer to it as the "single-station method".

User Equivalent Range Error (UERE)[15], for which ionosphere is the main contributor. Let us remind that replacing the relative DOP by the absolute DOP is valid if the baseline is short [61], which is the case here. The ionospheric positioning error which will be used in the correlation study can therefore be expressed as follows:

$$\Delta B_{UERE} = \frac{\Delta B}{PDOP_{rov}} \tag{6.11}$$

3. At a single GPS station, ionospheric activity is detected using σ_{RoTEC} measurements, based on a 15 min time interval. ΔB_{UERE} measurements have thus been aggregated into the same interval. However, it exists several statistical parameters that describe a 15 min sample: location parameters (mean, median, quantile...) and dispersion parameters, mainly standard deviation or InterQuartile Range (IQR). Given the non-gaussian character of the sample distribution, it has been decided to consider the median for our computations. Nevertheless, the methodology can be transposed to other parameters without any loss of generality. Indeed, similar conclusions have been drawn while investigating other quantile values. The median of ΔB_{UERE} measurements within the 15 min time interval will be denoted $M_{\Delta B}$.

4. As mentioned above, the ionospheric activity computed by the single-station method is related to each satellite in view. All these observations have to be merged into a single activity index to be compared to the ionospheric positioning error. Therefore, it has been chosen to average all σ_{RoTEC} measurements related to the station of BRUS, for each 15 min time interval. The resulting variable will be denoted $\overline{\sigma_{RoTEC}}$, as for the climatological model developed in chapter 5.

5. The computation of statistical regression is achieved with a weighted least-squares algorithm, expressing that the error on ΔB measurements depends on ionospheric activity (see section 6.2). Weight values correspond to the inverse of the IQR related to the 15 min time interval.

Figure 6.12 displays the scatter plot and the corresponding regression line of $M_{\Delta B}$ on $\overline{\sigma_{RoTEC}}$. Correlation coefficient r equals 0.41, meaning that only 16% of the total variance is explained by the relationship between ionospheric irregularities and the relative positioning error. This relatively weak value of r results from the large spread in $M_{\Delta B}$, more particularly for $\overline{\sigma_{RoTEC}}$ values ranging from 0 to 0.05 TECU/min.

[15]The UERE term is used to designate the total error budget related to a single observation. In the case of absolute positioning, all error sources appearing in the observation equations (3.3) and (3.4) contribute to the UERE. From a mathematical point of view, the total UERE corresponds to the square root of the sum of the squares of the individual errors.

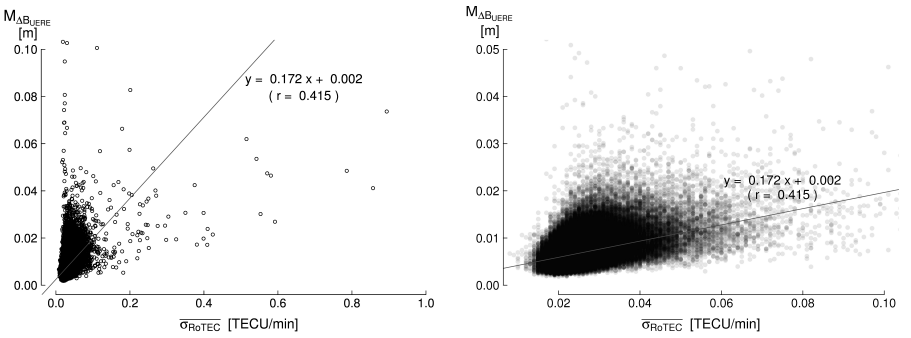

Figure 6.12 – Scatter plots of $\overline{\sigma_{\mathrm{RoTEC}}}$ and $\mathrm{M}_{\Delta\mathrm{B}}$ values and their associated regression line. (a) Original dataset (b) Zoom on the high density region.

The origin of these discrepancies is twofold. First, let us recall that relative positioning technique is sensitive to STEC differences between the four one-way measurements constituting the DDs. This residual term consists in spatial changes in TEC which, during undisturbed conditions (*i.e.* absence of irregularities), mainly consist in latitudinal and longitudinal TEC gradients. Those regular gradients are not observed in single-station measurements as the algorithm filters them out, by the use of the polynomial fit (see section 4.1). As a consequence, during periods of large TEC gradients, STEC_{AB}^{ij} term can be significantly large for one or several couples of satellites while the related $\overline{\sigma_{\mathrm{RoTEC}}}$ values remain very low.
Secondly, $\overline{\sigma_{\mathrm{RoTEC}}}$ is an averaged measurement, which merges ionospheric variability over all satellites in view. This effect has already been observed in chapter 5: the absolute level of $\overline{\sigma_{\mathrm{RoTEC}}}$ is by far smaller than that of a single σ_{RoTEC} value related to a given satellite. It comes that the effect of a single, isolated irregularity would be small on the $\overline{\sigma_{\mathrm{RoTEC}}}$ term, whereas its effect in positioning can be significant.
For these two aforementioned reasons, it is clear that the correlation between $\mathrm{M}_{\Delta\mathrm{B}}$ and $\overline{\sigma_{\mathrm{RoTEC}}}$ cannot be strong, as the two variables are aggregated and correspond to different aspects of the ionospheric error. The consideration of particular cases would be needed to improve the statistical significance of the results (see below).
Coming back to figure 6.12, one can observe that the slope value is about 0.17 while the intercept equals 2 mm, which seems underestimated in light of regression results performed in section 6.2, figures 6.6 to 6.8[16]. A solution consists in computing a

[16]Indeed, given the linear fit computed for quiet ionospheric conditions (figure 6.6), ΔB term for an 11.3 km baseline would be around 15 mm. Dividing this value by a mean PDOP value of 2.5, this lead to $\mathrm{M}_{\Delta\mathrm{B}_{\mathrm{UERE}}} \simeq 6$ mm. Therefore, it comes that the theoretical intercept, *i.e.* the $\mathrm{M}_{\Delta\mathrm{B}}$ value in the absence of ionospheric irregularity, should be three times larger than the value estimated by the least-squares adjustment.

DOY	type irreg.	r	slope
All	/	0.41	0.172
All (centered)	/	0.41	0.174
359/04 (centered)	WD	0.72	0.184
335/04 (centered)	WD	0.75	0.252
338/03 (centered)	WD	0.70	0.222
329/03 (centered)	WD	0.81	0.251
248/08 (centered)	SN	0.71	0.262
262/06 (centered)	SN	0.51	0.220
203/04 (centered)	SN	0.60	0.484

Table 6.2 – Results of linear regressions of $M_{\Delta B}$ on $\overline{\sigma_{RoTEC}}$ for specific days experiencing ionospheric irregularities. Types of irregularities analyzed are Winter Daytime (WD) and Summer Nighttime (SN).

new fit with the intercept fixed to zero, after applying a double translation to center the dataset. Coordinates of data centroid are the median of both $M_{\Delta B}$ and $\overline{\sigma_{RoTEC}}$ measurements, which corresponds to shifts of about -0.025 TECU/min for $\overline{\sigma_{RoTEC}}$ and -6 mm for $M_{\Delta B}$. Results of this second adjustment, together with those of the first one, are displayed in table 6.2, where similar slope values as well as no improvement of the significance level (r) between the two fitting procedures can be observed.

As suggested above, let us perform similar linear adjustments in the case of several quiet-time irregularities in order to deeply examine the slope value and the statistical significance (r). We analyzed four typical cases of Winter Daytime (WD) irregularities and three of Summer Nighttime (SN). These cases correspond to medium-amplitude irregularities: $\overline{\sigma_{RoTEC}}$ did not exceed 0.1 TECU/min for the strongest case while the weakest one is reponsible for values about 0.05 TECU/min. Results are given in table 6.2, where it comes that r is much larger than that related to the whole dataset. As an example, r related to DOY 329/03 slightly exceeds 0.8, meaning a highly significant correlation. Slope values are also larger than that of the whole dataset and range between 0.22 and 0.48, the largest value being observed during the SN irregularity of DOY 203/04.

As a conclusion, in spite of a mean positive slope of about 0.17, the analysis of specific irregularity cases tends to rise this value up to at least 0.25, with more statistical significance. However, it is important to stress that the aforementioned results are based on the analysis of a unique baseline oriented SW–NE. Considering another baseline purely oriented southwards, one could expect a larger slope value since bulk of irregularities observed over mid-latitudes are MSTIDs propagating equatorwards. Indeed, as baselines oriented parallel to the wave vector experience larger positioning errors, the $M_{\Delta B}$ term would be larger than that of GILL–LEEU baseline analyzed in the frame of this section. On the contrary, the slope value would be lower for a baseline oriented eastwards.

One should also point out that our results depend on the GPS station selected to compute $\overline{\sigma_{\mathrm{RoTEC}}}$ value (BRUS in this case). As mentioned in section 4.1.2 (figure 4.3), σ_{RoTEC} depends on the influence of multipath and noise effect, so that its level is varying with the considered station. As a result, to the same ionospheric conditions may correspond different $\overline{\sigma_{\mathrm{RoTEC}}}$ values, which leads to different slope/intercept couples. The results given in the frame of this chapter have therefore to be carefully considered.

6.4 Summary and perspectives

A study concerning the influence of ionospheric irregularities on relative positioning has been performed in this chapter. The 66 stations belonging to the Belgian Dense Network (BDN) were processed by the software SoDIPE-RTK, which allows to form double differences and to compute the positioning error, defined as the difference between the estimated position and the true one. More precisely, only the ionospheric contribution to the positioning error has been investigated; its value is available for each 30 s observation epoch. The ambiguities computed by the SoDIPE-RTK software are assumed to be fixed to their true integer values, so that the positioning error does not result from troubles that might occur in real-time during the ambiguity resolution step. This important difference with real-time processing softwares implies that real-time positioning errors (experienced by users in the field) can clearly exceed the values presented in the frame of this chapter.

Three particular cases were analyzed in detail: a quiet reference day (absence of ionospheric irregularity), a typical WD MSTID and a powerful geomagnetic storm. The first step proposed to assess the positioning error in the absence of irregularity in order to validate the software and assess the influence of baseline length on the positioning error. Results show that North (ΔN) and East (ΔE) components are more accurate than the vertical one (ΔH), which is usually the case with GPS positioning. Moreover, we computed the maximum usable length, defined as the baseline length for which the typical RTK accuracy of 1 cm was observed for 95% of the time. This value is about 25 km for ΔN and ΔE components but drops to about 13 km if 3-D positioning is considered (*i.e.* considering ΔH).

Next, the investigation of the two other cases showed that the ionospheric error is larger in the case of a powerful geomagnetic storm than in the case of an MSTID, as expected. The study also pointed out that the ionospheric error does not induce any bias on the mean positioning error but makes its variability to increase with baseline length. Values between 1 and 2.5 ppm were observed for the MSTID while they are ranging from 2.5 to 6.5 ppm during the geomagnetic storm. The related 3-D maximum usable length falls to 2 and 1 km, respectively.

The analysis of the 161 baselines of the BDN also allowed to assess the influence of baseline orientation on the positioning error. If the error is very small and almost isotropic in the case of the quiet reference day, it is not the case during disturbed

conditions, where a clear effect of the orientation can be observed. The preferred orientation, which is the one giving the largest values, indicates the direction of the strongest TEC gradient. In the case of a WD MSTID, this direction coincides with the wave vector, corresponding to the MSTID direction of propagation. As a consequence, baselines oriented southwards (+/-180°) experience a 30 to 50% larger variability in positioning error than other baselines. Turning to the geomagnetic storm event, one noticed similar differences between the north–south direction and the others, indicating that TEC gradients were mostly propagating southwards. RoTEC measurement performed at several stations allowed to confirm the southward motion of the MSTID but failed to prove the preferred direction of the TEC wall associated with the geomagnetic storm.

At last, an attempt was made to correlate the ionospheric variability detected by the single-station method and the positioning error computed by SoDIPE-RTK. The correlation value is rather weak, since only 16% of the total variance is explained by the relationship between the two variables. The main reason lies in the fact that each variable is measuring a different aspect of the ionospheric error. On the one hand, single-station measurements filter out regular TEC gradients and isolate the high-frequency changes, which correspond to the so-called irregularities. On the other hand, relative positioning is sensitive to both gradients and irregularities, which implies that single-station measurements only partially explain the enhanced values of the positioning error. Similar regressions have been performed on particular days, such as during the occurrence of typcial WD and SN irregularities. For these cases, the statistical significance was clearly improved with respect to the whole dataset, with r values reaching 0.8. Related slope values were about 0.25 on average, which is slightly larger than the value of 0.17 observed in the case of the whole dataset. If a strong positive correlation was found for a limited number of cases, it is worth mentioning that its extrapolation to other datasets seems unreliable, notably because statistics are derived from an unique baseline. However, let us stress that single-station measurements can provide valuable information in the case of medium or large-amplitude irregularities. Indeed, there is a $\overline{\sigma_{\mathrm{RoTEC}}}$ threshold beyond which the related cases do not correspond to regular TEC gradients but rather to irregularities. From this basis, detection of irregularities with the single-station method can be used to warn GPS users about a likely degradation of real-time positioning conditions.

As a conclusion, even if there is a rather clear relationship between single-station measurements and the positioning error, it has been seen that the existing single-station method is not adapted to reliably forecast the positioning error in the frame of relative or differential applications. Indeed, some adaptations of the algorithm are needed to correctly take into account the TEC gradients, which are the main contributors to the positioning error. In practice, several strategies can be imagined. For example, latitudinal and longitudinal gradients may be estimated based on the satellite geometry (the position of GPS satellites is known) and on TEC time differences, *i.e.* before the polynomial fitting step leading to the RoTEC computation (see section 4.1). Another option lies in the use of TEC models able to reproduce

spatial gradients; this is the case of the International Reference Ionosphere (IRI) or the NeQuick model. In this context, double differences of these TEC forecasts (*i.e.* STEC_{AB}^{ij}) could be used to compute a forecast of the ionospheric positioning error, only due to regular gradients.

Chapter 7

Conclusions and recommendations

Ionospheric irregularities constitute the main threat for real-time precise positioning techniques based on Global Positioning System (GPS), such as relative positioning mainly used by surveyors. In the frame of this thesis, a detailed analysis of such irregularities and their influence on positioning has been presented.

The use of the Geometric-Free (GF) combination for a given satellite-to-receiver path allowed to isolate high-frequency variability in the Total Electron Content (TEC), referred to as Rate of TEC (RoTEC). Based on 10 years of RoTEC data in Belgium, a climatological study of irregularities has been performed to determine their origin, and notably to assess the respective part of irregularities due to Space Weather (SW) events. As expected, it appears that the proportion of irregularities due to solar flares and geomagnetic storms is varying with solar cycle, with values ranging from 0 (at solar minimum) to about 25% for high solar activity periods. The remaining part is due to the so-called quiet-time irregularities on which chapter 4 was focused. The origin of quiet-time irregularities is partially unknown and has been investigated based on their occurrence rate and amplitude. Mainly, two types of quiet-time irregularities arose from the climatological study: Winter Daytime (WD) and Summer Nighttime (SN).
The first category corresponds to daytime Medium-Scale Traveling Ionospheric Disturbances (MSTIDs), which are understood as the ionospheric signature of Atmospheric Gravity Waves (AGWs) whose origin may be multiple. WD events generally occur between 0800 and 1600 LT during autumn and winter months and exhibit an amplitude of about 10% of the background Vertical TEC (VTEC). They are generally observed at low elevation for satellite traces mainly oriented northwards; this is the direct consequence of the observational bias induced by the orbital configuration of the GPS constellation. Indeed, it has been demonstrated that MSTIDs are detected by GPS if the relative velocity between the satellite and the MSTID is large. As a consequence, satellite traces opposite to equatorwards-directed MSTIDs as well as Ionospheric Pierce Points (IPPs) at low elevation would make the observation of MSTIDs easier. Furthermore, it has been shown that large MSTID amplitudes were observed at low elevation, due to the larger slant path crossed by the Line of Sight (LoS). The origin of AGWs does not seem to be related to the

solar terminator, even if this latter is not excluded as a secondary source. However, if the most probable source lies in the lower atmosphere, the spatial correlation between MSTID occurrence and jetstream led to weakly significant results. The lack of correlation could arise from the atmospheric filtering by neutral winds in the mesosphere/thermosphere. Indeed, some studies have highlighted the important role played by such winds in the propagation of AGWs originating from below up to the ionosphere. On the opposite, the assessment of spatial correlation between MSTID and orography led to significant results. It is however believed that this relatively strong correlation is due to an enhanced observational bias for satellites located south of the station and observed at low elevation.

SN irregularities occur during summer nights, between 2000 and 2200 LT and show a typical amplitude ranging from 8 to 20%, depending on solar conditions. Contrary to WD ones, they are observed at low but also at high elevations, for satellite traces moving not only northwards. Scientific literature associates SN irregularities to MSTIDs of electrical origin, moving preferentially southwestwards in the northern hemisphere. Comparison of some SN cases with Dourbes ionograms (80 km south from Brussels) showed that the major part of SN events were associated with spread-F phenomena, which, in turn, are linked to the occurrence of Es layers. The presence of spread-F in ionograms is the signature of small-scale irregularities in the F-region called Field-Aligned Irregularities (FAI), which are thought to explain the noise-like patterns observed in the associated RoTEC time series. However, some wave-like patterns typical of MSTIDs were also observed in RoTEC; it is therefore believed that SN irregularities may be the result of two distinct features: FAIs and electrical MSTIDs, whose origin is still subject to debate within the scientific community.

Further investigations concerning the origin of AGWs and SN irregularities should rely on external data sources and favor the multi-instrument approach. For example, the combination of ground-based measurements such as airglow, radars or ionosondes with satellite-based observations would certainly help to identify the AGW source location. Besides, the use of TEC coming from geostationary satellites might provide complementary MSTID measurements as they offer a static view of the ionosphere. However, let us point out that current geostationary constellations like the European EGNOS or the American WAAS are operating on the L_1 carrier only, which prevents frequency combinations such as the GF used for TEC computation. Evolution perspectives of geostationary services concern the broadcast on a second frequency: for example, EGNOS future implementations would provide an integrity service based on the L_5 frequency [31]. Another perspective consists in using scintillation measurements to reveal the presence of FAIs, these latter being generally responsible for short-time amplitude fadings. The observation of scintillations in our Belgian dataset would indicate that, in addition to the ionospheric refraction, trans-ionospheric measurements over mid-latitudes can also be prone to diffraction, which is generally assumed to happen over equatorial and polar regions only. This perspective might therefore bring new elements concerning the dynamics of the ionosphere over mid-latitudes.

In chapter 5, a climatological model of ionospheric irregularities has been built. The model is purely statistical and is based on the irregularity time series in Belgium over the time interval 2002–2011. The series has a 15 min time resolution and represent the ionospheric variability at a given station, averaged over all satellites in view. The aim of this model is to capture and reproduce the main patterns constituting the time series, like WD and SN irregularities, taking into account the seasonal and solar cycle variations. The climatological model is made up of two main parts: the first models the centered values of the series, which correspond to observations subtracted from the daily mean, called offsets. A Principal Component Analysis (PCA) has been applied to the centered series to extract the main patterns and filter out all transient events, such as the effects of geomagnetic storms. The first two principal components correspond to WD and SN irregularities respectively, which validates the results obtained in the previous chapter.
The second part of the model concerns the offset series which has a time resolution of 24 h. Offset series is modeled by a quadratic polynomial and harmonic functions to take into account the seasonal and solar cycle dependence of the mean variability level. In addition, residuals have been fitted with an AutoRegressive and Moving Average (ARMA) model whose the goal is to adapt the offset model to current conditions. The final climatological model, made up of PCA and offset models, has been validated over years of moderate (2011) and low (2008) solar activity. The model provides better results during summer than during winter, with a mean relative error of 10–15% and 20–25%, respectively. It is also shown that ARMA clearly improves the short-term forecast, with a significant contribution up to 4 or 5 days after the last observation.
Modeling perspectives are numerous and mainly aim at adapting the existing method. The first perspective lies in a more appropriate modeling function of the solar cycle. Indeed, the current offset model uses a second order polynomial which might be replaced by an harmonic function, expressing the morphology of the solar cycle: a rapid rise in the first four years before a slower decrease during the remaining 7 years. Secondly, as the occurrence of space weather phenomena like Corotating Interaction Regions (CIRs) or Coronal Mass Ejections (CMEs) can be forecast several hours in advance, the addition of a space weather component in the model would allow to take into account transient events. Another improvement concerns the PCA model, which is identically repeated year after year, so that no adaptation to solar conditions is implemented in the actual form. We propose to introduce a stretching parameter (smaller or larger than 1) allowing to adapt the mean model (as computed in this thesis) to current solar conditions. The last perspective lies in a better consideration of the day-to-day ionospheric variability. Indeed, it is believed that a semi-empirical model based on proxies of ionospheric irregularities constitutes the best way to model the irregular fluctuations of the variability level. However, the main obstacle is the lack of categorical identification of irregularity causes, as pointed out by the study carried out in the previous chapter. Therefore, such a promising formulation has to be developed over the long term only.

The last chapter deals with the effect of irregularities on relative positioning, which has been assessed based on three particular days. The 161 baselines belonging to the Belgian Dense Network (BDN) have been processed by the Software for Determining the Ionospheric Positioning Error on RTK (SoDIPE-RTK), developed to quantify the positioning error only due to the ionosphere for a given baseline. The three cases considered in this work correspond to a quiet reference day, the occurrence of a WD MSTID and the occurrence of an extreme geomagnetic storm.

The analysis of the quiet reference day allowed to validate the software and to assess the influence of baseline length on positioning error under quiet (*i.e.* nominal) conditions. We have defined the maximum usable length, which corresponds to the baseline length for which the nominal accuracy of 1 cm was observed 95% of the time. Considering a 3-D positioning, this length is about 13 km while the corresponding 2-D value is twice as large. Similar computations were performed during the occurrence of the MSTID and of the geomagnetic storm, which led to maximum lengths of 2 and 1 km, respectively. Indeed, during the MSTID, the variability of the positioning error lies between 1 and 2.5 mm/km (or ppm) while the geomagnetic storm was responsible for values ranging from 2.5 to 6.5 ppm.

Another conclusion of the BDN analysis lies in the clear influence of the baseline orientation during the occurrence of irregularities. Indeed, baselines oriented southwards (+/-180°) have observed a 30 to 50% increase in positioning error with respect to other azimuths. This preferential orientation is believed to be due to the mean motion of irregularities: if WD MSTIDs are generally known to propagate southwards in the northern hemisphere, it seems that this was also the case of the TEC gradients induced by the geomagnetic storm. These results are in good agreement with other independent studies in which the anti-sunward motion of polar ionization patches during the occurrence of ionospheric storms was highlighted [27, 36, 67].

Finally, the correlation between ionospheric irregularities and positioning error has been computed based on a 6 years dataset related to a single baseline. The weak correlation observed for the whole dataset ($r \simeq 0.4$) results from two elements. First, relative positioning is sensitive to TEC gradients, which are induced not only by ionospheric irregularities but also by the longitudinal and latitudinal gradients, which are recurrent features. RoTEC measurements do not contain these gradients (they are filtered out by a low order polynomial), so that ionospheric irregularities are responsible for a small proportion of significant positioning errors. However, let us point out that positioning errors due to irregularities (either quiet-time or due to SW events) are generally larger than those due to regular TEC gradients. As a consequence, detection and forecast of irregularities by the single-station method are still relevant as this latter allows to monitor and forecast positioning errors of medium/large amplitude. Secondly, the single-station variability (σ_{RoTEC}) used in our correlation study is averaged over all satellites in view. It results that the effect of a single irregularity occurring on a given satellite would lead to a small average value, whereas its contribution to the positioning error might be significant.

At the present time, we can therefore conclude that the current single-station method is not suitable to forecast the ionospheric positioning error experienced with differential or relative methods, for all reasons detailed above. Several perspectives can be drawn to improve the prediction capability of the existing methods. These future implementations should be considered over both short and medium/long term.
Short-term outlooks concern the assessment of regular TEC gradients; these latter are indeed responsible for a large part of the ionospheric error. Mainly, two options have been considered. The first consists in adapting the single-station method to estimate regular TEC gradients: these latter can be derived from the time differenced GF combination, taking into account the geometry of the GPS constellation. The second way of extracting latitudinal and longitudinal gradients is the use of ionospheric models such as International Reference Ionosphere (IRI) or NeQuick, able to provide Slant TEC (STEC) values for each satellite in view. Knowledge of such TEC gradients would therefore allow to simulate the part of the ionospheric positioning error due to the regular ionosphere.
Medium and long-term perspectives concern the development of physical models of ionospheric irregularities, as it was suggested in chapter 4. Such models might rely on multi-instrument observations, such as TEC, airglow and radar images or the 3-D electron density obtained by tomography with GNSS. In addition, they should consider each satellite separately, with their own observational conditions of the ionosphere. This latter point is of major interest as we proved that the observational bias plays an important role in the way that irregularities impact on GPS measurements.

Appendices

Appendix A

Mapping functions

This section aims at describing several mapping functions that are generally used in the frame of ionospheric studies with the Global Positioning System (GPS). A Mapping Function (MF) can be defined as the ratio between the Slant TEC (STEC) and the Vertical TEC (VTEC) values:

$$M = \frac{\text{STEC}}{\text{VTEC}} \quad \Rightarrow \quad M \geq 1 \tag{A.1}$$

Relationship between STEC and VTEC values is quite complex as it results from the combination of several factors:

- the satellite elevation (or the zenith angle z);
- the sphericity of the ionosphere;
- the non-negligible thickness of the ionospheric layer;
- the variable electron density profile within the ionosphere;
- the existence of latitudinal and longitudinal gradients in the electron density.

Several models M have therefore been developed to get the most realistic vertical projection of the observed STEC values. Developments and studies concerning MF can be notably found in [20, 62, 73, 87]. In the frame of this thesis, we will compare three models: the thin single layer model, the thick single layer model and the model derived from the geometric MF. Comparison between these models will be achieved based on ΔVTEC differences.

A.1 Three different mapping functions

A.1.1 Thin single layer model

This simple model assumes that all electrons of the ionosphere are confined in an infinitesimally thin spherical layer located at an altitude h (figure A.1)[1]. One defines

[1] The thin single layer model is the most common model used in GPS applications [47, 57, 111].

the Ionospheric Pierce Point (IPP) as the intersection between the shell and the satellite-to-receiver path while its projection on the Earth's surface is called Sub-Ionospheric Point (SIP). The mapping function M_1 associated with the thin single layer model corresponds to the inverse of the cosine of the zenith angle at the IPP (z_{IPP}), representing therefore the ratio between the vertical and slant directions at the IPP:

$$M_1 = \frac{1}{\cos(z_{\mathrm{IPP}})} \tag{A.2}$$

with

$$\frac{\sin(z_{\mathrm{IPP}})}{R_e} = \frac{\sin(z)}{R_e + h} \quad \Rightarrow \quad z_{\mathrm{IPP}} = \mathrm{asin}\left(\frac{R_e}{R_e + h}\sin(z)\right) \tag{A.3}$$

R_e corresponding to the mean radius of the Earth (R_e = 6371 km), z being the zenith angle of the line of sight at the antenna and h the ionospheric shell height. Considering equation (A.3), M_1 can also take the following form:

$$M_1 = \frac{1}{\sqrt{1 - \left(\frac{R_e}{R_e+h}\sin(z)\right)^2}} \tag{A.4}$$

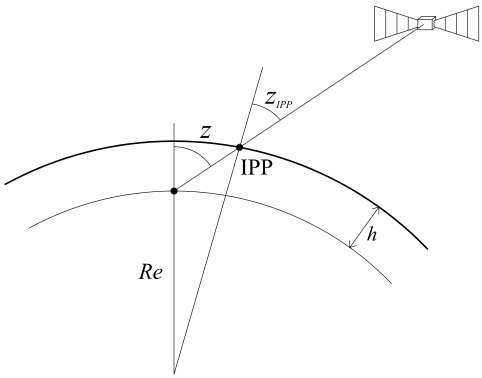

Figure A.1 – Thin single layer model.

The variation of M_1 with zenith angle z depends therefore on the shell height h where all electrons are assumed to be located. Considering a mid-latitude ionosphere, the altitude of maximum electron density lies generally between 250 and 400 km, depending on local time and season. As ionospheric topside profile decreases less rapidly with height than the bottomside, the shell height should be located above the density peak. Commonly used value for h parameter oscillates between 300

and 500 km and their corresponding M_1 value is plotted against zenith angle z in figure A.2.

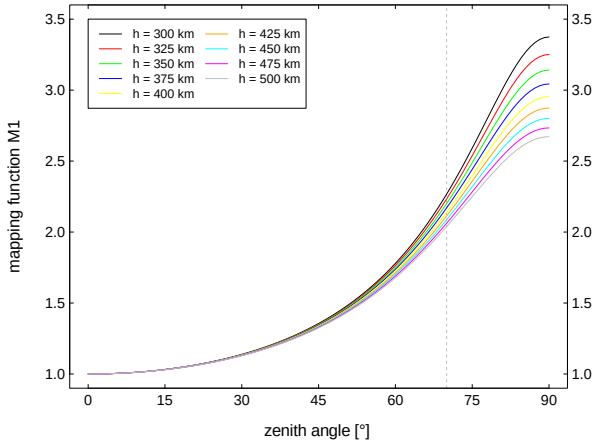

Figure A.2 – Influence of shell height h on M_1 term for several realistic h values.

It comes from figure A.2 that the larger h is, the larger M_1 will be; this is particularly true considering low elevations ($z > 70°$). However, all observations with $z > 70°$ have been removed from our dataset in order to limit the influence of multipath and noise on GPS observations. The influence of h can therefore be assessed by extracting minimum and maximum values at $z = 70°$: the minimum value occurs for $h = 300$ km and is equal to 2.038 while maximum is reached for $h = 500$ km and is equal to 2.267. The difference between these extreme values is about 0.229, which gives a relative difference of 10.6%.

A.1.2 Thick single layer model

In this model, the single layer exhibits a finite thickness, allowing to assume a given electron density profile. The layer extends from h_0 to h_1 (figure A.3) and we can define M_2 as the ratio between two integrals corresponding to STEC (numerator) and VTEC (denominator):

$$M_2 = \frac{\int_{h_0}^{h_1} N_e(h)\, M_1\, dh}{\int_{h_0}^{h_1} N_e(h)\, dh} \tag{A.5}$$

with M_1 corresponding to the mapping function relative to the thin single layer model at altitude h (see equation A.4) and $N_e(h)$ the electron density at altitude h. The integral forms of equation (A.5) can be very complex, depending on the density profile chosen (*e.g.* Chapman profile). If we consider a constant density profile

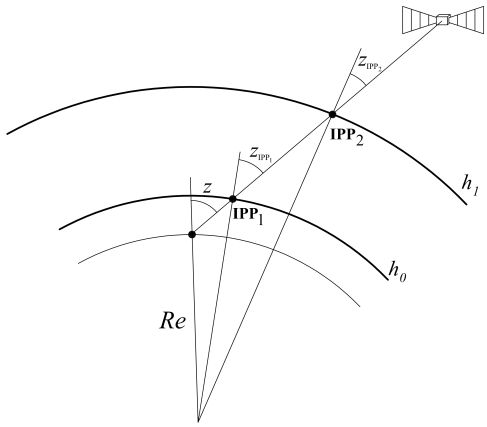

Figure A.3 – Thick single layer model. (Adapted from [73])

(*i.e.* an homogeneous electron density inside the whole layer), equation (A.5) can be simplified as follows:

$$\begin{aligned} M_2 &= \frac{\int_{h_0}^{h_1} M_1 \, dh}{\int_{h_0}^{h_1} dh} \\ &= \frac{\sqrt{(R_e + h_1)^2 - (R_e \sin(z))^2} - \sqrt{(R_e + h_0)^2 - (R_e \sin(z))^2}}{h_1 - h_0} \end{aligned}$$

As for the thin single layer, fixing the boundaries h_0 and h_1 remains challenging since one has to model an ideal ionosphere exhibiting a density peak varying with solar cycle, season and local time with two fixed parameters. Reliability of the constant density hypothesis has been studied in [73] by comparing this model with a Chapman profile. Moreover, as a particular case where $h_0 = h_1$, the thin single layer model has also been compared. It comes that thick single layer leads to better results than the thin one when the layer is not too thick; typical values for h_0 and h_1 can be 250 and 650 km respectively. Figure A.4 shows the influence of these boundaries on the computation of M_2.

We can observe that different combinations of h_0 and h_1 lead to very similar M_2 values, as it is the case for $(h_0 = 100, h_1 = 700)$ and $(h_0 = 200, h_1 = 500)$. We can conclude that not only the thickness of the layer matters but also the location of its boundaries. Considering M_2 values for $z < 70°$, one can also notice that they are quite similar with absolute differences of 0.239 at $z = 70°$, which corresponds to 11.1%.

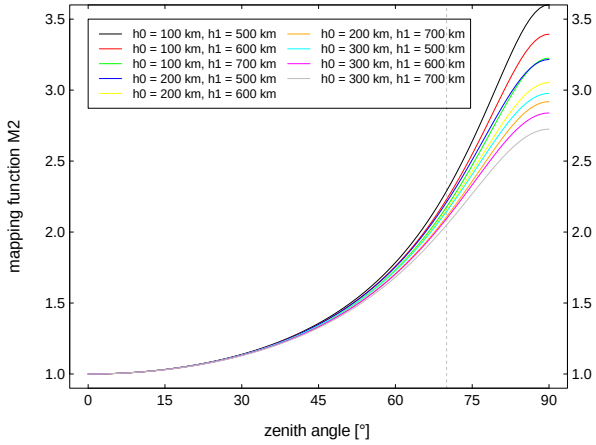

Figure A.4 – Influence of h_0 and h_1 on M_2 for several realistic h_1 and h_2 values.

A.1.3 The geometric mapping function

The third and last MF that will be considered in this study is the geometric one, which can be defined as follows:

$$ds = M_3\, dH \quad \Rightarrow \quad M_3 = \frac{ds}{dH} \tag{A.6}$$

with ds an infinitesimal length of the satellite-to-receiver path and dH an incremental height.

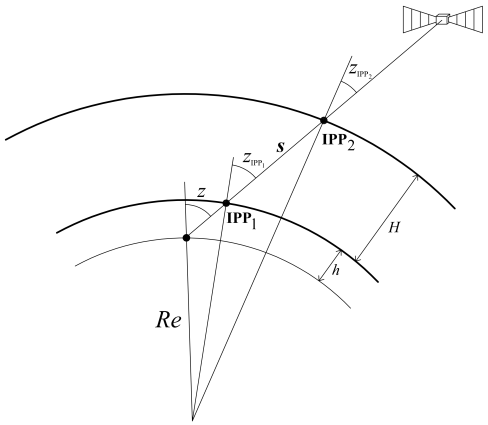

Figure A.5 – Geometric mapping function. (Adapted from [111])

In this formulation, s corresponds to the ionospheric path length and the ionosphere has a given thickness, extending from h to $(h + H)$, H being the ionospheric thickness parameter (figure A.5). Let us note that parameters h and H used in this model correspond to the real boundaries of the ionosphere, *i.e.* $h \simeq 75$ km and $H \simeq 700$ km.
Considering the intersection between the ray path and the ionospheric lower boundary, called Lower Ionospheric Pierce Point (IPP_l), we have the same relationship than that of the thin single layer model (see equation A.3):

$$\sin(z_{\mathrm{IPP_l}}) = \left(\frac{R_e}{R_e + h}\right) \sin(z) \tag{A.7}$$

After some mathematical operations (see [111]), the equation of the ionospheric path length s can be obtained:

$$s = -(R_e + h)\cos(z_{\mathrm{IPP_l}}) + \sqrt{(R_e + h + H)^2 - (R_e + h)^2 \sin^2(z_{\mathrm{IPP_l}})} \tag{A.8}$$

Computation of M_3 can therefore be achieved by differentiating equation (A.8):

$$\begin{aligned} M_3 &= \frac{ds}{dH} \\ &= -\left(\frac{R_e + h}{H}\right)\cos(z_{\mathrm{IPP_l}}) \\ &\quad + \frac{\sqrt{(R_e + h + H)^2 - (R_e + h)^2 \sin^2(z_{\mathrm{IPP_l}})}}{H} \end{aligned} \tag{A.9}$$

Based on equation (A.9), figure A.6 shows the influence of h and H on the computation of M_3, plotted as a function of the zenith angle. We can observe that several parameter combinations (h; H) give the same M_3 values; for example the pairs (h=50km; H=800km), (h=75km; H=700km) and (h=100km; H=600km). Considering the different parameter combinations at $z = 70°$, spread statistics can also be computed: absolute difference between the extreme models is 0.157, for a relative difference of 7.23%. These values are lower than those related to the two previous models, which makes the geometric MF model the less sensitive to changes in parameter values.

A.2 Comparison for ΔVTEC computation

Vertical TEC can be obtained by VTEC = STEC/M (equation A.1). The comparison between two MF M_i and M_j can be expressed in terms of TEC Unit (TECU) as follows:

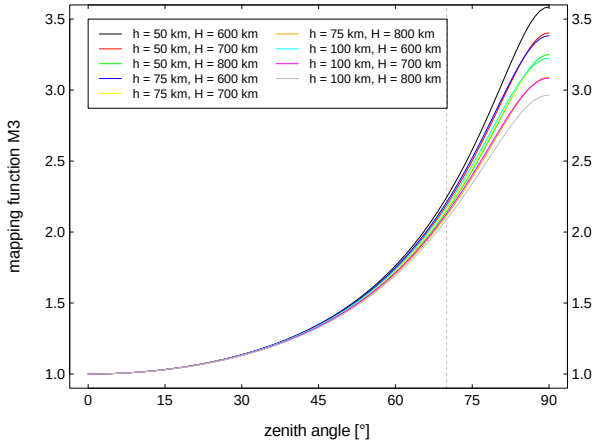

Figure A.6 – Influence of h and H on M_3.

$$\begin{aligned} \mathrm{VTEC}_i - \mathrm{VTEC}_j &= \frac{\mathrm{STEC}}{M_i} - \frac{\mathrm{STEC}}{M_j} \\ &= \left(\frac{1}{M_i} - \frac{1}{M_j}\right) \mathrm{STEC} \end{aligned} \tag{A.10}$$

However, as results of chapter 4 concern Total Electron Content (TEC) rate of change, equation (A.10) has to be translated into a differential form. Since we are dealing with two consecutive observation epochs t_k and t_{k-1}, we can consider that M_i and M_j do not vary with time and it comes from equation (A.10):

$$\begin{aligned} \Delta\mathrm{VTEC}_i - \Delta\mathrm{VTEC}_j &= \left(\frac{1}{M_i} - \frac{1}{M_j}\right) \Delta\mathrm{STEC} \\ &= \alpha\, \Delta\mathrm{STEC} \end{aligned} \tag{A.11}$$

Thanks to equation (A.11) we are now able to compare the different MF two by two. The error in ΔVTEC modeling between M_i and M_j corresponds to the multiplication of the α term and the observed ΔSTEC. As we have to compare three MF two by two, there will be three comparisons. Moreover, we chose two realistic[2] parameters for each MF, which leads to four combinations for each "M_i vs M_j" comparison. The resulting twelve curves are depicted in figure A.7.

We can observe from figure A.7 that α multiplicative factor exhibits both positive

[2]Considering a mid-latitude ionosphere.

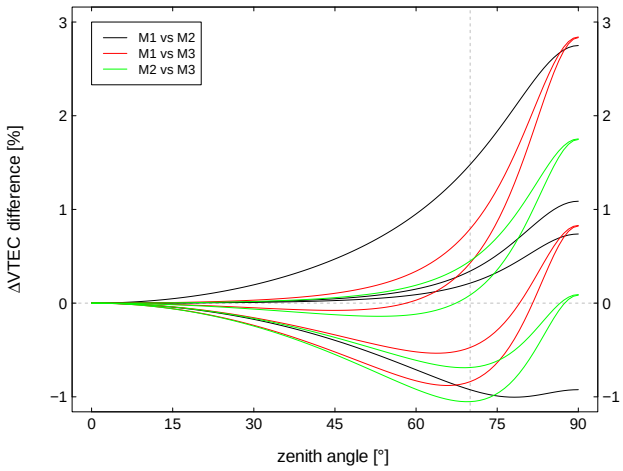

Figure A.7 – Comparison between the three mapping functions M_1, M_2 and M_3 in terms of ΔSTEC multiplicative factor. Two different values of parameters have been selected for each MF, so that each comparison leads to four curves. Parameters for M_1 are h=350 km and h=400 km. For M_2, parameter pairs are (h_0=200 km;h_1=500 km) and (h_0=200 km;h_1=600 km). Parameter pairs for M_3 are (h=75 km;H=700 km) and (h=100 km;H=600 km).

and negative values, depending on the comparison. As α reaches the value of 3% at $z \simeq 90°$, it does not exceed 1.5% for $z < 70°$. This means that considering realistic parameters for a given MF i, ΔVTEC accuracy (due to MF mismodeling) can be approximated by $0.015\,\Delta$STEC, so that

$$\Delta\mathrm{VTEC}_i \in [\Delta\mathrm{VTEC}_i - 0.015\,\Delta\mathrm{STEC}\,;\,\Delta\mathrm{VTEC}_i + 0.015\,\Delta\mathrm{STEC}] \qquad \text{(A.12)}$$

Let us consider a ΔSTEC value of 2 TECU/min, which is realistic during the occurrence of a large amplitude Medium-Scale Traveling Ionospheric Disturbance (MSTID) at low elevations. Equation (A.12) shows that MF error in ΔVTEC does not exceed 0.03 TECU/min, which is the order of combined noise and multipath level (see chapter 4).

Appendix B

IPP maps for WD irregularities

Below is the list of figures analyzed to investigate the spatial correlation between the tropospheric jetstream, orography and the occurrence of classical Medium-Scale Traveling Ionospheric Disturbances (MSTIDs).

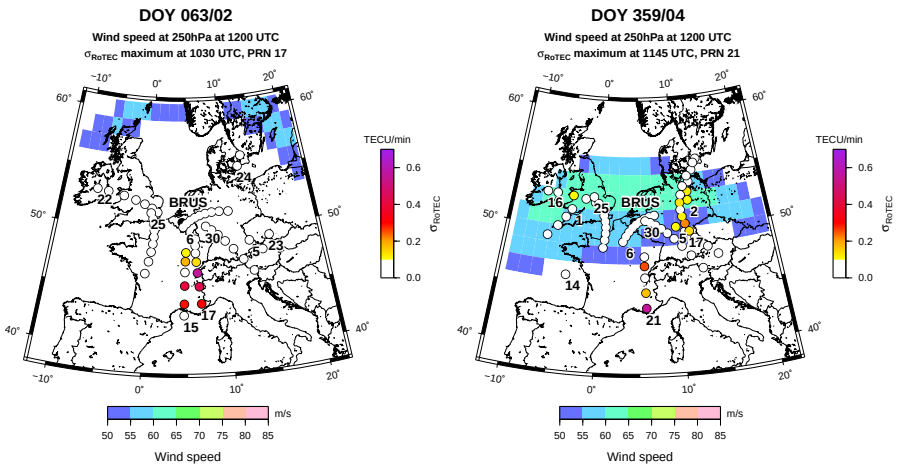

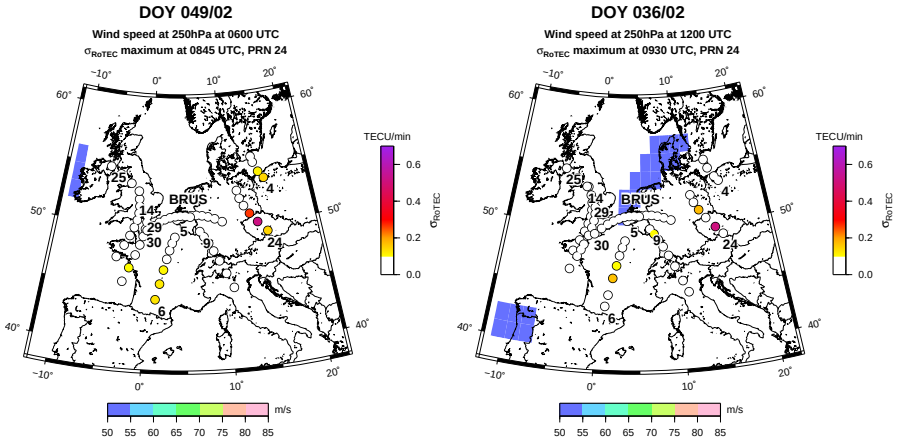
DOY 049/02
Wind speed at 250hPa at 0600 UTC
σRoTEC maximum at 0845 UTC, PRN 24
DOY 036/02
Wind speed at 250hPa at 1200 UTC
σRoTEC maximum at 0930 UTC, PRN 24
BRUS
TECU/min
σRoTEC
m/s
Wind speed

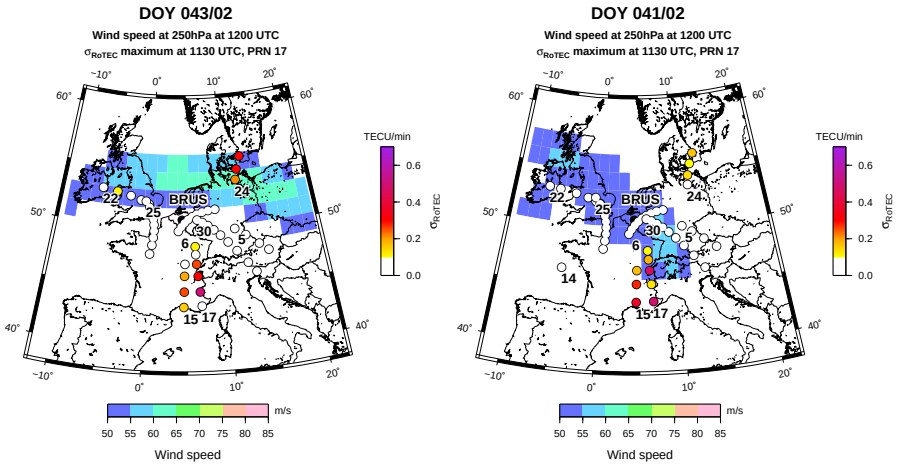
DOY 043/02
Wind speed at 250hPa at 1200 UTC
σRoTEC maximum at 1130 UTC, PRN 17
DOY 041/02
Wind speed at 250hPa at 1200 UTC
σRoTEC maximum at 1130 UTC, PRN 17
BRUS
TECU/min
σRoTEC
m/s
Wind speed

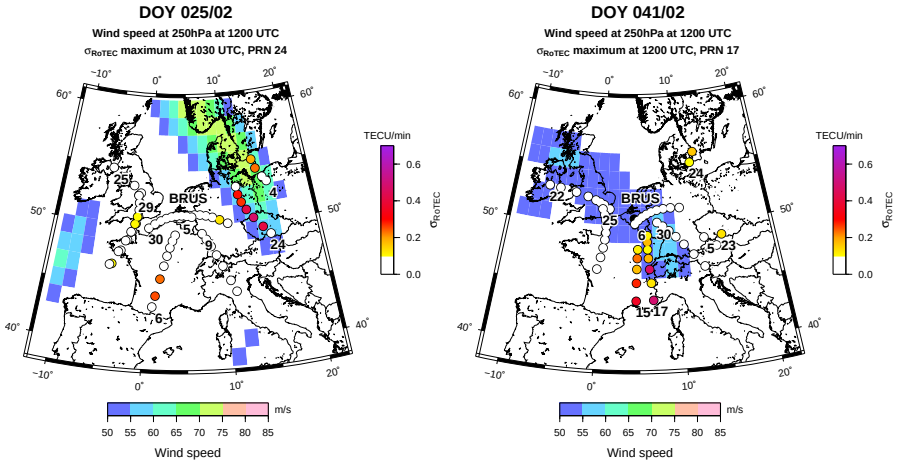
DOY 025/02
Wind speed at 250hPa at 1200 UTC
σRoTEC maximum at 1030 UTC, PRN 24
DOY 041/02
Wind speed at 250hPa at 1200 UTC
σRoTEC maximum at 1200 UTC, PRN 17
BRUS
TECU/min
σRoTEC
m/s
Wind speed

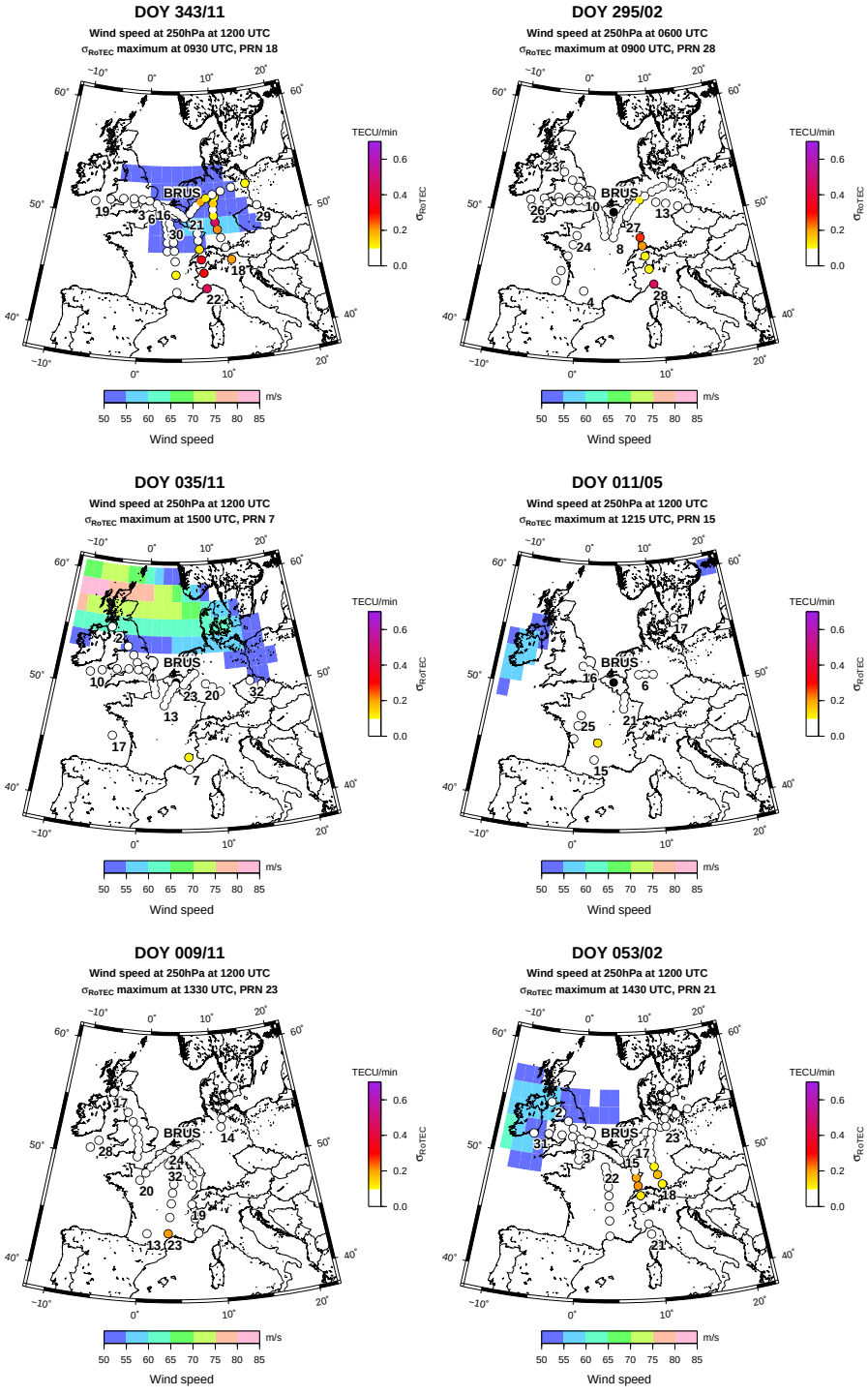
DOY 343/11
Wind speed at 250hPa at 1200 UTC
σRoTEC maximum at 0930 UTC, PRN 18
DOY 295/02
Wind speed at 250hPa at 0600 UTC
σRoTEC maximum at 0900 UTC, PRN 28
DOY 035/11
Wind speed at 250hPa at 1200 UTC
σRoTEC maximum at 1500 UTC, PRN 7
DOY 011/05
Wind speed at 250hPa at 1200 UTC
σRoTEC maximum at 1215 UTC, PRN 15
DOY 009/11
Wind speed at 250hPa at 1200 UTC
σRoTEC maximum at 1330 UTC, PRN 23
DOY 053/02
Wind speed at 250hPa at 1200 UTC
σRoTEC maximum at 1430 UTC, PRN 21
BRUS
TECU/min
σRoTEC
m/s
Wind speed

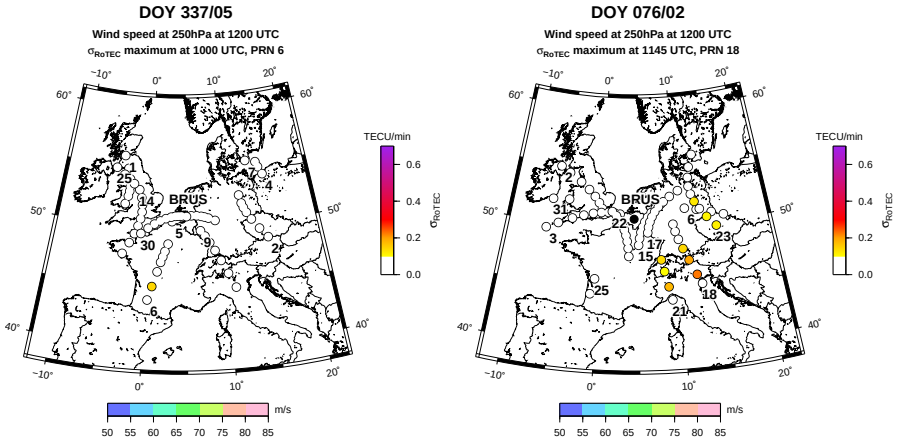
DOY 337/05
Wind speed at 250hPa at 1200 UTC
σRoTEC maximum at 1000 UTC, PRN 6
DOY 076/02
Wind speed at 250hPa at 1200 UTC
σRoTEC maximum at 1145 UTC, PRN 18
BRUS
TECU/min
σRoTEC
m/s
Wind speed

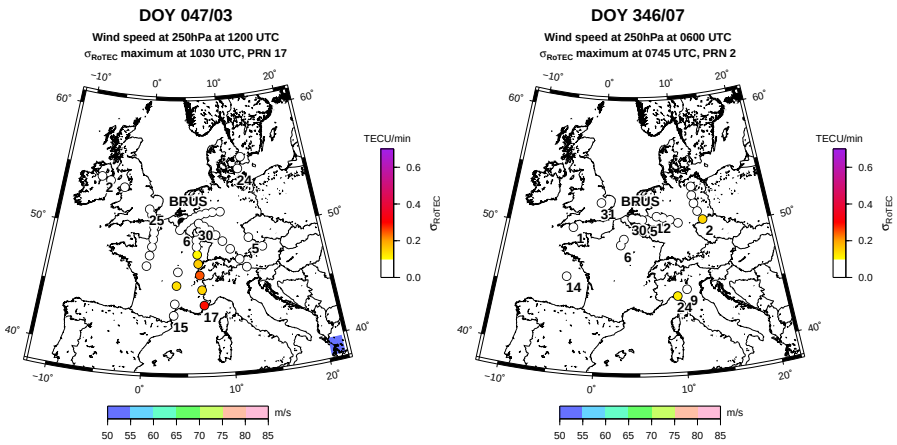
DOY 047/03
Wind speed at 250hPa at 1200 UTC
σRoTEC maximum at 1030 UTC, PRN 17
DOY 346/07
Wind speed at 250hPa at 0600 UTC
σRoTEC maximum at 0745 UTC, PRN 2
BRUS
TECU/min
σRoTEC
m/s
Wind speed

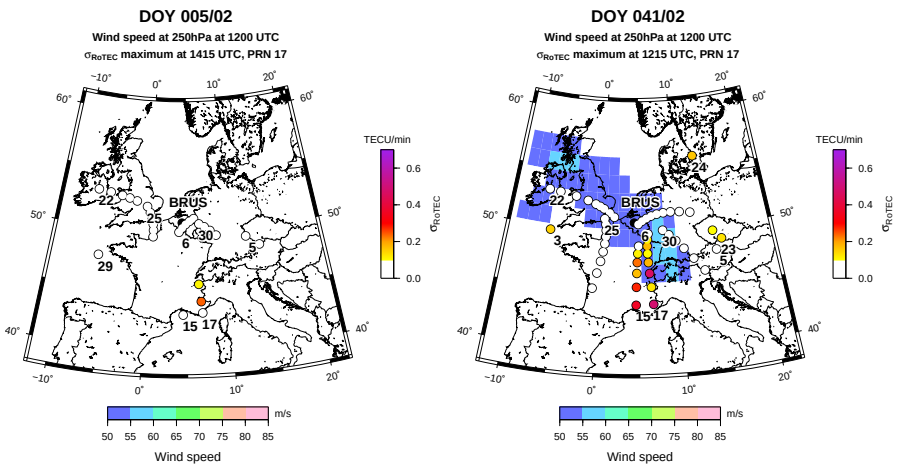
DOY 005/02
Wind speed at 250hPa at 1200 UTC
σRoTEC maximum at 1415 UTC, PRN 17
DOY 041/02
Wind speed at 250hPa at 1200 UTC
σRoTEC maximum at 1215 UTC, PRN 17
BRUS
TECU/min
σRoTEC
m/s
Wind speed

Appendix C

IPP maps for SN irregularities

Below is the list of Ionospheric Pierce Point (IPP) maps analyzed to investigate the correlation between the Es layers, spread-F phenomena and the occurrence of Summer Nighttime (SN) irregularities.

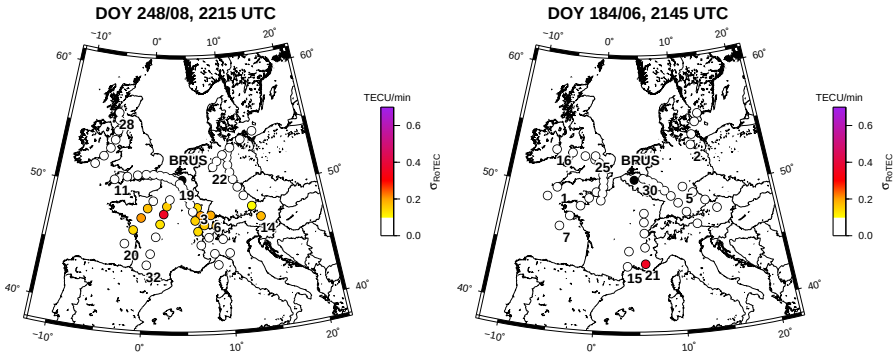

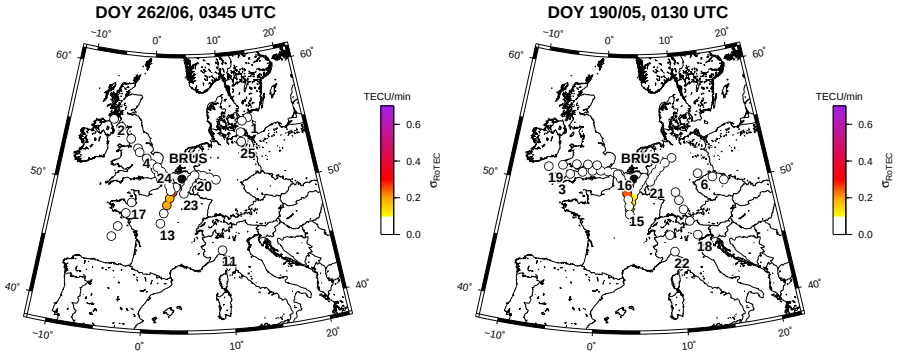
DOY 262/06, 0345 UTC
DOY 190/05, 0130 UTC
BRUS
TECU/min
σRoTEC

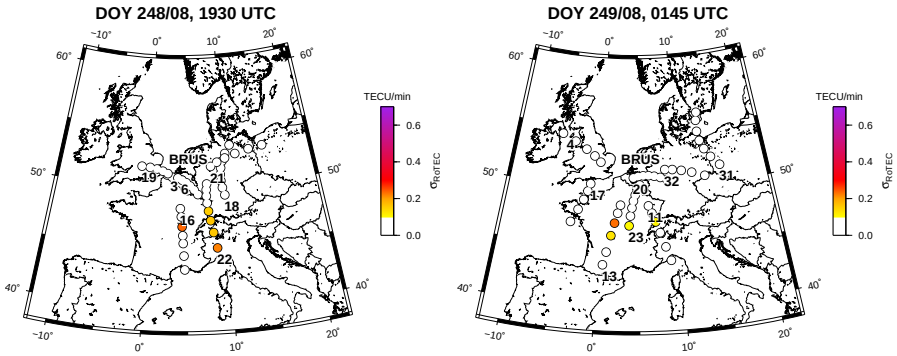
DOY 248/08, 1930 UTC
DOY 249/08, 0145 UTC
BRUS
TECU/min
σRoTEC

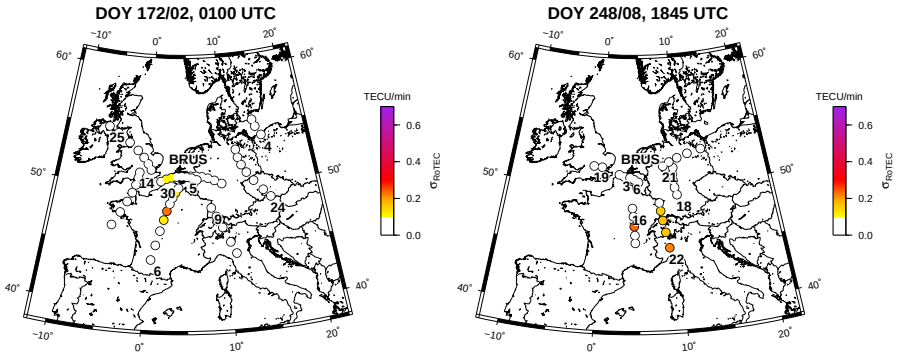
DOY 172/02, 0100 UTC
DOY 248/08, 1845 UTC
BRUS
TECU/min
σRoTEC

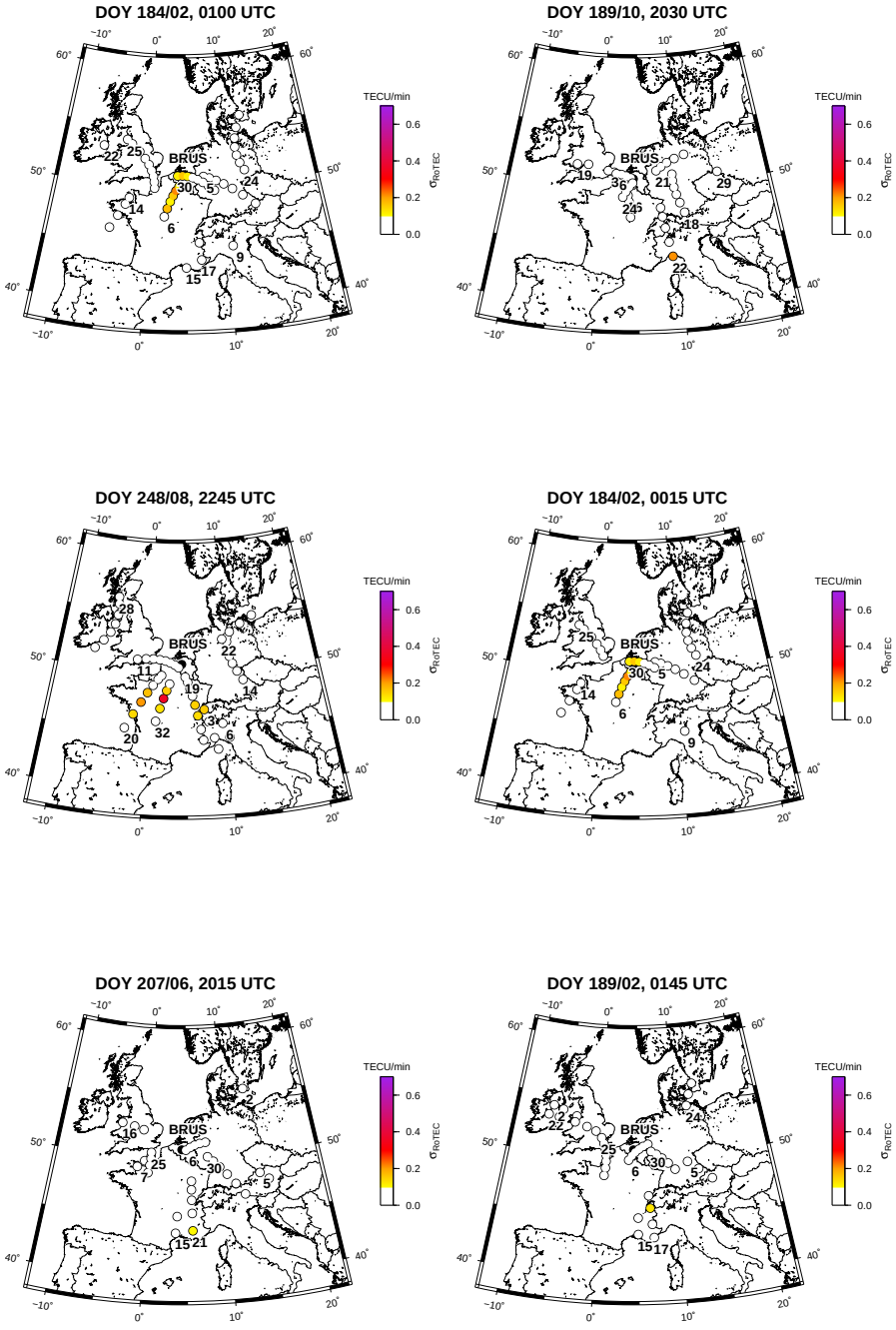
DOY 184/02, 0100 UTC
DOY 189/10, 2030 UTC
DOY 248/08, 2245 UTC
DOY 184/02, 0015 UTC
DOY 207/06, 2015 UTC
DOY 189/02, 0145 UTC
BRUS
TECU/min
σRoTEC

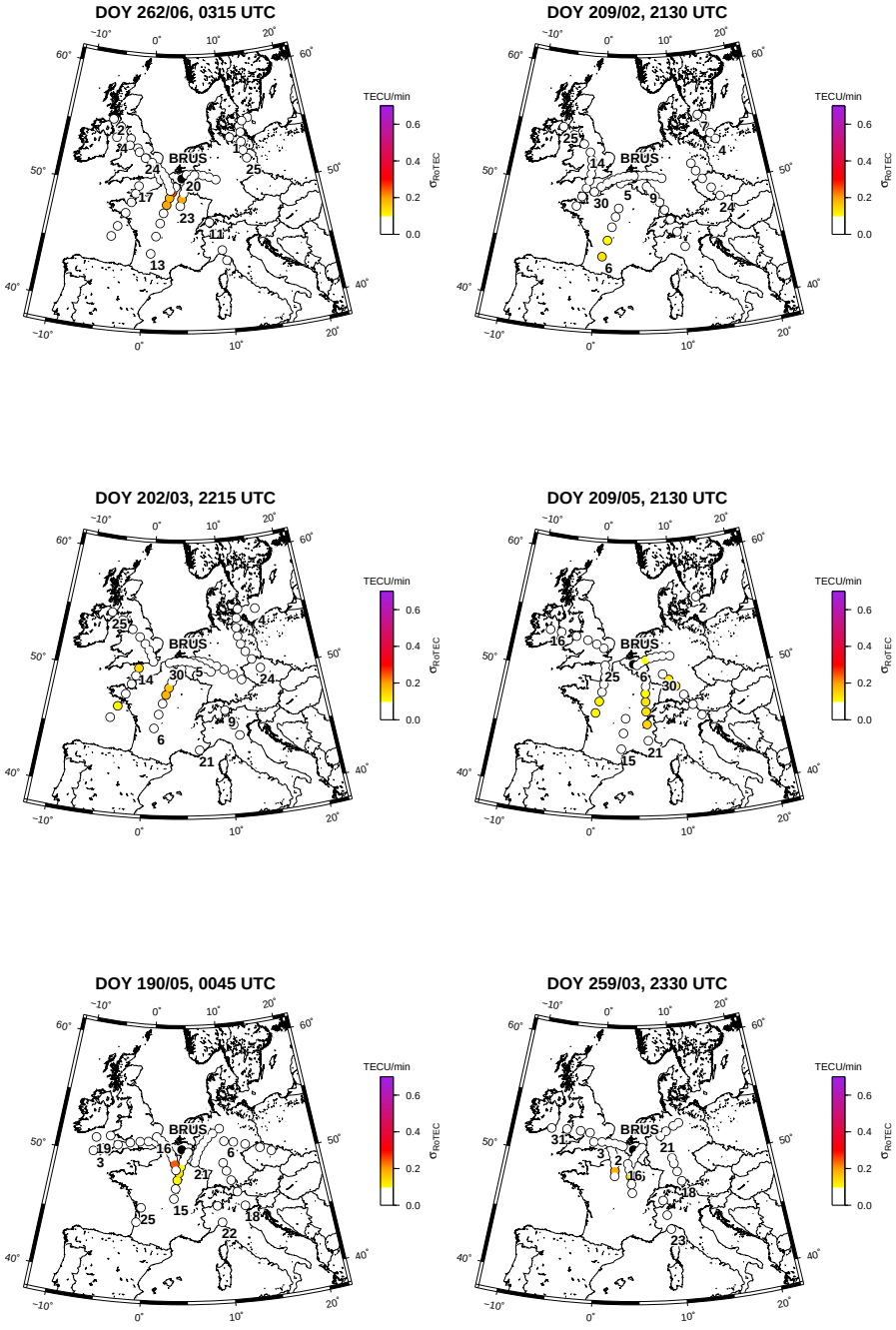
DOY 262/06, 0315 UTC
DOY 209/02, 2130 UTC
DOY 202/03, 2215 UTC
DOY 209/05, 2130 UTC
DOY 190/05, 0045 UTC
DOY 259/03, 2330 UTC
BRUS
TECU/min
σRoTEC

Appendix D

Influence of ionospheric height on IPP location

THE influence of the ionospheric shell height on the distance between the observing station and the Sub-Ionospheric Point (SIP) can be easily computed using plane trigonometry.

In this example, let us consider two infinitesimally thin spherical layers located at $h_1 = 400$ km and at $h_2 = 100$ km in order to compute Ionospheric Pierce Points (IPPs) in the F- and E-layers, respectively. The distance between the observing station (STAT) and the IPP related to the ith layer (IPP_i) is denoted D_i (figure D.1).

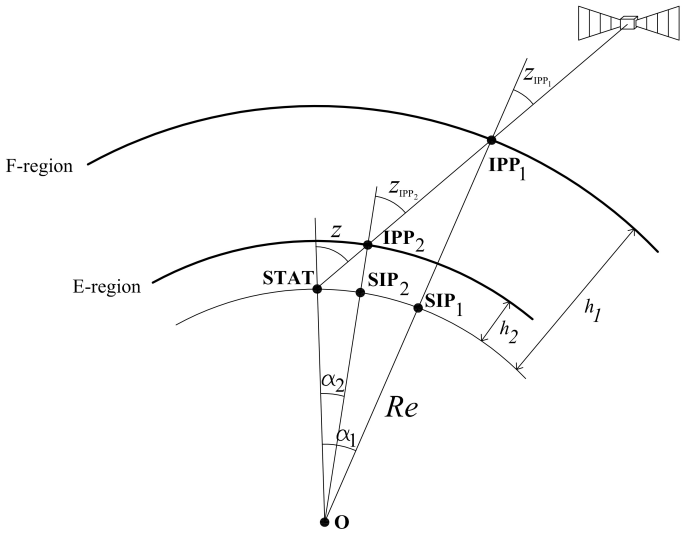

Figure D.1 – Thin single layer model considering two different heights: $h_1 = 400$ km and $h_2 = 100$ km.

Assuming a given elevation e (or its corresponding zenith angle z) of the Line of Sight (LoS), the computation of D_i is straightforward:

$$D_i = R_e\ \alpha_i \qquad with\ \ \alpha_i = \pi - (90 + e) - z_{\text{IPP}_i} \tag{D.1}$$

where R_e is the mean Earth's radius ($R_e = 6371$ km), α_i is the angle between the vertical straight lines |O - STAT| and |O - IPP$_i$| and z_{IPP_i} denotes the zenith angle at the IPP$_i$, computed by equation (A.3).
As a consequence, considering $h_1 = 400$ km and $h_2 = 100$ km, one can assess the ratio $\frac{D_2}{D_1}$ as a function of the zenith angle z, which is illustrated in figure D.2. One can observe that, when considering elevations larger than 20°, this ratio is smaller than 0.3. Furthermore, this value is closer to 0.25[1] for high and medium (40-50°) elevations.
As a rule of thumb, one would divide the distance between the station and the IPP$_{h=400\ km}$ by a factor 4 to obtain the distance between the station and IPP$_{h=100\ km}$.

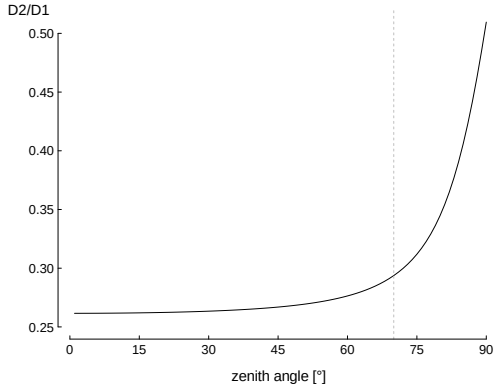

Figure D.2 – Influence of zenith angle z on the ratio between the distance joining the observation station and the IPPs related to $h_1 = 400$ km and $h_2 = 100$ km.

[1] Let us note that the value of 0.25 corresponds to the simplified case of an horizontally stratified ionosphere.

List of acronyms and abbreviations

AGW	Atmospheric Gravity Wave
AIC	Akaike Information Criterion
ANTEX	ANTenna EXchange
ARF	Antenna Reference Point
ARMA	AutoRegressive and Moving Average
BDN	Belgian Dense Network
C/A	Coarse/Acquisition
C/N_0	Carrier-to-Noise power density ratio
CIR	Corotating Interaction Region
CME	Coronal Mass Ejection
CORS	Continuously Operating Reference Stations
DD	Double Difference
DoD	Department of Defense
DOP	Dilution Of Precision
DOY	Day Of Year
DST	Disturbance Storm Time
ECMWF	European Center for Medium-range Weather Forecasts
EEJ	Equatorial Electrojet
EOF	Empirical Orthogonal Function
EUV	Extreme Ultraviolet
FAI	Field-Aligned Irregularities
FKP	Flachen Korrectur Parameter
FUV	Far Ultraviolet
GCR	Galactic Cosmic Ray
GF	Geometric-Free
GIM	Global Ionospheric Map
GLS	Generalized Least-Squares
GNSS	Global Navigation Satellite Systems
GPS	Global Positioning System

IF	Ionospheric-Free
IFB	Inter-Frequency Biases
IGS	International GNSS Service
IMF	Interplanetary Magnetic Field
IPP	Ionospheric Pierce Point
IQR	InterQuartile Range
IRI	International Reference Ionosphere
LEO	Low Earth Orbit
LoS	Line of Sight
LSTID	Large-Scale Traveling Ionospheric Disturbance
MEO	Medium Earth Orbit
MF	Mapping Function
MHD	MagnetoHydroDynamic
MSTID	Medium-Scale Traveling Ionospheric Disturbance
NL	Narrow-Lane
NNSS	Navy Navigation Satellite System
PC	Principal Component
PCA	Principal Component Analysis
PCO	Phase Center Offset
PCV	Phase Center Variations
PDOP	Positioning DOP
PPP	Precise Point Positioning
PRN	Pseudo Random Noise
RDOP	Relative DOP
RINEX	Receiver INdependent EXchange
RMS	Root Mean Square
RoTEC	Rate of TEC
RTK	Real-Time Kinematics
SBAS	Satellite-Based Augmentation System
SD	Single Difference
SID	Sudden Ionospheric Disturbance
SIP	Sub-Ionospheric Point
SITEC	Sudden Increase in TEC
SN	Summer Nighttime
SoDIPE-RTK	Software for Determining the Ionospheric Positioning Error on RTK
Sq	Solar quiet

SSTID	Small-Scale Traveling Ionospheric Disturbance
STEC	Slant TEC
SW	Space Weather
TEC	Total Electron Content
TECU	TEC Unit
TID	Traveling Ionospheric Disturbance
TIL	Tidal Ion Layer
TSI	Total Solar Irradiance
UERE	User Equivalent Range Error
VRS	Virtual Reference Station
VTEC	Vertical TEC
WD	Winter Daytime
WDC	World Data Center
WL	Wide-Lane

Bibliography

[1] Afraimovich, E.L.; Kosogorov, E.A.; Leonovich, L.A.; Palamartchouk, K.S.; Perevalova, N.P., and Pirog, O.M. Determining parameters of large-scale traveling ionospheric disturbances of auroral origin using GPS-arrays. *Journal of Atmospheric and Solar-Terrestrial Physics*, 62:553–565, 2000. (Cited on page 24.)

[2] Afraimovich, E.L.; Edemskiy, I.K.; Leonovich, A.S.; Leonovich, L.A.; Voeykov, S.V., and Yasyukevich, Y.V. MHD nature of night-time MSTIDs excited by the solar terminator. *Geophysical Research Letters*, 36(L15106), 2009. doi: 10.1029/2009GL039803. (Cited on page 30.)

[3] Artru, J.; Ducic, V.; Kanamori, H.; Lognonne, P., and Murakami, M. Ionospheric detection of gravity waves induced by tsunamis. *Geophysical Journal International*, 160:840–848, 2005. (Cited on page 29.)

[4] Banks, P.M. and Kockarts, G. *Aeronomy, A and B.* Academic Press, New York, 1973. (Cited on page 22.)

[5] Beach, T.L.; Kelley, M.C.; Kintner, P.M., and Miller, C.A. Total electron content variations due to nonclassical traveling ionospheric disturbances: Theory and global positioning system observations. *Journal of Geophysical Research*, 102(A4):7279–7292, 1997. (Cited on pages 28, 50 and 80.)

[6] Becerra, G.E. Vazquez. Analysis of stochastic properties of GPS observables. Technical report, The Ohio State Universtiy, Columbus, Ohio, October 2008. (Cited on page 41.)

[7] Becker-Guedes, F.; Sahai, Y.; Fagundes, P.R.; Espinoza, E.S.; Pillat, V.G.; Lima, W.L.C.; Basu, Su.; Basu, Sa.; Otsuka, Y.; Shiokawa, K.; MacKenzie, E.M.; Pi, X., and Bittencourt, J.A. The ionospheric response in the Brazilian sector during the super geomagnetic storm on 20 November 2003. *Annales Geophysicae*, 25:863–873, 2007. (Cited on page 24.)

[8] Beer, T. On atmospheric wave generation by the terminator. *Planetary and Space Science*, 26:185–188, 1978. (Cited on page 28.)

[9] Bertel, L.; Bertin, F., and Testud, J. The measurement of the total electron content applied to the observation of medium scale gravity wave. *Journal of Atmospheric and Terrestrial Physics*, 38:261–270, 1976. (Cited on page 29.)

[10] Bertin, F.; Testud, J.; Kersley, L., and Rees, P. The meteorological jet stream as a source of medium scale gravity waves in the thermosphere: an experimental study. *Journal of Atmospheric and Solar-Terrestrial Physics*, 40:1161–1183, 1978. (Cited on pages 29 and 86.)

[11] Blewitt, G. An automatic editing algorithm for GPS data. *Geophysical Research Letters*, 17(3):199–202, 1990. (Cited on page 53.)

[12] Box, G.E.P. and Jenkins, G.M. *Time Series Analysis: Forecasting and Control*. Holden-Day, 1976. (Cited on pages 117 and 118.)

[13] Bristow, W.A.; Greenwald, R.A., and Villain, J.P. On the seasonal dependence of medium-scale atmospheric gravity waves in the upper atmosphere at high latitudes. *Journal of Geophysical Research*, 101(A7):15685–15699, 1996. (Cited on pages 29 and 85.)

[14] Brockwell, P.J. and Davis, R.A. *Introduction to Time Series and Forecasting*. Springer, 2002. ISBN 978-0-387-95351-9. (Cited on pages 117 and 118.)

[15] Ciraolo, L.; Azpilicueta, F.; Brunini, C.; Meza, A., and Radicella, S.M. Calibration errors on experimental slant total electron content (TEC) determined with GPS. *Journal of Geodesy*, 81(2):111–120, 2007. (Cited on pages 18 and 53.)

[16] Collier, A.B. Principal component analysis of sub-ionospheric propagation conditions. In *International Conference on Ionospheric Radio Systems and Techniques (IRST)*, pages 86–90, Edinburgh, UK, 2009. The Institution of Engineering and Technology (IET). (Cited on page 108.)

[17] Corporation, ARINC Research. *Interface Control Document ICD-GPS-200: Navstar GPS Space Segment and Navigation User Interfaces*. CA, United States, April 2000. (Cited on pages 36 and 39.)

[18] Cosgrove, R.B. and Tsunoda, R.T. Instability of the E-F coupled nighttime midlatitude ionosphere. *Journal of Geophysical Research*, 109(A04305), 2004. (Cited on page 30.)

[19] Cosgrove, R.B.; Tsunoda, R.T.; Fukao, S., and Yamamoto, M. Coupling of the Perkins instability and the sporadic E layer instability derived from physical arguments. *Journal of Geophysical Research*, 109(A06301), 2004. (Cited on page 30.)

[20] Coster, A.J.; Gaposchkin, E.M., and Thornton, L.E. Real-time ionospheric monitoring system using the GPS. *Navigation*, 39(2):191–204, 1992. (Cited on page 165.)

[21] Cowpertwait, P.S.P. and Metcalfe, A.V. *Introductory Time Series with R*. Springer, 2009. ISBN 978-0-387-88697-8. (Cited on page 117.)

[22] Cravens, T.E. *Physics of Solar System Plasmas*. Cambridge University Press, 1997. (Cited on page 12.)

[23] Dach, R.; Hugentobler, U.; Fridez, P., and Meindl, M. *Bernese GPS software*. Astronomical Institute, University of Bern, January 2007. (Cited on page 44.)

[24] Davies, K. *Ionospheric radio*. Peter Peregrinus Ltd., London, 1990. ISBN 0-86341-186-X. (Cited on pages 3, 11, 13, 14, 16, 19, 22, 25, 26, 27, 36 and 115.)

[25] de Bakker, P.F.; van der Marel, H., and Tiberius, C.C.J.M. Geometry-free undifferenced, single and double differenced analysis of single frequency GPS, EGNOS and GIOVE-A/B measurements. *GPS solutions*, 13:305–314, 2009. (Cited on page 41.)

[26] de Bakker, P.F.; Tiberius, C.C.J.M.; van der Marel, H., and van Bree, R.J.P. Short and zero baseline analysis of GPS L1 C/A, L5Q, GIOVE E1B, and E5aQ signals. *GPS solutions*, 16(1):53–64, 2012. (Cited on page 41.)

[27] de Franceschi, G.; Alfonsi, L.; Romano, V.; Aquino, M.; Dodson, A.; Mitchell, C.N.; Spencer, P., and Wernik, A.W. Dynamics of high-latitude patches and associated small-scale irregularities during the October and November 2003 storms. *Journal of Atmospheric and Solar-Terrestrial Physics*, 70:879–888, 2008. (Cited on pages 23, 24, 61, 147 and 160.)

[28] de Toma, G.; White, O.R.; Knapp, B.G.; Rottman, G.J., and Woods, T.N. Mg II core-to-wing index: Comparison of SBUV2 and SOLSTICE time series. *Journal of Geophysical Research*, 102:2597–2610, 1997. (Cited on page 6.)

[29] de Toma, G.; White, O.R.; Chapman, G.A.; Walton, S.R.; Preminger, D.G.; Cookson, A.M., and Harvey, K.L. Differences in the Sun's Radiative Output in Cycles 22 and 23. *The Astrophysical Journal Letters*, 549:L131–L134, 2001. (Cited on page 6.)

[30] Ding, F.; Wan, W.; Ning, B., and Wang, M. Large-scale traveling ionospheric disturbances observed by GPS total electron content during the magnetic storm of 29-30 October 2003. *Journal of Geophysical Research*, 112(A06309), 2007. (Cited on pages 24 and 61.)

[31] ESA, the European Space Agency. EGNOS newsletter 5(2). `http://www.egnos-pro.esa.int/newsletter`, Sept. 2005. (Cited on page 158.)

[32] Garrison, J.L.; Lee, S-C.G.; Haase, J.S., and Calais, E. A method for detecting ionospheric disturbances and estimating their propagation speed and direction using a large GPS network. *Radio Science*, 42(RS6011), 2007. (Cited on page 50.)

[33] Gende, M.; Harris, E. Mohino; Brunini, C.; Radicella, S.M., and Herraiz, M. Ionospheric biases correction for coordinates derived from GPS single point positioning. *Annals of Geophysics*, 48(3), 2005. (Cited on page 45.)

[34] Georges, T.M. HF Doppler studies of traveling ionospheric disturbances. *Journal of Atmospheric and Terrestrial Physics*, 30:735–746, 1968. (Cited on page 24.)

[35] Georges, T.M. and Hooke, W.H. Wave-induced fluctuations in ionospheric electron content: a model indicating some observational biases. *Journal of Geophysical Research*, 75(31), 1970. (Cited on page 28.)

[36] Gomez, L.; Sabbione, J.I.; Zele, M.A. Van; Meza, A., and Brunini, C. Determination of a geomagnetic storm and substorm effects on the ionospheric variability from GPS observations at high latitudes. *Journal of Atmospheric and Solar-Terrestrial Physics*, 69:955–968, 2007. (Cited on pages 23, 24 and 160.)

[37] Gonzalez, W.D.; Joselyn, J.A.; Kamide, Y.; Kroehl, H.W.; Rostoker, G.; Tsurutani, B.T., and Vasyliunas, V.M. What is a geomagnetic storm? *Journal of Geophysical Research*, 99(A4):5771–5792, 1994. (Cited on pages 9, 10 and 23.)

[38] Guibas, L.J.; Knuth, D.E., and Sharir, M. Randomized incremental construction of Delaunay and Voronoi diagrams. *Algorithmica*, 7:381–413, 1992. (Cited on page 136.)

[39] Gurtner, W. RINEX: The Receiver Independent Exchange Format Version 2.10. `http://igscb.jpl.nasa.gov/igscb/data/format/`, Dec. 2007. (Cited on page 34.)

[40] Haldoupis, C.; Kelley, M.C.; Hussey, G.C., and Shalimov, S. Role of unstable sporadic-E layers in the generation of midlatitude spread F. *Journal of Geophysical Research*, 108(A12), 2003. (Cited on pages 26, 27, 97 and 101.)

[41] Haldoupis, C.; Meek, C.; Christakis, N.; Pancheva, D., and Bourdillon, A. Ionogram height-time-intensity observations of descending sporadic E layers at mid-latitude. *Journal of Atmospheric and Solar-Terrestrial Physics*, 68: 539–557, 2006. (Cited on pages 25 and 26.)

[42] Hartmann, G.K. and Leitinger, R. Range Errors due to Ionospheric and Tropospheric Effects for Signal Frequencies Above 100 MHz. *Bulletin Géodésique*, 58:109–136, 1984. (Cited on page 36.)

[43] Hernandez-Pajares, M.; Juan, J.M., and Sanz, J. Medium-scale traveling ionospheric disturbances affecting GPS measurements: spatial and temporal analysis. *Journal of Geophysical Research*, 111(A07S11), 2006. doi: 10.1029/2005JA011474. (Cited on pages 28, 29, 50, 54 and 86.)

[44] Hernandez-Pajares, M.; Juan, J.M.; Sanz, J.; Orus, R.; Garcia-Rigo, A.; Feltens, J.; Komjathy, A.; Schaer, S.C., and Krankowski, A. The IGS VTEC maps: a reliable source of ionospheric information since 1998. *Journal of Geodesy*, 83:263–275, 2009. (Cited on page 53.)

[45] Hernandez-Pajares, M.; Juan, J.M.; Sanz, J., and Aragon-Angel, A. Propagation of medium scale travelling ionospheric disturbances at different latitudes and solar cycle conditions. *Radio Science*, 2012. (Cited on page 24.)

[46] Hocke, K. and Schlegel, K. A review of atmospheric gravity waves and travelling ionospheric disturbances: 1982–1995. *Annales Geophysicae*, 14:917–940, 1996. (Cited on pages 27, 28 and 29.)

[47] Hofmann-Wellenhof, B.; Lichtenegger, H., and Collins, J. *GPS theory and practice*. Springer-Verlag, Wien, fifth, revised edition edition, 2001. (Cited on pages 31, 32, 34, 36, 53, 130, 131 and 165.)

[48] Hooke, W.H. Ionospheric irregularities produced by internal atmospheric gravity waves. *Journal of Atmospheric and Terrestrial Physics*, 30:795–823, 1968. (Cited on page 27.)

[49] Hoque, M.M. and Jakowski, N. Ionospheric bending correction for GNSS radio occultation signals. *Radio Science*, 46(RS0D06), 2011. (Cited on page 37.)

[50] Hunsucker, R.D. Atmospheric gravity waves generated in the high-latitude ionosphere: A review. *Reviews of Geophysics*, 20:293–315, 1982. (Cited on pages 24 and 29.)

[51] IGS, the International GNSS Service. Data and products. `http://igscb.jpl.nasa.gov/components/data.html`, Apr. 2012. (Cited on pages 18, 36, 39 and 40.)

[52] Jakowski, N.; Béniguel, Y.; Franceschi, G. De; Pajares, M. Hernandez; Jacobsen, K.S.; Stanislawska, I.; Tomasik, L.; Warnant, R., and Wautelet, G. Monitoring, tracking and forecasting ionospheric perturbations using GNSS techniques. *Journal for Space Weather and Space Climate*, 2(A22), 2012. (Cited on pages 23 and 24.)

[53] Kelley, M.C. On the origin of mesoscale TIDs at midlatitudes. *Annales Geophysicae*, 29:361–366, 2011. doi: 10.5194/angeo-29-361-2011. (Cited on pages 29 and 30.)

[54] Kotake, N.; Otsuka, Y.; Tsugawa, T.; Ogawa, T., and Saito, A. Climatological study of GPS total electron content variations caused by medium-scale traveling ionospheric disturbances. *Journal of Geophysical Research*, 111(A04306), 2006. doi: 10.1029/2005JA011418. (Cited on pages 28, 29 and 85.)

[55] Kouba, J. A guide to using international GNSS service (IGS) products. Technical report, Geodetic Survey Division, Natural Resources Canada, May 2009. (Cited on pages 36 and 40.)

[56] Lastovicka, J. Forcing of the ionosphere by waves from below. *Journal of Atmospheric and Solar–Terrestrial Physics*, 68:479–497, 2006. (Cited on page 29.)

[57] Leick, A. *GPS satellite surveying.* John Wiley & sons, Inc., Hoboken, New Jersey, third edition edition, 2004. (Cited on pages 36, 44 and 165.)

[58] Lejeune, S. *Influence de l'ionosphère sur le positionnement différentiel par GNSS.* PhD thesis, Université de Liège, 2010. (Cited on page 132.)

[59] Lejeune, S. and Warnant, R. A novel method for the quantitative assessment of the ionosphere effect on high accuracy GNSS applications, which require ambiguity resolution. *Journal of Atmospheric and Solar–Terrestrial Physics*, 70:889–900, 2008. (Cited on page 128.)

[60] Lejeune, S.; Wautelet, G., and Warnant, R. Ionospheric effects on relative positioning within GPS dense network. *GPS Solutions*, 16(1):105–116, 2012. (Cited on page 129.)

[61] Lonchay, M. Précision du positionnement par satellites: influence de la géométrie de la constellation. Master's thesis, Université de Liège, 2009. (Cited on pages 134 and 151.)

[62] Mannucci, A.J.; Wilson, B.D.; Yuan, D.N.; Ho, C.H.; Lindqwister, U.J., and Runge, T.F. A global mapping technique for GPS-derived ionospheric total electron content measurements. *Radio Science*, 33(3):565–582, 1998. (Cited on pages 18, 24 and 165.)

[63] Mastrantonio, G.; Einaudi, F.; Fua, D., and Lalas, D.P. Generation of gravity waves by jet streams in the atmosphere. *Journal of the Atmospheric Sciences*, 33:1730–1738, 1976. (Cited on pages 29 and 86.)

[64] Matsushita, S. *Physics of geomagnetic phenomena I*, chapter Solar quiet and lunar daily variation fields. Academic press, New-York, 1967. (Cited on page 15.)

[65] Mekaoui, S. and Dewitte, S. Total Solar Irradiance Measurement and Modelling during Cycle 23. *Solar Physics*, 247(1):203–216, 2007. (Cited on page 6.)

[66] Memarzadeh, Y. *Ionospheric modeling for precise GNSS applications.* PhD thesis, Technische Universiteit Delft, Netherlands, 2009. (Cited on pages 13 and 19.)

[67] Meyer, C.; Jakowski, N.; Borries, C.; Pannowitsch, T., and Belabbas, B. Extreme ionospheric conditions over Europe observed during the last solar cycle. In *Proceedings of the 4th ESA workshop on Satellite Navigation User Equipment Technologies (NAVITEC)*, ESTEC, Noordwijk, The Netherlands, December 2008. (Cited on pages 23 and 160.)

[68] Mohino, E. Understanding the role of the ionospheric delay in single-point single-epoch GPS coordinates. *Journal of Geodesy*, 82:31–45, 2008. (Cited on page 45.)

[69] NASA, Jet Propulsion Laboratory (JPL). GIM demo. `http://iono.jpl.nasa.gov/images/gim_demo.gif`, May 2012. (Cited on page 20.)

[70] NASA, The Goddard Space Flight Center (GSFC). `http://www.nasa.gov/centers/goddard/home/index.html`, Feb. 2012. (Cited on page 9.)

[71] Odijk, D. *Fast precise positioning in the presence of ionospheric delays.* PhD thesis, Delft University of Technology, Netherlands, 2002. (Cited on page 37.)

[72] Ogawa, T.; Nishitani, N.; Otsuka, Y.; Shiokawa, K.; Tsugawa, T., and Hosokawa, K. Medium-scale traveling ionospheric disturbances observed with the SuperDARN Hokkaido radar, all-sky imager, and GPS network and their relation to concurrent sporadic E irregularities. *Journal of Geophysical Research*, 114(A03316), 2009. (Cited on page 27.)

[73] Orus, R. *Contribution on the improvement, assessment and application of the Global Ionospheric VTEC Maps computed with GPS data.* PhD thesis, Universitat Politecnica de Catalunya (UPC), Spain, 2005. (Cited on pages 18, 165 and 168.)

[74] Otsuka, Y.; Shiokawa, K.; Ogawa, T., and Wilkinson, P. Geomagnetic conjugate observations of medium-scale traveling ionospheric disturbances at midlatitude using all-sky airglow imagers. *Geophysical Research Letters*, 31 (L15803), 2004. (Cited on page 27.)

[75] Perkins, F. Spread F and ionospheric currents. *Journal of Geophysical Research*, 78(1):218–226, 1973. (Cited on page 30.)

[76] Piggot, W.R. and Rawer, K. U.R.S.I. handbook of ionogram interpretation and reduction. Technical Report UAG-23A, World data center A for Solar-Terrestrial Physics, Warsaw, Poland, July 1978. Adopted by U.R.S.I. Commission III. (Cited on pages 16, 17, 26, 27 and 99.)

[77] Remondi, B.W. NGS Second Generation ASCII and Binary Orbit Formats and Associated Interpolated Studies. In *Proceedings of the Twentieth General Assembly, International Union of Geodesy and Geophysics*, Vienna, Austria, August 1991. (Cited on page 36.)

[78] Rishbeth, H. How the thermospheric circulation affects the ionospheric F2-layer. *Journal of Atmospheric and Solar–Terrestrial Physics*, 60:1385–1402, 1998. (Cited on pages 20 and 22.)

[79] Rishbeth, H. F–region links with the lower atmosphere? *Journal of Atmospheric and Solar–Terrestrial Physics*, 68:469–478, 2006. (Cited on page 29.)

[80] Rodger, A.S.; Moffett, R.J., and Quegan, S. The role of ion drift in the formation of ionisation troughs in the mid- and high-latitude ionosphere: review. *Journal of Atmospheric and Terrestrial Physics*, 54(1):1 – 30, 1992. doi: 10.1016/0021-9169(92)90082-V. (Cited on page 21.)

[81] Rothacher, M. and Schmid, R. Antex: The Antenna Exchange Format, Version 1.4. `http://igscb.jpl.nasa.gov/igscb/station/general/antex14.txt`, 15 September 2010. (Cited on page 40.)

[82] Saito, A.; Nishimura, M.; Yamamoto, M.; Fukao, S.; Kubota, M.; Shiokawa, K.; Otsuka, Y.; Tsugawa, T.; Ishii, M.; Sakanoi, T., and Miyazaki, S. Traveling ionospheric disturbances detected in the FRONT compaign. *Geophysical Research Letters*, 28(4):689–692, 2001. (Cited on pages 27, 28 and 29.)

[83] Schenewerk, M. A brief review of basic GPS orbit interpolation strategies. *GPS Solutions*, 6:265–267, 2003. (Cited on page 36.)

[84] Seeber, G. *Satellite Geodesy*. Walter de Gruyter, Berlin, New York, 2nd edition, 2003. (Cited on pages 34 and 37.)

[85] Skone, S.H. The impact of magnetic storms on GPS receiver performance. *Journal of Geodesy*, 75:457–468, 2001. (Cited on page 24.)

[86] Soicher, H. Traveling ionospheric disturbances (TIDs) at mid-latitudes: Solar cycle phase dependence. *Radio Science*, 23(3):283–291, 1988. (Cited on page 28.)

[87] Sparks, L.; Iijima, B.A.; Mannucci, A.J.; pi, X., and Wilson, B.D. A New Model for Retrieving Slant TEC Corrections for Wide Area Differential GPS. In *Proceedings of the 2000 National Technical Meeting of The Institute of Navigation*, pages 464–473, Pacific Hotel Disneyland, Anaheim, CA, January 2000. (Cited on page 165.)

[88] Spits, J. *Total Electron Content reconstruction using triple frequency GNSS signals*. PhD thesis, Université de Liège, 2012. (Cited on pages 18, 37, 40, 41 and 43.)

[89] Stankov, S.M.; Warnant, R., and Stegen, K. Trans-ionospheric GPS signal delay gradients observed over mid-latitude Europe during the geomagnetic storms of October-November 2003. *Advances in Space Research*, 43:1314–1324, 2009. (Cited on pages 23, 61 and 147.)

[90] Stankov, S.M.; Stegen, K., and Warnant, R. K-type geomagnetic index nowcast with data quality control. *Annals of Geophysics*, 54(3):285–295, 2011. (Cited on page 15.)

[91] Tsugawa, T.; Saito, A.; Otsuka, Y., and Yamamoto, M. Damping of large-scale traveling ionospheric disturbances detected with GPS networks during the geomagnetic storm. *Journal of Geophysical Research*, 108(A3), 2003. (Cited on page 24.)

[92] Tsugawa, T.; Kotake, N.; Otsuka, Y., and Saito, A. Medium-scale traveling ionospheric disturbances observed by GPS receiver network in Japan: a short review. *GPS Solutions*, 11:139–144, 2007. (Cited on pages 27, 28, 29, 30, 78, 79, 80, 81 and 82.)

[93] Tsurutani, B.T.; Judge, D.L.; Guarnieri, F.L.; Gangopadhyay, P.; Jones, A.R.; Nuttall, J.; Zambon, G.A.; Didkovsky, L.; Mannucci, A.J.; Iijima, B.; Meier, R.R.; Immel, T.J.; Woods, T.N.; Prasad, S.; Floyd, L.; Huba, J.; Solomon, S.C.; Straus, P., and Viereck, R. The October 28, 2003 extreme EUV solar flare and resultant extreme ionospheric effects: Comparison to other Halloween events and the Bastille Day event. *Geophysical Research Letters*, 32, 2005. (Cited on page 24.)

[94] Uppala, S.M.; Kallberg, P.W.; Simmons, A.J.; Andrae, U.; Da Costa Bechtold, V.; Fiorino, M.; Gibson, J.K.; Haseler, J.; Hernandez, A.; Kelly, G.A.; Li, X.; Onogi, K.; Saarinen, S.; Sokka, N.; Allan, R.P.; Andersson, E.; Arpe, K.; Balmaseda, M.A.; Beljaars, A.C.M.; van de Berg, L.; Bidlot, J.; Bormann, N.; Caires, S.; Chevallier, F.; Dethof, A.; Dragosavac, M.; Fisher, M.; Fuentes, M.; Hagemann, S.; Holm, E.; Hoskins, B.J.; Isaksen, L.; Janssen, P.A.E.M.; Jenne, R.; McNally, A.P.; Mahfouf, J.F.; Morcrette, J.J.; Rayner, N.A.; Saunders, R.W.; Simon, P.; Sterl, A.; Trenberth, K.E.; Untch, A.; Vasiljevic, D.; Viterbo, P., and Woollen, J. The ERA–40 re–analysis. *Quarterly Journal of the Royal Meteorological Society*, 131(612):2961–3012, 2005. (Cited on page 88.)

[95] van Velthoven, P.F.J. *Medium scale irregularities in the ionospheric electron content*. PhD thesis, Technische Universiteit Eindhoven, 1990. (Cited on pages 11, 28, 29, 79, 80, 85 and 86.)

[96] Viereck, R.A. and Puga, L.C. The NOAA Mg II core-to-wing solar index: Construction of a 20-year time series of chromospheric variability from multiple satellites. *Journal of Geophysical Research*, 104:9995–10005, 1999. (Cited on page 6.)

[97] Wanninger, L. The performance of virtual reference stations in active geodetic GPS-networks under solar maximum conditions. In *ION GPS '99*, Nashville TN,USA, 1999. (Cited on pages 145 and 149.)

[98] Warnant, R. *Étude du comportement du Contenu Électronique Total et de ses irrégularités dans une région de latitude moyenne. Application aux calculs de positions relatives par le GPS*. PhD thesis, Université Catholique de Louvain, 1996. (Cited on pages 18, 21, 40, 43, 52, 53, 54 and 60.)

[99] Warnant, R. and Pottiaux, E. The increase of the ionospheric activity as measured by GPS. *Earth Planets Space*, 52:1055–1060, 2000. (Cited on pages 54, 101, 136 and 138.)

[100] Warnant, R.; Kutiev, I.; Marinov, P.; Bavier, M., and Lejeune, S. Ionospheric and geomagnetic conditions during periods of degraded GPS position accuracy: 2. RTK events during disturbed and quiet geomagnetic conditions. *Advances in Space Research*, 39(5):881–888, 2007. (Cited on page 23.)

[101] Warnant, R.; Wautelet, G.; Spits, J., and Lejeune, S. Characterization of the ionospheric small-scale activity. Technical Report WP 220, GALOCAD Project, contract GJU/06/2423/CTR/GALOCAD, Royal Meteorological Institute of Belgium, June 2008. (Cited on page 59.)

[102] Wautelet, G. Étude des TID's à l'aide des GNSS : influence de la géométrie de la constellation. Master's thesis, Université de Liège, 2006. (Cited on pages 47, 48 and 49.)

[103] Wautelet, G. Étude climatologique des irrégularités ionosphériques détectées à l'aide des GNSS. D.E.A. thesis, Université de Liège, 2007. (Cited on pages 53 and 80.)

[104] Wautelet, G. and Warnant, R. Local climatological modeling of ionospheric irregularities detected by GPS in mid-latitude region. *Journal of Atmospheric and Solar–Terrestrial Physics*, 89:132–143, 2012. doi: 10.1016/j.jastp.2012.08.015. (Cited on page 106.)

[105] Wautelet, G.; Lejeune, S.; Stankov, S.; Brenot, H., and Warnant, R. Effects of small-scale atmospheric activity on precise positioning. Technical Report WP 230, GALOCAD Project, contract GJU/06/2423/CTR/GALOCAD, Royal Meteorological Institute of Belgium, June 2008. (Cited on page 130.)

[106] Whitehead, J.D. Production and Prediction of Sporadic E. *Reviews of Geophysics and Space Physics*, 8(1):65–144, 1970. (Cited on page 25.)

[107] Whitehead, J.D. Recent work on mid-latitude and equatorial sporadic-E. *Journal of Atmospheric and Terrestrial Physics*, 51(5):401–424, 1989. (Cited on pages 25 and 26.)

[108] Whitten, R.C. and Poppoff, I.G. *Fundamentals of aeronomy.* John Wiley & Sons, Inc., 1971. (Cited on pages 15, 16, 18, 19, 20, 21, 22 and 25.)

[109] Wintoft, P. and Cander, L.R. Twenty-four hour predictions of f0F2 using time delay neural networks. *Radio Science*, 35(2):395–408, 2000. (Cited on page 108.)

[110] World Data Center for Geomagnetism, Kyoto. `http://wdc.kugi.kyoto-u.ac.jp`, Feb. 2012. (Cited on page 10.)

[111] Xu, G. *GPS Theory, algorithms and applications.* Springer-Verlag, Berlin Heidelberg New York, 2003. (Cited on pages 165, 169 and 170.)

[112] Yashiro, S.; Gopalswamy, N.; Michalek, G.; Cyr, O.C. St.; Plunkett, S.P.; Rich, N.B., and Howard, R.A. A catalog of white light coronal mass ejections observed by the SOHO spacecraft. *Journal of Geophysical Research*, 109 (A07105), 2004. (Cited on page 8.)

[113] Yokoyama, T.; Hysell, D.L.; Otsuka, Y., and Yamamoto, M. Three-dimensional simulation of the coupled Perkins and Es-layer instabilities in the nighttime midlatitude ionosphere. *Journal of Geophysical Research*, 114 (A03308), 2009. (Cited on page 30.)